Kinematics Analysis of Two Parallel Locomotion Mechanisms

Ping Ren

DISSERTATION SUBMITTED TO
THE FACULTY OF THE VIRGINIA POLYTECHNIC INSTITUTE
AND STATE UNIVERSITY IN PARTIAL FULFILLMENT OF THE
REQUIREMENTS FOR THE DEGREE OF

DOCTOR OF PHILOSOPHY
IN
MECHANICAL ENGINEERING

Dennis W. Hong, Chair
Mehdi Ahmadian
Corina Sandu
Robert H. Sturges
Robert L. West

AUGUST 27, 2010
BLACKSBURG, VIRGINIA

Keywords: Kinematics, Mobile Robotics, Parallel Mechanisms, Mechanisms with Variable Topologies, Screw Theory

Kinematics Analysis of Two Parallel Locomotion Mechanisms

Ping Ren

ABSTRACT

This dissertation presents the kinematics study on two cases of parallel locomotion mechanisms. A parallel locomotion mechanism can be defined as "a mechanism with parallel configuration and discrete contact with respect to the ground which renders a platform the ability to move". The first case is a tripedal robot and the second case is an actuated spoke wheel robot. The kinematics study on these two mobile robots mainly includes mobility, inverse and forward kinematics, instantaneous kinematics, singularity and so on.

The tripedal robot STriDER (Self-excited Tripedal Dynamic Experimental Robot) is expected to walk utilizing its built-in passive dynamics, but in its triple stance phase, the kinematic configuration of the robot behaves like an in-parallel manipulator. The locomotion of this novel walking robot and its unique tripedal gait are discussed, followed by the definitions of its coordinate frames. Geometric methods are adopted for the forward and inverse displacement analysis in its triple stance phase. Simulations are presented to validate both the inverse and the forward displacement solutions. The instantaneous kinematics and singularity analysis are developed respectively. Based on the screw theory, the Jacobian matrices are assembled. Using *Grassmann Line Geometry*, each row of the Jacobian matrices is interpreted as a line in 3D space and the analytical conditions of the linear dependency cases are identified, which corresponds to the forward singular configurations of the robot.

The actuated spoke wheel robot IMPASS (Intelligent Mobility Platform with Active Spoke System) is investigated as the second case. It is revealed that this robot has multiple modes of locomotion on the ground and it is able to change its topology by changing the contact scheme of its spokes with the ground. This robot is treated as a mechanism with variable topologies and *Modified Grübler-Kutzbach criterion* and *Grassmann Line Geometry* are adopted to identify the degrees of freedom (DOF) for each case of its topological structures. The characteristic DOF are then verified through the testing on the robot prototype. The forward and inverse kinematics is investigated for two cases of its topologies. In order to improve the computation efficiency of the inverse kinematics formulation, virtual serial manipulator models are constructed. The effectiveness of the virtual serial manipulator models has been validated with numerical simulations.

In conclusion, kinematics analyses have been successfully performed on the two parallel locomotion mechanisms. The results are utilized to control the robots' motions in specific configurations. The foundation has been laid for the future development of the robot prototypes and the future research on dynamics, control, intelligence and so on.

ACKNOWLEDGEMENT

This dissertation is dedicated to the memory of all my relatives that passed away. Grandfather Mr. Zheng, Jinzhang, Grandmother Mrs. Wang, Zhiwen, Aunt Ren, Feng, and Cousin Li, Hao.

My greatest thanks go to my parents, Mr. Ren, Qiang, and Mrs. Zheng, Jianhua for their love and support through all my life and studies.

Many thanks to Dr. Dennis Hong. As my advisor, you guided me through my graduate study in RoMeLa Lab and assigned me the most fantastic robot projects in the world.

Many thanks to Dr. Mehdi Ahmandian, Dr. Corina Sandu, Dr. Robert Sturges and Dr. Bob West. As my committee members, you have given me great amount of valuable suggestion from which I benefit a lot.

Many thanks to my collaborators Ivette Morazzani, Jeremy Heaston, Derek Lahr, J.Blake Jeans, Shawn Kimeel, Marilyn Worley, for your great effort in the fabrication of the robot prototypes, testing of the hardware and collection of the testing data.

Many thanks to National Science Foundation and Office of Naval Research for their funding support to the robot projects I worked on.

Many thanks to my uncle Mr. Witt Wang, my aunt Mrs. Min Ma, my cousins Luna and Alex. I enjoy the days spent with you during my breaks.

Best wishes to STriDER and IMPASS. I hope that someday in the near future you two can walk out of the lab with your elegant motions!

Table of Contents

INTRODUCTION 1

I. Parallel Locomotion Mechanisms 1

II. Literature Review on Parallel Manipulators and Mechanisms with Variable Topologies 2

1. Parallel Manipulators 2

2. Mechanisms with Variable Topologies 6

III. Contribution 7

Case I: STriDER (Self-excited Tripedal Dynamic Experimental Robot)

Chapter 1 Introduction to STriDER 7

1.1. Locomotion 10

1.2. Triple Stance Phase 12

1.3. Summary 17

Chapter 2 Forward and Inverse Displacement Analysis 18

2.1. Mobility Analysis 18

2.2. Inverse Displacement Analysis 19

2.3. Forward Displacement Analysis 22

2.3.1. Nomenclature "N_1 - N_2 – N_3" and Introduction 22

2.3.2. Nine Joint Angles Sensed Case [3-3-3] 22

2.3.3. Eight Joint angles sensed case [3-3-2] 24

2.3.4. Seven Joint angles sensed case [3-3-1 & 3-2-2] 25

2.3.5. Six Joint Angles Sensed Case [2-2-2 & 3-2-1] 30

2.4. Application of Forward Displacement Analysis in Joint Sensor Fault Detection 34

2.4.1. Sensor Fault Detection Scheme 34

2.4.2. Summary and Discussion 36

Chapter 3 Simulation of the Inverse and Forward Kinematics Algorithm 37

3.1. Inverse Kinematics Example 37

3.2. Forward Kinematics Example 38

Chapter 4 Jacobian Analysis 45

4.1. Introduction to Screws, Wrenches, and Twists 45

4.2. Jacobian Analysis Using Reciprocal Screws 46
4.3. Identification of Reciprocal Screws 46
4.4. Screw-Based Jacobian Matrix of STriDER 48
Chapter 5 Singularity Identification and Elimination 53
5.1. Inverse Singularities 54
5.2. Introduction to Grassmann Line Geometry 55
5.3. Possible Forward Singular Configurations and Their Elimination 56
5.4. Inverse and Forward Singular Configurations 69
5.4.1. Inverse Singular Configurations 69
5.4.2. Forward Singular Configurations 70

Case II: IMPASS (Intelligent Mobility Platform with Actuated Spoke-Wheel Systems)

Chapter 6 Introduction to IMPASS 75
6.1. Classification of the Variable Topologies 77
6.2. Locomotion 79
Chapter 7 Mobility Analysis on the Variable Topologies 81
7.1. "1-1: Parallel" Contact Cases 82
7.2. "2-1", "1-2" and "2-2" Contact Cases 88
7.2.1. "2-1" and "1-2" Cases 88
7.2.2. "2-2" Cases 91
7.3. "1-1: skew" Contact Case 99
7.4. Other Contact Cases 100
Chapter 8 Experimental Verification of the Characteristic Motions 106
8.1. Straight-line Walking 107
8.2. Steady State Turning 110
8.3. Turning Gait Transition 110
8.4. Geometric Characteristics of Steady State Turning and Turning Gait Transition 112
8.5. Rotation of the Body in the "3-3" Contact Case 114
Chapter 9 Forward and Inverse Kinematics Analysis 115
9.1. Formulation of the Forward Kinematics 116
9.2. Inverse Kinematics Based on the Forward Kinematics Model 120

9.3. Numerical Examples of the Forward and Inverse Kinematics 122
9.3.1. Forward Kinematics Simulation 122
9.3.2. Two Cases of the Inverse Kinematics Simulation and Potential Computation Issues 122
9.4. Inverse Kinematics Formulation with Reduced Equation Systems 127
9.4.1. Kinematic Models based on Virtual Serial Manipulators 127
9.4.2. Derivation of the Reduced Equation Systems 132
9.4.3. Numerical Examples and Results 137
CONCLUSION AND FUTURE RESEARCH 143
I. Approaches 143
II. Conclusions 143
1. STriDER 143
2. IMPASS 143
III. Future Research 144
REFERENCES 146

List of Figures and Tables

FIG.I GENERAL STEWART PLATFORM……3

FIG.II AN EXAMPLE OF AN IN-PARALLEL MANIPULATOR……4

FIG.III THE RELATIONSHIP OF PARALLEL LOCOMOTION MECHANISM WITH RELATED DISCIPLINES……...7

FIG.1.1 STriDER (SELF-EXCITED TRIPEDAL DYNAMIC EXPERIMENTAL ROBOT) ……...9

FIG.1.2 SINGLE STEP TRIPEDAL GAIT……11

FIG.1.3 GAIT FOR CHANGING DIRECTIONS……..11

FIG.1.4 STRIDER PROTOTYPES……12

FIG.1.5 COORDINATE FRAMES AND JOINT DEFINITIONS ……13

TABLE 1.1 NOMENCLATURES……..14

TABLE 1.2 LINK PARAMETERS……15

FIG.1.6 GENERAL KINEMATIC REPRESENATION ……...16

FIG. 2.1 ELBOW MANIPULATOR REPRESENTATION……..19

FIG.2.2 INTERSECTION OF TWO CIRCLES [3-3-2 CASE] ……25

FIG.2.3 SPHERE AND CIRCLE INTERSECTION……..27

FIG.2.4 SELF-INTERSECTION HORN TORUS……..28

FIG.2.5 TORUS AND CIRCLE INTERSECTION……28

FIG.2.6 CIRCULAR PLANE AND CIRCLE INTERSECTION……...29

FIG.2.7 GENERAL NON REDUNDANT [2-2-2 CASE] ……31

TABLE 3.1 BODY POSITION AND ORIENTATION RELATIVE TO

GLOBAL COORTINATES……37

TABLE 3.2 GLOBAL FOOT POSITIONS FOR EACH LEG……..38

TABLE 3.3 INVERSE DISPLACEMENT ANALYSIS RESULTS (ELBOW DOWN) ……38

TABLE 3.4 FORWARD DISPLACEMENT ANALYSIS RESULTS……..……39

FIG.3.1 FORWARD DISPLACEMENT SOLUTION 1……39

FIG.3.2 FORWARD DISPLACEMENT SOLUTION 2……40

FIG.3.3 FORWARD DISPLACEMENT SOLUTION 3……41

FIG.3.4 FORWARD DISPLACEMENT SOLUTION 4……42

FIG.3.5 FORWARD DISPLACEMENT SOLUTION 5…….43

FIG.3.6 FORWARD DISPLACEMENT SOLUTION 6……..……44

FIG.4.1 THE JOINT SCREWS AND RECIPROCAL SCREWS IN LEG I……...…48

FIG.5.1. INVERSE SINGULARITY, CASE ONE…….54

FIG.5.2. INVERSE SINGULARITY, CASE TWO……...55

FIG.5.3 VARIOUS TYPES OF LNE VARIETIES……56

FIG.5.4 CASE 1……..58

FIG.5.5 CASE 1 (DOUBLE) …….58

FIG.5.6 CASE 1 (TRIPLE) ……59

FIG.5.7 CASE 2b-1…….....60

FIG.5.8 CASE 2b-1(DOUBLE) ……..……...61

FIG.5.9 CASE 2b-2(SPECIAL) ……..……..…..61

FIG.5.10 CASE 3b……..62

FIG.5.11 CASE 3c……..63

FIG.5.12 CASE 3d-1……...64

FIG.5.13 CASE 3d-2……...65

FIG.5.14 CASE 4b……..66

FIG.5.15 CASE 4d……..67

FIG.5.16 CASE 5a ……68

FIG.5.17 CASE 5b ……69

FIG.5.18 INVERSE SINGULAR CONFIGURATIONS……...…70

FIG.5.19 CASE 1……....71

FIG.5.20 CASE 2b……..72

FIG.5.21 CASE 3d……..73

FIG 5.22 CASE 4d……..73

FIG.5.23 CASE 5d……..74

FIG.6.1 THE PROTOTYPE OF IMPASS……..76

FIG.6.2 KINEMATIC MODEL OF THE IMPASS WITH TWO SPOKES AND THE TAIL IN CONTACT WITH THE SMOOTH GROUND……..…78

FIG.6.3 TOPOLOGY TRANSFORMATIONS OF THE COMMON CONTACT CASES OF IMPASS ……..80

FIG.7.1 SPHERICAL-PRISMATIC DYAD AND ITS RECIPROCAL SCREW SYSTEM……82

FIG.7.2 CONSTRAINT SCREW SYSTEM AND DOF OF: (A) THE "1-1: PARALLEL &UNEQUAL" CASE; (B) THE "1-1: PARALLEL & EQUAL" CASE……83

FIG.7.3 MOTION SCREW SYSTEM OF A RPPR MECHANISM WITH $q_{11} \neq q_{21}$ AND $q_{12} = q_{22} \neq 90°$……...…85

FIG.7.4 MOTION SCREW SYSTEM OF A SPECIAL RPPR MECHANISM WITH $q_{11} = q_{21}$ AND $q_{12} = q_{22} = 90°$……..87

FIG.7.5 CONSTRAINT SCREW SYSTEM OF: (A) THE "2-1: PARALLEL &UNEQUAL" CASE; (B) THE "1-2: PARALLEL & UNEQUAL" CASE……..…89

FIG.7.6 CONSTRAINT SCREW SYSTEM OF: (A) THE "2-1: PARALLEL &EQUAL" CASE; (B) THE "1-2: PARALLEL & EQUAL" CASE……..……90,91

FIG.7.7 CONSTRAINT SCREW SYSTEM OF THE "2-2: PARALLEL & EQUAL" CASE……..…92

FIG.7.8 2D PROJECTION OF THE DOF IN THE "2-2: PARALLEL & EQUAL" CASE……..…93

FIG.7.9 (A) CONSTRAINT ELLIPSE AND (B) EFFECTIVE REGION……..…94

FIG.7.10 (A) CONTINUOUS EFFECTIVE RANGE OF φ AND (B) DISCONTINUOUS EFFECTIVE RANGE OF φ ……...…95,96

FIG.7.11 TWO EXTREME CASES WHEN φ HAS EMPTY EFFECTIVE RANGE……..…96,97

FIG.7.12 RELATIONSHIP OF φ, l_1 AND l_2……...97

FIG.7.13 CONSTRAINT SCREW SYSTEM OF THE "2-2: PARALLEL & UNEQUAL" CASE…....99

FIG.7.14 CONSTRAINT SCREW SYSTEM AND DOF OF THE "1-1: SKEW" CASE……..…100

FIG.7.15 CONSTRAINT SCREW SYSTEM OF THE "3-3: PARALLEL & EQUAL" CASE……..…101

FIG.7.16 CONSTRAINT SCREW SYSTEM OF: (A) THE "1-2: PARALLEL & EQUAL" CASE; (B) THE "2-2: PARALLEL & EQUAL" CASE…….102

FIG.7.17 CONSTRAINT SCREW SYSTEM OF: (A) THE "1-3: PARALLEL & EQUAL" CASE; (B) THE "1-2: SKEW" CASE……....103

FIG.7.18 THREE EXAMPLES OF THE CONTACT CASES WITH THE AXLE'S DOF AS ZERO..104

FIG.7.19 CONSTRAINT SCREW SYSTEM OF A SPECIAL "2-2: PARALLEL & UNEQUAL" CASE WITH FOUR NON-COPLANAR CONTACT POINTS……..…105

FIG.8.1 THE INTERNAL MECHANISM OF THE HUB……...…106

FIG.8.2 STRAIGHT-LINE WALKING USING "1-1: PARALLEL & EQUAL" AND "2-2: PARALLEL & EQUAL" ……..107

FIG.8.3 IMPASS' CLIMBING AN 18-INCH OBSTACLE USING "1-1: PARALLEL & EQUAL" AND "2-2: PARALLEL & EQUAL" ……109

FIG.8.4 STRAIGHT-LINE WALKING USING "2-2: PARALLEL & EQUAL" AND "3-3: PARALLEL & EQUAL" ……..109

FIG.8.5 STEADY STATE TURNING ……....110

FIG.8.6 TURNING GAIT TRANSITION……..……..111

FIG.8.7 DISCRETE MOTION OF STEADY STATE TURNING……..……112

FIG.8.8 LIFTING OF THE TAIL IN THE "3-3: PARALLEL & EQUAL" CONTACT CASE….……114

FIG.9.1 "1-1: PARALLEL" CONTACT CASE……...115

FIG.9.2 "1-1: SKEW" CONTACT CASE……116

FIG.9.3 SURFACE CONTACT PAIR……118

TABLE 9.1 BASIC GEOMETRIC PARAMETERS OF THE IMPASS MODEL……..…122

FIG.9.4 FORWARD KINEMATICS SOLUTION FOR A "1-1: PARALLEL & UNEQUAL" CASE……..123

TABLE 9.2 INVERSE KINEMATICS SOLUTIONS TO CASE 1: B_x AND B_y SPECIFIED……123

FIG.9.5 FOUR SOLUTIONS TO THE INVERSE KINEMATICS SIMULATION CASE 1……..…124

TABLE 9.3 INVERSE KINEMATICS SOLUTIONS TO CASE 2: y_{bx} AND y_{by} SPECIFIED……...…125

FIG.9.6 EIGHT SOLUTIONS TO THE INVERSE KINEMATICS SIMULATION CASE 2……125,126

FIG.9.7 VIRTUAL SERIAL MANIPULATOR MODEL FOR THE "1-1: PARALLEL" CONTACT CASE……..128

FIG.9.8 VIRTUAL SERIAL MANIPULATOR MODEL FOR THE “1-1:SKEW” CONTACT CASE……..130,131

FIG.9.9 FORWARD KINEMATICS SOLUTION FOR A “1-1: SKEW” CASE……...140

INTRODUCTION

One focus of today's robotics science and technology is to develop novel locomotion mechanisms that possess adequate mobility in various environments. With the implementation of appropriate locomotion schemes, mobile platforms can perform those tasks that are dirty, dull, dangerous or inaccessible to human beings, such as scientific exploration of remote areas, military surveillance, search and rescue missions and so on. The locomotion of traditional manned ground vehicles mainly includes wheels, tracks and hybrid combinations of both. However, the growing demand for lightweight mobile robots calls for innovative concepts on alternative locomotion.

I. Parallel Locomotion Mechanisms

The scientific study on legged locomotion as an alternative to wheels and tracks began over a century ago, and a human-controlled, four-legged walking machine with adjustable gaits was firstly built at General Electric in mid-1960s, as was introduced in [1].

Through the viewpoint of modern kinematics, wheeled or tracked vehicles are inherently different from legged walking machines in that the former always maintain continuous contact with the ground while the latter have discrete contact with the ground. Additionally, in any of its stable configurations, the body or platform of the walking machine is always connected to the ground through multiple in-parallel branches. As the legs or branches are lifted above and then put down, the body is moved from place to place. Meanwhile, as the machine walks, the location and geometry of the virtual base formed by the contact feet on the ground change as well.

Based on the preliminary discussion above, a class of alternative locomotion mechanisms can be proposed which distinguish themselves by their kinematically parallel configurations. A parallel locomotion mechanism can be defined as "a mechanism with parallel configuration and discrete contact with respect to the ground which renders a platform the ability to move". Another important and necessary characteristic of a parallel locomotion mechanism is its ability to change topologies. Usually, a parallel locomotion mechanism has more than one topology; when a branch is lifted above the ground, the topology of the mechanism changes correspondingly, as well as the geometry of its virtual base on the ground. For such locomotion mechanisms, a fundamental research on their kinematics is quite necessary, as it will lay the foundation for other studies such as design optimization, dynamics modeling, nonlinear control, motion planning and so on.

Previous examples of parallel locomotion mechanisms can be found in biped humanoid robots, four legged or six legged biomimetic robots and so on. This dissertation presents the kinematics analysis of two novel mobile robots currently under development at RoMeLa: Robotics and Mechanisms Laboratory in Virginia Tech. Each robot features a different case of parallel locomotion mechanism. The first robot is named STriDER (Self-excited Tripedal Dynamic Experimental Robot), which is a three-legged robot utilizing its build-in passive dynamics for walking. Its novel tripedal gait and triple stance phase are introduced in Chapter 1, with Chapter 2 to 5 mainly addressing the inverse and forward kinematics, instantaneous kinematics and singularities in its triple stance phase. The second robot is named IMPASS (Intelligent Mobility Platform with Active Spoke System), which is an actuated spoke

wheeled robot that has various topologies with respect to the ground. The uniqueness of this spoke wheel is that each spoke can be actuated to stretch in or out independently. The robot's multiple modes of locomotion are introduced in Chapter 6. The DOF (Degrees Of Freedom), inverse and forward kinematics in each topology are analyzed through Chapter 7 to 9. Finally, Chapter 10 summaries the conclusions obtained based on the current research on these two robots, and discusses the future research.

Please note that the term "mobility" referred in this work has two types of definitions. One is defined as the overall quality of a mobile robot's free moving over all types of terrains while retaining its ability to perform its primary mission. The other is defined as the continuous or instantaneous DOF in the configuration of a mechanism, which has quantitative values.

II. Literature Review on Parallel Manipulators and Mechanisms with Variable Topologies

Previous works in the areas of parallel manipulators and mechanisms with variable topologies (MVTs) provide background and insight for the work with the two cases of parallel locomotion mechanisms: three-legged robot STriDER and spoke-wheeled robot IMPASS. In this section, a literature review of the past research on parallel manipulators is presented firstly, followed by the review on the works of mechanisms with variable topologies.

1. Parallel Manipulators

In this section, the concept of parallel manipulators is introduced at first. The literature reviews on parallel manipulators can mainly be divided into three areas. First, inverse and forward kinematics, also called the inverse and forward displacement analysis. This area focuses on the calculation of the position/orientation of the end-effector (body) with the known joint variables and the calculation of the joint variables with given position/orientation of the end-effector. The second area is the Jacobian kinematics, also called instantaneous kinematics. The Jacobian matrix is developed for the mapping between the joint rate space and the end-effector velocity space. The third area is singularity analysis. With various methods, the singularity configurations of parallel manipulators are identified and the elimination scheme is proposed.

During the last two decades, many researchers have studied extensively the kinematics of parallel manipulators. A typical parallel manipulator consists of a moving platform that is connected to a fixed base by several branches. Compared with serial manipulators, parallel manipulators usually can provide better motion accuracy, rigidity, speed and larger load-to-weight ratio. One reason is that the accumulated error and load are shared by multiple branches instead of one. However, due to the existence of multiple close loops in their mechanical architectures, the workspace generated by parallel manipulators is smaller than their serial counterparts and the kinematics are much more complicated. Although those two drawbacks exist for parallel manipulators, in a large number of operation cases which require high precision and high speed positioning in smaller workspace, the noticeable advantages of parallel manipulators can overcome their drawbacks. Nowadays, parallel manipulators are

widely used in machine tools, medical applications, haptics devices, motion simulators and so on.

In 1965, Stewart first introduced a novel six DOF mechanism with six independent extensible limbs, which is mainly used in flight simulators and widely known as the Stewart platform [2]. Fig.I displays the typical structure of s Stewart platform. Hunt considered the Stewart platform and other parallel mechanisms as robot manipulators in [3] and among various types of parallel manipulators, Stewart platform is not only the most representative but also the most complicated. Many other researchers who studied the kinematics of parallel manipulators demonstrated that parallel manipulators have many inverse characteristics to that of serial manipulators.

Podhorodeski and Pittens considered strictly-serial and fully-parallel manipulators (Stewart platform, see Fig.I) as two extreme cases of a broader class of manipulator structures, which consist of several branches, each comprised of actuated and passive joints distributed in a serial manner, acting in parallel on a common end-effector [4]. Manipulators possessing such structures are termed in-parallel manipulators. Through proper design, in-parallel manipulators can exploit the advantages of both fully-parallel and strictly-serial devices. Considering the various types of joint, the in-parallel manipulators can expand into a huge family. Fig.II shows the concept of an in-parallel manipulator. Note that, the most right branch of this in-parallel manipulator is claimed by the author to be kinematically simple. This property can be utilized to make the solutions of its kinematic problems relative easy to obtain.

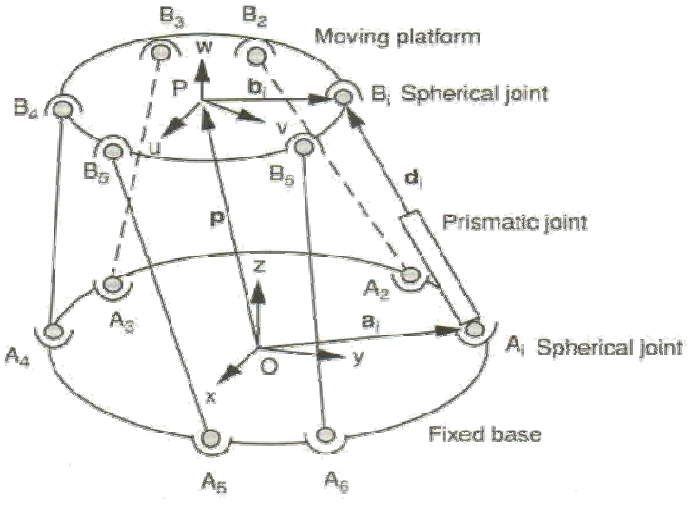

FIG.I GENERAL STEWART PLATFORM [2]

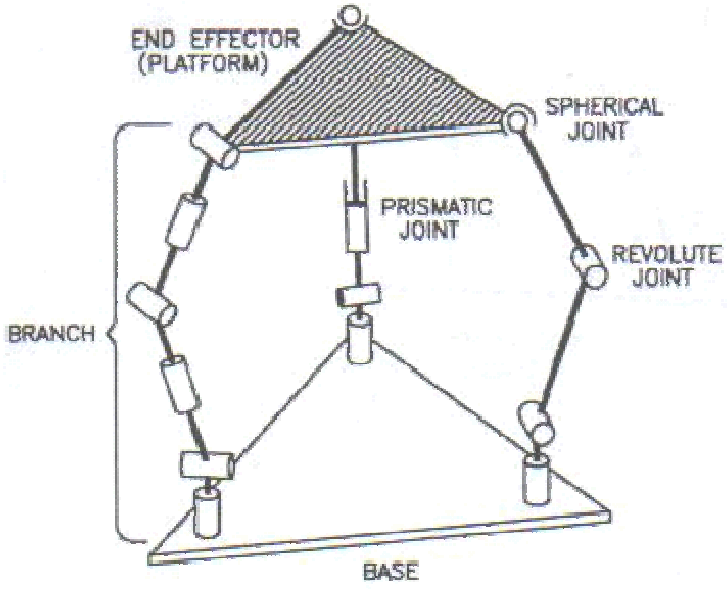

FIG.II AN EXAMPLE OF AN IN-PARALLEL MANIPULATOR [4]

In general, forward kinematics problem of a parallel manipulator is more difficult than its inverse kinematics problem due to the existence of multiple forward displacement solutions. As for a serial manipulator, the opposite is usually true. Numerical methods such as continuation method have often been used to solve the forward displacement problems of 6 DOF parallel manipulators. Closed-form solutions can also be obtained in some special cases of the Stewart platform as in [5-7] and often end up with solving a 16th order polynomial equation with respect to a single variable. Specifically, as discussed in [8], there are mainly two methods to the FDP of parallel manipulators: numerical approach and closed-form solution approach. In 1993, Raghavan successfully applied a numerical method utilizing the continuation method originally proposed by Garcia in [9] to solve the FDP of general Stewart Platforms and obtain all 40 solutions in complex field [10]. Unlike numerical approach, closed-form solution approach usually firstly eliminates the unknown variables from the polynomial system to reach an analytical characteristic polynomial equation with respect to a single variable, and then solve for the closed-form solutions. If the characteristic equation has an order lower than five, then the solutions can be represented with analytical expressions. Based on the development of the closed-form solution to the FDP of Stewart Platforms, the FDP of three-branch in-parallel manipulators can now be solved by treating the in-parallel manipulator as a special case of a Stewart Platform. The forward position analysis on a general 3/6 Stewart Platform, referred as Triangular Symmetric Simplified Manipulator (TSSM) in [11], was developed by Innocenti and Parenti-Castelli in [6]. Later, Merlet solved the FDP of a Stewart Platform with hexagonal mobile platform in [12] and concluded that a general parallel manipulator with a triangular platform had at most 16 forward displacement solutions (assembly modes). Based on the concept of kinematically simple branches in [4],

Notash and Podhorodeski proposed a class of three-branch six DOF. in-parallel manipulators with revolute joins and passive spherical joints in [13]. The FDP of this class of manipulators with non-redundant sensing schemes can still refer to [4]. The authors of [13] examined all the redundant sensing cases with more than six known joint angles and came up with the complete forward displacement solutions for this class of in-parallel manipulators with actuated revolute joints. Later, in their following work in [14], the FDP with not only actuated revolute joints but also prismatic ones are discussed. The three-branch six DOF minimanipulator invented by Tahmasebi and Tsai in 1994 uses three five-bar linkage drivers as inputs and it also has at most 16 closed-form forward displacement solutions [15].

In the past twenty years, the study on in-parallel manipulators with three legs was particularly addressed. Notash and Podhorodeski proposed a three-legged Revolute-Revolute-Revolute-Spherical (RRRS) in-parallel manipulator with kinematically simple joint-layouts in [13] and provided analysis on its complete forward displacement solutions. Later, they expanded their method to general three legged parallel manipulators which not only have revolute joints but also have prismatic joints. Other types of three legged in-parallel manipulators were also studies. Such three-legged manipulators included the Prismatic-Prismatic-Spherical-Revolute (PPSR) mini-manipulator built by Tsai and Tahmasebi [15, 16], the PPRS built by Ben-Horin and Shoham [17], the PPSP built by Byun and Cho [20], the Universal-Spherical-Revolute (USR) proposed by Simaan [18], the URS built by Angeles et al [19] and so on. All those three-legged in-parallel manipulators share a common kinematic characteristic, that is, each leg has one passive 3 DOF spherical joint and three actuated or unactuated 1 DOF., thus allowing the mobile platform of the manipulator to have 6 DOF.

Among these literatures, the work done by Notash and Podhorodeski are the most notable, because they not only studied the forward kinematics with 6 actuated joints but also the redundant cases with more than 6 active joints. The results from their research demonstrated that redundant active joints are really an asset for the in-parallel manipulator because they can reduce the number of forward displacement solutions, thus allowing for fault tolerance operations.

Not only the forward and inverse kinematics but also the Jacobian and singularity analysis of three legged in-parallel manipulators received a lot of attention from previous researchers. Tsai outlined two methods to develop the Jacobian matrices for parallel manipulators in [20]. One is conventional Jacobian analysis based on velocity vector-loop method; the other is screw-based Jacobian utilizing theory of reciprocal screws. Since these in-parallel manipulators have three serial legs connecting the platform to the base, it is necessary to examine singularities of both forward and inverse kinematics. Singularity analysis with conventional Jacobian requires finding the conditions under which the determinant of the Jacobian matrix is equal to zero. Singularity identification with screw-based Jacobian can be developed using line geometry, a.k.a *Grassmann Line Geometry*, because each row of the screw-based Jacobian matrix is equivalent to a Plücker line coordinate. By checking the linear dependency of these spatial lines as described in [21] and [22], the singularities can be identified.

Due to the existence of multiple loops in an in-parallel manipulator, the analytical expression of the Jacobian matrix in an in-parallel manipulator is very complicated.

Therefore, it is extremely difficult to derive the determinant of the Jacobian matrix and factorize the huge expression to derive the analytical conditions of singularity. Compared with conventional Jacobian, screw-based Jacobian in associate with line geometry shows a lot of advantages in identifying the singularity from a Jacobian matrix with very complicated form, especially when the in-parallel manipulator can be actuated either non-redundantly or redundantly. Since under redundant actuation, the Jacobian matrix of the kinematic system is no longer a six by six square matrix, such matrices have no determinant and checking the linear dependency of each column is quite inefficient. Notash [23, 24] and Dash [25] used screw-based Jacobian together with line geometry to consider the dependency of actuated joint wrenches and find singularities. Notash also proposed the elimination of joint wrench degeneracy by appropriate redundant actuation. Hao and McCathy [26] investigated the conditions required for parallel manipulators to have line-based singularities and concluded that having spherical joints on the mobile platform is a sufficient condition to ensure the line-based singularities of parallel manipulators.

Various approaches other than line geometry have been performed for the singularity analysis on three-legged parallel manipulators. Ebert-Uphoff et al. [27] investigated the singularity of a characteristic tetrahedron which corresponds to the singularity of the manipulator. Yang et al. [28] developed his singularity analysis by focusing on the velocities of passive joints. Angeles et al. [19] found the singularities of the three legged URS robot by analyzing the singularities of the serial-equivalent manipulator. Recently, Ben-Horin and Shoham enumerated all possibilities of the kinematic structure of three-legged in-parallel manipulator and proposed Grassmann-Cayley algebra as a tool to obtain the singularity conditions of this family of manipulators [29].

2. Mechanisms with Variable Topologies

MVTs are a special type of mechanisms sophisticatedly designated with the ability of changing topologies. During the topology changing process of MVTs, not only the numbers and/or kinematic types of links and joints are changeable but also the mobility of mechanisms is variable [30, 31]. Some notable MVTs presented in recent years include:

Kinematotropic linkages, originally proposed by Wohlhart in 1996 in [32] and then extended to four basic kinematotropic single-loop chains by Galletti *et al*. based on the theory of displacement groups in [33]. In such mechanisms, the types of the joints and the number of the links are not changing. However, the mobility of the complete mechanical system changes due to the variation of the joint variables.

Metamorphic mechanisms of foldable/erectable kinds, suggested by Dai et al. in [34, 35]. The first type of metamorphic mechanism is a “mechanism whose number of effective links changes as it moves from one configuration to another” [34]. It was inspired by a cardboard box comprised of flat card creased to enable the folding or unfolding of a structure. Its mobility changes through the combination of card panels (treated as kinematic links) as well as the predetermined location of the creases (treated as revolute joints). The pop-up paper mechanisms presented by Winder *et al.* in [36] could also be classified into this type.

Metamorphic mechanisms with variable joints. In the second type of metamorphic mechanism, the change of the topological structure is achieved through applying adjustable geometric constraints to certain joints. A notable example is the metamorphic parallel

mechanism with rT joints in [37]. In this novel rT joint, one of its revolute joint is used to modify the assembly of the other two joints. The rT joint is actually a variable universal joint. As the directions of the rT joint's two principal rotation axes change, the mobility of the platform changes as well. Similar work can be found in [31], in which a logical foundation based on graph theory was provided for the analysis on variable kinematic joints.

III. Contribution

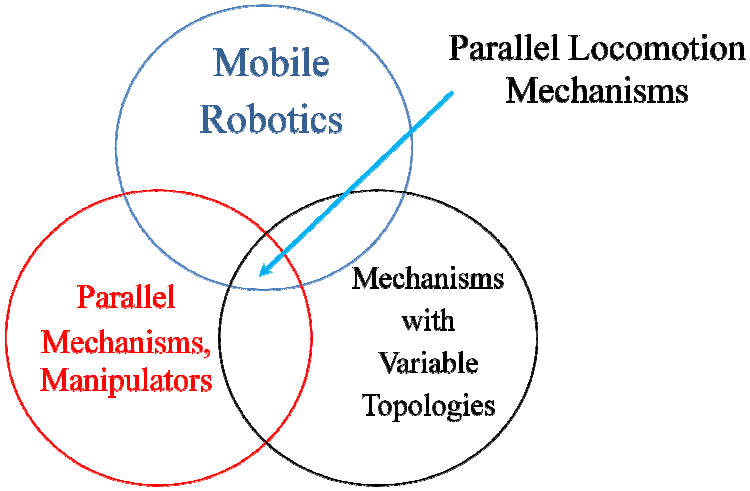

FIG.III THE RELATIONSHIP OF PARALLEL LOCOMOTION MECHANISM WITH RELATED DISCIPLINES

As a summary, the parallel locomotion mechanisms proposed is a new interdisciplinary area, which requires background knowledge in mobile robotics, parallel mechanisms and mechanisms with variable topologies. The contribution of this work mainly lies in three aspects. First, the scope and depth of mechanism kinematics are expanded through solving the practical problems in the two novel robotic systems, i.e. STriDER and IMPASS. Secondly, the conclusions and results obtained from this kinematics study can be used to guide the design and testing of the robot prototypes for the two projects and establish frameworks for their future research in dynamics, control, intelligence and so on. Thirdly, the author wishes this work could have broader impact on other researchers, thus promoting more innovations of locomotion mechanisms to improve robots' general mobility in various environments.

Case I: STriDER (Self-excited Tripedal Dynamic Experimental Robot)

Chapter 1 Introduction to STriDER

STriDER (Self-Excited Tripedal Dynamic Experimental Robot) is an innovative three-legged mobile robot that utilizes the concept of passive dynamic locomotion for walking. To initiate a novel tripedal gait, two of its legs are oriented to push the center of gravity outside a support triangle formed by the three foot contact points. As the robot begins to fall forward, the body rotates and the swing leg swings naturally in between the two stance legs and catches the fall. This enables it to walk with high energy efficiency and also allows it to be statically stable when standing with all three legs on the ground. Some examples of previous work on three-legged mobile robots mainly include, the rotating tripedal robot developed by Lyons and Pamnany, which could move its body by rotating about one of its legs[38]; the micro scale walking robot proposed by Martel et al., which had three piezoelectric legs [39, 40]; and the modular robot ASHIGARU which is formed by individual three-legged modules which has primitive mobility through crawling on the ground [41, 42]. Lee and Hirose also described the walking strategy for a four-legged robot when it lost one of its legs [43]. However, these robots are fundamentally different from the robot presented in this paper.

The forward and inverse displacement analysis in STriDER's triple stance phase is presented in this thesis. STriDER can be modeled as a three-branch in-parallel manipulator given the assumption that in the triple stance phase, all three foot contact points are fixed on the ground with no slipping. This kinematics study can be implemented to control the motions of the robot in its triple stance phase and it also lays the foundation for the dynamics analysis on gaits, path planning and so on. Note that the methods used in the following analysis are only valid in this phase and they are not valid when at least one foot leaves the ground or slips significantly. The stability margin of STriDER is described in [44] and the friction constraints of the feet are studied in [45, 46], which can be used to develop the criteria under which the feet of this robot neither leave the ground nor slip.

In this chapter, Section 1.1 presents the locomotion concept of STriDER including a novel tripedal gait and the strategy of changing directions. Section 1.2 introduces the triple stance phase of the robot, and describes its kinematic configuration and adaptation to a three-branch in-parallel manipulator. This model is then adopted in Chapter 2 to solve the inverse and forward displacement problems for STriDER in its triple stance phase. Section 1.3 summaries the organization of the chapters about the first case of parallel locomotion mechanism.

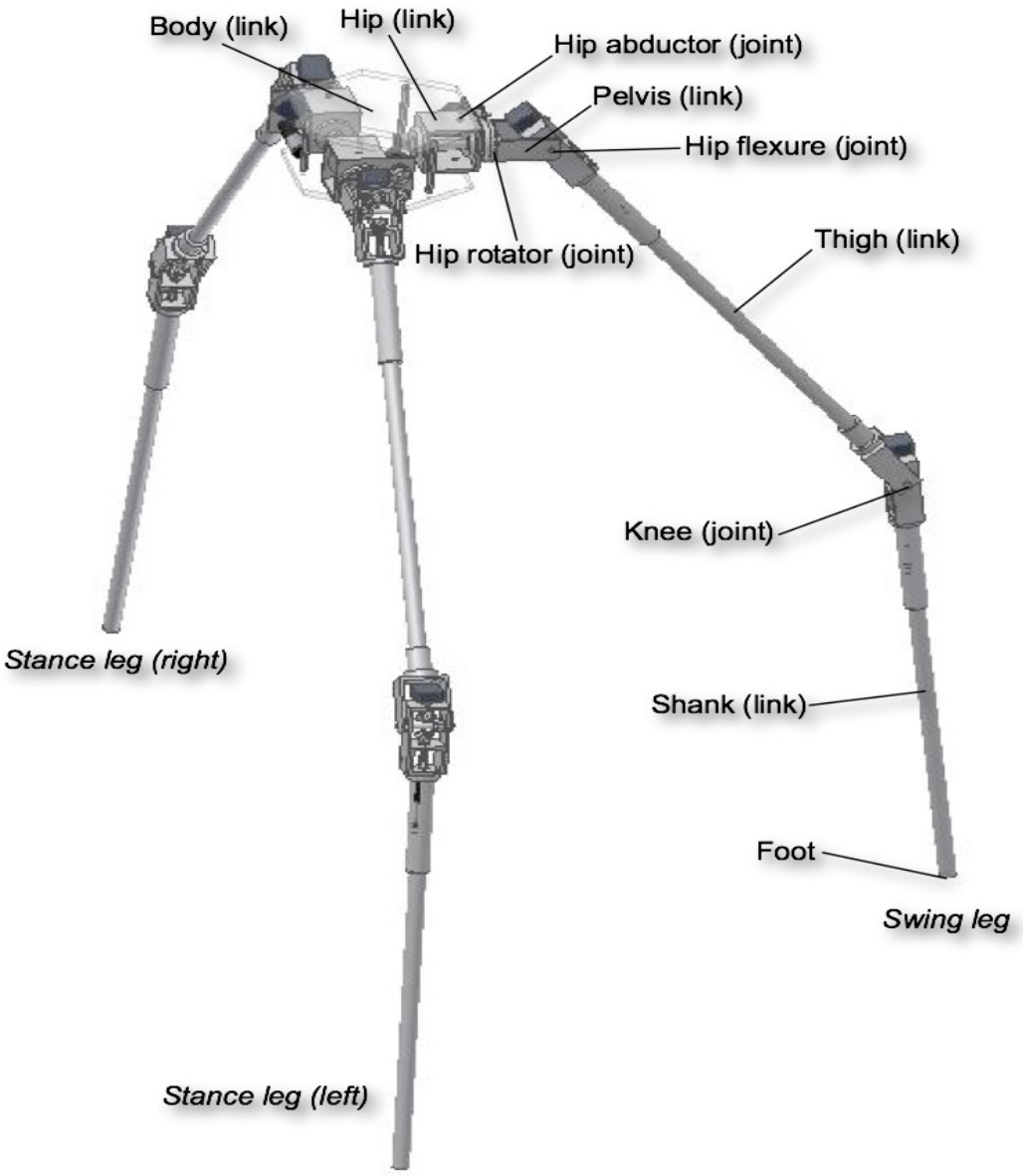

FIG.1.1 STriDER (SELF-EXCITED TRIPEDAL DYNAMIC EXPERIMENTAL ROBOT)

1.1. Locomotion

The design and locomotion of robots are often inspired by nature; however, the three-legged walking machine presented here exemplifies an innovative tripedal gait. In this section, the kinematic configuration, link parameters, kinematic analysis for in-parallel manipulators are briefly reviewed and the connection between this mobile robot and three-branch in-parallel manipulators is explained.

Unlike common bipeds, quadrupeds, and hexapods, STriDER, shown in Fig.1.1, is an innovative three-legged walking machine that incorporates the concept of actuated passive dynamic locomotion. This idea, introduced by Tad McGeer in the late 1980s, uses the natural built-in dynamics of the robot to create the most efficient walking motion [47]. Furthermore, the proper mechanical design of a robot can provide energy efficient locomotion without sophisticated control methods [48, 49].

The novel tripedal gait is simply implemented, as shown in Fig.1.2 for a single step; a video can be seen in [50]. During a step, two legs act as stance legs while the other acts as a swing leg. STriDER begins with a stable triple stance phase (Fig.1.2(a)), then the hip links are oriented to push the center of gravity forward by aligning the stance legs' pelvis links (Fig.1.2(b)). As the body of the robot falls forward, the swing leg naturally swings in between the two stance legs (Fig.1.2(c)) and then extends out to catch the fall (Fig.1.2(d, e)). When the swing leg touches the ground, the robot embraces its balance again (Fig.1.2(e)). As the robot is taking one step (Fig.1.2(b - e), its body needs to rotate 180° to prevent the legs from tangling up. Once all three legs are in contact with the ground, the robot regains its stability and the posture of the robot is reset in preparation for the next step (Fig.1.2(f)) [51, 52]. The strategy of changing directions with multiple steps can be found in Ref.[44].

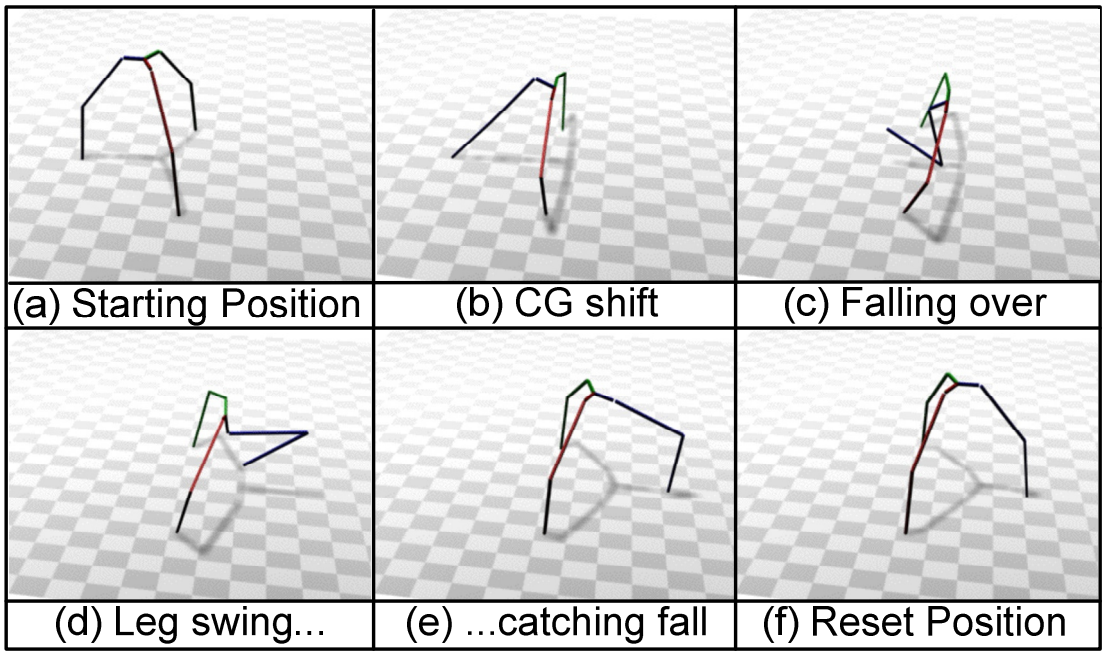

FIG.1.2 SINGLE STEP TRIPEDAL GAIT

Gaits for changing directions can be implemented in a way as illustrated in Fig.1.3. By changing the sequence of choice of the swing leg, the tripedal gait can move the robot in 60° interval directions for each step.

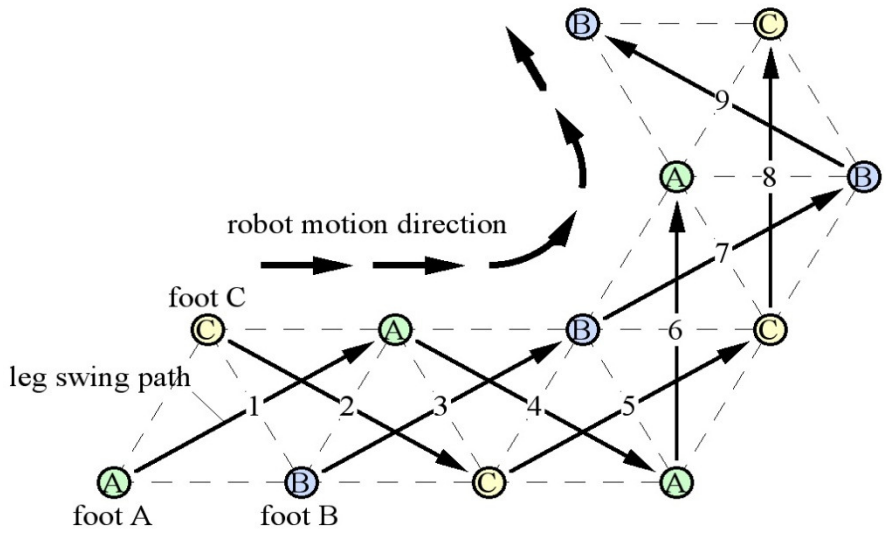

FIG.1.3 GAIT FOR CHANGING DIRECTIONS

1.2. Triple Stance Phase

STriDER is developed for deploying sensors such as cameras, rather than for manipulating tasks. The tall nature of STriDER makes it ideal for sensor surveillance at high positions. Two working prototypes of STriDER have been fabricated, as shown in Fig.1.4. The first prototype on the left in this figure, which is approximately 1.8 meters tall, is used to test the validity of passive dynamic gait for a single step[51]. The second prototype on the right, with a height of approximately 0.7 meters and nine actuated revolute joints, is used to study STriDER's kinematics in triple stance phase, stability margin, transitions between gaits, controlled walking gaits etc.

FIG.1.4 STriDER PROTOTYPES

The definition of coordinate systems for each leg is shown in Fig.1.5. The configurations for all three legs of STriDER are identical, thus the analysis for one leg is presented here as the other two legs will follow the same procedure. The subscript i in the coordinate frames, links, and joint labels, denotes a general leg number (i = 1, 2 or 3).

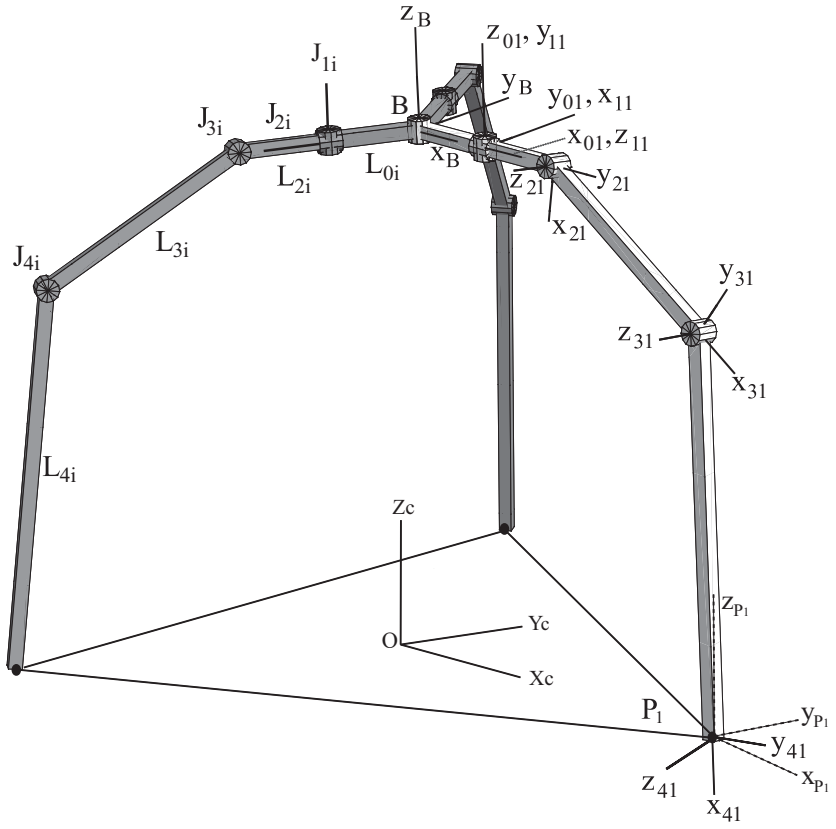

FIG.1.5 COORDINATE FRAMES AND JOINT DEFINITIONS

Table 1.1 lists the nomenclature used to define the coordinate frames, joints and links. First, as shown in Fig1.5, a global coordinate system $\{X_C, Y_C, Z_C\}$, is established with its origin at the centroid of the triangle formed by three foot contact points and axis X_C pointing to P_1, the foot position of leg 1. It is used as the reference for positions and orientations of the body. Next, the body coordinate frame $\{x_B, y_B, z_B\}$ is defined. Each leg is separated by 120º, leg 1, leg 2 and leg 3 are 0º, 120º, and 240º from the positive x_B axis, respectively. Each leg includes four actuated joints, J_{1i}, J_{2i}, J_{3i}, and J_{4i}. The hip abductor joint, J_{1i}, with the direction parallel to z_B axis, controls the stance legs' rotator joints to align during a step.[1] In the first prototype of STriDER developed in [50, 51], three independent abductor joints are used to accomplish the alignment. Later in [52], a novel abductor joint mechanism to align the rotator joints, driven by only one actuator, is used to replace the three abductor joints and reduce the weight of the body. This joint aligning mechanism can efficiently switch between the modes

[1] Please note that the arrangement of three rotator joints in FIG.1.5 is slightly different from those in Fig1.1, where two rotator joints are aligned and the swing leg is ready to take a step (Fig1.2(b)). The following sections use the configuration in Fig1.5 to elaborate the displacement analysis, without losing generality.

in which two of the three rotator joints are aligned to prepare for a step, as the case in Fig.1.1, and the mode in which all three rotator joint axes, i.e. J_{2i}, intersect at the center of the body, as shown in Fig.1.5. Thus, J_{1i} is not treated as an active joint in this paper. Next, J_{2i}, the hip rotator joint, allows the legs to rotate around the z_{1i} axis. J_{3i}, the hip flexure joint and $J_{4i,}$ the knee joint are both revolute joints that rotate around the z_{2i} and z_{3i} axes, respectively. Two coordinate frames $\{x_{4i}, y_{4i}, z_{4i}\}$ and $\{x_{Pi}, y_{Pi}, z_{Pi}\}$ are established at each foot, e.g. the foot of leg 1 in Fig.1.5. The three unit vectors in frame $\{x_{Pi}, y_{Pi}, z_{Pi}\}$ are defined to be parallel to the global vector units. The foot contact points denoted by P_i are modeled as spherical joints during this analysis and $\{x_{4i}, y_{4i}, z_{4i}\}$ relates to $\{x_{Pi}, y_{Pi}, z_{Pi}\}$ with three mutually orthogonal passive joint angles. Finally, the links listed as L_{0i}, L_{1i}, L_{2i}, L_{3i}, and L_{4i} are clearly labeled in Fig.1.4 and represent the body link, hip link which is equal to zero, pelvis link, thigh link and shank link. Furthermore, links L_{01}, L_{02}, and L_{03} are constant values that form the body triangle.

TABLE 1.1 NOMENCLATURES

Nomenclature	
i:	Leg number (i=1,2,3)
$\{X_0, Y_0, Z_0\}$:	Global fixed coordinate system
$\{x_B, y_B, z_B\}$:	Body center coordinate system
J_{1i}:	Hip abductor joint for leg i
J_{2i}:	Hip rotator joint for leg i
J_{3i}:	Hip flexure joint for leg i
J_{4i}:	Knee joint for leg i
P_i:	Foot contact point for leg i
L_{0i}:	Body link for leg i
L_{1i}:	Hip link for leg i (length =0)
L_{2i}:	Pelvis link for leg i
L_{3i}:	Thigh link for leg i
L_{4i}:	Shank link for leg i

The coordinate systems are defined following the standard Denavit-Hartenberg's convention [53] and the link parameters are listed in Table 1.2, where k is the link number, (k = 1,2,3,4), i is the leg number (i = 1, 2, 3). a_{ki} equals the distance along x_{ki} from J_{ki} to the intersection of the x_{ki} and $z_{(k-1)i}$ axes. d_{ki} is the distance along $z_{(k-1)i}$ from $J_{(k-1)i}$ to the intersection of the x_{ki} and $z_{(k-1)i}$ axes. α_{ki} is the twist angle between $z_{(k-1)i}$ and z_{ki} measured about x_{ki}, and θ_{ki} is the twist angle between $x_{(k-1)i}$ and x_{ki} measured about $z_{(k-1)i}$. Also, when all θ_{ki} are equal to zero, the legs form a right angle between L_{2i} and L_{3i}. With these D-H parameters, the homogenous transformation matrices $\mathbf{H}_{0i}^{1i}$, $\mathbf{H}_{1i}^{2i}$, $\mathbf{H}_{2i}^{3i}$, $\mathbf{H}_{3i}^{4i}$ between two adjacent joints in leg i are developed, which represent the relative positions and orientations of two adjacent local joint frames. These matrices are the foundation of the analysis in Chapter 2.

TABLE 1.2 LINK PARAMETERS

Link	a_{ki}	α_{ki}	d_{ki}	θ_{ki}
1	$L_{1i}=0$	90°	0	$\theta_{1i}+90°$
2	0	0	L_{2i}	$\theta_{2i}-90°$
3	L_{3i}	0	0	θ_{3i}
4	L_{4i}	0	0	θ_{4i}

In the triple stance phase, STriDER can be considered as a three-branch in-parallel manipulator given the assumption that all three foot contact points are fixed on the ground, as shown in Fig.1.6. Since the position of the foot doesn't change and the link can rotate around the contact point freely, the point contact between the rigid foottip and the ground is modeled as a spherical joint. This frictional point contact model was adopted by previous reseachers to analyze the contact interaction between a multifinger gripper and a rigid object, as in [54-57]. The ground is then modeled as "the base" of the parallel manipulator, with the body as "the moving platform". Given the fact that the knee joints, hip flexure joints and hip rotator joints are all revolute joints and each of the three legs mainly has two segments i.e. thigh and shank link, STriDER belongs to the class of in-parallel manipulators with kinematically simple branches proposed by Podhorodeski in 1994 [4]. The term in-parallel manipulator is used to characterize a broader class of hybrid manipulation structures with fully-parallel actuated manipulators, such as Stewart Platform [2], and strictly serial manipulators, such as UNIMATE® PUMA robot, as two extreme cases. As stated in [4], such structures contain serial branches acting parallelly on a common end effector and are capable of exploiting the advantages of both fully-parallel and strictly-serial devices through proper design. Since the foot joint is treated as a passive spherical joint with three degrees of freedom, each leg has a total of six degrees of freedom including both actuated and passive joints (3 DOF for the foot contact point, 1 DOF for the knee, flexure, rotator, respectively), thus allowing the body of STriDER to have full six degrees of freedom. The possible kinematic configurations of 6 DOF. three-branch in-parallel manipulators are enumerated by Ben-Horin [29]. According to his classifications based on joint types, the configuration of STriDER is an example of 3-SRRR (Spherical-Revolute-Revolute-Revolute) manipulators.

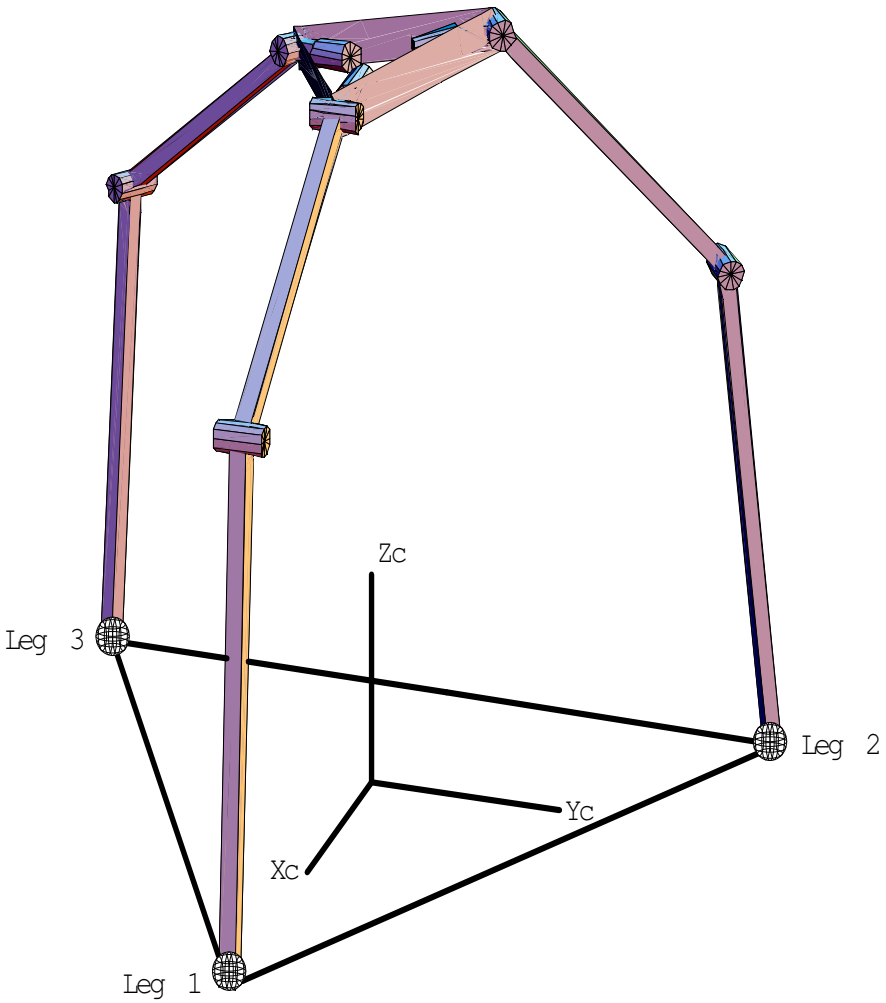

FIG.1.6 GENERAL KINEMATIC REPRESENATION

When STriDER changes its position and orientation of its body without moving the feet of the legs, the characteristics of its motion can be analyzed with the well-established kinematics methodology of three-branch in-parallel manipulators. The methodology in the research mentioned above can be adopted to solve STriDER's inverse and forward displacement problem in triple stance phase under its new configuration of 3-SRRR. Note that, because the feet of the robot are not really constrained to the ground, the stability region of STriDER is limited and the ground cannot generate reaction forces in any direction, which results in STriDER's smaller actual workspace in triple stance phase than conventional in-parallel manipulators.

Generally, Section 1.1 and 1.2 present the basic information regarding STriDER. More detailed information about the design of the hardware structure, the arrangement and testing of the motors and the transmission mechanisms can be found in [51, 52].

1.3. Summary

As introduced in Section 1.1 and 1.2, the kinematic configuration of STriDER when all of its feet are in contact with the ground without slippery is equivalent to a three legged spherical-revolute-revolute-revolute (SRRR) in-parallel manipulator when the contact point between the foot and the ground is modeled as a passive spherical joint. This point contact model has been adopted by several researchers to model the contact between multi-fingered grippers such as [55]. In such a model, the contact interaction can be represented as a force through a contact center; no moments can be transmitted through the contact. Thus, each leg has three mutually orthogonal passive revolute joins with intersecting axes (equivalent to a passive spherical joint) in additional to the three joints with motors mounted.

It is necessary to investigate the motion of STriDER when it stands on the ground with three feet. The research presented in this thesis focuses on the kinematic analysis on its equivalent three legged SRRR in-parallel manipulator. The structure of this thesis is as follows. Chapter 2 deals with the forward and inverse displacement analysis of the robot under both redundant sensing and non-redundant sensing. Chapter 3 demonstrates the numerical example of STriDER to verify the analysis in Chapter 2. Chapter 4 briefly introduces the theory of screws and shows the development of Jacobian matrix based on reciprocal screws. In the beginning of Chapter 5, the line geometry is briefly introduced. Then, possible singular configurations of this three-legged SRRR in-parallel manipulator are proposed and the corresponding elimination method based on redundant actuation is discussed.

Chapter 2 Forward and Inverse Displacement Analysis

This chapter presents the forward and inverse displacement analysis of a novel three-legged walking robot STriDER (Self-excited Tripedal Dynamic Experimental Robot). STriDER utilizes the concept of passive dynamic locomotion to walk, but when all three feet of the robot are on the ground, the kinematic structure of the robot behaves like an in-parallel manipulator. To plan and control its change of posture, the kinematics of its forward and inverse displacement must be analyzed.

The concept of this novel walking robot and its unique tripedal gait is already discussed in Chapter 1 including strategies for changing directions, followed by the overall kinematic configuration and definitions of its coordinate frames. When all three feet of the robot are on the ground, by assuming there are no slipping at the feet, each foot contact point are treated as a passive spherical joint. Kinematic analysis methods for in-parallel manipulators are briefly reviewed and adopted for the forward and inverse displacement analysis for this mobile robot. Both loop-closure equations based on geometric constraints and the intersection of the loci of the feet are utilized to solve the forward displacement problem. Closed-form solutions are identified and discussed in the cases of redundant sensing with displacement information from nine, eight and seven joint angle sensors. For the non redundant sensing case using information from six joint angle sensors, it is shown that closed-form solutions can only be obtained when the displacement information is available from non-equally distributed joint angle sensors among the three legs. As for the case when joint angle sensors are equally distributed among the three legs, it will result in a 16th-order polynomial of a single variable. Numerical method for polynomial systems such as continuation method can be used to solve the problem. It was found that at most sixteen forward displacement solutions exist if displacement information from two joint angle sensors per leg are used and one is not used.

2.1. Mobility Analysis

The moving platform of this in-parallel manipulator is connected to the fixed base through three legs. Each leg is a chain with three actuated or unactuated revolute joints arranged in a serial manner. One joint connects the end of each leg to the base. By using conventional *Grübler-Kutzbach criterion* [58, 59], the number of the DOF of the moving platform can be easily obtained as follows.

$$\begin{aligned} F &= \lambda(n - j - 1) + \sum_i f_i \\ &= 6 \times (11 - 12 - 1) + (1 \times 9 + 3 \times 3) \\ &= 6 \end{aligned}$$

where F denotes the number of the DOF., i.e., mobility of the moving platform, $\lambda = 6$ for spatial mechanisms, n is the number of links in this manipulator, j is the number of joints, f_i is the DOF of joint i, and $\sum_i f_i$ is the sum of the DOF of each joint. Therefore, the three-legged S-R-R-R in-parallel manipulator proposed above has 6 DOF.. Regarding the

mobility of this family of in-parallel manipulators, Tsai and Tahmasebi proved in [15] that if each leg of the parallel manipulator has 6 DOF, then the mobility of the parallel manipulator is 6, regardless of the number of legs.

2.2. Inverse Displacement Analysis

The inverse displacement analysis is to calculate the unknown internal angles θ_{2i}, θ_{3i}, and θ_{4i} for the hip rotator, hip flexure and knee joints, respectively from the given configuration of the body. It is important for the position control of STriDER's body in triple stance phase. As previously mentioned, the angle between the positive x_B axis and leg 1, leg 2 and leg 3 is 0 degrees, 120 degrees, and 240 degrees, respectively. The angle between x_{0i} and x_{1i} measured about z_{0i}, θ_{1i}, is set equal to zero and treated as a constant in these calculations. Also, the orientation and position of the body in relation to the global coordinate are known. So, the unknown angles θ_{2i}, θ_{3i}, and θ_{4i} are calculated from the global body position and orientation, θ_{1i} the angle between x_B and each leg, and global foot positions. By treating the system as an "elbow manipulator" problem as in [53], the unknown joint angle values can be easily determined. Thus, for the ease of viewing, the leg is rotated 90 degrees around the x_{1i} axis in Fig.2.1.

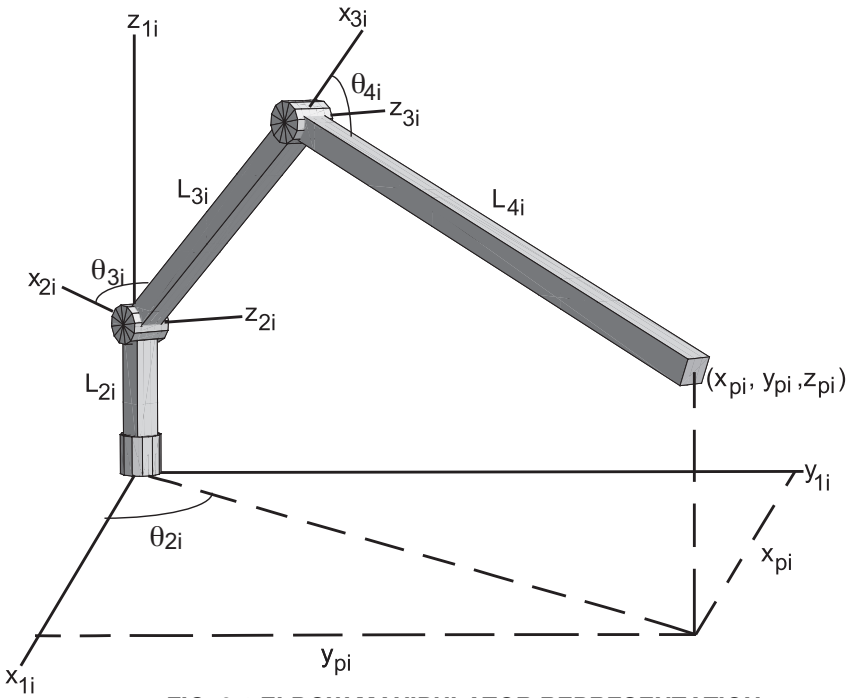

FIG. 2.1 ELBOW MANIPULATOR REPRESENTATION

Following the coordinate systems in Fig.2.1, a homogeneous transformation from the global coordinate to the hip rotator joint was derived, as shown in Eq.(2.1),

$$\mathbf{H}_o^{1i} = \mathbf{H}_o^B \mathbf{H}_B^{0i} \mathbf{H}_{0i}^{1i} = \begin{bmatrix} \mathbf{R}_o^{1i} & \mathbf{d}_o^{1i} \\ 0 & 1 \end{bmatrix}_{4x4} \qquad (2.1)$$

where $\mathbf{R}_o^{1i}$ and $\mathbf{d}_o^{1i}$ specify the orientation and translation of frame $\{x_{1i}, y_{1i}, z_{1i}\}$ relative to global frame $\{X_C, Y_C, Z_C\}$ respectively. $\mathbf{H}_o^B$ is the transformation matrix from body frame $\{x_B, y_B, z_B\}$ to global frame $\{X_C, Y_C, Z_C\}$, which represents the body's orientation and position expressed in $\{X_C, Y_C, Z_C\}$, while $\mathbf{H}_B^{0i}$ is a constant matrix representing the relative position of the abductor in leg i with respect to the center of the body. Next, the orientation and translation of $\{X_C, Y_C, Z_C\}$ relative to $\{x_{1i}, y_{1i}, z_{1i}\}$ are found using Eq. (2.2) and (2.3),

$$\mathbf{R}_{1i}^{o} = \left[\mathbf{R}_{o}^{1i} \right]^T \qquad (2.2)$$

$$\mathbf{d}_{1i}^{o} = -\mathbf{R}_{1i}^{o} \mathbf{d}_o^{1i} \qquad (2.3)$$

The orientation matrix, $\mathbf{R}_{1i}^{o}$, and translation vector, $\mathbf{d}_{1i}^{o}$, are used to relate the position vector of the foot in frame $\{X_C, Y_C, Z_C\}$ to that in frame $\{x_{1i}, y_{1i}, z_{1i}\}$ as shown in Eq. (2.4),

$$\mathbf{d}_{1i}^{Pi} = \mathbf{R}_{1i}^{o} \mathbf{d}_o^{Pi} + \mathbf{d}_{1i}^{o} = \begin{bmatrix} x_{Pi} \\ y_{Pi} \\ z_{Pi} \end{bmatrix} \qquad (2.4)$$

where $\mathbf{d}_o^{Pi}$ is the foot position in relation to the global coordinates and vector $\begin{bmatrix} x_{Pi} & y_{Pi} & z_{Pi} \end{bmatrix}^T$ represents the foot position relative to the local hip rotator coordinates, which is also the base of the elbow manipulator shown in Fig.2.1. This now becomes a common elbow manipulator problem [53].

The angle at the hip flexure joint, θ_{2i}, is found using Eq.(2.5),

$$\theta_{2i} = \text{Arctan 2}\left(x_{Pi}, y_{Pi}\right) + \frac{\pi}{2} \qquad (2.5)$$

where x_{Pi} and y_{Pi} are the x and y foot positions relative to the elbow manipulator base. Notice that 90 degrees are added to this value due to the link parameter definition listed in Table 2. Next, the angle at the knee joint, θ_{4i}, is calculated, as shown in Eq.(2.6),

$$\theta_{4i} = \text{Arctan2}\left(D, \pm\sqrt{1-D^2}\right) \qquad (2.6)$$

where D is a constant term determined from Eq. (2.7),

$$D = \frac{x_{Pi}^{\ 2} + y_{Pi}^{\ 2} + \left(z_{Pi} - L_{2i}\right)^2 - L_{3i}^{\ 2} - L_{4i}^{\ 2}}{2L_{3i}L_{4i}} \qquad (2.7)$$

where $L_{2i,}$ L_{3i}, and L_{4i} are link lengths and z_{Pi} is the z foot position relative to the base. As shown, with "±" in Eq. (2.6) there will be two values for θ_{4i}, each corresponds to an elbow up or elbow down case. Thus, there will also be two corresponding values for θ_{3i}, as calculated in Eq.(2.8),

$$\begin{aligned}\theta_{3i} = {} & \text{Arctan2}(\sqrt{x_{Pi}^{\ 2} + y_{Pi}^{\ 2}}, z_{Pi} - L_{2i}) \\ & - \text{Arctan2}(L_{3i} + L_{4i}\cos\theta_{4i}, L_{4i}\sin\theta_{4i})\end{aligned} \qquad (2.8)$$

In conclusion, if the body global position and orientation, the hip abductor joint angle θ_{1i}, and the global foot positions are known, then the internal joint angles, hip rotator joint angle θ_{2i}, hip flexure joint angle θ_{3i}, and knee joint angle θ_{4i} can be calculated by modeling the legs as elbow manipulators where the base is at the hip rotator joint and all link lengths are known and constant.

2.3. Forward Displacement Analysis

The forward displacement solution requires resolving the position and orientation of the body with displacement information from the joint angle sensors. For the case of STriDER, it has a total of nine joints that can be actuated and sensed.

2.3.1. Nomenclature "N_1 - N_2 – N_3" and Introduction

The nomenclature "N_1 - N_2 – N_3" will be used to describe the sensing where N_i corresponds to the number of available displacement readings from the joint angle sensors in leg i. For example, 3-2-1 means there are three sensed joint angles in leg 1, two sensed joint angles in leg 2 and 1 sensed joint angles in leg 3.

Since the body has 6 DOF, at least six joint angles out of nine are needed for feasible forward displacement solutions and each leg must have at least one known joint angle. All possible cases of joint sensing are listed as follows: (1) 3-3-3 (nine joint angles sensed); (2) 3-3-2(eight joint angles sensed); (3) 3-3-1 and 3-2-2 (seven joint angles sensed); and (4) 3-2-1 and 2-2-2 (six joint angles sensed). Case 1, 2 and 3 are redundant sensing and case 4 is non-redundant sensing. Especially, in case 4, 3-2-1 is referred to non-equally distributed sensing and 2-2-2 is known as equally distributed sensing.

In triple stance phase, forward displacement analyses on redundant and non-redundant sensing cases are both necessary. The fully sensed case of joint angles leads to a unique solution of the body position and orientation, which has been utilized to realize the velocity control of the body as in [60]. It also lays the foundation for a continuous joint-sensor-based position monitoring throughout the cycle of multi-step walking of STriDER. If one or more joint angle sensor is broken or faulty, the information of the body can still be obtained by solving the forward displacement problems with less than 9 joint angles. By comparing the solutions from different cases of sensor readings and checking the existence of common solutions, the sensors with erroneous information can be detected. A similar work on fault detection for in-parallel manipulators can be found in [61].

Note that, in the following analysis, the X_C axis of global frame $\{X_C, Y_C, Z_C\}$ in Fig.1.5, is always chosen to point to the foot position of leg 1.

2.3.2. Nine Joint Angles Sensed Case [3-3-3]

If all nine displacements from the joint angle sensors are available, the location and orientation of the body has a unique solution. First assume the body is positioned at the global origin with zero orientation, and then with 3-3-3 sensing, the global position vector of each foot $\mathbf{P}_i$, i = 1,2,3, representing the leg number, can be calculated by performing the multiplications of homogeneous transformation matrices as shown in Eq.(2.9.1). These three contact points constitute a triangle in 3D space, which is treated as the virtual base of the in-parallel manipulator. The location of the centroid of the base is described by Eq.(2.9.2):

$$\begin{bmatrix} \mathbf{P}_i \\ 1 \end{bmatrix} = \mathbf{H}_B^{0i}\, \mathbf{H}_{0i}^{1i}\, \mathbf{H}_{1i}^{2i}\, \mathbf{H}_{2i}^{3i}\, \mathbf{H}_{3i}^{4i} \begin{bmatrix} \mathbf{0} \\ 1 \end{bmatrix} \tag{2.9.1}$$

$$\mathbf{P}_C = (\mathbf{P}_1 + \mathbf{P}_2 + \mathbf{P}_3)/3 \tag{2.9.2}$$

Three orthogonal unit vectors describing the orientation of the base can be found as:

$$\begin{aligned} \mathbf{u}_x &= (\mathbf{P}_1 - \mathbf{P}_c)/\|(\mathbf{P}_1 - \mathbf{P}_c)\| \\ \mathbf{u}_z &= \mathbf{u}_x \times (\mathbf{P}_2 - \mathbf{P}_c)/\|\mathbf{u}_x \times (\mathbf{P}_2 - \mathbf{P}_c)\| \\ \mathbf{u}_y &= \mathbf{u}_z \times \mathbf{u}_x \end{aligned} \tag{2.10}$$

with $\mathbf{u}_z$ being the unit vector normal to the plane of the base, $\mathbf{u}_x$ being the unit vector pointing to the foot of leg 1, and $\mathbf{u}_y$ being the unit vector perpendicular to $\mathbf{u}_x$ and $\mathbf{u}_z$. The sign of "$\|\ \|$" denotes the Euclidean norm. As indicated in Eq.(2.11.1), three unit direction vectors, $\mathbf{u}_x$, $\mathbf{u}_y$, $\mathbf{u}_z$ together with the position vector $\mathbf{P_c}$ are assembled to form the homogenous transformation matrix $\mathbf{H}_B^o$ which represents the relative position and orientation of the global frame {X_C, Y_C, Z_C} located on the virtual base plane with respect to the body frame {x_B, y_B, z_B}. Since the body is firstly assumed at the origin with zero configuration, by taking the inverse of $\mathbf{H}_B^o$, homogeneous transformation matrix $\mathbf{H}_o^B$, which represents the actual configuration of the body with respect to the real global frame {X_C, Y_C, Z_C} can be derived, with three unit vectors $\mathbf{U}_x, \mathbf{U}_y, \mathbf{U}_z$ denoting the orientation and vector **B** denoting the position. The geometric relationship is shown in the following equations:

$$\mathbf{H}_B^o = \begin{bmatrix} \mathbf{u}_x & \mathbf{u}_y & \mathbf{u}_z & \mathbf{P_c} \\ 0 & 0 & 0 & 1 \end{bmatrix} \tag{2.11.1}$$

$$\begin{aligned} \mathbf{H}_o^B = \left(\mathbf{H}_B^o\right)^{-1} &= \begin{bmatrix} \begin{bmatrix} \mathbf{u}_x & \mathbf{u}_y & \mathbf{u}_z \end{bmatrix}^T & -\begin{bmatrix} \mathbf{u}_x & \mathbf{u}_y & \mathbf{u}_z \end{bmatrix}^T \mathbf{P_c} \\ \mathbf{0} & 1 \end{bmatrix} \\ &= \begin{bmatrix} \mathbf{U}_x & \mathbf{U}_y & \mathbf{U}_z & \mathbf{B} \\ 0 & 0 & 0 & 1 \end{bmatrix} \end{aligned} \tag{2.11.2}$$

Note that STriDER, as a mobile robot, doesn't have a real base with fixed geometry. If the robot only has joint sensors installed, the fully-sensed case with all sensors functional is the only way to get the geometry of the virtual base in the triple stance phase. As long as the geometry of the base is known, the constraint equations of the foot position can be established. Then, fewer sensed joint angles can be used to derive the position and orientation of the body. This leads to the discussions of other sensing modes. The geometric relationships in the forward displacement problem of a three-branch in-parallel manipulator in redundant cases (eight or seven sensors) and the asymmetric non-redundant case (3-2-1) were discussed in [13], where Notash and Podhorodeski interpreted the feasible solutions as the intersections of different spatial shapes. Based on their method, the forward displacement solutions of

STriDER in similar cases can be derived.

Generally, the calculation of the position and orientation of STriDER's body with less than 9 joint angles requires two steps. First assume the body is positioned at the global origin with zero orientation and solve the unsensed joint angles to obtain locations of the feet by using geometric constraints, either through looking for the intersections of various 3D shapes or through solving the loop-closure equations. Then use Eq.(2.9), (2.10) and (2.11) to derive the transformation matrix which represents the relative position and orientation of the body frame $\{x_B, y_B, z_B\}$ with respect to the real global coordinates $\{X_C, Y_C, Z_C\}$. Note that in the following sections, the geometric parameters of the base are assumed to be known and utilized to establish the constraints.

2.3.3. Eight Joint angles sensed case [3-3-2]

Assume one sensor on leg 3 is broken or intentionally shut down. However, all the other joint sensors in leg 1 and 2 are still functional. The location of P_1 and P_2 can be expressed in terms of the known joint angles. As described in [13], with two points P_1 and P_2 fixed, the locus of the P_3 given the constraint of the base triangle becomes a spatial circle $C_{1,2}$ about the line passing through P_1 and P_2 with a radius MP_3. M is the projected point of P_3 on line P_1P_2. Meanwhile, with only one unknown joint angle in leg 3, the locus of P_3 under the constraint of leg 3 is also a spatial circle C_3 about certain joint axis.

As illustrated in Fig.2.2, θ_4 in leg 3 is assumed as the unsensed joint angle. Therefore two spatial circles $C_{1,2}$ and C_3 must intersect in at least one location in order to have a feasible solution. Once the location is determined, the position vector of P_3 is known. Using Eq.(2.9) and (2.10) and taking the inverse of $\mathbf{H}_0^B$, the position and orientation of the body are determined. Note that the centers, radii and unit mutual orthogonal vectors of $C_{1,2}$ and C_3 respectively, can be found from known geometric parameters and sensed joint angles. $C_{1,2}$ and C_3 have at most two real intersections, which corresponds to two feasible forward displacement solutions. Since both $C_{1,2}$ and C_3 can be expressed as quadratic equations, closed-form solutions of the common roots can be derived.

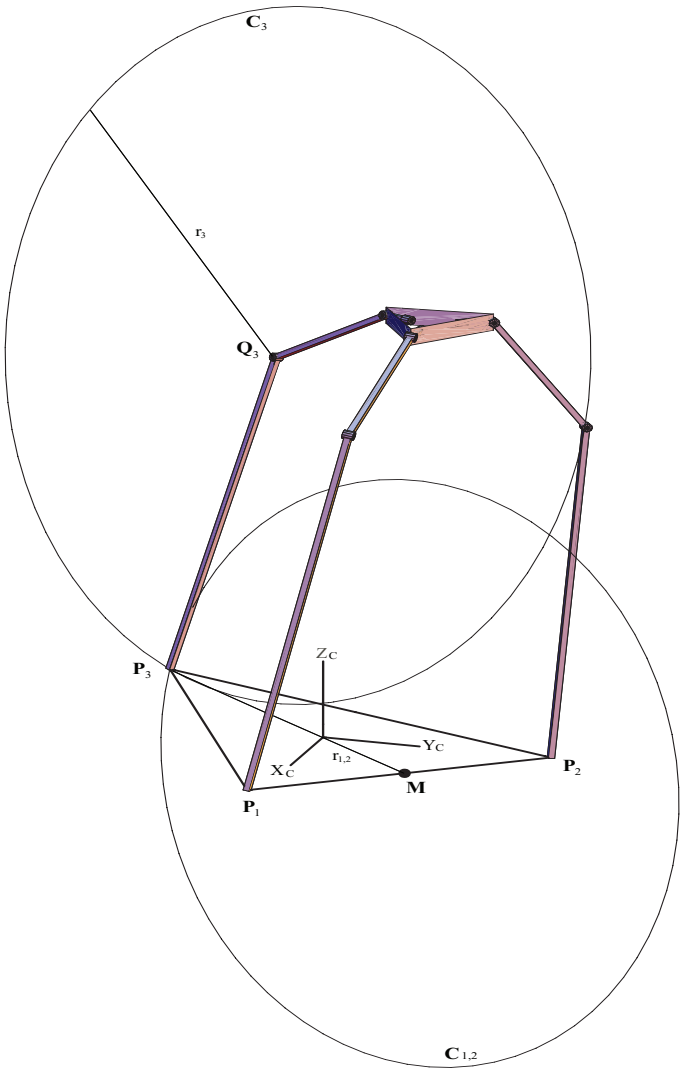

FIG.2.2 INTERSECTION OF TWO CIRCLES [3-3-2 CASE]

2.3.4. Seven Joint angles sensed case [3-3-1 & 3-2-2]

3-3-1 Sensing

When the information of all six joint angles in leg 1 and leg 2 is assumed to be available, the location of P_1 and P_2 can be expressed in terms of the sensed joint angles. Considering the constraint of the base triangle, the locus of P_3 is a spatial circle $C_{1,2}$ again. The locus of P_3 under the constraint of leg 3 will be a sphere, a torus, or a ring plane, depending on the relative position and directions of the unsensed joints. The implementation of this method in the triple stance phase of STriDER is discussed in the following subsections for each of these three cases. Each intersection of the spatial shapes represents a feasible forward displacement solution.

θ_{2i} & θ_{3i} unsensed

θ_{23} and θ_{33} in leg 3 are assumed to be the unsensed joints, whose axes are intersecting with each other. The locus of the foot P_3 is the sphere S_3 as shown in Fig.2.3, with the center Q_3 locating at the intersecting point of axis z_{13} and z_{23}. The intersections of the sphere S_3 and the circle $C_{1,2}$ will be used to derive the forward displacement solutions. Generally, this case has up to two intersections.

θ_{2i} & θ_{4i} unsensed

θ_{23} and θ_{43} in leg 3 are assumed to be the unsensed joints. Since the axes of these two joints are skew axes and L_{4i} is longer than L_{3i}, the locus of foot P_3 is the horn torus T_3. A self-intersecting horn torus is illustrated in Fig.2.4. It is a special type of torus when the length of the radius from the center of the hole to the center of the torus is smaller than the length of the radius of the tube as described in [62]. As shown in Fig.2.5, the intersections of the torus T_3 and the circle $C_{1,2}$ will be used to derive the forward displacement solutions. There are a maximum of four intersections existing in this case.

θ_{3i} & θ_{4i} unsensed

θ_{33} and θ_{43} are assumed to be the unsensed joints in leg 3. Since their axes are parallel and L_{43} is longer than L_{33}, the locus of foot P_3 is the planar circular ring CR_3 as shown in Fig.2.6. The intersections of the planar circular ring CR_3 and the circle $C_{1,2}$ will be used to derive the forward displacement solutions. There are up to two intersections of the circle $C_{1,2}$ and the circular ring CR_3

As a summary of the three cases discussed above, the geometric parameters of various spatial shapes (circle, sphere, torus, planar ring) are developed with known parameters and sensed joint angles. All of these shapes can be described with quadratic equations. The intersection points are determined through solving for the common roots of equation systems representing the spatial circle and those 3D shapes (circle, sphere, torus, planar ring). Since the orders of the polynomial equation systems are less or equal to four, closed-form solutions can be obtained and represented with analytical expressions. With each solution of the unsensed joint angle, the position vector P_3 is derived and the same procedures as the all joint angle sensed case [3-3-3] can be carried out to obtain the information of the body's position and orientation.

Mathematically, if a circle happens to be part of the sphere, the torus, or the planar ring, there exist infinity intersections which correspond to infinity forward displacement solutions. This is actually the singularity case in kinematic analysis, which will be fully addressed in future research.

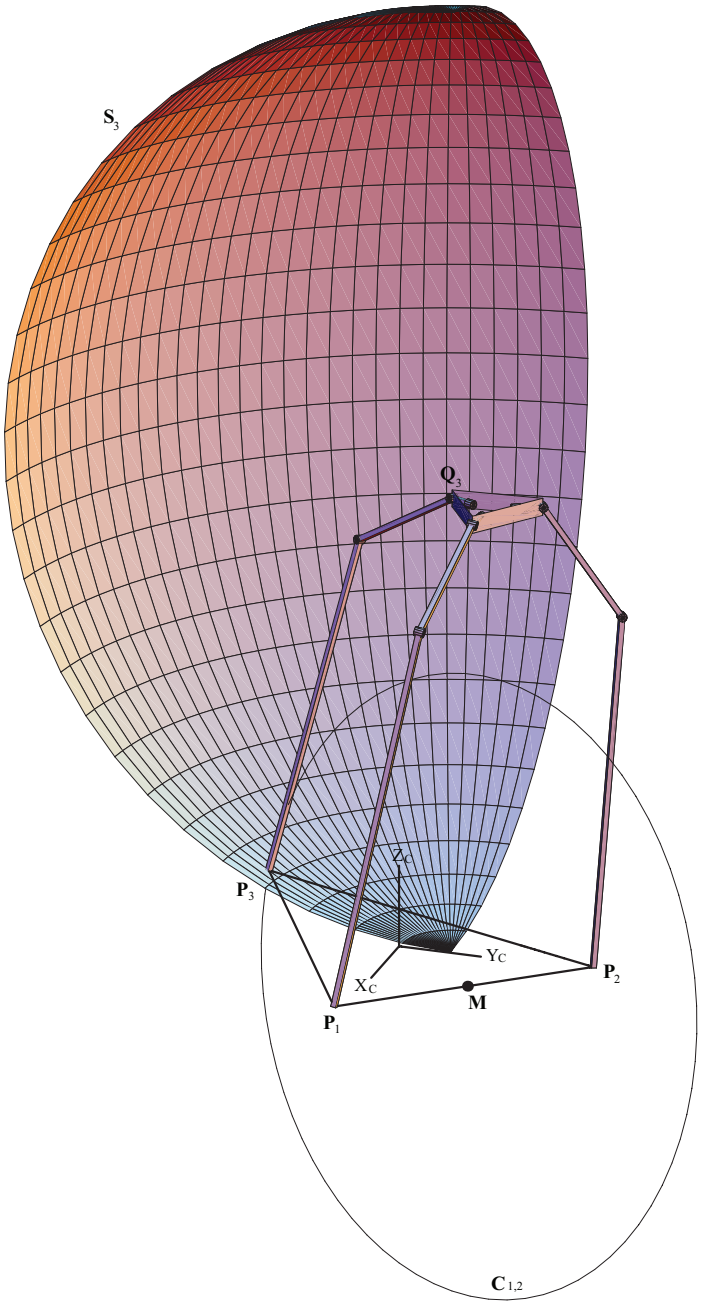

FIG.2.3 SPHERE AND CIRCLE INTERSECTION

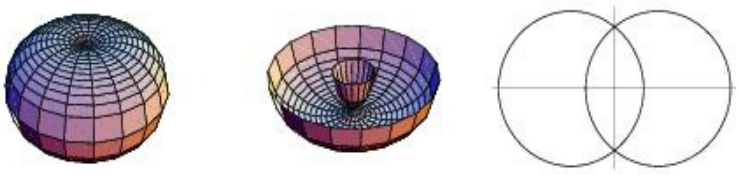

FIG.2.4 SELF-INTERSECTION HORN TORUS

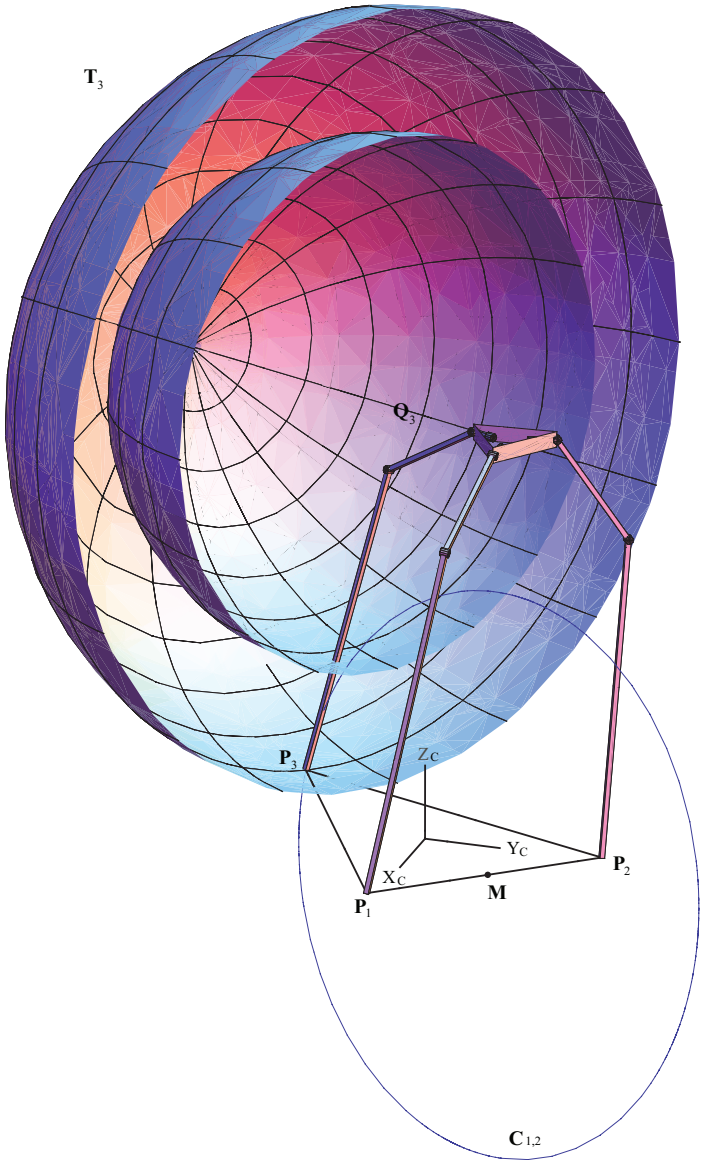

FIG.2.5 TORUS AND CIRCLE INTERSECTION

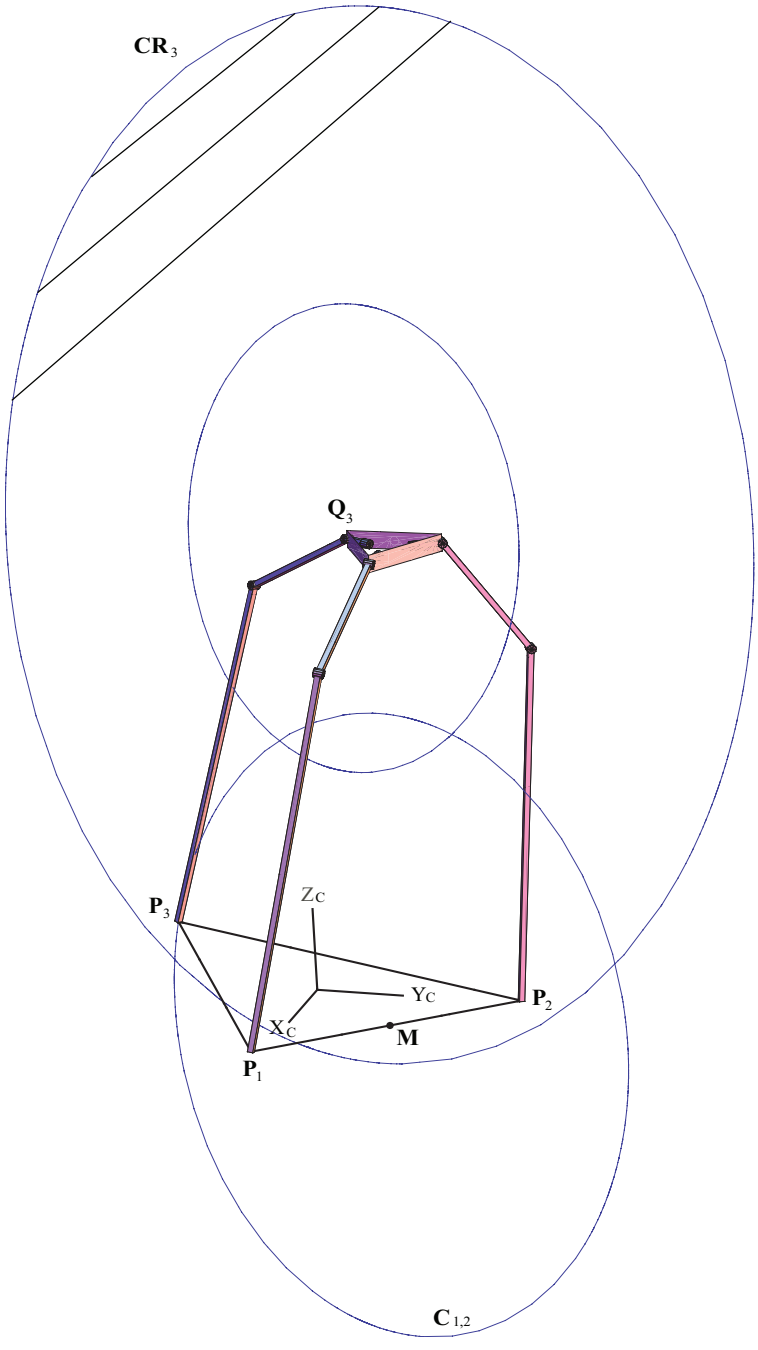

FIG.2.6 CIRCULAR PLANE AND CIRCLE INTERSECTION

3-2-2 Sensing

In the case of 3-2-2 sensing, the location of P_1 can be expressed with the sensed joint angles. For the leg with three sensed joint angles and any leg with two sensed joint angles, there exists a loop-closure constraint equation with respect to a single unsensed joint angle. For each of the solutions derived, the case of 3-2-2 sensing reduces to the 3-3-2 sensing and there are at most four solutions with closed-form as described in [13].

2.3.5. Six Joint Angles Sensed Case [2-2-2 & 3-2-1]

2-2-2 Sensing

The 2-2-2 sensing case in the triple stance phase of STriDER is kinematically identical to the 3/6 Stewart platform studied by Innocenti and Parenti-Castelli in [6]. Three loop-closure equations are utilized to derive a 16th-order polynomial with respect to a single variable. This indicates that at most 16 solutions may exist for 2-2-2 sensing. Closed-form solutions can be derived by solving this higher order polynomial. Geometrically, the locus of each foot when two joint angles in each leg are sensed and one joint angle is not sensed is a spatial circle C_i (i = 1,2,3). These three equations will solve for the particular points on the circles that satisfy the geometric constraints of the base triangle $P_1P_2P_3$. A general example of this case is displayed in Fig.2.7.

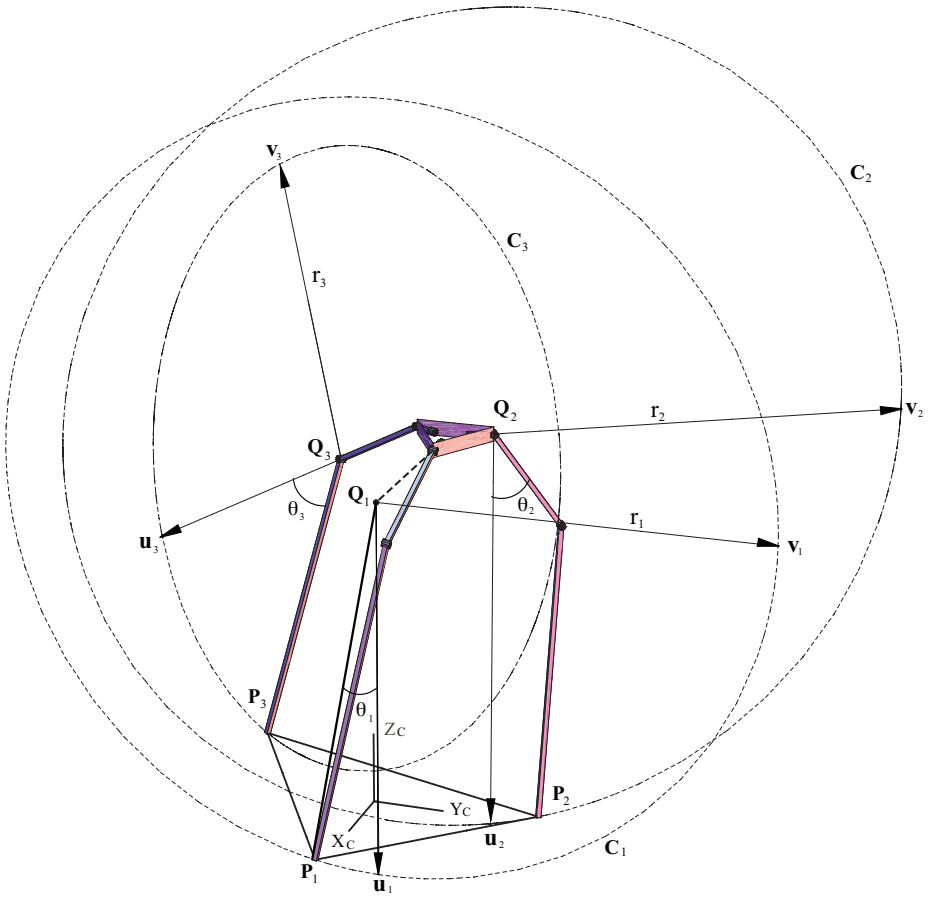

FIG.2.7 GENERAL NON REDUNDANT [2-2-2 CASE]

As shown in Fig.2.7, each leg has two sensed joint angles and one unsensed joint angle. The loci of P_1, P_2 and P_3 are three independent spatial circles C_1, C_2 and C_3 with the centers at Q_1, Q_2 and Q_3 respectively. For each loop $P_iP_{i+1}Q_{i+1}Q_i$, i = 1,2,3 (modulo3), the following vector equations can be written:

$$\mathbf{P}_{i+1} - \mathbf{P}_i = (\mathbf{P}_{i+1} - \mathbf{Q}_{i+1}) + (\mathbf{Q}_{i+1} - \mathbf{Q}_i) - (\mathbf{P}_i - \mathbf{Q}_i) \tag{2.12}$$

$$\left|\mathbf{P}_{i+1} - \mathbf{P}_i\right| = d_{i(i+1)} \tag{2.13}$$

$$\mathbf{P}_i - \mathbf{Q}_i = r_i\left(\mathbf{u}_i \cos\theta_i + \mathbf{v}_i \sin\theta_i\right) \tag{2.14}$$

$$\mathbf{P}_{i+1} - \mathbf{Q}_{i+1} = r_{i+1}\left(\mathbf{u}_{i+1} \cos\theta_{i+1} + \mathbf{v}_{i+1} \sin\theta_{i+1}\right) \tag{2.15}$$

where $\mathbf{u_i}$ and $\mathbf{v_i}$ are mutual orthogonal vector units parallel to the plane of the C_i circle,

the direction of these two vector units are chosen such that the definitions of θ_i are consistent with Chapter 1; $d_{i(i+1)}$ represents the distance between P_i and P_{i+1}; r_i is the radius of C_i. Again, the information of $\mathbf{u_i}$, $\mathbf{v_i}$,Q_i ,r_i and $d_{i(i+1)}$ are uniquely defined by the know geometric parameters and sensed joint angles.

By squaring Eq.(2.12), the following scalar equation is obtained:

$$\begin{aligned} &{}^iq_1C_iC_{i+1} + {}^iq_2C_iS_{i+1} + {}^iq_3S_iC_{i+1} + {}^iq_4S_iS_{i+1} + \\ &{}^iq_5C_i + {}^iq_6S_i + {}^iq_7C_{i+1} + {}^iq_8S_{i+1} + {}^iq_9 = 0 \end{aligned} \qquad (2.16)$$

where $C_i = \cos\theta_i$, $S_i = \sin\theta_i$, i = 1,2,3 (modulo3), and

$${}^iq_1 = 2\, r_i\, r_{i+1}\, \mathbf{u_i}\, \mathbf{u_{i+1}} \qquad (2.16.1)$$

$${}^iq_2 = 2\, r_i\, r_{i+1}\, \mathbf{u_i}\, \mathbf{v_{i+1}} \qquad (2.16.2)$$

$${}^iq_3 = 2\, r_i\, r_{i+1}\, \mathbf{v_i}\, \mathbf{u_{i+1}} \qquad (2.16.3)$$

$${}^iq_4 = 2\, r_i\, r_{i+1}\, \mathbf{v_i}\, \mathbf{u_{i+1}} \qquad (2.16.4)$$

$${}^iq_5 = 2\, r_i\, (\mathbf{Q}_{i+1} - \mathbf{Q}_i)\mathbf{u_i} \qquad (2.16.5)$$

$${}^iq_6 = 2\, r_i\, (\mathbf{Q}_{i+1} - \mathbf{Q}_i)\mathbf{v_i} \qquad (2.16.6)$$

$${}^iq_7 = 2\, r_{i+1}\, (\mathbf{Q}_i - \mathbf{Q}_{i+1})\mathbf{u_{i+1}} \qquad (2.16.7)$$

$${}^iq_8 = 2\, r_{i+1}\, (\mathbf{Q}_i - \mathbf{Q}_{i+1})\mathbf{v_{i+1}} \qquad (2.16.8)$$

$${}^iq_9 = d_{i(i+1)}^2 - r_i^2 - r_{(i+1)}^2 - (\mathbf{Q}_{i+1}-\mathbf{Q}_i)^2 \qquad (2.16.9)$$

Converting Eq.(2.16) into a system of polynomial equations by substituting the trigonometric identities:

$$S_i = 2t_i/(1+t_i^2) \quad \text{and} \quad C_i = (1-t_i^2)/(1+t_i^2)$$

where $t_k = \tan(\theta_i/2)$, then Eq. (2.16) can be written as follows:

$$\sum_{\substack{j=0,1,2 \\ k=0,1,2}} {}^ia_{jk}\, t_i^j\, t_{i+1}^k = 0 \qquad (2.17)$$

where i = 1,2,3 (modulo3)

$$^{i}a_{00} = {}^{i}q_1 + {}^{i}q_5 + {}^{i}q_7 + {}^{i}q_9 \quad (2.17.1)$$

$$^{i}a_{01} = 2({}^{i}q_2 + {}^{i}q_8) \quad (2.17.2)$$

$$^{i}a_{02} = -{}^{i}q_1 + {}^{i}q_5 - {}^{i}q_7 + {}^{i}q_9 \quad (2.17.3)$$

$$^{i}a_{10} = 2({}^{i}q_3 + {}^{i}q_6) \quad (2.17.4)$$

$$^{i}a_{11} = 4\,{}^{i}q_4 \quad (2.17.5)$$

$$^{i}a_{12} = -2({}^{i}q_3 - {}^{i}q_6) \quad (2.17.6)$$

$$^{i}a_{20} = -{}^{i}q_1 - {}^{i}q_5 + {}^{i}q_7 + {}^{i}q_9 \quad (2.17.7)$$

$$^{i}a_{21} = -2({}^{i}q_2 - {}^{i}q_8) \quad (2.17.8)$$

$$^{i}a_{22} = {}^{i}q_1 - {}^{i}q_5 - {}^{i}q_7 + {}^{i}q_9 \quad (2.17.9)$$

$^{i}q_n$, n= 1-9 , are given in Eq.(2.16.1)-(2.16.9)

The traditional 1-homogeneous Bezout number of Eq.(2.16) is 4^3=64, however the 3-homogenous Bezout number is 16, which indicates this polynomial systems has 16 solutions. Using the Sylvester dialytic elimination method, Eq.(2.16) can be reduced to a 16^{th}-degree polynomial with respect to a single variable and close-form solutions can be obtained. Detailed procedures can be found in [6].

3-2-1 Sensing

In this case, there exists a loop-closure equation with 5 joint angles sensed and 1 joint angle unsensed. For each closed-form solution derived from this equation, the problem of locating P_3 reduces to the case of 3-3-1 sensing. The number of the solutions depends on the relative position and directions of the unsensed joints as discussed in Section 3.2.3. If two unsensed joint axes are intersecting or parallel, there are up to four forward displacement solutions. If two unsensed joint axes are skew, up to eight solutions may exist. All these solutions can be expressed in analytical forms.

2.4. Application of Forward Displacement Analysis in Joint Sensor Fault Detection

Since STriDER is expected to perform field tasks such as deploying vision/sound sensors, surveillance and so on, the study on the robot's fault tolerant operation thus becomes necessary. The successful implementation of the fault tolerant operation can allow a field robot to remain operational after a failure without any degradation in performance, or with limited performance but still able to terminate the task safely.

As a fundamental step towards a complete framework of the fault tolerant operation, the detection of the faulty joint sensors in STriDER's three legs should be considered firstly. Based on the forward displacement analysis presented in previous chapters, a sensor fault detection method is proposed which utilizes the comparison of multiple forward displacement solutions for different sensing cases. The existence of common solutions based on the sensed joint angles can effectively identify the existence of a failed sensor.

2.4.1. Sensor Fault Detection Scheme

The method proposed in this chapter utilizes the readings from all nine joint sensors including both the failed and accurate sensors, as well as the premeasured lengths of STriDER's base in its triple stance phase. The side lengths of STriDER's triangular base are used as the actual values in the detection process. The objective of the detection scheme is to identify the possibly erroneous readings from all nine joint sensor candidates. Depending on the actual number and distribution of failed sensors in the three legs, the results of the detection scheme could have three levels:

1. If there is only one failed sensor out of the nine, the failed sensor can be marked;
2. If there are at least two failed sensors in one leg, then the leg can be identified;
3. If more than one leg has a failed sensor, the faulty sensing case can be detected but neither the legs with failed sensors nor the corresponding failed sensors can be identified.

Assume the readings from the failed joint sensors have small errors around their expected values; the two steps of the detection scheme are as follows:

Step 1. Check if any joint sensor is failed by calculating $\left\|\mathbf{P}_i - \mathbf{P}_j\right\|$, $i, j = 1,2,3$ and $i \neq j$.

Compare these values with the premeasured lengths p_ip_j. If they are within a specified tolerance, then the joint sensors of the legs can be considered accurate. If not, there are two possible cases:

- **Case 1:** If $\left\|\mathbf{P}_j - \mathbf{P}_k\right\|$ - $p_i\,p_k$ and $\left\|\mathbf{P}_i - \mathbf{P}_k\right\|$ - $p_i\,p_k$ are greater than the error tolerance, then leg k has at least one failed sensor.
- **Case 2:** If none of the three quantities $\left\|\mathbf{P}_i - \mathbf{P}_j\right\|$, $i, j = 1,2,3$ satisfies the tolerance, then more than one leg has failed sensors. Unfortunately, in this case, neither the legs with failed sensors nor the failed sensors can be identified. More

sensing information of STriDER, e.g., the position and orientation of the body, is needed in order to calibrate all failed sensors.

Step 2. Use the sensing case with seven joint angles (3-3-1) to mark the joint with the failed sensor. Following Case 1 in Step 1, if there is only one leg k has a failed joint sensor(s),

- Similar to the 3-3-1 sensing case discussed in Section 2.3, the global position vectors of the feet $\mathbf{P}_i$ and $\mathbf{P}_j$ are considered accurate. Then, the locus of the foot $\mathbf{P}_k$ is a spatial circle $C_{i,j}$ because of the constraints implemented by the base triangle. For the readings of the three joint sensors in leg k, one reading is treated as a sensed joint angle and the other two are treated as unsensed joint angles in each calculation of the forward displacement solutions. Depending on the layout of the unsensed joints, the locus of $\mathbf{P}_k$ under the constraints of leg k can be a sphere, a torus or a ring plane. Inspecting the three sets of forward displacement solutions generated, if only one sensor in leg k is failed, then two of the solution sets obtained are based on the accurate readings and they must have common solutions. The forward displacement solution calculated with the erroneous reading will not have common solutions with the other two, thus allowing the failed sensor to be marked.
- However, if no pairs of solutions sets have any common solutions, then leg k must have at least two failed joint sensors and the two sensors cannot be marked exactly.

In Step 2 of the method presented above, the constraints in all three legs are considered. A second detection approach that considers the constraints of only two legs at a time could be used as an alternative way to double-check or confirm the results obtained from Step 1 and 2.

Consider the closed loop generated by leg i and j. The location of $\mathbf{P}_j$ is constrained by leg i to be on a sphere SP_{ji} with the center at $\mathbf{P}_i$ and radius p_ip_j. Assume the joint sensors on leg i are perfect and leg j has one failed sensor. In each calculation, treat two out of the three joints sensors in leg j as sensed angles, the locus of $\mathbf{P}_j$ is then a spatial circle C_{lj} with the center at the unsensed joint. A sphere and a circle typically have two intersection points. Inspecting the three solution sets generated from the sphere and the circle, if no common solution can be found, then leg j at least has one failed sensor. This is because two of the three solution sets are based on the erroneous reading. The two accurate joint sensors can guarantee that at least one solution set exists. Therefore, if no solution exists at all for the intersection of the sphere and the circle (only imaginary solutions exist), leg j must have at least two failed sensors.

The second detection method can confirm the results of Step 1 and 2 through the following three ways:

1. If $SP_{ji} \cap C_{lj}$, l = 1,2,3 for the hip rotator, flexure and knee joints, have a common solution, then the joint sensors of leg i and j are accurate.
2. If the joint sensors of leg i and j are accurate, $SP_{ki} \cap C_{lk}$ and $SP_{kj} \cap C_{lk}$ do not have common solutions, then leg k has at least one failed sensors.
3. If $SP_{ki} \cap C_{lk}$ and $SP_{kj} \cap C_{lk}$ do not even have a solution, then leg k has at least two failed sensors.

2.4.2. Summary and Discussion

The sensor fault detection method in Sec.2.4.1 utilizes the common solutions of the forward displacement in some redundant sensing cases to identify the leg with failed sensors or mark the failed sensor. Theoretically, this approach can work effectively for the cases with erroneous reading from one or two joint sensor in one leg, i.e. 3-3-2 and 3-3-1, where the number is used to denote the perfect sensors in one leg. If at least two legs have failed sensors, such as 3-2-2, 3-2-1 or 2-2-2, only the cases themselves can be detected and neither the legs with failed sensors nor the inaccurate sensors can be identified.

Note that, since the detection method does not use any information of the current position and orientation of STriDER's body, it is unable to detect the fault cases if the erroneous readings coincident with one of the forward displacement solutions. A complete calibration of all nine joint sensors requires more information as the input.

Chapter 3 Simulation of the Inverse and Forward Kinematics Algorithm

Examples and results are presented in this chapter to verify the theory discussed in the previous chapters. The parameters of the kinematic configuration are measured from the first prototype of STriDER. Based on these data, the inverse displacement problem and the forward displacement problem of the non-redundant 2-2-2 case of sensing are successfully solved. The results obtained from calculations match each other very well.

Using the equations developed in Chapter 4, examples of the inverse and forward singular configurations of the robot is displayed. For each forward singular case presented, the unconstrained DOF is identified and the elimination scheme based on redundant actuation is proposed.

3.1. Inverse Kinematics Example

The inverse displacement analysis displayed here relates to a general case. As mentioned in the inverse displacement analysis section, the known values for this calculation include; the global body position and orientation, θ_{1i}, as well as all foot positions. Also the following link lengths were taken from the prototype and used in this simulation, L_{0i}=0.0935 m, L_{1i}= 0 m, L_{2i}=0.0935 m, L_{3i}=0.5 m, and L_{4i}=1.3 m. The base is assumed to be a equilateral triangle with the length of the side $d_{i(i+1)}$ = 1.24m.

Based on the coordinates setup in Fig.1.5, Table 3.1 and Table 3.2 list the global body position and orientation and the global foot positions for each leg respectively. Once these values are selected, the step by step approach previously discussed in Chapter 2 is preformed.

TABLE 3.1 BODY POSITION AND ORIENTATION RELATIVE TO GLOBAL COORTINATES

X Rotation (roll)	10°
Y Rotation (pitch)	5°
Z Rotation (yaw)	0°
X Translation	0 m
Y Translation	0 m
Z Translation	1.6 m

TABLE 3.2 GLOBAL FOOT POSITIONS FOR EACH LEG

Foot Position	X (m)	Y (m)	Z (m)
P_1	0.716	0	0
P_2	-0.358	0.620	0
P_3	-0.358	-0.620	0

First, a homogenous transformation from the global coordinated to the hip rotator joint is preformed, as shown in Eq. (2.1). Next, the relative location of each foot position to hip rotator joint is calculated using Eq. (2.4). As previously stated, by treating each leg as an serial manipulator the internal joint angles θ_{2i}, θ_{3i} and θ_{4i} are calculated as shown in Eq.(2.5), (2.6) and (2.8). Table 3.3 lists the results of these calculations for a knee-up scenario.

TABLE 3.3 INVERSE DISPLACEMENT ANALYSIS RESULTS (ELBOW DOWN)

Leg Number (i)	θ_{2i}	θ_{3i}	θ_{4i}
1	-10°	59.628°	-49.243°
2	0.802°	34.781°	-38.275°
3	9.817°	61.252°	-49.877°

3.2. Forward Kinematics Example

With the data listed in Table 5, the forward displacement analysis in a 2-2-2 symmetric non-redundant sensing case is conducted. Without losing the generality, θ_{21}, θ_{32} and θ_{43} are assumed to be the three unsensed joint angles and the rest joint angles are sensed. By carrying out the method in Section 3.2.4, 16 solutions are found and 6 among them are real solutions. These real solutions are verified by substituting back to Eq. (2.17). The corresponding solutions of θ_{ki} are listed in Table 3.4 and the postures of STriDER are plotted in Fig.3.1 to Fig.3.6. All six postures only differ in the three unsensed joint angles. Among those solutions, solution 1, 2, 3 and 6 don't have a stable posture because the positions of the body are either below the ground or projected out of the range of base triangle. Solution 4 and 5 are stable with very subtle difference and note that solution 5 matches exactly with the pre-specified joint angles.

TABLE 3.4 FORWARD DISPLACEMENT ANALYSIS RESULTS

Simulation number	θ_{21}	θ_{32}	θ_{33}
1	174.937°	100.922°	138.802°
2	170.639°	190.845°	172.999°
3	-11.224°	34.111°	-132.854°
4	-6.965°	36.389°	-51.980°
5	**-10°**	**34.781°**	**-49.877°**
6	-10.416°	-38.078°	-49.597°

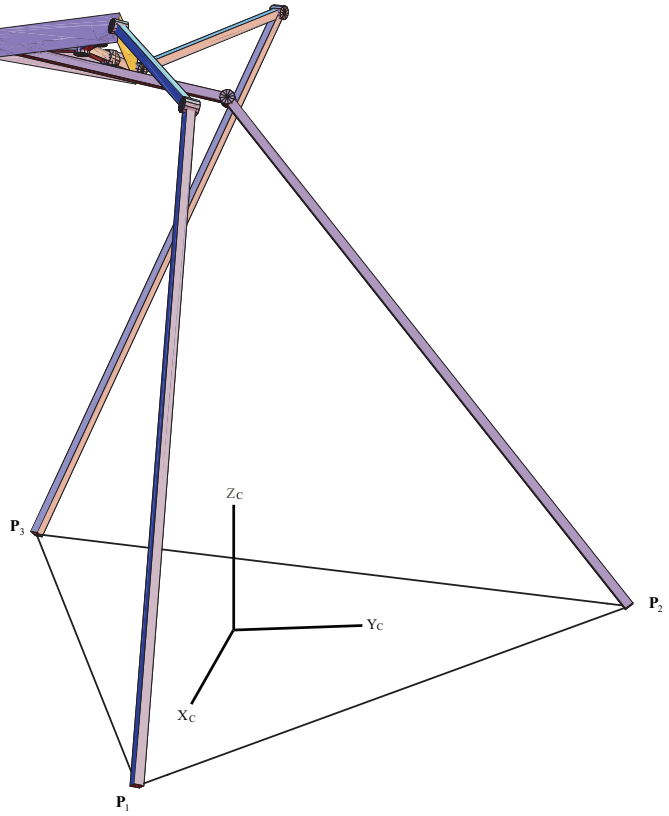

FIG.3.1 FORWARD DISPLACEMENT SOLUTION 1

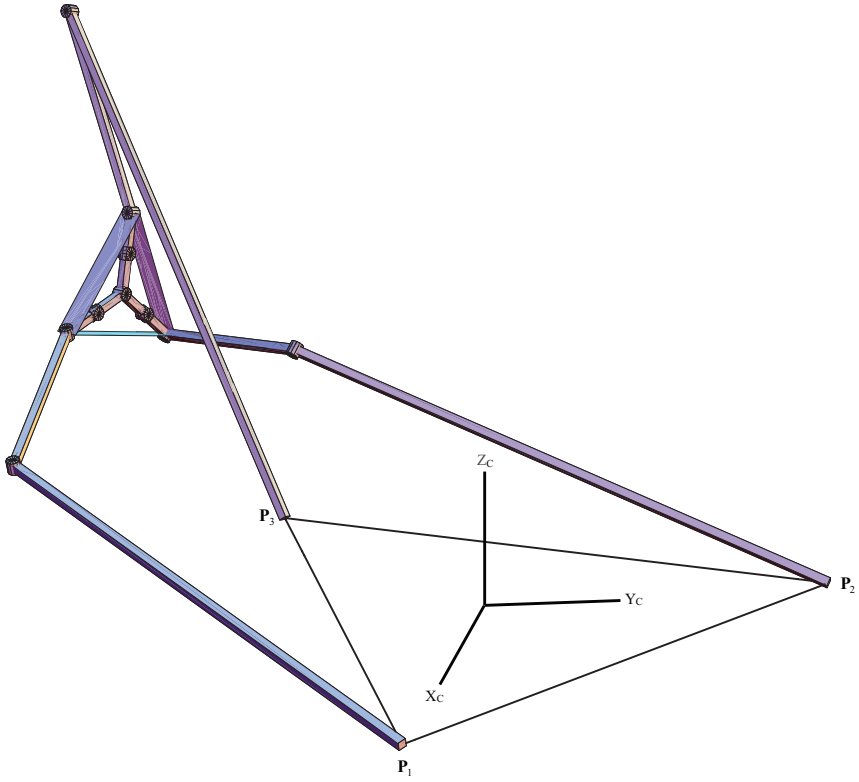

FIG.3.2 FORWARD DISPLACEMENT SOLUTION 2

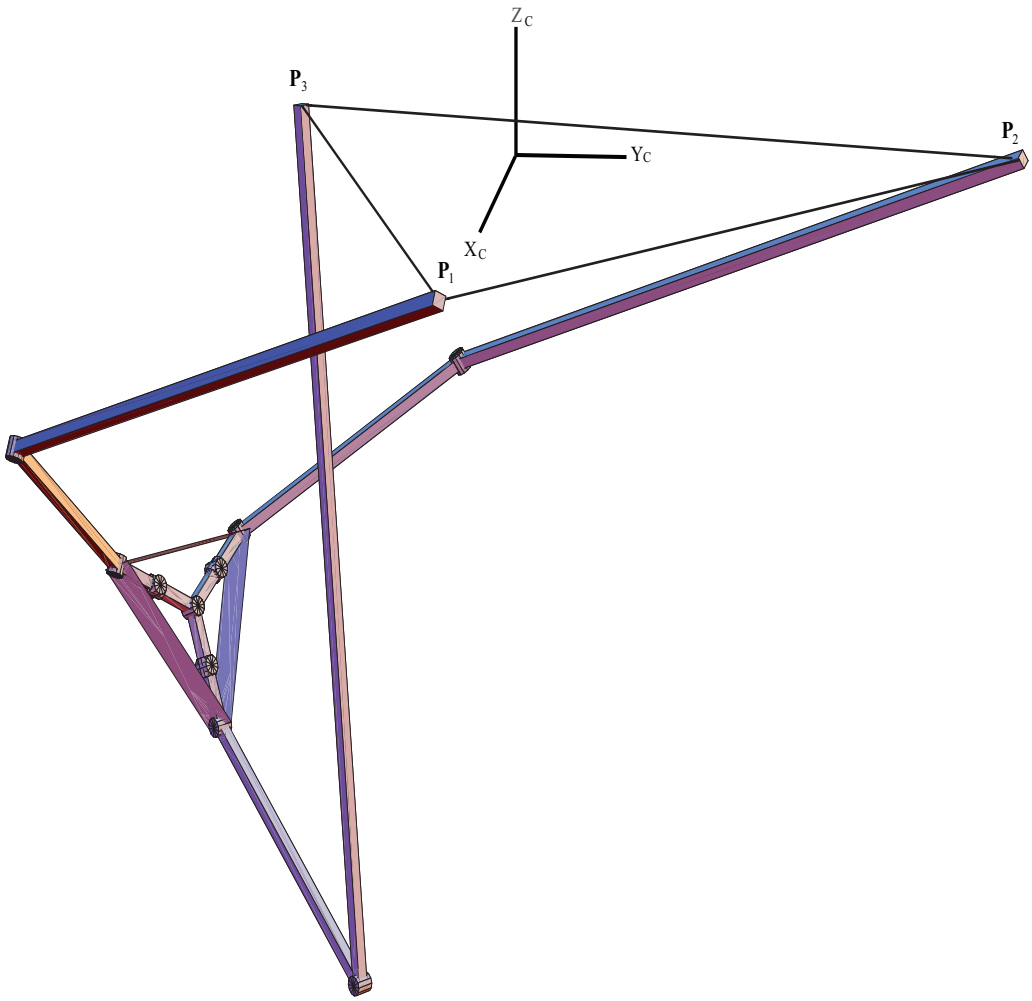

FIG.3.3 FORWARD DISPLACEMENT SOLUTION 3

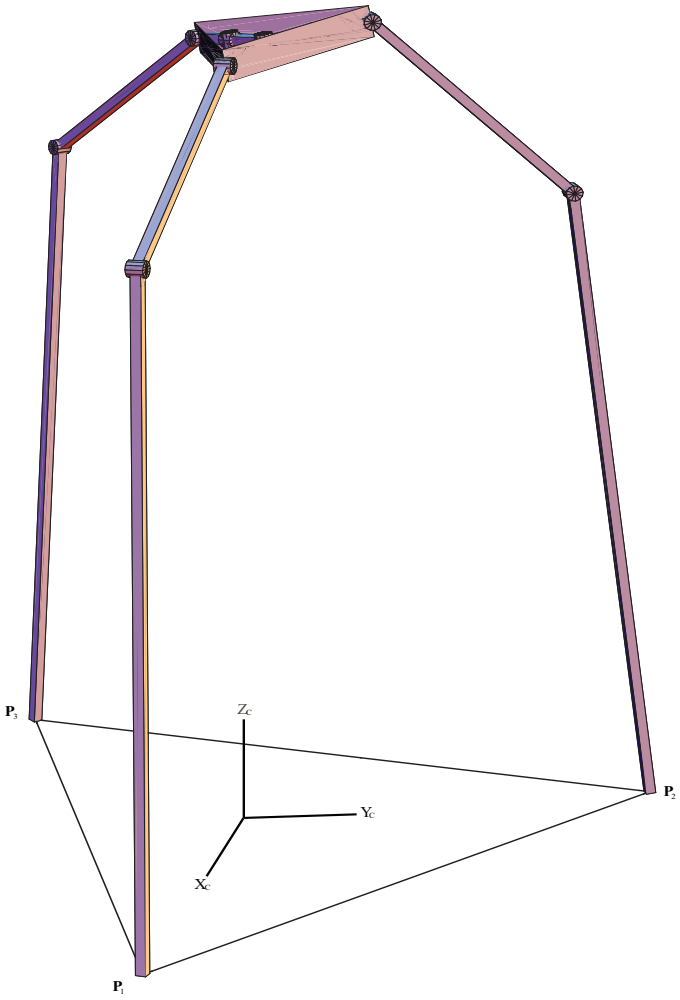

FIG.3.4 FORWARD DISPLACEMENT SOLUTION 4

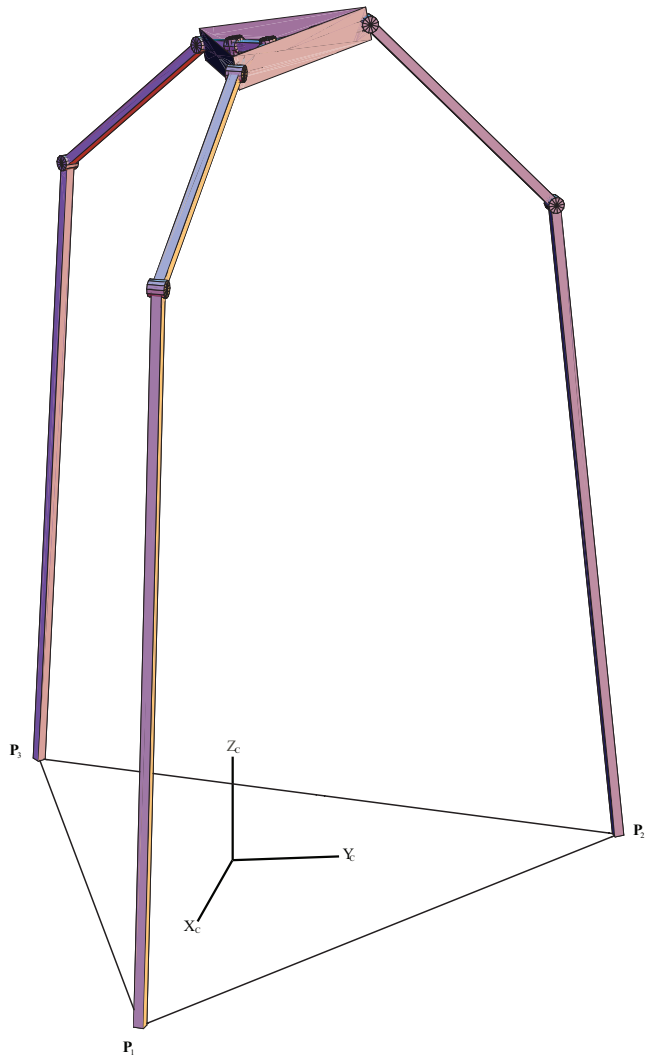

FIG.3.5 FORWARD DISPLACEMENT SOLUTION 5

FIG.3.6 FORWARD DISPLACEMENT SOLUTION 6

Chapter 4 Jacobian Analysis

Jacobian analysis, also known as instantaneous kinematics analysis, relates the velocity space of the body of the in-parallel manipulator to the internal joint rates space. It also provides insights into the singular configurations of the manipulator system. Theory of screws and reciprocal screws are frequently used to develop Jacobian matrices of various parallel manipulators. Gosselin and Angeles studied the singularities of closed-loop mechanisms in [63] and suggested a separation of the Jacobian into two matrices: one associated with the forward kinematics and the other with the inverse kinematics. Tsai gave a specific procedure to derive screw-based Jacobian in [64]. Because of the duality of kinematics and statics, screw theory can also be applied to the force analysis of robotic manipulators as in [65].

In this chapter, the screw and reciprocal screw theory are introduced in the beginning. The screw-based Jacobian matrix is developed for STriDER. Detailed procedures to obtain the matrix are listed and for each active joint screw, its associated reciprocal screw is identified. Note that, the Jacobian analysis of the in-parallel manipulators must be developed after the forward kinematics problems are solved, i.e. the location and direction of the joint screws can be expressed with respect to a known reference coordinate system.

4.1. Introduction to Screws, Wrenches, and Twists

The screw theory is extensively treated in [66, 67] and [68]. We briefly introduce this theory in this section.

Both finite and infinitesimal displacement of a rigid body can conveniently be expressed as a rotation about a unique axis and a translation along the same axis. This combined motion is called *twist*, and the unique axis is called a *screw axis* of the displacement. Due to the duality of statics and instantaneous kinematics, a similar concept can be defined. Any system of forces and couples acting on a rigid body can be reduced to a resultant force and a couple acting on the same axis. The force and couple combination is called a *wrench*. The twist and the wrench can be denoted as 6-D vectors called screws as follows:

$$\mathbf{T} = [\mathbf{w}, \mathbf{q} \times \mathbf{w} + \mathbf{v}]; \quad \mathbf{W} = [\mathbf{f}, \mathbf{p} \times \mathbf{f} + \mathbf{t}] \qquad (4.1)$$

where **w** is the angular velocity and **v** is the linear velocity of point q, represented by vector **q**, **f** and **t** are the force and torque of the wrench acting on point p, represented by vector **p**. The pitch h of **T** satisfies $\mathbf{v} = h\omega$ and the pitch h' of **W** satisfies $\mathbf{t} = h' f$, ω and f are the magnitude of **w** and **f**, respectively. A wrench and a twist are said to be *reciprocal* if the virtual work of the wrench on the twist is zero. The basic reciprocal condition is as follows:

$$(h + h')\cos\lambda - r\sin\lambda = 0 \qquad (4.2)$$

where r is the shortest distance between the screws and λ is the angle between them. A list of reciprocal screws based on Eq. (4.2) is provided in [67]. The reciprocal screws of 1 DOF joints (revolute, prismatic), 2 DOF joint (universal) and 3 DOF joint (spherical) are addressed by Tsai in [20]. Tsai also described the reciprocal screws associated with various kinematic

chains. Since the joints of the three legged S-R-R-R in-parallel manipulator can be considered as all revolute joints (spherical joint is treated as three revolute joint concurrent at a common point), zero-pitch (h = 0) screws and reciprocal screws needs particular attention. The zero-pitch screws also coincide with the Plücker coordinates of straight lines. Thus finding reciprocal screws for a given zero-pitch screw can be solved by considering the intersecting lines of the given line. In the following sections, reciprocal screws are extensively used to develop the Jacobian matrices and singularity analysis.

4.2. Jacobian Analysis Using Reciprocal Screws

The instantaneous twist, $\$_B$, of the body of the parallel manipulator can be expressed as a linear combination of l instantaneous twists, which was demonstrated in [69].

$$\$_B = \sum_{j=1}^{l} \dot{q}_{j,i} \hat{\$}_{j,i} \qquad \text{,for} i = 1, 2, ..., m \qquad (4.3)$$

where $\dot{q}_{j,i}$ and $\hat{\$}_{j,i}$ denote the intensity and the unit screw associated with the j th joint of the i th leg, m is the number of legs of the parallel manipulator.

When Eq.(4.3) is assembled into matrix form, the screw-based Jacobian matrix can be established. However the unactuated joint rates in Eq. (4.3) must be eliminated at first. This elimination can be accomplished using the theory of reciprocal screws. Assume that g actuated joints appear in leg i, for an actuated joint j of the g joints, a reciprocal screw is identified that is reciprocal to all the other joint screws in leg i, except for joint j. Take the orthogonal product of both sides of Eq. (4.3) with each reciprocal screw. Then g equations can be written which correspond to g actuated joints in leg i. Repeating this procedure for each of the m legs yields $n = m \times g$ linear equations which can be assembled in matrix form:

$$\mathbf{J}_x \mathbf{\$}_B = \mathbf{J}_q \dot{\mathbf{q}} \qquad (4.4)$$

Thus, the Jacobian matrices associated with the forward kinematics J_x and the inverse kinematics J_q are derived. Note that both J_x and J_q are screw-based Jacobian matrices and the rows of J_x are actually the reciprocal screws identified for each actuated joint.

4.3. Identification of Reciprocal Screws

The identification of appropriate reciprocal screws is crucial for the development of screw based Jacobian matrix about in-parallel manipulators. If each reciprocal screw is chosen to be reciprocal to all the joint screws, except for just one of the actuated joint screws, then J_q is greatly reduced to a diagonal matrix. Thus, the Jacobian matrices have more compact forms and the computation time of solving a matrix equation will be much shorter.

As for the case of the three legged SRRR kinematic model of STriDER, the reciprocal screws associated with each active joint is much easier to identify. Due to the all-revolute

joint type in each leg of STriDER (the passive spherical joint is considered as three passive orthogonal revolute joints intersecting at the foot), all joint screws are zero-pitch screws corresponding to straight lines in 3D space. Finding a reciprocal screw to an active joint screw is equivalent to finding a line that intersects all the other joint axes in a given leg except the axis of the active joint. Fig.4.1 is used to assist the identification of the reciprocal screws, which shows the joint screws and reciprocal screws in Leg i. In this figure, $\$_1$, $\$_2$ and $\$_3$ are the three actively controlled joint screws in Leg i. These three joint screws are equivalent to the axes of joint 2,3 and 4 in Leg i, i.e. the hip rotator joint, the hip flexure joint and the keen joint. There are also three passive joint screws $\$_4$, $\$_5$ and $\$_6$ at the foot the Leg i. These three joints screws are orthogonal to each other and interesting at the foot contact point with the ground. Therefore, identification of the reciprocal screws to any screw of $\$_1$, $\$_2$ and $\$_3$ is solved by locating a line that intersects the rest two screws of $\$_1$, $\$_2$ and $\$_3$ and three passive joint screws $\$_4$, $\$_5$ and $\$_6$. These identified reciprocal screws are represented with red dash lines and denoted with $\$r_1$, $\$r_2$ and $\$r_3$ in Fig.4.1.

$\$r_1$ is the reciprocal screw to $\$_1$. It is a line that passes through the foot contact point Pi and parallel to $\$_2$ and $\$_3$. If one line is parallel to another line, the angle λ between the two parallel lines is zero, which means the Eq.(4.2) still holds true and parallel lines can be considered as intersecting at “infinity”.

$\$r_2$ is the reciprocal screw to $\$_2$. It passes Pi thus intersecting $\$_4$, $\$_5$ and $\$_6$. By inspecting the geometric relationship between, a line with a same direction as the shank line of STriDER is the only candidate that intersects all joint axes except $\$_2$.

$\$r_3$ is the reciprocal screw to $\$_3$. Since $\$_1$ and $\$_2$ intersects at the origin of joint 3, a line that connects the intersection point and the foot contact point is the reciprocal screw we are looking for.

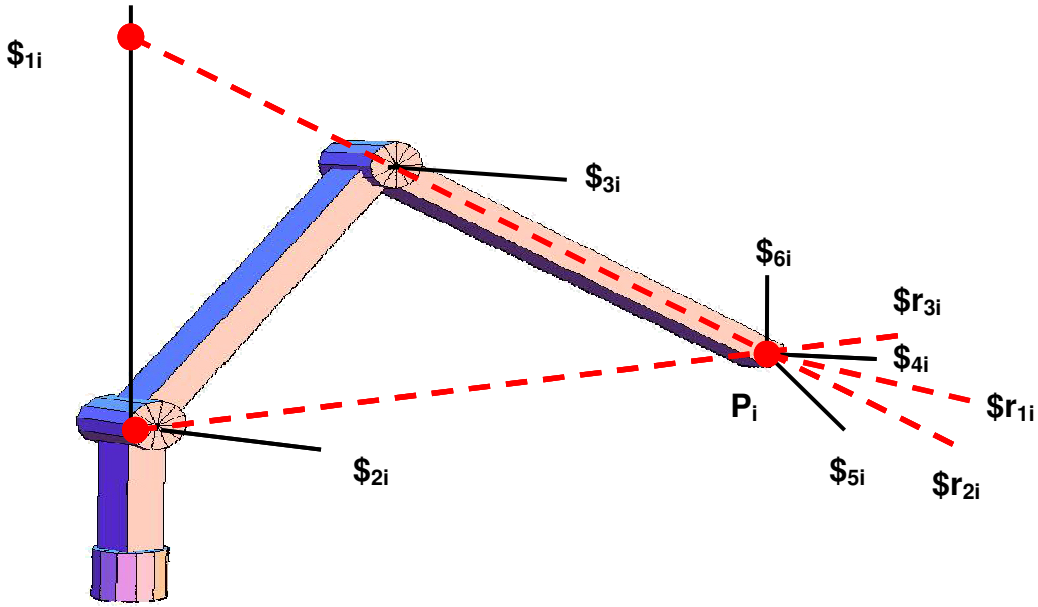

4.4. Screw-Based Jacobian Matrix of STriDER

As described in Chapter 1, two Cartesian coordinate systems $\{X_0,Y_0,Z_0\}$ and $\{x_B,y_B,z_B\}$ are attached to the virtual base and the body of STriDER, respectively. An instantaneous reference frame is set at the body center coordinate system $\{x_B,y_B,z_B\}$. Then, all joint screws and reciprocal screws are expressed with respect to the body frame.

There are six joint screws associated with each leg and three of them can be actively controlled. Since the motion of the body is controlled with at least six joints actuation, a total of nine possible active joints can not only provide more actuation schemes but also elimination the forward singularities. Detailed discussion on the forward singularity elimination can be found in Chapter 5. In this chapter, we mainly focus on the development of Jacobian matrix. The term $\$_{ji}$ is used to represent any joint in any leg, with i = 1,2,3 (numbering of the legs) and j = 1,2,3,4,5,6 (numbering of the joints in a leg). Each unit screw $\$_{ji}$ has two parts. The real unit is denoted with $\mathbf{S}_{ji}$ and the dual unit is denoted with $\mathbf{So}_{ji.}$ A point on the axis of $\$_{ji}$ is represented with $\mathbf{r}_{ji}$ and often set at the origin of a joint. According to the definition of screw, the due unit $\mathbf{So}_{ji.} = \mathbf{r}_{ji} \times \mathbf{S}_{ji}$. Using the DH parameters listed in Table 2, the joint screws can be written as follows:

$$
\begin{aligned}
\mathbf{S}_{1i} &= {}^{B}\mathbf{R}_{0i}\,{}^{0i}\mathbf{R}_{1i}\begin{bmatrix}0 & 0 & 1\end{bmatrix}^{T} \\
\mathbf{S}_{2i} &= {}^{B}\mathbf{R}_{0i}\,{}^{0i}\mathbf{R}_{1i}\,{}^{1i}\mathbf{R}_{2i}\begin{bmatrix}0 & 0 & 1\end{bmatrix}^{T} \\
\mathbf{S}_{3i} &= {}^{B}\mathbf{R}_{0i}\,{}^{0i}\mathbf{R}_{1i}\,{}^{1i}\mathbf{R}_{2i}\,{}^{2i}\mathbf{R}_{3i}\begin{bmatrix}0 & 0 & 1\end{bmatrix}^{T} \\
\mathbf{S}_{4i} &= \begin{bmatrix}1 & 0 & 0\end{bmatrix}^{T} \\
\mathbf{S}_{5i} &= \begin{bmatrix}0 & 1 & 0\end{bmatrix}^{T} \\
\mathbf{S}_{6i} &= \begin{bmatrix}0 & 0 & 1\end{bmatrix}^{T}
\end{aligned}
\qquad (4.5)
$$

where matrices **R** are the 3 by 3 rotational part of the homogeneous transformation matrices **H.**

The points ro_{ji} on the joint axes are set at the origin of the joint. Homogeneous transformation matrices **H** can be utilized to calculate the position vector.

$$
\begin{aligned}
\begin{bmatrix}\mathbf{r}_{1i}\\ 1\end{bmatrix} &= {}^{B}\mathbf{H}_{0i}\,{}^{0i}\mathbf{H}_{1i}\begin{bmatrix}0 & 0 & 0 & 1\end{bmatrix}^{T} \\
\begin{bmatrix}\mathbf{r}_{2i}\\ 1\end{bmatrix} &= {}^{B}\mathbf{H}_{0i}\,{}^{0i}\mathbf{H}_{1i}\,{}^{1i}\mathbf{H}_{2i}\begin{bmatrix}0 & 0 & 0 & 1\end{bmatrix}^{T} \\
\begin{bmatrix}\mathbf{r}_{3i}\\ 1\end{bmatrix} &= {}^{B}\mathbf{H}_{0i}\,{}^{0i}\mathbf{H}_{1i}\,{}^{1i}\mathbf{H}_{2i}\,{}^{2i}\mathbf{H}_{3i}\begin{bmatrix}0 & 0 & 0 & 1\end{bmatrix}^{T} \\
\begin{bmatrix}\mathbf{r}_{4i}\\ 1\end{bmatrix} &= {}^{B}\mathbf{H}_{0i}\,{}^{0i}\mathbf{H}_{1i}\,{}^{1i}\mathbf{H}_{2i}\,{}^{2i}\mathbf{H}_{3i}\,{}^{3i}\mathbf{H}_{4i}\begin{bmatrix}0 & 0 & 0 & 1\end{bmatrix}^{T}
\end{aligned}
\qquad (4.6)
$$

$$\mathbf{r}_{6i} = \mathbf{r}_{5i} = \mathbf{r}_{4i}$$

Again, with the assistance of transformation matrices **R** and **H**, the unit reciprocal screws $\$r_1$, $\$r_2$ and $\$r_3$ are calculated as follows:

$$
\begin{aligned}
\mathbf{Sr}_{1i} &= \mathbf{S}_{2i} = \mathbf{S}_{3i} \\
\mathbf{r}_{r,1i} &= \mathbf{r}_{4i} = \mathbf{r}_{5i} = \mathbf{r}_{6i}
\end{aligned}
\qquad (4.7)
$$

$$
\begin{aligned}
\mathbf{Sr}_{2i} &= (\mathbf{r}_{4i} - \mathbf{r}_{3i}) / \left\|\mathbf{r}_{4i} - \mathbf{r}_{3i}\right\| \\
\mathbf{r}_{r,2i} &= \mathbf{r}_{4i} = \mathbf{r}_{5i} = \mathbf{r}_{6i}
\end{aligned}
\qquad (4.8)
$$

$$
\begin{aligned}
\mathbf{Sr}_{3i} &= (\mathbf{r}_{4i} - \mathbf{r}_{2i}) / \left\|\mathbf{r}_{4i} - \mathbf{r}_{2i}\right\| \\
\mathbf{r}_{r,3i} &= \mathbf{r}_{4i} = \mathbf{r}_{5i} = \mathbf{r}_{6i}
\end{aligned}
\qquad (4.9)
$$

Recall Eq.(4.3)

$$\$_B = \sum_{j=1}^{l} \dot{q}_{j,i} \hat{\$}_{j,i} \qquad \text{,for } i = 1, 2, ..., m$$

Substitute the joint screws obtained from Eq.(4.5) and Eq.(4.6) in to Eq.(4.3) and take the orthogonal product of both sides of Eq.(4.5) with the reciprocal screws obtained from Eq.(4.7) to (4.9). Perform the operations for each of the three legs and assemble the equations in matrix form, we obtain

$$\mathbf{J}_x \$_B = \mathbf{J}_q \dot{\mathbf{q}} \tag{4.10}$$

where $\$_B = \begin{bmatrix} {}^B\boldsymbol{\omega}_n \\ {}^B\mathbf{v}_0 \end{bmatrix} = \begin{bmatrix} {}^B\omega_x & {}^B\omega_y & {}^B\omega_z & {}^Bv_{px} & {}^Bv_{py} & {}^Bv_{pz} \end{bmatrix}^T$

$\dot{\mathbf{q}} = \begin{bmatrix} \dot{\theta}_{11} & \dot{\theta}_{21} & \dot{\theta}_{31} & \dot{\theta}_{12} & \dot{\theta}_{22} & \dot{\theta}_{32} & \dot{\theta}_{13} & \dot{\theta}_{23} & \dot{\theta}_{33} \end{bmatrix}^T$

$$\mathbf{J}_x = \begin{bmatrix} \mathbf{Sor}_{11}^T & \mathbf{Sr}_{11}^T \\ \mathbf{Sor}_{21}^T & \mathbf{Sr}_{21}^T \\ \mathbf{Sor}_{31}^T & \mathbf{Sr}_{31}^T \\ \mathbf{Sor}_{12}^T & \mathbf{Sr}_{12}^T \\ \mathbf{Sor}_{22}^T & \mathbf{Sr}_{22}^T \\ \mathbf{Sor}_{32}^T & \mathbf{Sr}_{32}^T \\ \mathbf{Sor}_{13}^T & \mathbf{Sr}_{13}^T \\ \mathbf{Sor}_{23}^T & \mathbf{Sr}_{23}^T \\ \mathbf{Sor}_{33}^T & \mathbf{Sr}_{33}^T \end{bmatrix}$$

which contains the screw transpose of the reciprocal screws

and $\boldsymbol{J}_q$ is a diagonal matrix which equals:

$$\mathbf{J}_q = \text{Diag}\Big[\ \hat{\$}r_{11}{}^T\hat{\$}_{11} \quad \hat{\$}r_{21}{}^T\hat{\$}_{21} \quad \hat{\$}r_{31}{}^T\hat{\$}_{31} \quad \hat{\$}r_{12}{}^T\hat{\$}_{12} \quad \hat{\$}r_{22}{}^T\hat{\$}_{22} \quad \hat{\$}r_{32}{}^T\hat{\$}_{32} \quad \hat{\$}r_{13}{}^T\hat{\$}_{13} \quad \hat{\$}r_{23}{}^T\hat{\$}_{23} \quad \hat{\$}r_{33}{}^T\hat{\$}_{33} \ \Big]$$

The analytical expressions of $\$r_{1i}{}^T\$_{1i}$, $\$r_{2i}{}^T\$_{2i}$ and $\$r_{2i}{}^T\$_{2i}$ are listed below. The numerator of the expressions can be used to identify the conditions of inverse singularities of the in-parallel manipulators.

$$\hat{\$}\mathbf{r}_{1i}{}^T\hat{\$}_{1i} = -\cos\theta_{3i}\mathrm{L}_{3i} - \cos(\theta_{3i} + \theta_{4i})\,\mathrm{L}_{4i}$$

$$\hat{\$}\mathbf{r}_{2i}{}^{T}\hat{\$}_{2i} = \frac{4\sin\theta_{4i}\ L_{3i}\ L_{4i}}{f_1(\theta_{2i},\theta_{3i},\theta_{4i})}$$

$$\hat{\$}\mathbf{r}_{3i}{}^{T}\hat{\$}_{3i} = \frac{-4\sin\theta_{4i}\ L_{3i}\ L_{4i}}{f_2(\theta_{2i},\theta_{3i},\theta_{4i})}$$

where f_1 and f_2 are non zero functions of θ_{2i}, θ_{3i} and θ_{4i}.

Since the instantaneous reference frame is coincident with the body center coordinate system $\{x_B,y_B,z_B\}$, all the reciprocal screws and joint screws are expressed with respect to the body frame. Note that, $\$_B = \begin{bmatrix} {}^{B}\boldsymbol{\omega}_n \\ {}^{B}\mathbf{v}_0 \end{bmatrix}$ is also defined in the instantaneous reference frame which represents the angular velocity and the linear velocity of a point (could be imaginary point) of the body that is coincident with the origin of the reference frame. However, in most cases of operations in reality especially the operations requiring velocity control, the desired velocity state of the body is usually defined with respect to the global fixed coordinate system $\{X_0,Y_0,Z_0\}$. Therefore the transformation between $\$_B = \begin{bmatrix} {}^{B}\boldsymbol{\omega}_n \\ {}^{B}\mathbf{v}_0 \end{bmatrix}$ and $\$_G = \begin{bmatrix} {}^{G}\boldsymbol{\omega}_n \\ {}^{G}\mathbf{v}_n \end{bmatrix}$ must be established. These two velocity state vectors are related by the following equations:

$$\begin{aligned} {}^{G}\boldsymbol{\omega}_n &= {}^{0}\mathbf{R}_B\ {}^{B}\boldsymbol{\omega}_n \\ {}^{G}\mathbf{v}_n &= {}^{0}\mathbf{R}_B\left({}^{B}\mathbf{v}_0 + {}^{B}\boldsymbol{\omega}_n \times {}^{B}\mathbf{p}_n\right) \end{aligned} \qquad (4.11)$$

where ${}^{0}\mathbf{R}_B$ is the 3 by 3 rotation transformation matrix between the global fixed system $\{X_0,Y_0,Z_0\}$ and the body center frame $\{x_B,y_B,z_B\}$. ${}^{B}\mathbf{p}_n$ denotes the position vector of the origin of body frame with respect to the instantaneous reference frame. In this particular case, since the body frame is coincident with the instantaneous reference frame, ${}^{B}\mathbf{p}_n = [0 \quad 0 \quad 0]^T$.

Eq.(4.10) establishes the mapping between the velocity space of the body and the space of all nine joint rates. Actually, for a desired velocity state of the body, six out of nine joints can be actively controlled to reach that state. Among all nine joints, only six of them are independent and the velocity profiles of rest three joints are dependent on the six joints due to the existence of multiple closed loops in the kinematic structure. The redundancy of the active joints provides various actuation schemes such as seven, eight or nine joints actuation. These additional joints can either passively follow a time profile or actively track it. Actuation with more than six joints can improve the performance of the robot in particular operations because the required load or speed is shared with more joint motors.

For the inverse instantaneous kinematics, the velocity state of the body is known. Assume that Eq.(3-10) is not in a singularity configuration, then both active and passive joint rates can

be calculated. At least six joints will be chosen to track the profiles in order to reach the desired state. Redundant actuation of additional joints can increase the ability of the robot to resist the disturbance forces or moments from outside. For example, redundant actuation can eliminate the forward singularities, which is discussed in details in Chapter 5.

As for the forward instantaneous kinematics, if at least six joint rates are known, then not only the velocity state of the body but also the rates of the rest joint, either active or passive, can be obtained through Eq.(4.3-4.10).

Chapter 5 Singularity Identification and Elimination

Due to the existence of two Jacobian matrices in Eq. (4.3-4.4), an in-parallel manipulator can have two types of singularities. One is inverse kinematic singularity and the other is forward kinematic singularity.

Inverse kinematic singularity occurs when the determinant of $\mathbf{J}_q$ is equal to zero. Under such singular configurations, the infinitesimal motion of the body of parallel manipulator along certain directions cannot be accomplished; the manipulator loses one or more DOF.. The inverse singularity of the in-parallel manipulators is similar to the singularity of a serial manipulator. Therefore, checking the singular configurations of one leg is also a method to identify the inverse singularity of the whole in-parallel manipulator.

A forward kinematic singularity occurs when the $\mathbf{J}_x$ is not full rank. Unlike inverse kinematic singularity, the manipulator gains one or more DOF while all the joint actuators are completely locked. The forward kinematic singularity of the three-legged S-R-R-R in-parallel manipulator, i.e. the equivalent kinematic model of STriDER, becomes more complicated as the manipulator can implement non-redundant actuation mode or redundant actuation mode. Since more than six joints will be actuated in redundant actuation, $\mathbf{J}_x$ is no longer a square matrix. Identification of the singular configurations requires checking the linear dependency of each row in J_x. Compared with conventional Jacobian matrix, screw-based Jacobian is more powerful in solving such problems. Each row of $\mathbf{J}_x$ is the screw transpose of the reciprocal screw identified for each actuated joint. These zero-pitch screws are equivalent to the Plücker line coordinate, so each screw represents uniquely a line in 3D space. Using the theory of line geometry, the linear dependent cases of the rows of J_x can be identified, which corresponds to the singularities of the forward kinematics.

In this chapter, the inverse singularities are identified at first, which shows that the inverse singular configurations of the whole in-parallel manipulator can be identified by investigating the singularities of a single leg. Since line geometry is frequently used in the identification of forward singularities, the theory of line geometry is introduced at first, followed by a detailed discussion on the line varieties and its order. The analytical conditions under which the forward singularities of a non-redundant 2-2-2 actuated SRRR in-parallel manipulators occur are identified. Correspondingly, the elimination method based on redundant actuation is discussed.

The method addressed in this chapter can also be used to identify the forward singularities of a family of three legged in-parallel manipulators with a completely passive spherical joint at each leg.

5.1. Inverse Singularities

The $\mathbf{J}_q$ matrix in Eq.(4.10) is diagonal matrix with $\$r_{ji}^{T}\$_{ji}$ as its diagonal elements. The conditions of inverse singularities can be derived by equating the diagonal elements to zero. Two types of singularities are identified and the conditions are listed below:

$$-\cos\theta_{3i} L_{3i} - \cos(\theta_{3i} + \theta_{4i}) L_{4i} = 0 \qquad (5.1)$$

and

$$4 \sin\theta_{4i} L_{3i} L_{4i} = 0, \text{ that is, } \theta_{4i} = 0, \pi \qquad (5.2)$$

The singularity derived from Eq.(5.1) corresponds to a configuration in which the axis of the hip rotator joint is passing the foot contact point. Thus the rotational DOF. of the hip rotator is lost. Any input to the hip rotator cannot change the position of the body. The singularity derived from Eq.(5.2) corresponds to a configuration in which the leg is either fully extended or fully retracted. Under this singular configuration, the body reaches the edge of its effective workspace and any motion along the direction of the shank is unreachable. Thus, the in-parallel manipulator loses one DOF.. These two singularities are shown in Fig.5.1 and Fig.5.2. The results exactly match the singularities of an elbow manipulator discussed in [53].

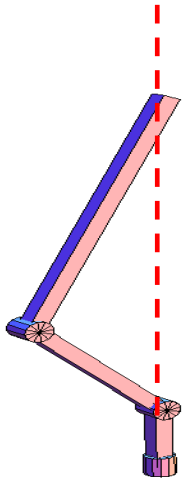

FIG.5.1. INVERSE SINGULARITY, CASE ONE

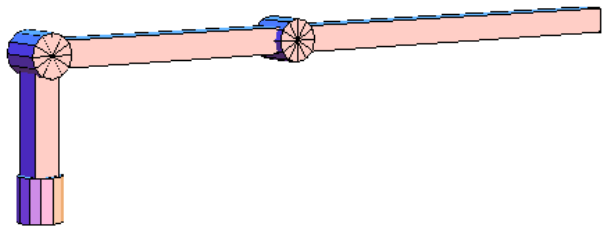

FIG.5.2. INVERSE SINGULARITY, CASE TWO

5.2. Introduction to Grassmann Line Geometry

A set of spatial lines is a variety if no line outside the set is dependent on the lines in the set. The varieties of spatial lines were first studied by H.Grassmann. It is also referred as *Grassmann Line Geometry*. The line varieties of rank 2,3,4,5 are summarized in [21]. More mathematical justifications can be found in [70]. Fig.5.3 provides illustrations of these various varieties of lines.

J.P. Merlet used line geometry first to find the singular configurations of the 6-3 Stewart Platform in [22]. The rank of any line variety represents the order of the corresponding zero-pitch system, i.e., the forward Jacobian matrix. If n zero-pitch screws (lines) belong to a variety of rank less than n, these screws are linearly dependent. The following discussions follow the notations used by Merlet to describe various types of line dependency.

An empty set of lines is of order zero. A single line in 3D space is of order one. The line variety with order 2 is either a pair of skew lines in 3D space or a flat pencil of lines. A flat pencil of lines is defined as the lines lying in a plane and passing through the same point on that plane. If more than two lines belong to a flat pencil, then the order of this line variety is still two and all these lines are linearly dependant.

The line variety with order of three is of four types:

1. A regulus (3a); Take three skew lines in space and consider the set of lines that intersect these three lines: this set of lines builds a surface that is a hyperboloid of one sheet and is called a regulus.
2. The union of two flat pencils having a line in common, but lying in distinct planes and with distinct centers (3b);
3. All lines through a point (3c);
4. All lines in plane (3d).

Line varieties of order four are called linear conguences and are also of four types:

1. A linear spread generated by four skew lines (i.e., no line meets the regulus generated by the three other lines in a proper point (4a);
2. All the lines concurrent with two skew lines (4b);
3. A one-parameter family of flat pencils, have one line in common (4c);
4. All the lines in a plane or passing through one point in that plane(4d).

Line varieties of order five are called linear complexes and are of two types:

1. General complex: generated by five independent skew lines and all lines of a general complex that are coplanar intersect at one point(5a);
2. Special complex: all the lines intersecting with a given line(5b);

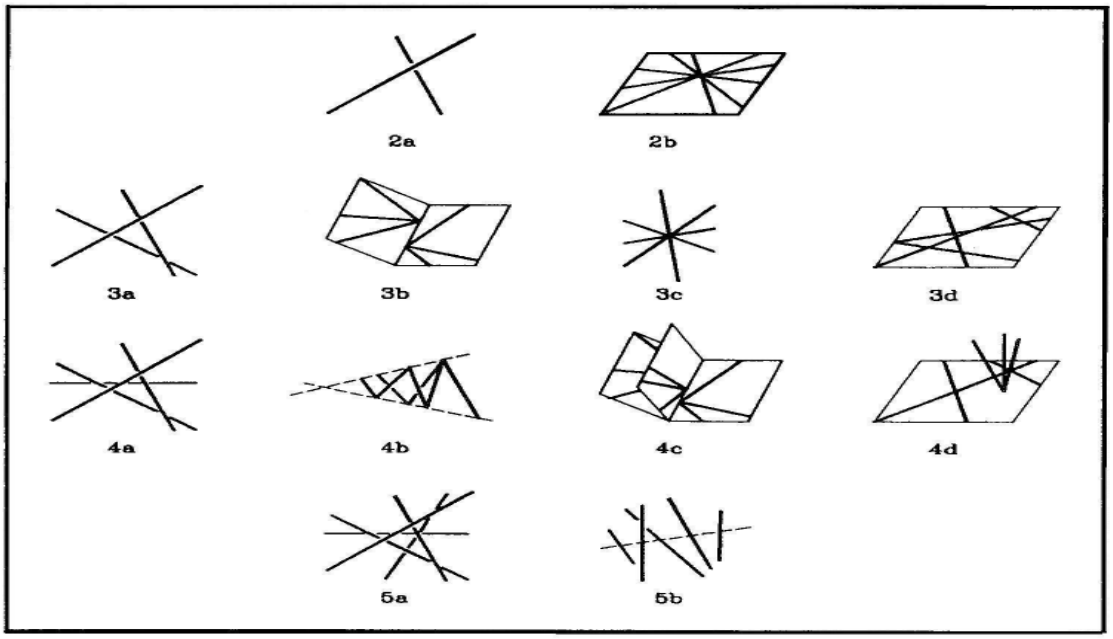

FIG.5.3 VARIOUS TYPES OF LNE VARIETIES [22]

5.3. Possible Forward Singular Configurations and Their Elimination

As mentioned in Section 4.2, the inverse kinematic singularities of the three legged in-parallel manipulator can be found by investigating the singularities of a single leg. However, the singularities of forward kinematics are more complicated to identify than inverse singularities. Theory of reciprocal screws and line geometry are used to solve the problem. The identification of reciprocal screws can refer to Chapter 4 and the locations and directions of both the joint screws and reciprocal screws are displayed in Fig.4.1.

STriDER is assumed to have an initial actuation scheme of 2-2-2, i.e., each leg has two active joints and the reciprocal screws associated with them constitute a wrench plane. Both of these two reciprocal screws pass through the foot contact point, thus making up a planar

pencil. The cases of the linear dependency among all three sets of planar pencils are investigated using line geometry. If certain case of line dependency occurs, the wrench system spanned by the reciprocal screws will have an order *m* lower than 6. Under such forward singular configurations, the body of STriDER gains extra instantaneous DOF and cannot resist wrenches in certain directions even all the active joints are locked. In order to eliminate the singularities, redundant actuations of 3-2-2, 3-3-2 and 3-3-3 are proposed for various singular cases. It is shown that all possible forward singular configurations can be eliminated with 3-3-3 actuation at worse.

For the convenience and clarification, when the geometric relationships of the reciprocal screws and wrench planes are described, the terms Lr_{ni} and Lr_{mi} are used to denote the two reciprocal joint screws at leg *i*. The term Lr_{qi} represents the third reciprocal joint screw under redundant actuation in leg *i*. X_{mni} is used to represent the wrench plane generated by Lr_{ni} and $Lr_{mi.}$ When these geometric relationships are interpreted into vector equations to obtain the analytical conditions of forward singularities, the homogeneous coordinates of line Lr_{ni} and plane X_{mni} are represented with $\$\mathbf{r}_{ni} = \begin{bmatrix} \mathbf{Sr}_{ni} \\ \mathbf{Sor}_{ji} \end{bmatrix}$ and $C_{mni} = \begin{bmatrix} \mathbf{N}_{mni} \\ No_{mni} \end{bmatrix}$.

Note that the following analysis not only works for the SRRR robot, but also works for a family of three-legged six DOF in-parallel with line-based singularities.

Case 1 – Collinear lines:

Two zero-pitch screws are dependent if they lie on the same line. Such two screws can only constraint one translational DOF along the axes of reciprocal screws. Case 1 occurs when one reciprocal screw of leg *i*, is collinear with a reciprocal of leg *j*. For the S-R-R-R in-parallel manipulator, this case is possible only if the reciprocal screws are collinear with P_iP_j**.** This case is shown in Fig.5.4. The condition under which this case occurs is that Lr_{ni} passes P_j and Lr_{nj} passes $P_{i.}$ The vector equations are written as follows:

$$\mathbf{P}_j \times \mathbf{Sr}_{ni} = \mathbf{Sor}_{ni}$$
$$\mathbf{P}_i \times \mathbf{Sr}_{ni} = \mathbf{Sor}_{nj}$$

Redundant actuation at leg j is able to eliminate this singularity. The additional reciprocal screw is represented with a diamond arrow in Fig.5.4.

Note that, Case 1 can occur doubly or triply as shown in Fig.5.5 and Fig.5.6. Then 3-3-2 actuation and 3-3-3 actuation are used to eliminate the singularities. The additional joint reciprocal screws are represented with diamond arrows.

Case 1

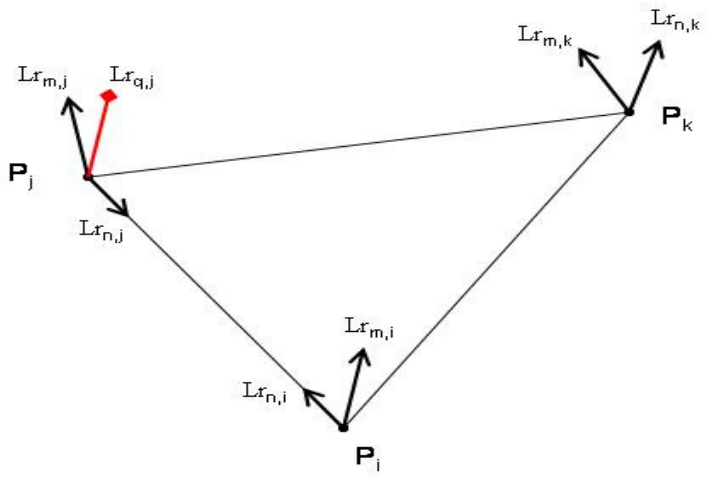

FIG.5.4 CASE 1

Case 1 (Double)

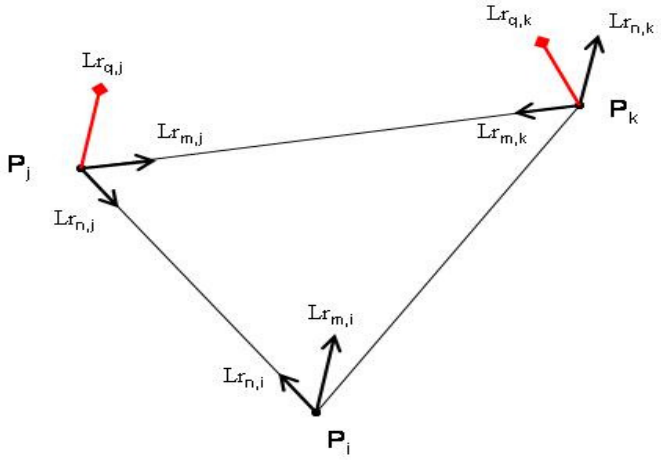

FIG.5.5 CASE 1 (DOUBLE)

Case 1 (Triple)

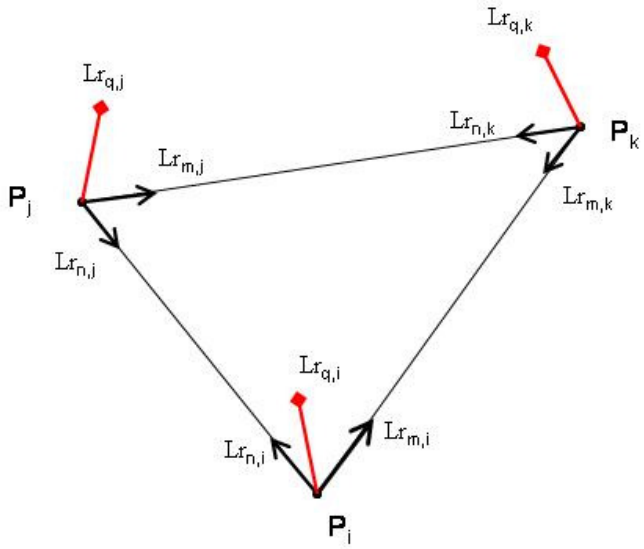

FIG.5.6 CASE 1 (TRIPLE)

Case 2a – Two skew lines:

Two skew zero-pitch screws cannot generate a third screw that is a linear combination of the two screws. Therefore, this case cannot happen.

Case 2b – Coplanar concurrent lines:

Two intersecting lines define a plane. If a third line lies in the plane and passes through the concurrent point of the two screws, Case 2b will happen. The order of the flat pencil defined by the three lines is 2. This case is shown in Fig.5.7.

Case 2b - 1

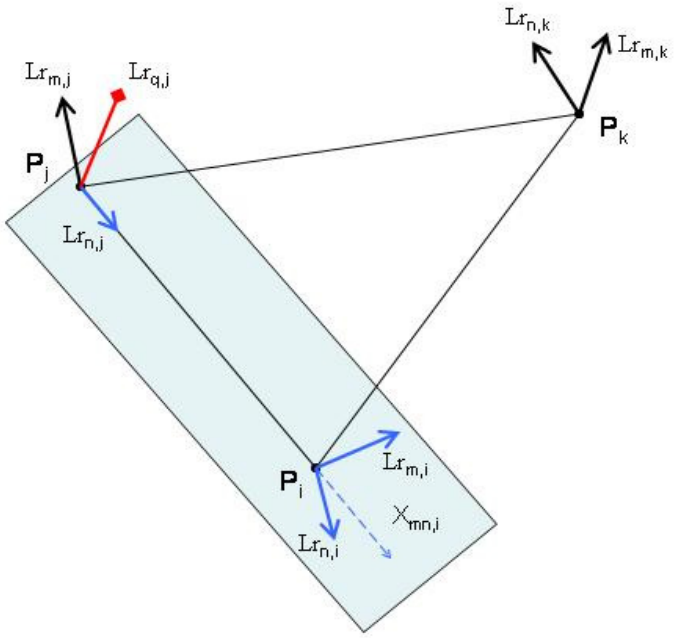

FIG.5.7 CASE 2b-1

The condition under which Case 2b occurs is that Lr_{nj} has the same direction as P_jP_i and P_j lies on the plane X_{mni}. The vector equations are as follows:

$$\mathbf{Sr}_{nj} \times \mathbf{P}_j\mathbf{P}_i = 0$$

$$\mathbf{P}_j \bullet \mathbf{N}_{mni} = No_{mni}$$

The redundant actuation with 3-2-2 can eliminate this singularity. The effective additional reciprocal screw is represented with diamond arrows in Fig.5.7. The double Case 2b is shown in Fig.5.8, in that case, 3-3-2 actuation with two additional active joints can be used to eliminate it.

A special Case 2b is also demonstrated in Fig.5.9. There are three reciprocal screws lying on the virtual base plane of $P_iP_jP_k$ and intersecting at the same point.

Case 2b – 1 (Double)

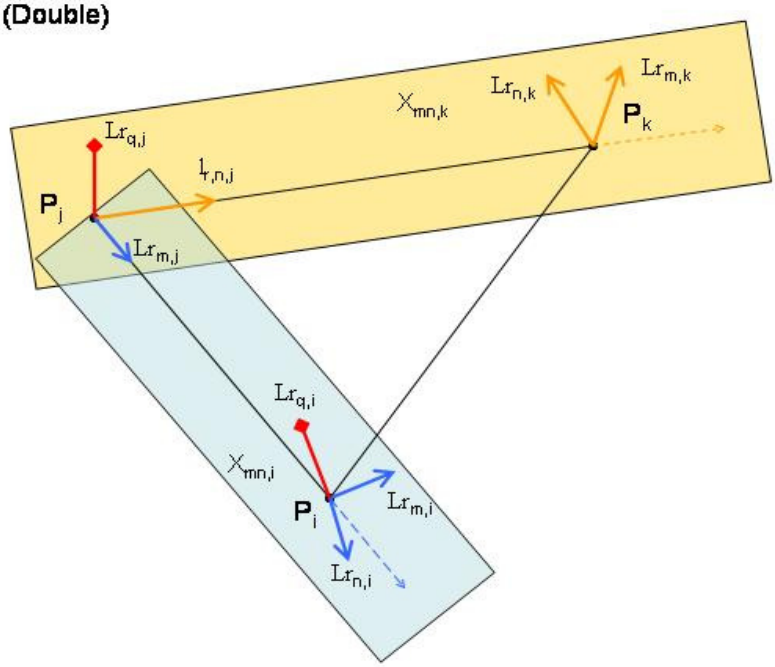

FIG.5.8 CASE 2b-1 (DOUBLE)

Case 2b – 2

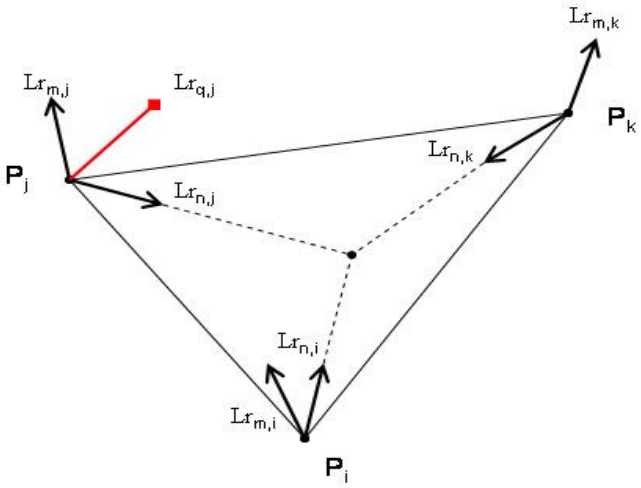

FIG.5.9 CASE 2b-2 (SPECIAL)

Case 3a – Regulus:

This case doesn't exist for the SRRR in-parallel manipulators, because the maximum number of skew lines is only three in this manipulators.

Case 3b – Union of two flat pencils:

This case will occur when the common line of the plane defined by two reciprocal screws in leg *i* and *j* coincides with the side of the base triangle P_iP_j. The screw system has an order of 3. As shown in Fig.5.10, four lines Lr_{nj} ,Lr_{mj} , Lr_{ni} and Lr_{mi} constitute a union of two flat pencils with the common line of P_iP_j. The condition of this case is that P_j lies in X_{mni} and P_i lies in X_{mnj}. The vector equations are written as:

$$\mathbf{P}_j \bullet \mathbf{N}_{mni} = No_{mni}$$
$$\mathbf{P}_i \bullet \mathbf{N}_{mnj} = No_{mnj}$$

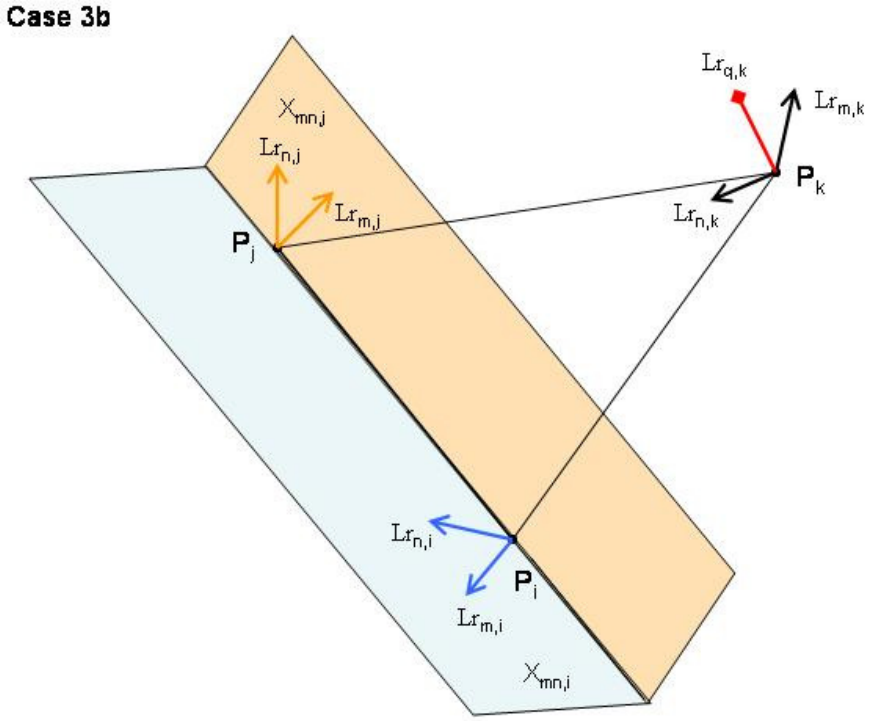

FIG.5.10 CASE 3b

3-2-2 actuation will eliminate this singularity.

Case 3c – A bundle of lines

This case is shown in Fig.5.11, both Lr_{nj} and Lr_{mk} pass P_i and then four lines intersect at one point. The condition of this case is similar to Case 1, with the vector equations as:

$$\mathbf{P}_i \times \mathbf{Sr}_{mj} = \mathbf{Sor}_{mj}$$
$$\mathbf{P}_i \times \mathbf{Sr}_{mk} = \mathbf{Sor}_{mk}$$

Note that, the redundant actuation of leg *i*, denoted with an oval arrow, cannon eliminate the singularity. The effective additional reciprocal screw is again represented with a diamond arrow.

Case 3c

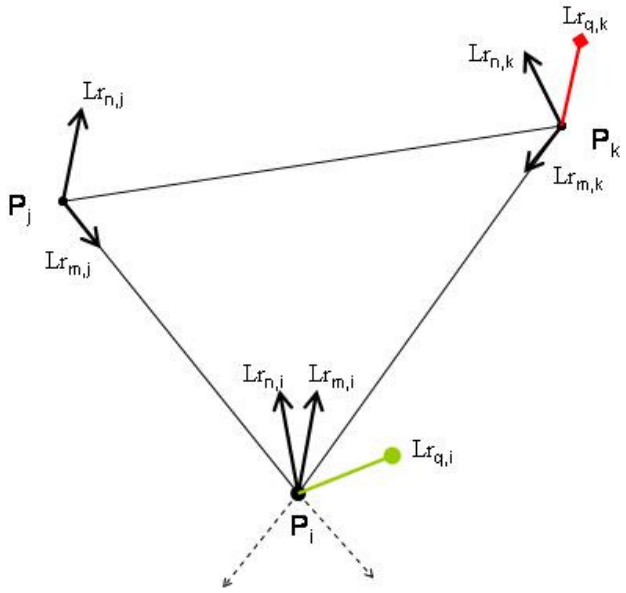

FIG.5.11 CASE 3c

Case 3d Coplanar non-concurrent lines:

This case arises when at least four non-concurrent lines are lying on the same plane. If the plane is the virtual base plane of the robot, then Fig.5.12 demonstrates this case. The criteria that a line passing P_i or P_j or P_k lies in plane $P_i\, P_j\, P_k$ is that the direction vector of the line is perpendicular to the normal of the base $P_i\, P_j\, P_k$.

$$\mathbf{Sr}_{ni} \bullet \mathbf{N}_{\text{Base}} = 0 \qquad \mathbf{Sr}_{mi} \bullet \mathbf{N}_{\text{Base}} = 0$$
$$\mathbf{Sr}_{nj} \bullet \mathbf{N}_{\text{Base}} = 0 \qquad \mathbf{Sr}_{nk} \bullet \mathbf{N}_{\text{Base}} = 0$$

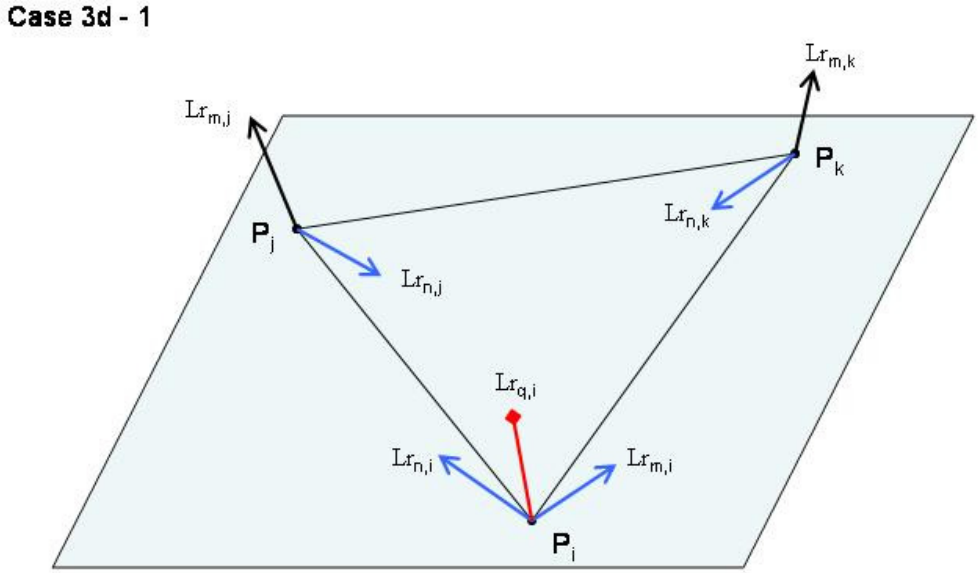

FIG.5.12 CASE 3d-1

This case also occurs when the wench planes of two planar pencils are coincident, which is demonstrated in Fig.5.13. The condition for this case can be interpreted as P_i lies on the wrench plane of the two reciprocal screws at P_j, and vice verse, P_j lies on the wrench plane of the two reciprocal screws at P_i.

$$\mathbf{P}_j \bullet \mathbf{N}_{mni} = No_{mni}$$
$$\mathbf{P}_i \bullet \mathbf{N}_{mnj} = No_{mnj}$$

Note that, if the two legs with coplanar wrench planes are both actuated redundantly, all of these six reciprocal screws still belong to a singularity case of 5b. The redundant actuation of the third leg is able to provide the effective reciprocal screw to eliminate the singularity.

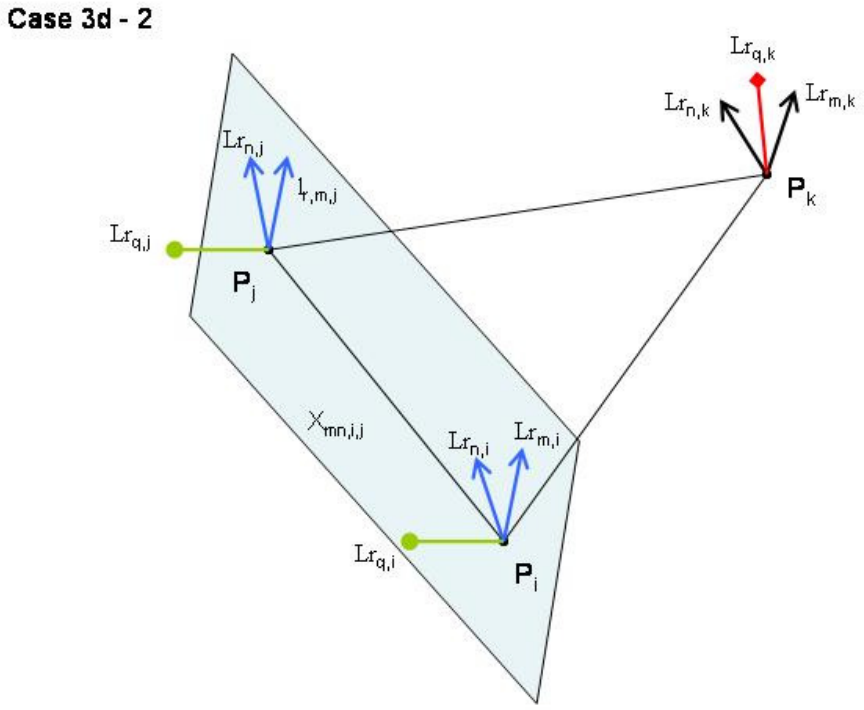

FIG.5.13 CASE 3d-2

Case 4a Four independent skew lines:

Similar to Case 3a, it is impossible to have five skew lines in this robot.

Case 4b Lines concurrent with two skew lines:

In order to investigate the condition of this case, the potential lines that intersect five reciprocal screws must be identified first. By taking the reciprocal product of the two potentials, whether or not the two lines are skew can be determined. Fig.4.14 shows such an example, with the two possibly skew lines denoted as L_1 and L_2. The first candidate L_1 can refer to line P_i P_j straightforwardly, and the second candidate could be the intersecting line L_2 of wrench plane X_{mni} and X_{mnj}. Its screw coordinate can be determined as:

$$\hat{\$}_{L_1} = \left[\mathbf{S}_{L_1}; \mathbf{So}_{L_1}\right]^{\mathrm{T}} = \left[\mathbf{N}_{mni} \times \mathbf{N}_{mnj}; No_{mnj}\mathbf{N}_{mni} - No_{mni}\mathbf{N}_{mnj}\right]^{\mathrm{T}}$$

Based on their reciprocal products, the cases whether L_2 intersects Lr_{mk} or Lr_{nk}, and whether L_2 is skew to L_1 can be quickly determined.

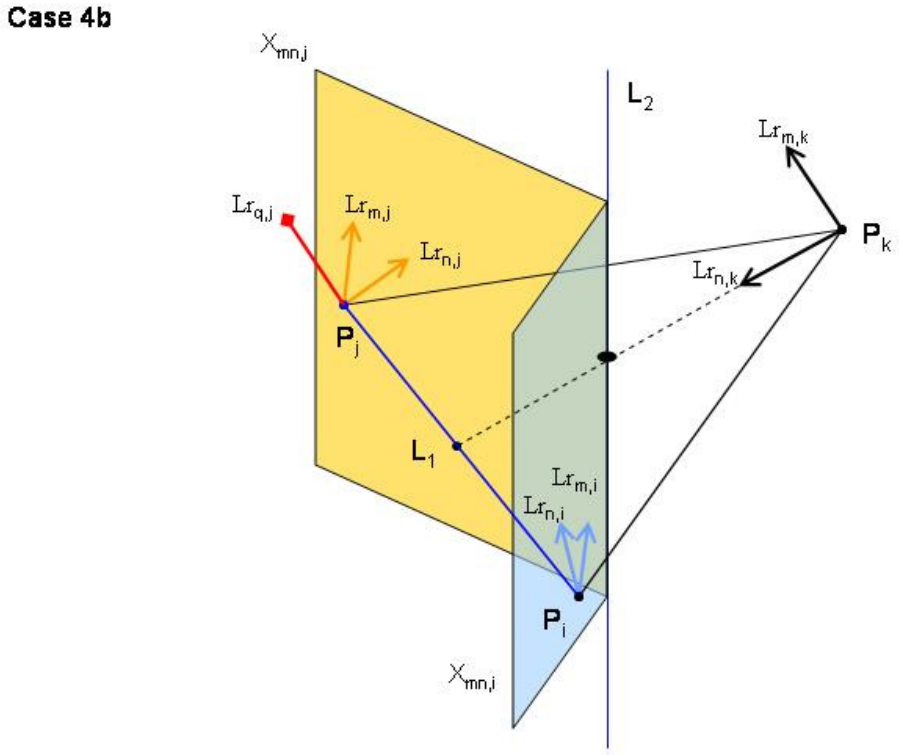

FIG.5.14 CASE 4b

Case 4c One-parameter family of flat pencils:

For this case to occur, the centers of the three planar pencils must be on the same line and this line is also the common line of the three wrench planes. This case is impossible for the robot discussed in this report because the virtual base plane is assumed to have a triangle shape.

Case 4d Lines on a plane or passing through one point of the plane:

This case exists in at least five reciprocal screws where a minimum of two screws must be coplanar and the remaining screws, which must be larger or equal to one, intersect the plane of the coplanar screws at one point. The two-system of unconstrained DOF can be described as combinations of twists about two orthogonal axes lying on the plane and having directions perpendicular to the normal to the plane passing the intersection point. An example of Case 4d is presented in Fig.5.15. In this example, P_i lies in the wrench plane X_{mnj}. Even all three joints at leg *i* are actuated, the three reciprocal screws at P_i and the two at P_j still form a line variety with the rank of 4.

Case 4d-1

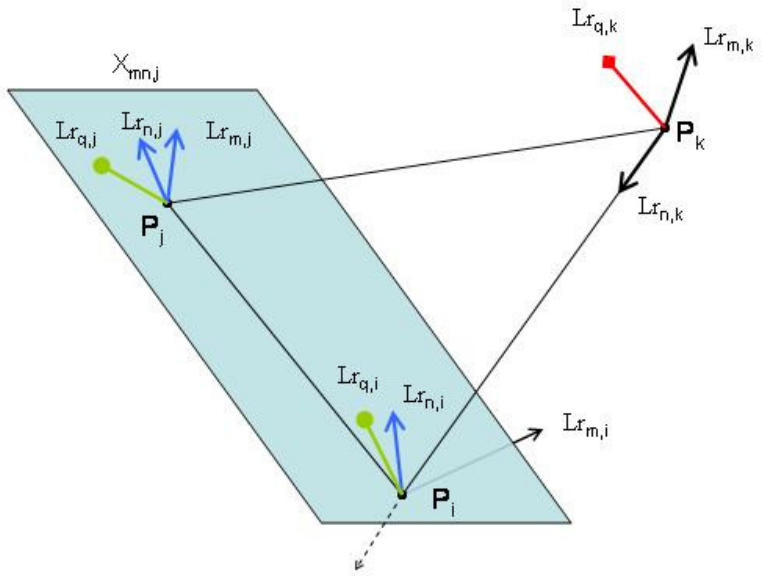

FIG.5.15 CASE 4d

Case 5a General complex:

If one screw can be expressed as a linear combination of the other five independent screws, the variety of the six screws is called a *complex,* which has a rank of five. The coplanar lines of a complex meet at a common point. This property can be utilized to identify whether six screws belong to a complex. The example of this case is shown in Fig.5.16. The intersecting line L_i of wrench plane X_{mni} and the base $P_1P_2P_3$ can be determined as:

$$\hat{\$}_{L_i} = \left[\mathbf{S}_{L_i}; \mathbf{So}_{L_i}\right]^{\mathrm{T}} = \left[\mathbf{N}_{mni} \times \mathbf{N}_{\mathrm{Base}}; No_{mni}\mathbf{N}_{\mathrm{Base}} - No_{\mathrm{Base}}\mathbf{N}_{mni}\right]^{\mathrm{T}}$$

Between the three interesting lines L_i, L_j and L_k, the common point of any two lines has the following homogeneous coordinates:

$$\mathbf{ri}_{ij} = \left[\mathbf{So}_{L_i} \times \mathbf{So}_{L_j}; \mathbf{S}_{L_j} \bullet \mathbf{So}_{L_i}\right]^{\mathrm{T}}$$

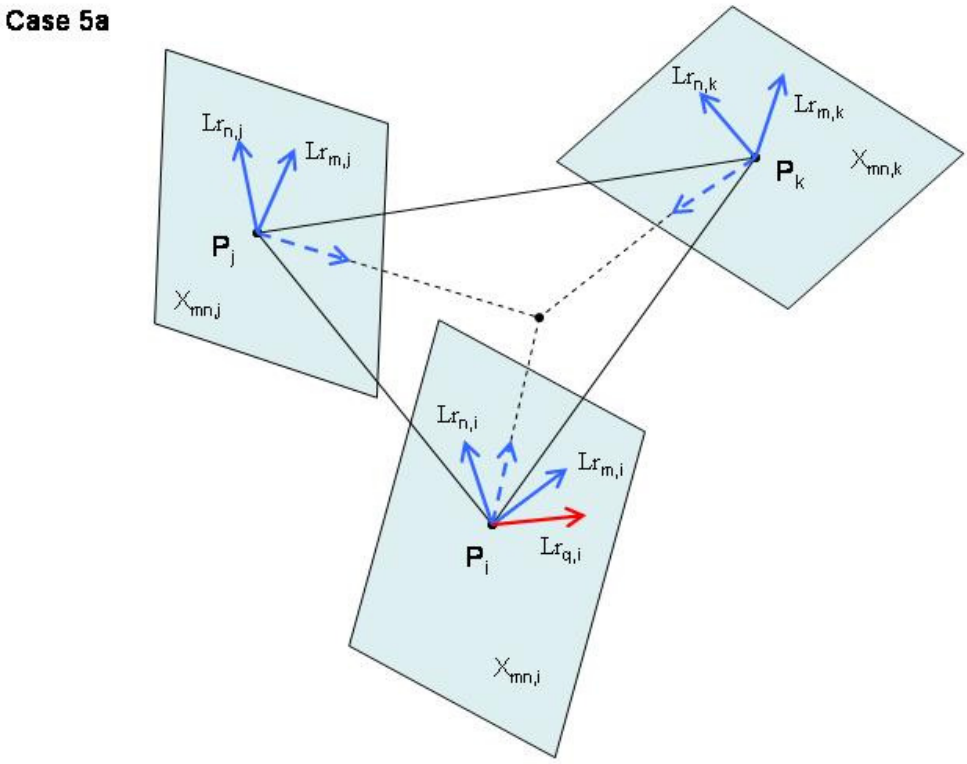

FIG.5.16 CASE 5a

Case 5b –Special complex:

Case 5b happens when six reciprocal screws intersect one line. The unconstrained DOF is any rotation along the common line. One example is shown in Fig.5.17, the redundant actuation of any leg is able to eliminate the singularity. For any two planes out of X_{mni}, X_{mnj} and X_{mnk}, the interesting line can be determined as:

$$\hat{\$}_{L_{ij}} = \left[\mathbf{S}_{L_{ij}}; \mathbf{So}_{L_{ij}}\right]^{\mathrm{T}} = \left[\mathbf{N}_{mni} \times \mathbf{N}_{mnj}; No_{mni}\mathbf{N}_{mnj} - No_{mnj}\mathbf{N}_{mni}\right]^{\mathrm{T}}$$

Again, using the screw coordinates and the reciprocal projects, whether the three planes X_{mni}, X_{mnj} and X_{mnk} intersect at one common line can be identified.

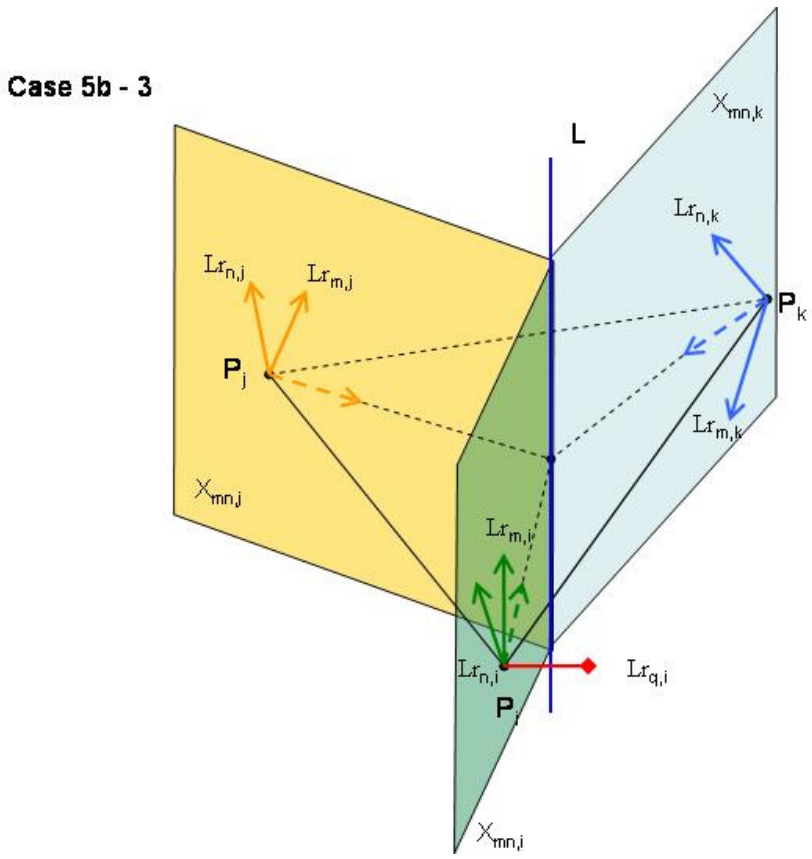

FIG.5.17 CASE 5b

As a summary, line geometry has laid a solid framework for the identification of all possible forward singular configurations. The redundant actuation can eliminate the forward singularities by introducing additional reciprocal screws, thus increasing the order of the forward Jacobian matrix. The actuation scheme of 3-3-3 is able to eliminate all possible forward singularities in the enumerated cases.

5.4. Inverse and Forward Singular Configurations

5.4.1. Inverse Singular Configurations

An example of the inverse singular configuration is shown in Fig.5.18. In this configuration, since the knee joint angles are zero, the body of STriDER reaches the limit of its workspace and lose three DOF.. This example is actually a combined singular configuration, because the shank and thigh of one leg is collinear, thus making the reciprocal screws of the flexure and knee joint collinear. The unconstrained DOF are three orthogonal rotational DOF. with the centers at the intersection the leg lines. In order to eliminate the forward singularities, all three rotator joints have to be actuated. The 3-3-3 actuation scheme is able to resist the disturbance wrenches from outside.

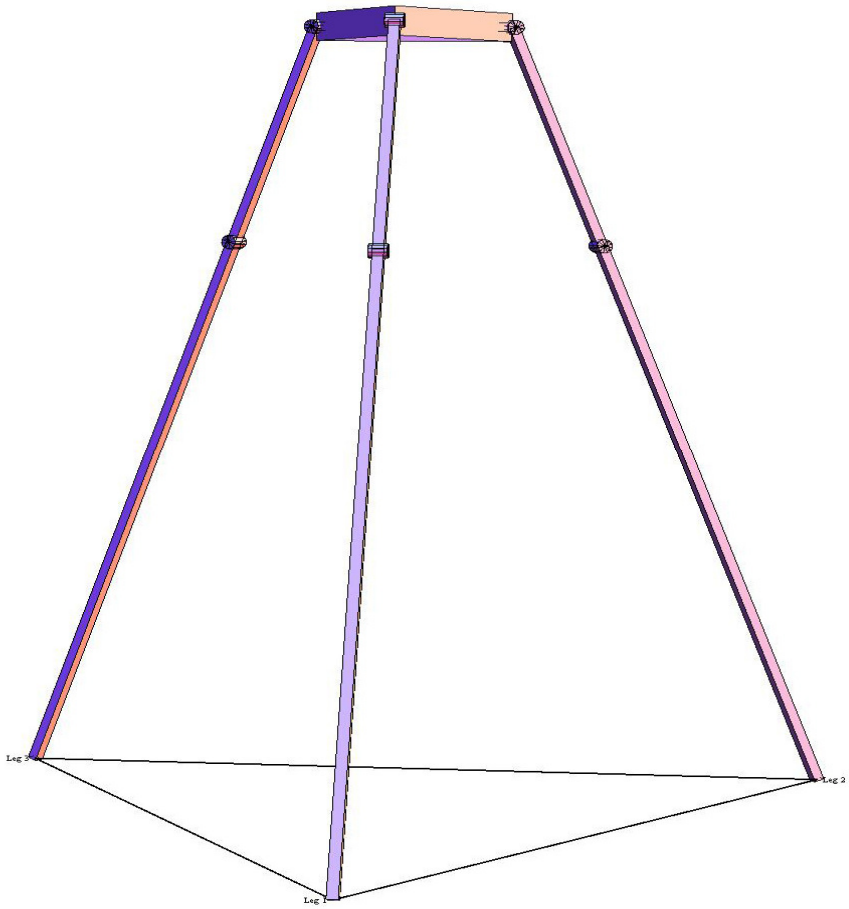

FIG.5.18 INVERSE SINGULAR CONFIGURATIONS

5.4.2. Forward Singular Configurations

This section mainly presents the examples of the forward singular cases discussed in previous sections. The geometric relationships between the reciprocal screws and the vector equations are used as tools to identify these singular cases whose screw systems have orders less than 6. Effective elimination method is proposed based on redundant actuation.

Fig.5.19 presents an example of Case 1. In this case, the flexure joint and knee joint in each leg are chosen as the active joints. The wrench plane of leg 1 and leg 2 are coincident with the plane of the body. The associated reciprocal screws to the flexure joints in leg 1 and 2 are collinear. These six reciprocal screws belong to a line variety with the order of 5. Assume the reciprocal screws in leg 3 intersect the body plane at two points. Then the unconstrained DOF. is a rotation along the line in the body plane that passes the two points. Redundant actuation at any leg can eliminate this singular configuration.

Fig.5.20 presents an example of Case 2b. The active controlled joints are the knee joints and flexure joints. Again, the wrench plane of leg 1 and 2 are coincident with the body plane. The reciprocal screw associated with the flexure joint of leg 1 passed the foot contact point of leg 2. There reciprocal screws make up a planar pencil with order 2. The unconstrained DOF is the same as the case shown in Fig.5.19. The elimination method is similar.

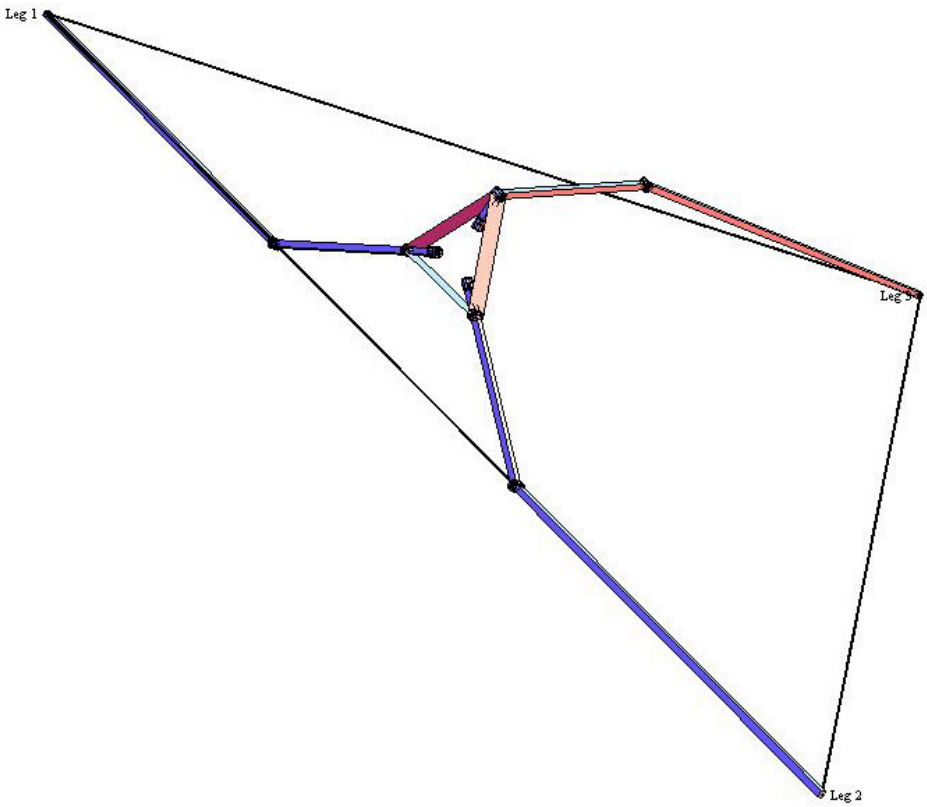

FIG.5.19 CASE 1

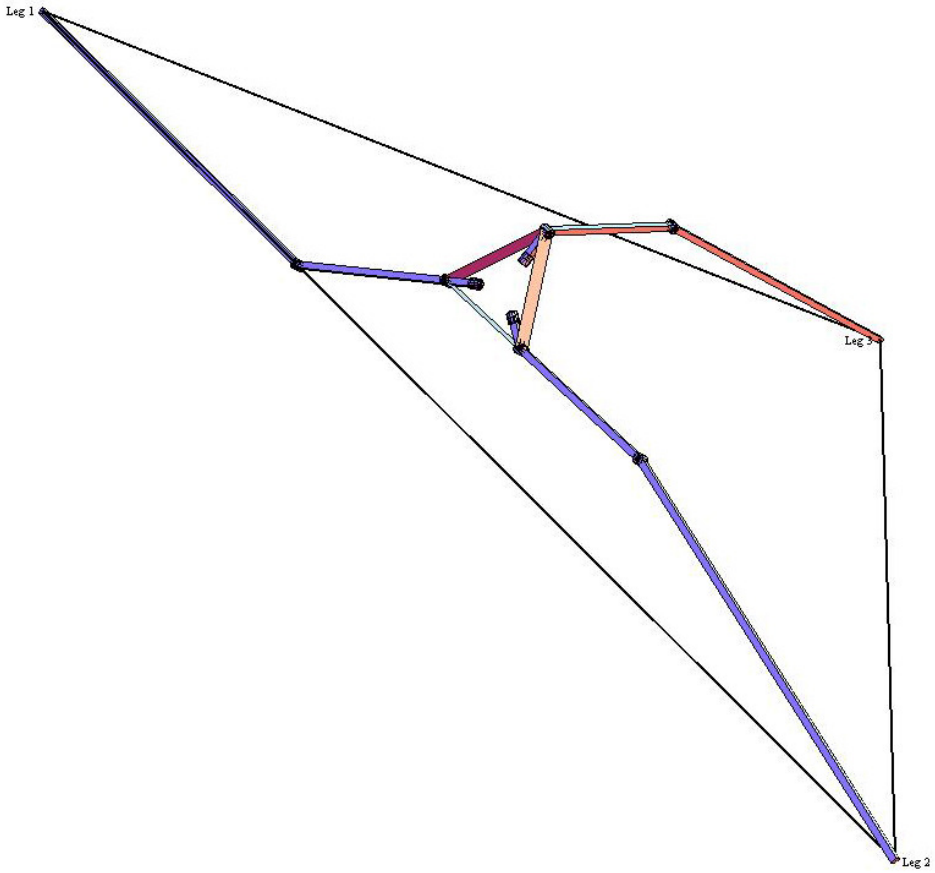

FIG.5.20 CASE 2b

The example of Case 3d singularity is displayed in Fig.5.21. Four non-concurrent reciprocal screws lie on the body plane. The unconstrained 1 DOF. is the same as the previous two examples and the elimination method is similar.

Fig.5.22 shows the example of Case 4d. Assume that STriDER is actuated with 3-2-1 scheme. The wrench plane of leg 2 contains the foot contact point of leg 1. If all three joints at leg 1 are actuated. Then the five reciprocal screws constitute a line variety with order 4. One reciprocal screw at leg 3 will intersect the body plane at one point. A straight line that connects the point with the foot contact point at leg 1 will intersect all six reciprocal screws. The unconstrained DOF is a rotational motion along that line. Redundant actuation at leg 3 can eliminate this singularity.

Fig.5.23 shows the example of Case 5b. Although in this figure, STriDER stands on the ground with stable tripod pattern, however, the robot is actually in a forward singular configuration if only the flexure joints and knee joints are actuated. The three wrench planes have a common line which passes the center of the body. All six reciprocal screws intersect this common line. The screws parallel to this line is considered as intersecting at infinity.

Therefore, the robot has one unconstrained rotational DOF along the common line. Actuation of any rotator joint will eliminate this singularity.

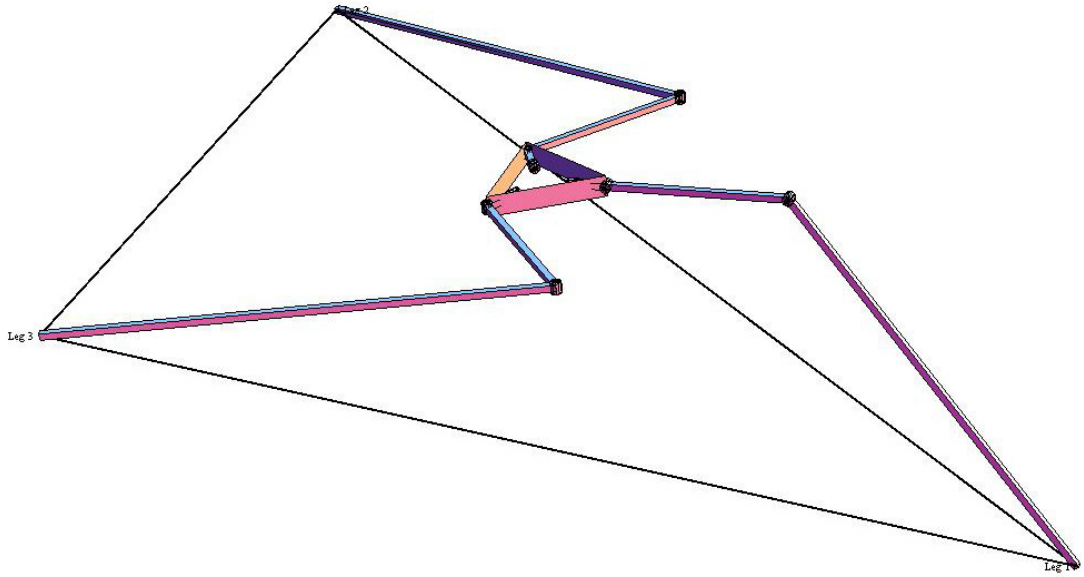

FIG.5.21 CASE 3d

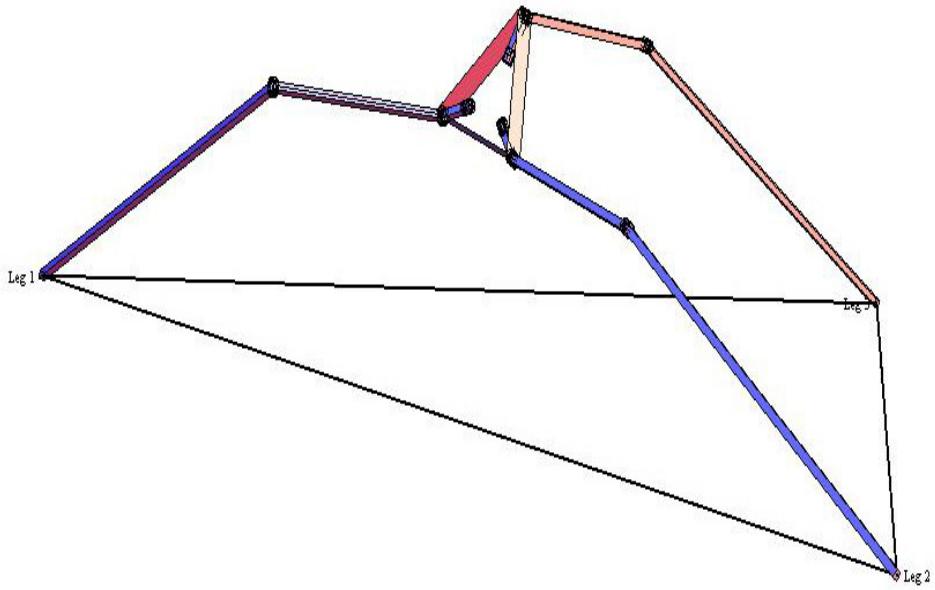

FIG 5.22 CASE 4d

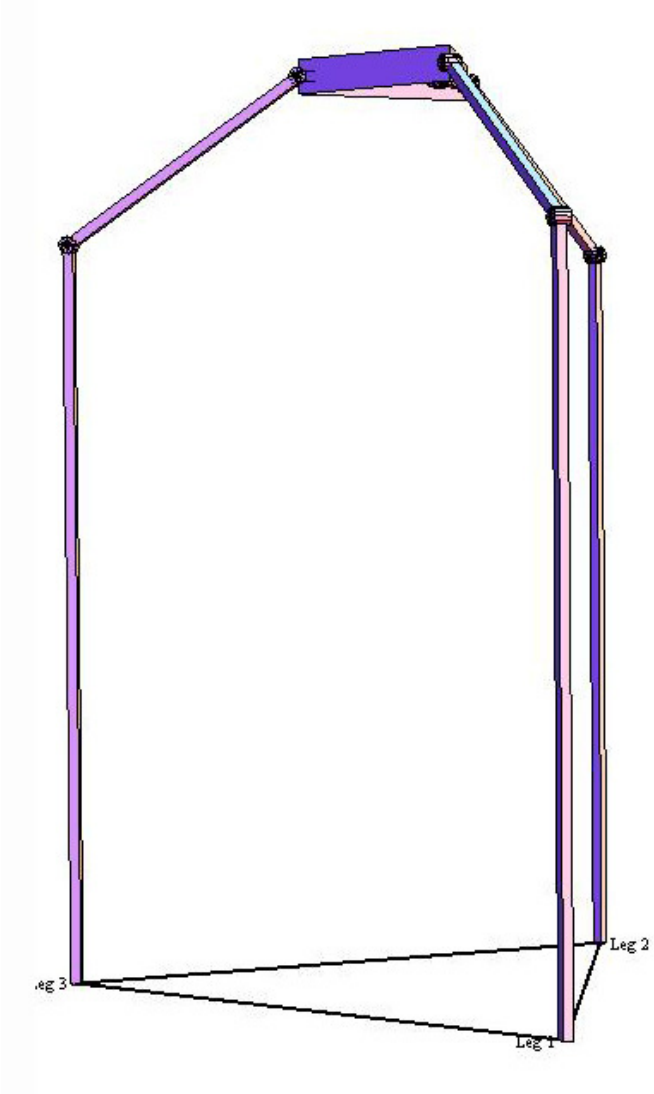

FIG.5.23 CASE 5b

Chapter 6 Introduction to IMPASS

Robot mobility[2] is an area in need of much improvement, as today's robots are often limited by their lack of general mobility in unstructured environments. Specialized robots have been designed for limited and specific tasks, but their mobility is not yet robust enough to handle varying terrains. Wheeled robots often have high efficiency and speed, but tend to be limited to relatively smooth terrains. Legged robots are adaptable and have good mobility on rough terrains; however, the main disadvantage of legged mobile robots is that the complexity of the leg usually necessitates a slow and inefficient mechanism [71].

The locomotive limitations of these two main types of mobile robots are currently countered in research by developing hybrid leg-wheel robots that combine the benefits of both locomotion schemes. In one group of such robots, articulated limbs are added as the connection between the wheels and the vehicle's body, thus rendering them improved mobility. For example, the SHRIMP rover developed by EPFL [72], is a lightweight robot with six motorized wheels and uses a combination of actuated and passive mechanisms to raise and lower its wheels to climb objects up to twice the wheel diameter. The Anthropomorphically Legged and Wheeled Duisburg Robot (ALDURO), developed by Muller *et. al.* [73], and the All-Terrain Hex-Legged Extra-Terrestrial Explorer (ATHLETE), developed in JPL (Jet Propulsion Laboratory) [74] both have wheels at the end of their limbs and are designed to handle heavy load in unstructured terrains. Another group of robots utilizes compliant spoke wheels to improve their mobility. Such mobile platforms mainly include RHex [75] and Whegs^{TM} [76]. RHex is a compliant-legged hexapod with a simple clock-driven open-loop tripod gait. It is different from other robots in that each of its legs rotates in full circles acting as a single spoke wheel. The Whegs^{TM} series of robots is another derivation of the spoke wheel concept that adopts a compliant tri-spoke configuration in each wheel.

As a novel concept for creating a series of hybrid mobile robots with robust mobility that includes the benefits of both legged and wheeled locomotion, the Intelligent Mobility Platform with Active Spoke System (IMPASS) is introduced in this paper. This locomotion concept is based on the rimless wheel with multiple spokes that pass through the axis of the wheel. The uniqueness of this wheel is that each spoke can be actuated to stretch in or out independently. A passive rimless wheel has been studied for its application in the research on human gaits [77]. However, the actuated spoke wheel we presented here can move using different modes of locomotion, which enable it to step over large obstacles like legs, adapt to uneven surfaces like tracks, yet retaining the speed and simplicity of wheels.

Based on the IMPASS concept, this chapter firstly elaborates the locomotion schemes of a walking machine with two actuated spoke wheels and one tail, including both the straight-line walking and the steering. Observations on its multiple modes of locomotion necessitate the mobility study on the mobile robot's unique metamorphic configuration, so Chapter 8 briefly reviews some notable mechanisms with variable topologies (MVTs), such as the metamorphic mechanisms, the kinematotropic linkages and so on, and then utilizes the

[2] Note that the term "mobility" referred in this paper has two types of definitions. One is defined as the quality of a mobile robot's free moving over all types of terrains. The other is defined as the continuous or instantaneous DOF of a mechanism.

Modified Grübler-Kutzbach criterion and *Grassmann Line Geometry* to calculate the DOF in each topology of the IMPASS robot. In Chapter 9, the predicted DOF in the variable topologies are verified through the experimental testing of the IMPASS prototype. The inverse and forward kinematics is investigated in Chapter 10 and Chapter 11 summarizes the conclusions and discusses future research.

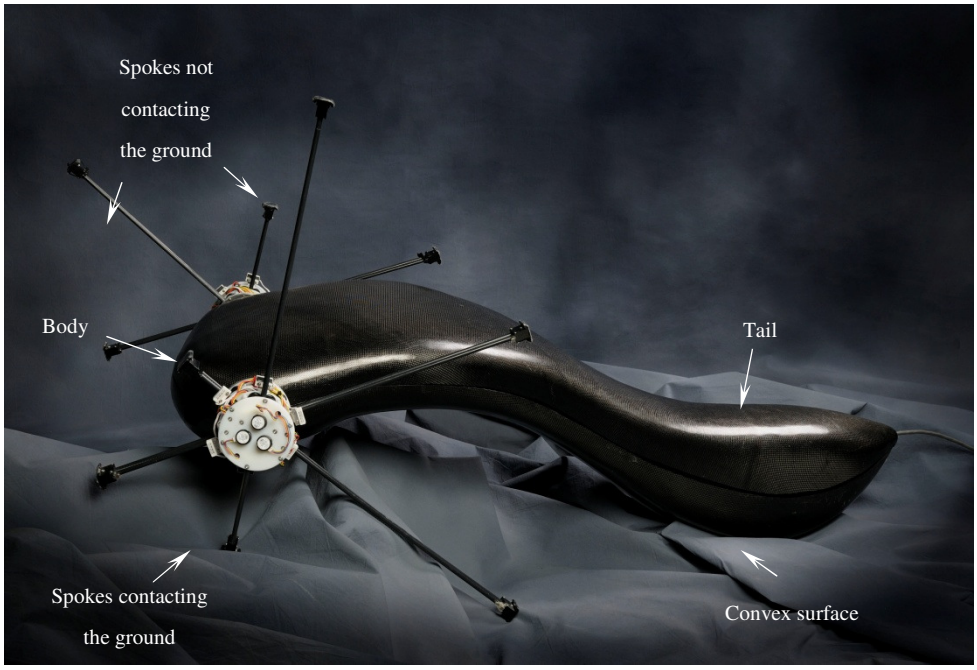

FIG.6.1 THE PROTOTYPE OF IMPASS

The concept of IMPASS was initially proposed in [78] in the year of 2005. The design of a prototype with two actuated spoke wheels and one tail was then presented in [79].The latest working prototype of IMPASS that has two actuated spoke wheels and one passive tail is demonstrated in Fig.6.1, with key components labeled. Each spoke wheel now has three linearly actuated spokes that pass through the hub of the wheel, thus providing totally six effective spokes that are set 60 degrees from each other. These spokes can be actuated to stretch in or out independently. The two spoke wheels are connected with a single axle, which allows the robot to rotate the spoke wheels like conventional wheeled vehicles. The body is covered with a carbon fiber shell. The shell has a tail, with its lower portion designed as a convex surface. As the robot walks on various terrains, climbs up steps and so on, its tail passively touches the ground. Therefore, at any instant, there exist at least three contact points between the IMPASS and the ground (two or more come from the contact spokes and one could come from the tail), thus providing a support region to maintain its stability.

6.1. Classification of the Variable Topologies

Since each spoke wheel has three independently actuated spokes, one wheel could have one, two or at most three contact points with the ground. As the robot rotates the two spoke wheels to move on various surfaces, the contact scheme between the actuated spokes of the wheels and the ground keeps changing, thus generating different kinematic configurations and various modes of locomotion.

In order to classify these various configurations into the most essential groups, a few assumptions have to be made ahead of the analysis:

1. The IMPASS robot consists of rigid links, such as the spokes and the axle. Particularly, the body and tail as a whole is considered as one rigid link;
2. The two spoke wheels rotate in the same phase, so for each spoke in the left wheel, there is always a parallel spoke in the right wheel;
3. When a spoke touches the ground, the generated contact point is kept stationary, i.e. no slip or bounce occurs at the contact tips when the spokes rotate or translate;

With the assumptions above, each type of configurations is now characterized by the contact case of the spokes. Therefore, a topology of the IMPASS robot is defined as a type of configurations with the same contact case and all possible contact cases constitute the complete group of the robot's variable topological structures.

Extracting the characteristic geometry of the IMPASS prototype in Fig.6.1, the kinematic model for a particular contact case is presented in Fig.6.2. In this case, one spoke of the left and right wheel respectively and the tail are contacting the smooth ground. To make the demonstration straightforward, the contacting and un-contacting spokes are represented with solid and transparent cylinders respectively. The two contacting spokes are of equal length and parallel to each other. The two spoke wheels are connected with an axle and the axle is perpendicular to each spoke. The geometry of the body and tail in Fig.6.1 is simplified, and represented with a rectangle plane connecting to a convex surface through a rigid bar, as is shown in Fig.6.2. The body and tail as a whole is attached to the axle that connects the two spoke wheels. The actuation of this robot includes the rotation θ of the spoke wheels about the axle in the direction indicated by the double arrow in this figure, and the translations l_l and l_r of the contacting spokes through the hub of the wheel. The un-contacting spokes could also stretch in or out locally, but their displacements do not affect the current topology of the robot, unless they touch the ground and transform the topology to another form. This model can also be used to represent other topologies with different contact cases.

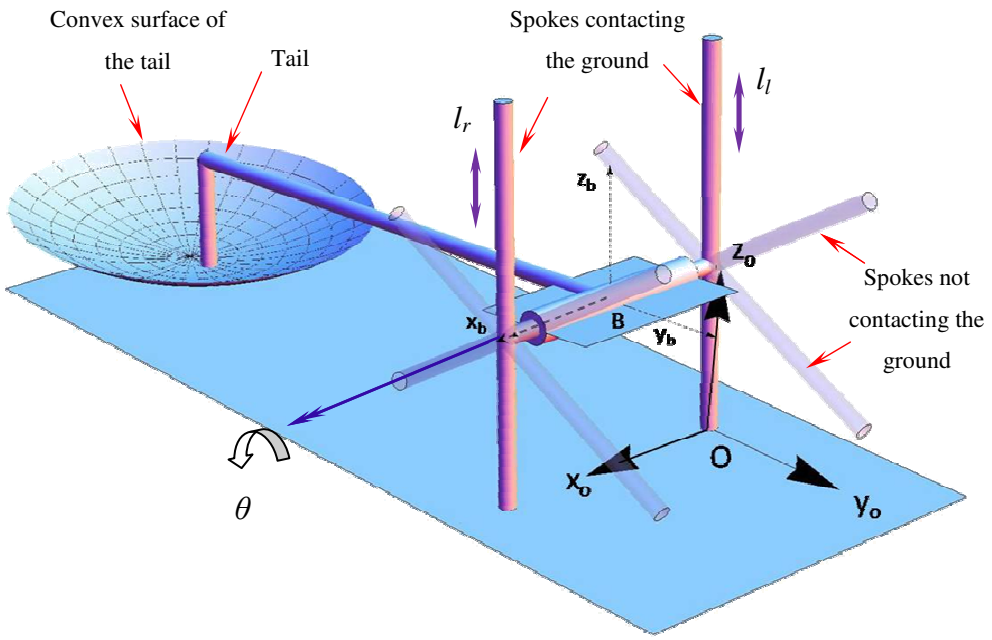

FIG.6.2 KINEMATIC MODEL OF THE IMPASS WITH TWO SPOKES AND THE TAIL IN CONTACT WITH THE SMOOTH GROUND

The walking and steering of the IMPASS can be seen in the videos in [80, 81]. Various contact cases are observed from its ground locomotion. So for the convenience of analysis, a simple and straightforward nomenclature is composed to describe the contact case in each topology. This nomenclature generally follows the format of "n_1-n_2: parallel & equal / parallel & unequal / skew". The term "n_1-n_2" is used to represent the numbers of the contacting spokes in the left and right wheels respectively, with the term "parallel & equal / parallel & unequal" indicating whether or not the geometrically parallel contacting spokes in this case are of equal length. The term "skew" is used only when the left contacting spoke is skew to the right contacting spoke. For example, the case in Fig.6.2 can be addressed as "1-1: parallel & equal" because the left contact spoke is parallel and equal to the right one. The most commonly used contact cases of the IMPASS on flat ground are presented in Fig.6.3, with the arrows denoting the transformation relationships between the correlated cases. Since the tail always touches the ground passively as the robot moves, and the body does not affect any contact cases, they are both omitted in this figure. The contacting points between the spoke tips and the ground are connected with dashed lines, which also demonstrate the shape of the virtual base in each topology. Inspecting all the contact cases in Fig.6.3, it is notable that the IMPASS' various modes of locomotion can now be uniformly interpreted as a series

of topology transformations between the contact cases, and during such process, the virtual base is changing as well. The DOF possessed by each topology will be identified and discussed in Sec. 6.3.

6.2. Locomotion

As demonstrated in Fig.6.3, the IMPASS robot generally has two modes of straight-line walking. The first mode is the repeated transformation between the “1-1: parallel & equal” case and the “2-2: parallel & equal” case. Since the effective length of the contacting spokes in “1-1: parallel & equal” is adjustable, this mode of locomotion can walk over moderately rough terrain and climb high steps. The second mode of straight-line walking is the transformation between the “2-2: parallel & equal” case and the “3-3: parallel & equal” case. Compared with the first mode, the advantage of this mode is that the robot can take a wider stance on the ground for improved stability.

The steering of the IMPASS is realized through the steady state turning and turning gait transition. For the steady state turning, the robot starts from the “1-1: parallel & unequal” case and transits to the “2-2: parallel & unequal” case back and forth. Keeping the proportion of the two contacting spokes as a constant, the robot can accomplish a right or a left turning discretely. The turning gait transition functions as the transitional phase between the left turning, the right turning and the straight-line walking. For example, the IMPASS originally walking in a straight line can transform its topology to the “2-1: parallel & equal” case and then rotate about the pivot line on the ground that is skew to the axle to reach the “1-1: skew” case. Manipulating both the contacting and un-contacting spokes in the “1-1: skew” case, the robot can change its topology to the “2-2: parallel & unequal” case for a left or right turn as needed. Similarly, the robot that is making a left turning can switch to a right turning through the topologies of “2-1: parallel & unequal” and “1-1: skew”.

Therefore, using the modes of straight-line walking and steady state turning as the fundamental modulus, and the turning gait transition as the transitional module, the complete ground locomotion of the IMPASS robot is established. Different from that of conventional wheeled or tracked mobile robots, this type of locomotion features discrete contact with the ground.

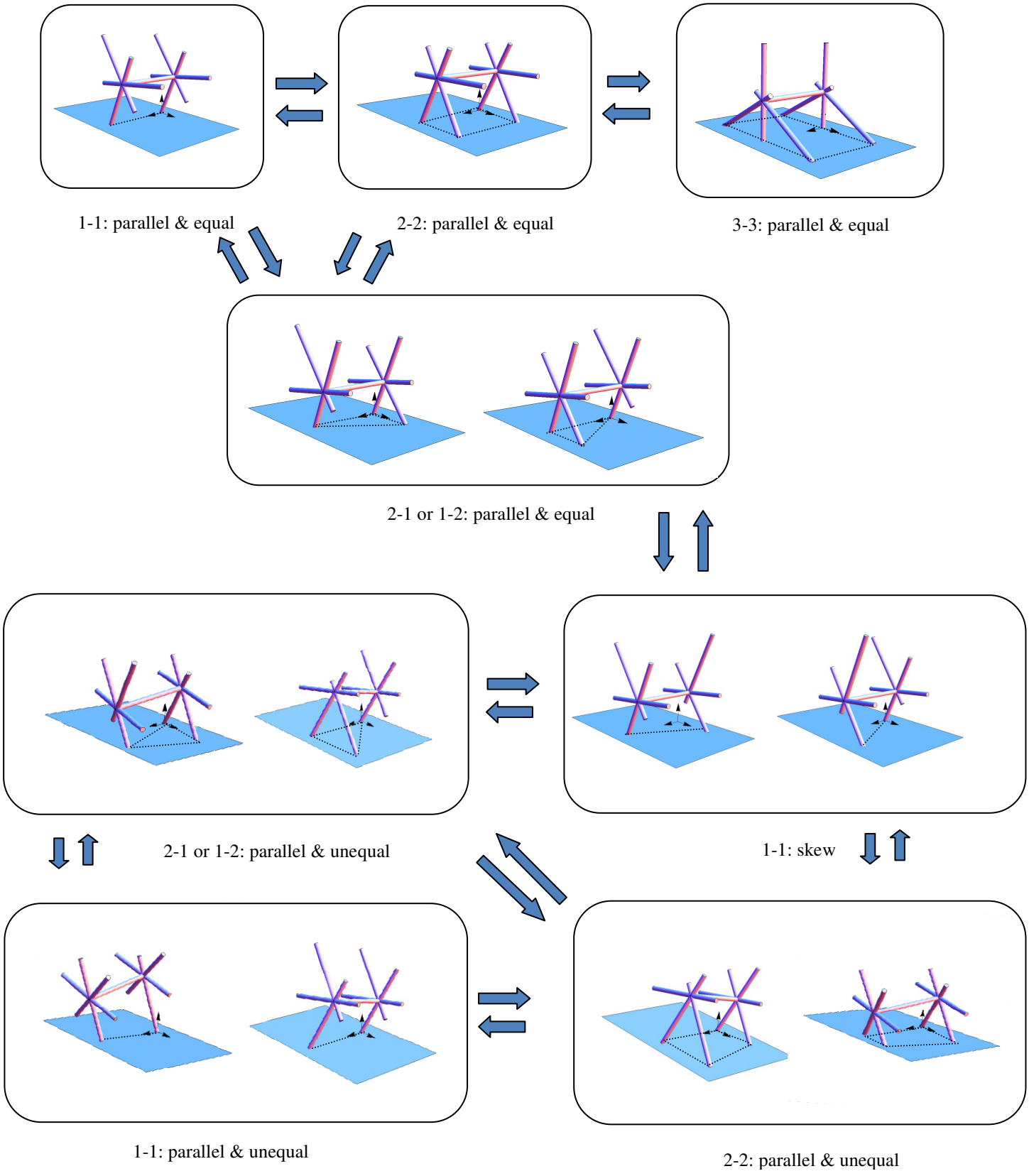

FIG.6.3 TOPOLOGY TRANSFORMATIONS OF THE COMMON CONTACT CASES OF IMPASS

Chapter 7 Mobility Analysis on the Variable Topologies

Examining all the contact cases in Fig.6.3, it is observed that the axle is always connected to the ground through multiple actuated spokes. Since the contact points generated between the spoke tips and the ground are assumed to be stationary in any cases, they can be modeled as spherical joints based on the frictional point contact model, which was adopted by previous researchers to study the contact interaction between a multi-finger gripper and a rigid object, as in [54-57]. By treating the smooth ground as the base, and the actuation axle of the two spoke wheels as the platform, each topology in Fig.7.3 can now be modeled as a parallel mechanism, in which each contacting spoke is considered as a limb consisting of a Spherical-Prismatic dyad (SP). If the changeable mobility of the axle in the variable topologies is determined, the DOF of the IMPASS' body can be simply inferred.

The complex mobility of MVTs was investigated using various criteria such as the general *Grübler-Kutzbach criterion* [58, 59], the *Grübler-Kutzbach criterion* integrated with the screw system's order [82, 83], and the *Modified Grübler-Kutzbach criterion* for overconstrained parallel mechanisms [84]. The effectiveness of these criteria was validated by the examples in [30, 35, 37]. In particular, the *Modified Grübler-Kutzbach criterion* is a new version of the classical criterion, which involves the reciprocal screw system of each limb. By eliminating the redundant constraints, the DOF of the platform of a parallel mechanism can be accurately predicted. This approach is adopted in this paper to analyze the mobility of the IMPASS robot, since its variable topologies can be modeled as parallel mechanisms will SP limbs.

As discussed in [20], the joint screws associated with a SP dyad form a four-system, which has a two-system as their reciprocal. Because of the presence of a spherical joint together with a prismatic joint, this two-system becomes a planar pencil passing through the center of the sphere and lying on a plane that is perpendicular to the axis of the prismatic joint. As is illustrated in Fig.7.1, each line belonging to the planar pencil corresponds exactly to one reciprocal screw of the SP screw system. These reciprocal screws provide constraints to the platform and determine its DOF [84]. As for the particular variable topologies of the IMPASS, the decomposition of its constraint screw system and the identification of the redundant virtual constraints can be converted, with the assistance of *Grassmann Line Geometry*, to the investigation on the linear dependency of multiple planar pencils. Previous applications of *Grassmann Line Geometry* in solving kinematics problems such as singularities can be found in [22, 23, 85]. Based on Merlet's notation, Ref.[26] provides complete illustrations of various line varieties with the orders from one to six. These analytical methods are utilized in the following sections to study the variable mobility of the IMPASS' contact cases.

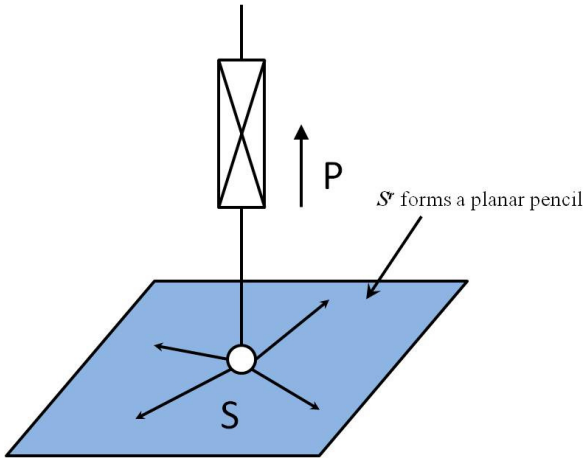

FIG.7.1 SPHERICAL-PRISMATIC DYAD AND ITS RECIPROCAL SCREW SYSTEM

7.1. "1-1: Parallel" Contact Cases

As shown in Fig.7.3, there are two sub-cases in this group depending on whether or not the two parallel spokes are of the equal length. Ignoring those un-contacting spokes, the reciprocal screws of each SP limb in the contact cases of "1-1: parallel & unequal" and "1-1: parallel & equal" are demonstrated in Fig.7.2(a) and (b). To make the illustration straightforward, the body, the un-contacting spokes and the ground are omitted. Each planar pencil is represented with two linearly independent lines. Inspecting the orders of the two sets of lines in Fig.7.2, it can be found that, the four lines s_{11}, s_{12}, s_{21}, s_{22} in Fig.7.2(a) are linearly independent and thus form a hyperbolic congruence with an order of four. This is because the four lines are intersecting two independent lines with one passing through the two spherical centers and the other at infinity with a direction perpendicular to the two parallel planes containing the pencils. However, as for the case in Fig.7.2(b), the four lines all lie on the same plane and only form a line variety with an order of three, which indicates that s_{11}, s_{12}, s_{21}, s_{22} are linearly dependent and the screw or plücker line vector of any line out of s_{11} to s_{22} can be represented as a linear combination of the rest three.

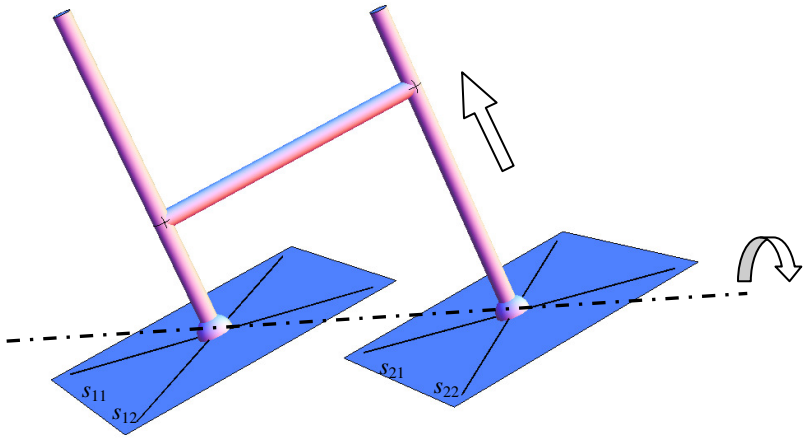

(a)

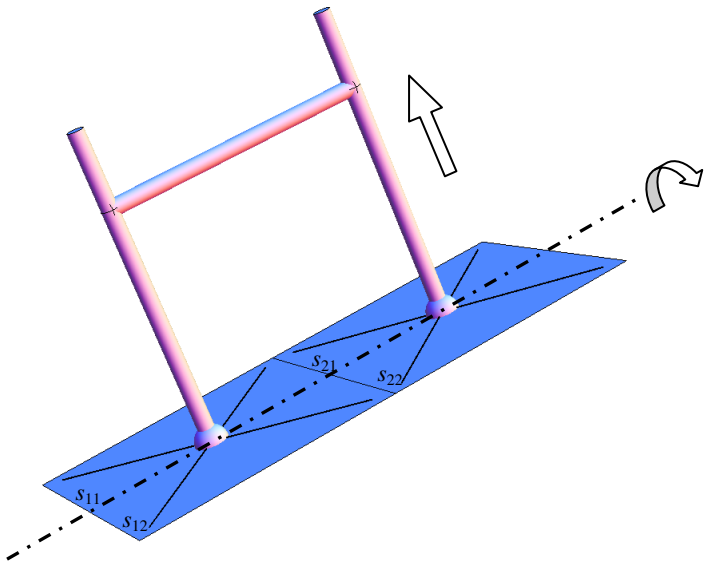

(b)

FIG.7.2 CONSTRAINT SCREW SYSTEM AND DOF OF: (A) THE "1-1: PARALLEL &UNEQUAL" CASE; (B) THE "1-1: PARALLEL & EQUAL" CASE

The decomposition process of the mechanism constraint system in the two cases is shown as follows.

For "1-1: parallel & unequal":

$$\begin{aligned}\left\langle \boldsymbol{S}^r \right\rangle &= \left\langle \boldsymbol{S}_{11}^r, \boldsymbol{S}_{12}^r, \boldsymbol{S}_{21}^r, \boldsymbol{S}_{22}^r \right\rangle = \left\langle \boldsymbol{S}^c \right\rangle + \left\langle \boldsymbol{S}_c^r \right\rangle = \left\langle \boldsymbol{S}^c \right\rangle + \left\{ \boldsymbol{S}_c^r \right\} + \left\langle \boldsymbol{S}_v^r \right\rangle \\ &= \underbrace{\varnothing}_{\left\langle \boldsymbol{S}^c \right\rangle} + \underbrace{\left\{ \boldsymbol{S}_{11}^r, \boldsymbol{S}_{12}^r, \boldsymbol{S}_{21}^r, \boldsymbol{S}_{22}^r \right\}}_{\left\{ \boldsymbol{S}_c^r \right\}} + \underbrace{\varnothing}_{\left\langle \boldsymbol{S}_v^r \right\rangle}\end{aligned} \tag{7.1}$$

While for "1-1: parallel, equal":

$$\begin{aligned}\left\langle \boldsymbol{S}^r \right\rangle &= \left\langle \boldsymbol{S}_{11}^r, \boldsymbol{S}_{12}^r, \boldsymbol{S}_{21}^r, \boldsymbol{S}_{22}^r \right\rangle = \left\langle \boldsymbol{S}^c \right\rangle + \left\langle \boldsymbol{S}_c^r \right\rangle = \left\langle \boldsymbol{S}^c \right\rangle + \left\{ \boldsymbol{S}_c^r \right\} + \left\langle \boldsymbol{S}_v^r \right\rangle \\ &= \underbrace{\varnothing}_{\left\langle \boldsymbol{S}^c \right\rangle} + \underbrace{\left\{ \boldsymbol{S}_{11}^r, \boldsymbol{S}_{12}^r, \boldsymbol{S}_{21}^r \right\}}_{\left\{ \boldsymbol{S}_c^r \right\}} + \underbrace{\left\{ \boldsymbol{S}_{22}^r \right\}}_{\left\langle \boldsymbol{S}_v^r \right\rangle}\end{aligned} \tag{7.2}$$

where $\boldsymbol{S}_{mn}^r$ denotes the screw of line s_{mn}, multiset $\left\langle \boldsymbol{S}^r \right\rangle$ represents the total constraints on the axle by all SP limbs, which may contain common and redundant constraints. Multiset $\left\langle \boldsymbol{S}^c \right\rangle$ represents the common constraint of all limbs and $\left\langle \boldsymbol{S}_c^r \right\rangle$ represents all the rest constraints not included in $\left\langle \boldsymbol{S}^c \right\rangle$. $\left\langle \boldsymbol{S}_c^r \right\rangle$ is further decomposed into $\left\{ \boldsymbol{S}_c^r \right\}$ and $\left\langle \boldsymbol{S}_v^r \right\rangle$, with $\left\{ \boldsymbol{S}_c^r \right\}$ containing the largest linearly independent set of screws in $\left\langle \boldsymbol{S}_c^r \right\rangle$ and $\left\langle \boldsymbol{S}_v^r \right\rangle$ containing the remaining redundant constraints.

The *Modified Grübler-Kutzbach criterion* elaborated in Ref.[84] states as follows:

$$m = d(n - g - 1) + \sum_{i=1}^{g} f_i + v - v_{\text{local}} \tag{7.3}$$

where m is the mobility of a parallel mechanism, n the number of links and g the number of joints. f_i represents the DOF permitted by each joint. d is defined as the dimension of the mechanism motion-screw system and can be calculated from $d = 6 - \dim(\boldsymbol{S}^c)$, where $\dim(\boldsymbol{S}^c)$ is the dimension of the common constraint set $\left\langle \boldsymbol{S}^c \right\rangle$. v is the number of redundant constraints; it is determined as the cardinal number of the multiset $\left\langle \boldsymbol{S}_v^r \right\rangle$, i.e. $v = \text{card}\left\langle \boldsymbol{S}_v^r \right\rangle$. Finally, v_{local} is the number of local DOF in ach limb of a parallel mechanism. As for the SP limbs in the IMPASS' all contact cases, v_{local} is equal to zero and no local DOF exists.

Apply Eq.(7.1) and (7.3) for the "1-1: parallel, unequal" contact case. Since $v = \text{card}\left\langle \boldsymbol{S}_v^r \right\rangle$ = 0, $d = 6 - \dim(\boldsymbol{S}^c) = 6 - 0 = 6$, $n = 4$, $g = 4$, the mobility of the axle is calculated as $m = 6(4\text{-}4\text{-}1) + 8 + 0 - 0 = 2$. The result obtained from the criterion match with the observations on the robot's motion and both DOF are continuous. As illustrated in Fig. 7.2(a), one DOF of the axle is the translation along the two parallel spokes and the other is the rotation about the

pivot line passing the two contact points. The robot's tail passively touches the ground during its walking, thus providing a triangular support region to maintain the stability. In order to eliminate slip or bounce at the contact points, the difference of the two spokes' lengths must be kept as constant.

The mobility of the "1-1: parallel, equal" case is different from that of "1-1: parallel, unequal" in that the constraint multiset $\langle \boldsymbol{S}^r \rangle$ degenerates in the former case. Examining Eq.(7.2), since $v = \text{card}\langle \boldsymbol{S}_v^r \rangle = 1$, $d = 6 - \dim(\boldsymbol{S}^c) = 6 - 0 = 6$, $n = 4$, $g = 4$, the mobility m is calculated as 3, instead of 2. The difference between the mobility of the two topologies is further revealed in the following analysis.

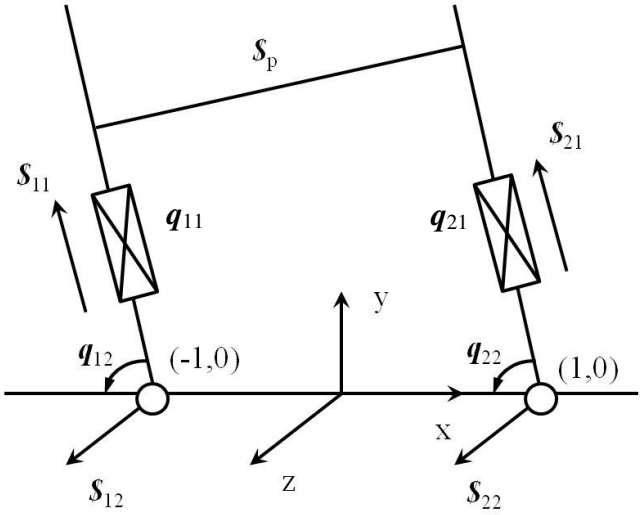

FIG.7.3 MOTION SCREW SYSTEM OF A RPPR MECHANISM WITH $q_{11} \neq q_{21}$ AND $q_{12} = q_{22} \neq 90^o$

Assume a planar mechanism has a single-loop Revolute-Prismatic-Prismatic-Revolute (RPPR) configuration and lies on the XY plane, as is illustrated in Fig.7.3. Kinematically, the motion screw system of this RPPR mechanism is a subset of the motion screw system of the "1-1: parallel, unequal" contact case. Start from a general case with the lengths of the two branches $q_{11} \neq q_{21}$ and the joint angles $q_{12} = q_{22} \neq 90^o$ initially. Assign simple coordinates to the joint locations for the convenience of computation. Without losing generality, the screws in each of the two RP branches are developed.

Screws in Branch 1:

$$\begin{aligned} \$_{11} &= [0 \quad 0 \quad 0 \quad \cos q_{12} \quad \sin q_{12} \quad 0]^T; \\ \$_{12} &= [0 \quad 0 \quad 1 \quad 0 \quad 1 \quad 0]^T; \end{aligned} \tag{7.4.1}$$

Screws in Branch 2:

$$\begin{aligned} \$_{21} &= [0 \quad 0 \quad 0 \quad \cos q_{22} \quad \sin q_{22} \quad 0]^T; \\ \$_{22} &= [0 \quad 0 \quad 1 \quad 0 \quad -1 \quad 0]^T; \end{aligned} \tag{7.4.2}$$

Thus, the screw equation of the moving platform in Branch 1 is:

$$\$_{\mathrm{P}} = \$_{11}\dot{q}_{11} + \$_{12}\dot{q}_{12}$$

$$\Rightarrow \begin{bmatrix} \omega_x \\ \omega_y \\ \omega_z \\ v_x \\ v_y \\ v_z \end{bmatrix} = \begin{bmatrix} 0 \\ 0 \\ 0 \\ \cos q_{12} \\ \sin q_{12} \\ 0 \end{bmatrix} \dot{q}_{11} + \begin{bmatrix} 0 \\ 0 \\ 1 \\ 0 \\ 1 \\ 0 \end{bmatrix} \dot{q}_{12} \tag{7.5.1}$$

And in Branch 2:

$$\$_{\mathrm{P}} = \$_{21}\dot{q}_{21} + \$_{22}\dot{q}_{22}$$

$$\Rightarrow \begin{bmatrix} \omega_x \\ \omega_y \\ \omega_z \\ v_x \\ v_y \\ v_z \end{bmatrix} = \begin{bmatrix} 0 \\ 0 \\ 0 \\ \cos q_{22} \\ \sin q_{22} \\ 0 \end{bmatrix} \dot{q}_{21} + \begin{bmatrix} 0 \\ 0 \\ 1 \\ 0 \\ -1 \\ 0 \end{bmatrix} \dot{q}_{22} \tag{7.5.2}$$

Inspect Eq.(7.5.1) and (7.5.2), obviously:

$$\omega_x = 0;\ \omega_y = 0; v_z = 0;$$

From the rest equations:

$$\left.\begin{array}{l} v_x = \cos q_{12}\ \dot{q}_{11} = \cos q_{22}\ \dot{q}_{21} \\ q_{12} = q_{22} \neq 90^\circ \end{array}\right\} \Rightarrow \dot{q}_{11} = \dot{q}_{21}$$

$$\left.\begin{array}{l} \left.\begin{array}{l} v_y = \sin q_{12}\ \dot{q}_{11} + \dot{q}_{12} = \sin q_{22}\ \dot{q}_{21} - \dot{q}_{22} \\ \dot{q}_{11} = \dot{q}_{21} \end{array}\right\} \Rightarrow \dot{q}_{12} = -\dot{q}_{22} \\ \omega_z = \dot{q}_{12} = \dot{q}_{22} \end{array}\right\} \Rightarrow \begin{cases} \omega_z = \dot{q}_{12} = \dot{q}_{22} = 0 \\ v_y = \sin q_{12}\ \dot{q}_{11} = \sin q_{22}\ \dot{q}_{21} \end{cases} \tag{7.6}$$

So the only input variable to this system is $\dot{q}_{11}$ or $\dot{q}_{21}$; ω_z, $\dot{q}_{12}$ and $\dot{q}_{22}$ are always constrained to be zero. The output v_y or v_x is integrable over time so that the platform can translate continuously along the two branches. If the two revolute joints in the RPPR configuration are replaced with two spherical joints, with the addition of the rotation about the x axis, the new mechanism will resume exactly the same DOF as the "1-1: parallel, unequal" case.

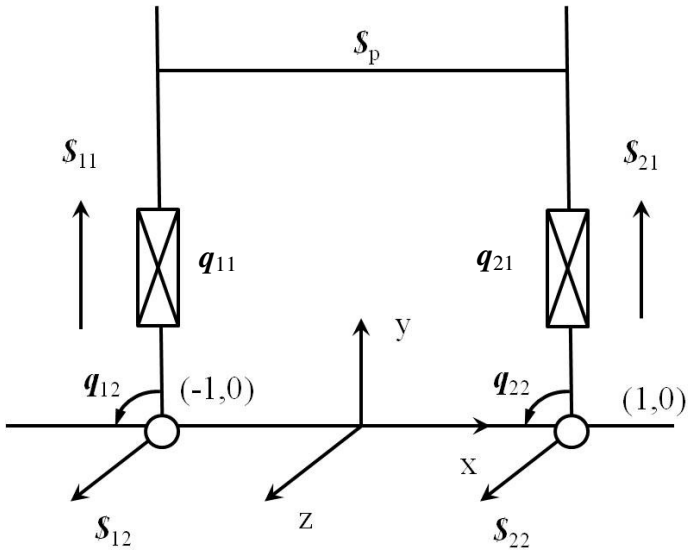

FIG.7.4 MOTION SCREW SYSTEM OF A SPECIAL RPPR MECHANISM WITH $q_{11} = q_{21}$ AND $q_{12} = q_{22} = 90^o$

However, additional DOF occurs when $q_{11} = q_{21}$ and $q_{12} = q_{22} = 90^o$, as illustrated in Fig.7.4. For this special case, since cos q_{12} = cos q_{22} = 0, and sin q_{12} = sin q_{22} = 0, Eq.(7.6) becomes

$$\begin{aligned} v_x &= 0 \cdot \dot{q}_{11} = 0 \cdot \dot{q}_{21} = 0 \\ v_y &= \dot{q}_{11} + \dot{q}_{12} = \dot{q}_{21} - \dot{q}_{22} \\ \omega_z &= \dot{q}_{12} = \dot{q}_{22} \end{aligned} \tag{7.7}$$

It can be found that, under such conditions, this system has two independent input variables, $\dot{q}_{12}(\dot{q}_{22})$ as well as $\dot{q}_{11}(\dot{q}_{21})$, with the outputs as v_y and ω_z. v_x is constrained to be zero in this configuration. Again, replacing the revolute joints in the special RPPR configuration with spherical joints, the new mechanism will obtain 3 DOF, which explains why the mobility of the "1-1: parallel, equal" case is calculated as 3 based on the *Modified Grübler-Kutzbach criterion*. Among the three DOF, ω_z is instantaneous and only exists in the special RPPR configuration. As a brief explanation, assume a non-zero input $\dot{q}_{12}$ is applied to the system and generates a non-zero ω_z, then in the next instant, q_{12} and q_{22} will not be equal to 90°, the screw equations reassume the forms of Eq.(7.5) and ω_z is constrained back to zero as in Eq.(7.6). Since the *Modified Grübler-Kutzbach criterion* is essentially based on the screw theory, the DOF obtained using this method are instantaneous in the first place and not all of them can become continuous. Therefore, it is necessary to investigate all the velocity variables further, identify the instantaneous only DOF if exists, and develop

appropriate input schemes to constrain those instantaneous DOF that are unnecessary for required motions. Inspecting Eq.(7.7), if $\dot{q}_{11} = \dot{q}_{21}$ is implemented as an additional constraint of the inputs, then

$$\begin{aligned} \omega_z &= \dot{q}_{12} = \dot{q}_{22} = 0 \\ v_y &= \dot{q}_{11} = \dot{q}_{21} \end{aligned} \tag{7.8}$$

thus, the infinitesimal motion ω_z with the direction normal to the *x*-*y* plane can be eliminated and the platform can translate continuously along the two branches in the *y* direction. Technically, the enforcement of $\dot{q}_{11} = \dot{q}_{21}$ is realized by setting the two contacting spokes' linear displacements and velocities equal to each other at any instant. Then, the instantaneous rotation normal to the plane containing the axle and the two contacting spokes of the robot is constrained, which does not interfere with the robot's locomotion. Therefore, although the mobility of the "1-1: parallel, equal" case is 3, the two continuous DOF that are actuated in operations are the same as those of the "1-1: parallel, unequal" case, i.e. the translation along the two parallel spokes and the rotation about the pivot line passing the two contact points.

7.2. "2-1", "1-2" and "2-2" Contact Cases

7.2.1. "2-1" and "1-2" Cases

The topologies of the "2-1" and "1-2" contact cases are very similar to each other, so they are analyzed together in this subsection. Depending on whether the parallel contacting spokes are of equal length, different mobilities are demonstrated. Fig.7.5(a) and (b) shows the mechanism constraint systems of the "2-1: parallel & unequal" case and the "1-2: parallel & unequal" case. The decomposition process for both cases is as follows:

$$\begin{aligned} \left\langle \boldsymbol{S}^r \right\rangle &= \left\langle \boldsymbol{S}_{11}^r, \boldsymbol{S}_{12}^r, \boldsymbol{S}_{21}^r, \boldsymbol{S}_{22}^r, \boldsymbol{S}_{31}^r, \boldsymbol{S}_{32}^r \right\rangle = \left\langle \boldsymbol{S}^c \right\rangle + \left\langle \boldsymbol{S}_c^r \right\rangle = \left\langle \boldsymbol{S}^c \right\rangle + \left\{ \boldsymbol{S}_c^r \right\} + \left\langle \boldsymbol{S}_v^r \right\rangle \\ &= \underbrace{\varnothing}_{\langle \boldsymbol{S}^c \rangle} + \underbrace{\left\{ \boldsymbol{S}_{11}^r, \boldsymbol{S}_{12}^r, \boldsymbol{S}_{21}^r, \boldsymbol{S}_{22}^r, \boldsymbol{S}_{31}^r, \boldsymbol{S}_{32}^r \right\}}_{\{\boldsymbol{S}_c^r\}} + \underbrace{\varnothing}_{\langle \boldsymbol{S}_v^r \rangle} \end{aligned} \tag{7.9}$$

In these two contact cases, multiset $\langle \boldsymbol{S}_v^r \rangle$ is empty because any two out of the three planar pencils are not coplanar and the six lines are linearly independent. Since $v = \text{card}\langle \boldsymbol{S}_v^r \rangle = 0$, $d = 6 - \dim(\boldsymbol{S}^c) = 6 - 0 = 6$, $n = 5$, $g = 6$, the mobility of the axle is calculated as $m = 6(5\text{-}6\text{-}1) + 12 + 0 - 0 = 0$. Since the axle has no DOF in these cases, it can be inferred that the possible motion of the boy is only the rotation about the axle itself. The result obtained is verified by the actual observations and such cases function mainly as the transitions between the contact cases with non-zero DOF.

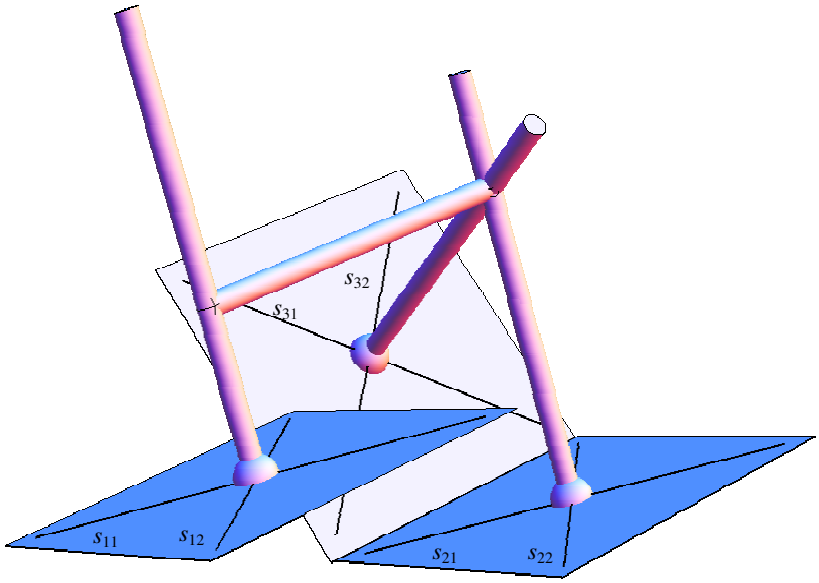

(a)

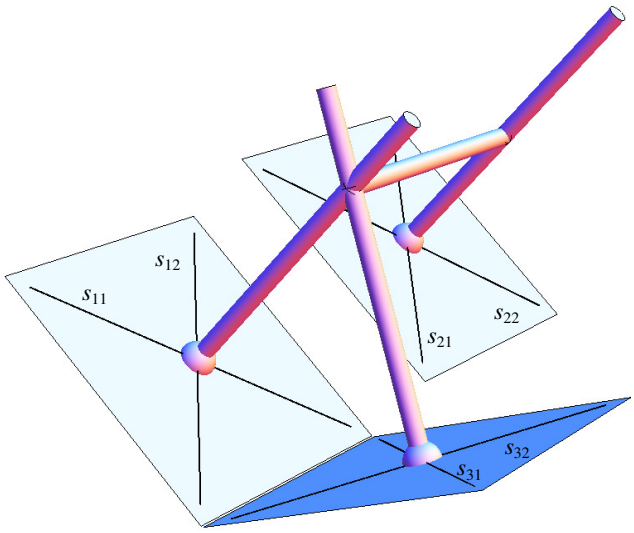

(b)

FIG.7.5 CONSTRAINT SCREW SYSTEM OF: (A) THE "2-1: PARALLEL &UNEQUAL" CASE; (B) THE "1-2: PARALLEL & UNEQUAL" CASE

However, the mobility changes if the two parallel contacting spokes are equal, as in the "2-1 or 1-2: parallel & equal" cases. Their constraint systems are demonstrated in Fig.7.6(a) and (b). Inspecting the linear dependency of the three planar pencils, it can be found that the four lines s_{11}, s_{12}, s_{21}, s_{22} lie on the same plane a, and plane a has an intersection line l with plane b which contains lines s_{31}, s_{32}. Since all six lines are intersecting line l, the line variety they form is a special complex with an order of five. The decomposition of the constraint screw system then becomes:

$$\begin{aligned}\left\langle \boldsymbol{S}^r \right\rangle &= \left\langle \boldsymbol{S}_{11}^r, \boldsymbol{S}_{12}^r, \boldsymbol{S}_{21}^r, \boldsymbol{S}_{22}^r, \boldsymbol{S}_{31}^r, \boldsymbol{S}_{32}^r \right\rangle = \left\langle \boldsymbol{S}^c \right\rangle + \left\langle \boldsymbol{S}_c^r \right\rangle = \left\langle \boldsymbol{S}^c \right\rangle + \left\{ \boldsymbol{S}_c^r \right\} + \left\langle \boldsymbol{S}_v^r \right\rangle \\ &= \underbrace{\varnothing}_{\left\langle \boldsymbol{S}^c \right\rangle} + \underbrace{\left\{ \boldsymbol{S}_{11}^r, \boldsymbol{S}_{12}^r, \boldsymbol{S}_{21}^r, \boldsymbol{S}_{22}^r, \boldsymbol{S}_{31}^r \right\}}_{\left\{ \boldsymbol{S}_c^r \right\}} + \underbrace{\left\{ \boldsymbol{S}_{32}^r \right\}}_{\left\langle \boldsymbol{S}_v^r \right\rangle}\end{aligned} \tag{7.10}$$

With $v = \mathrm{card}\left\langle \boldsymbol{S}_v^r \right\rangle = 1$, $d = 6 - \dim(\boldsymbol{S}^c) = 6 - 0 = 6$, $n = 5$, $g = 6$, the mobility m of the axle is calculated as 1.

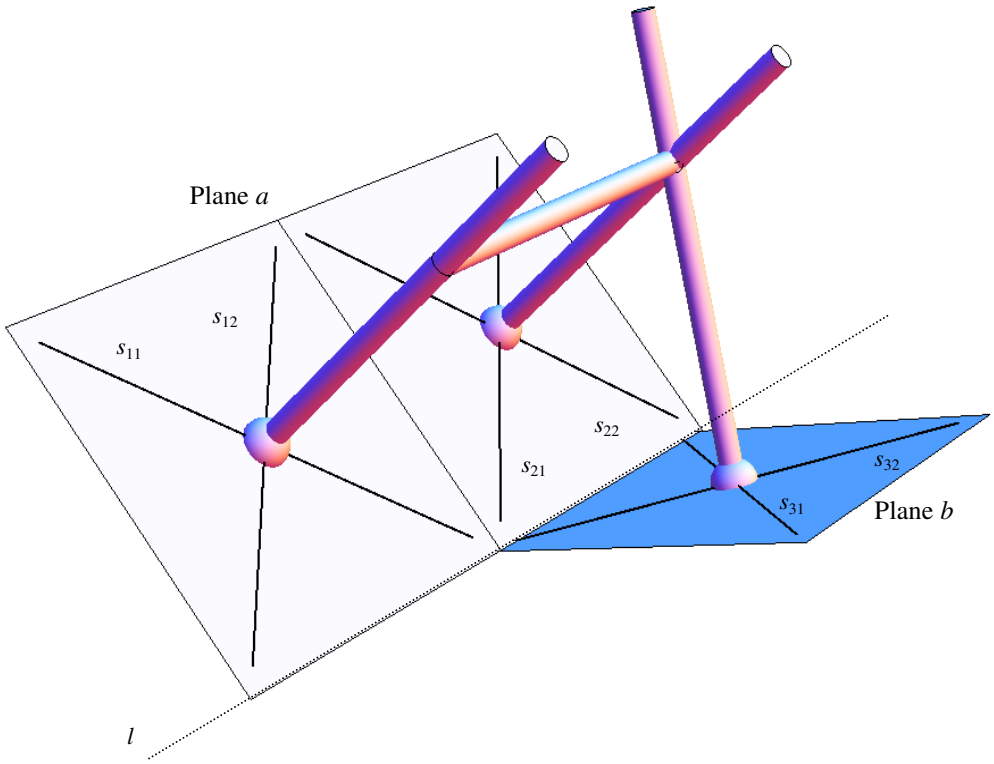

(a)

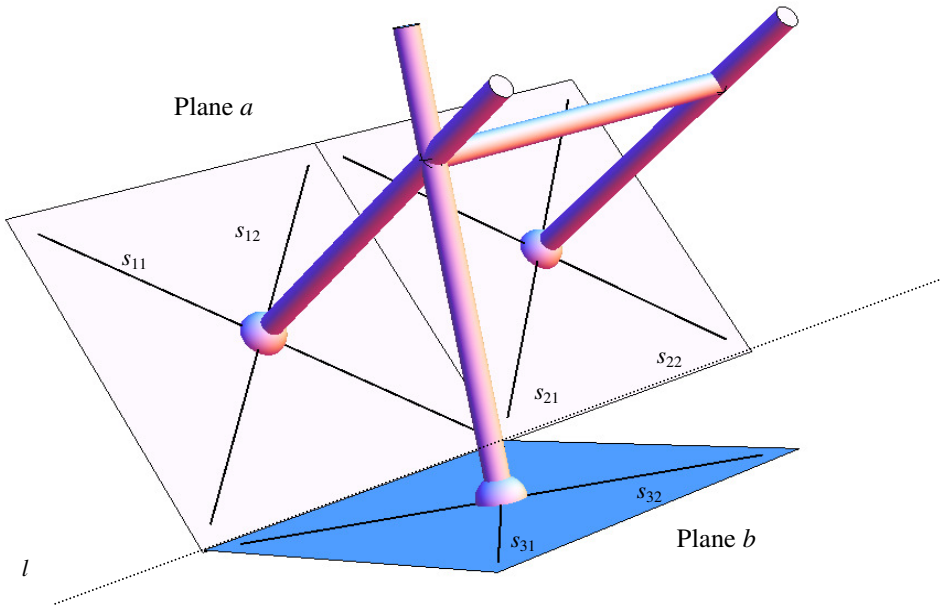

(b)

FIG.7.6 CONSTRAINT SCREW SYSTEM OF: (A) THE "2-1: PARALLEL &EQUAL" CASE; (B) THE "1-2: PARALLEL & EQUAL" CASE

7.2.2. "2-2" Cases

Similarly, as presented in Fig.7.7, the four planar pencils in the "2-2: parallel & equal" contact case also form a special complex with the order of five because plane *a* containing lines s_{11}, s_{12}, s_{21}, s_{22} intersects plane *b* containing s_{31}, s_{32}, s_{41}, s_{42} at line *l*. The decomposition is as follows:

$$\begin{aligned}\left\langle \boldsymbol{S}^{r}\right\rangle &= \left\langle \boldsymbol{S}_{11}^{r},\boldsymbol{S}_{12}^{r},\boldsymbol{S}_{21}^{r},\boldsymbol{S}_{22}^{r},\boldsymbol{S}_{31}^{r},\boldsymbol{S}_{32}^{r},\boldsymbol{S}_{41}^{r},\boldsymbol{S}_{42}^{r}\right\rangle = \left\langle \boldsymbol{S}^{c}\right\rangle + \left\langle \boldsymbol{S}_{c}^{r}\right\rangle = \left\langle \boldsymbol{S}^{c}\right\rangle + \left\{\boldsymbol{S}_{c}^{r}\right\} + \left\langle \boldsymbol{S}_{v}^{r}\right\rangle \\ &= \underbrace{\varnothing}_{\left\langle \boldsymbol{S}^{c}\right\rangle} + \underbrace{\left\{\boldsymbol{S}_{11}^{r},\boldsymbol{S}_{12}^{r},\boldsymbol{S}_{21}^{r},\boldsymbol{S}_{22}^{r},\boldsymbol{S}_{31}^{r}\right\}}_{\left\{\boldsymbol{S}_{c}^{r}\right\}} + \underbrace{\left\{\boldsymbol{S}_{32}^{r},\boldsymbol{S}_{41}^{r},\boldsymbol{S}_{42}^{r}\right\}}_{\left\langle \boldsymbol{S}_{v}^{r}\right\rangle}\end{aligned} \tag{7.11}$$

For this case, with $v = \mathrm{card}\left\langle \boldsymbol{S}_{v}^{r}\right\rangle = 3$, $d = 6 - \dim(\boldsymbol{S}^{c}) = 6 - 0 = 6$, $n = 6$, $g = 8$, the mobility m of the axle is calculated as $m = 6(6\text{-}8\text{-}1) + 16 + 3 - 0 = 1$.

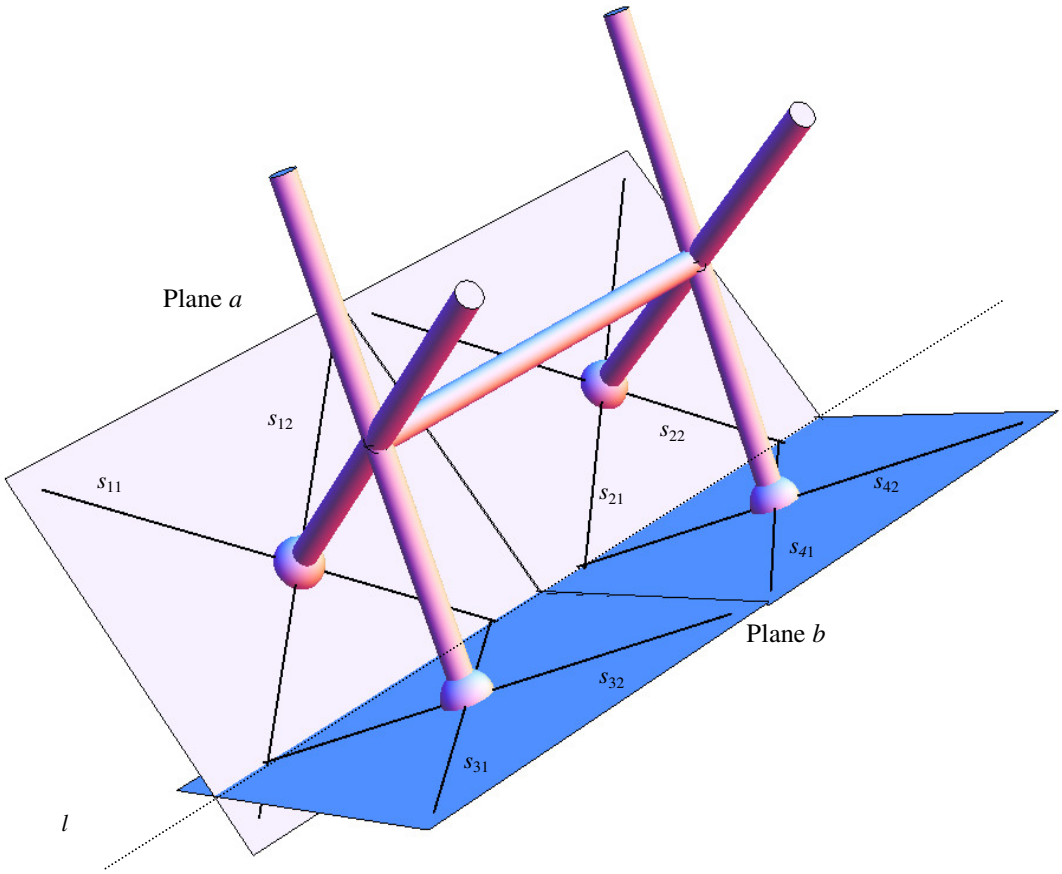

FIG.7.7 CONSTRAINT SCREW SYSTEM OF THE "2-2: PARALLEL & EQUAL" CASE

The one DOF in the "2-2: parallel & equal" case is exactly the same as that in the "2-1 or 1-2: parallel & equal" cases. Due to the existence of parallel and equal contacting spokes, the characteristics of this DOF can be revealed by inspecting the 2D projection of the two spoke wheels on their lateral plane. As shown in Fig.7.8, point A represents the position of the axle in lateral view. The separation angle β between the two contacting spokes is 60º as designed. The distance between the contact point P_1 and P_2 is also a constant because of the no slip condition. Based on the definitions of the inscribed angle and the central angle within a circle, it is found that the trajectory of point A is a circle defined by β and P_1P_2, with the center at O. Therefore, the DOF of the axle in the "2-1 or 1-2: parallel & equal" and "2-2: parallel & equal" cases can be described as the rotation about a virtual axis passing through O, with the direction always parallel to the axle and the ground. This motion is apparently continuous.

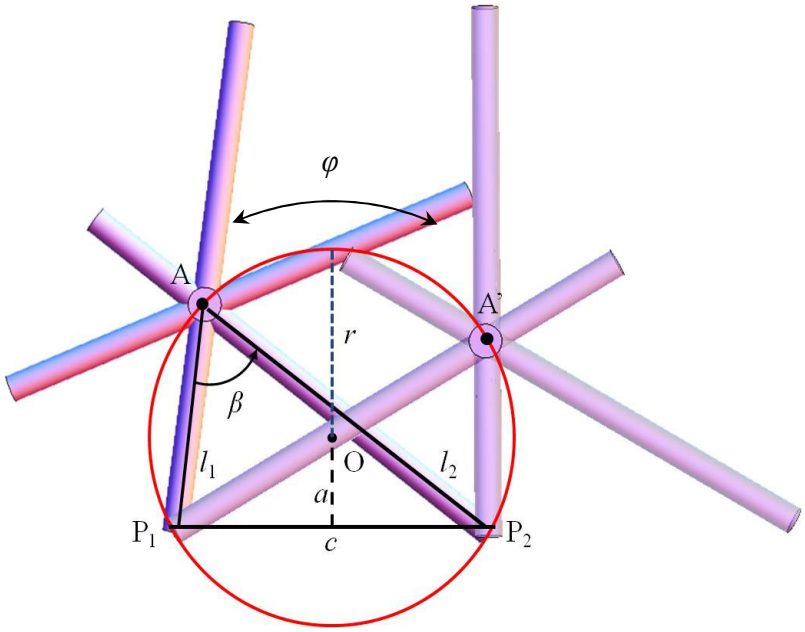

FIG.7.8 2D PROJECTION OF THE DOF IN THE "2-2: PARALLEL & EQUAL" CASE

Inspecting Fig.7.8, the geometric parameters of the circular trajectory can be determined straightforwardly. Assume the length of P_1P_2 is c, then the radius of this circle is $r = c/\sqrt{3}$ and the distance from O to P_1P_2 is $a = c/2\sqrt{3}$. In order to enforce the no slip condition, the lengths of the two contacting spokes in one wheel, l_1 and l_2, must follow a quadratic constraint as:

$$\cos\beta = \frac{l_1^2 + l_2^2 - c^2}{2l_1l_2} = \frac{1}{2}$$
$$l_1^2 + l_2^2 - l_1l_2 = c^2 \qquad (7.12)$$

In this contact case, the rotation of the axle is realized by the actuation of the contacting spokes following the constraint equation of Eq.(7.11). This motion is the basis of the second mode of straight-line walking. Utilizing this DOF, the IMPASS robot can move its body forward and transform “2-2: parallel & equal” to “3-3: parallel & equal” for a step. The body can also rotate about the axle itself. And this DOF is used to ensure that the tail of the robot touches the ground for stable walking.

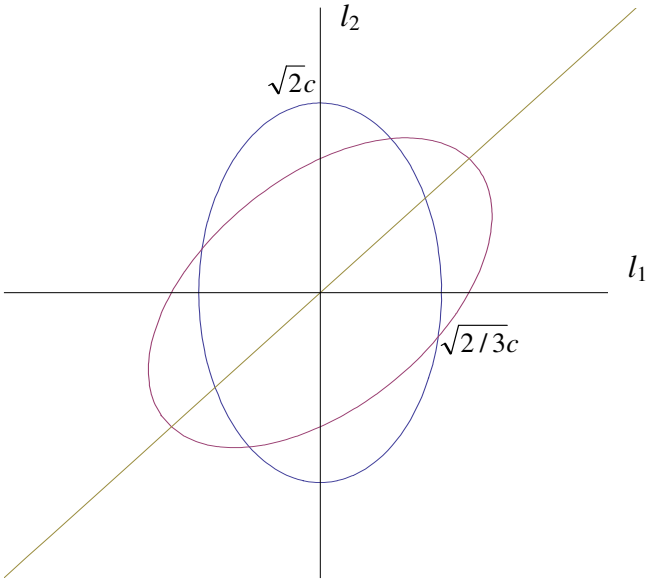

(a)

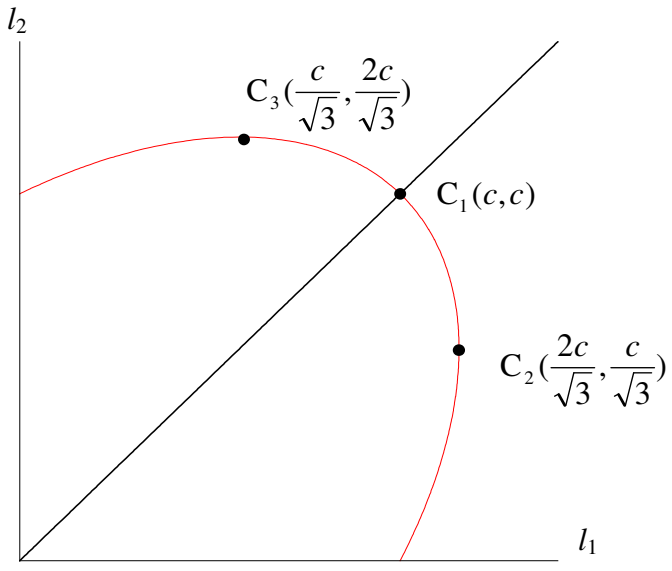

(b)

FIG.7.9 (a) CONSTRAINT ELLIPSE AND (b) EFFECTIVE REGION

The quadratic constraint in Eq.(7.12) is plotted in Fig.7.9(a), with is a ellipse after a

rotation of 45º in clockwise direction, represented with the red curve. The ellipse in blue is the original one with the semiminor axis $\sqrt{2/3}c$ and the semimajor axis $\sqrt{2}c$. Since the length of the spoke link is non-negative, the effective region of the ellipse is plotted in Fig.7.9(b).

The following comments can be made after inspecting Fig.7.9(b):

(1) The effective segment of the constraint ellipse is symmetric about the line $l_1 = l_2$;
(2) If $l_1 = l_2$, then $l_1 = l_2 = c$, as illustrated by point C_1 in Fig.7.9(b);
(3) For a given constant c, the maximum length of the spoke link is $2c/\sqrt{3}$, as illustrated by point C_2 and C_3 in Fig.7.9(b).

Denote this rotational DOF as φ, then the effective range of φ needs particular attention because it is dependent on the physical limits of l_1 and l_2. Fig.7.9(b) is used to assist our analysis. Again, assume all the spokes have identical design and the range of the length of each spoke is $[l_{min}, l_{max}]$. Note that, c is usually determined by the configuration just before the current one. Depending on the choice of c, the range of θ_2 can be continuous or discontinuous or empty.

In the following figures, $[l_{min}, l_{max}]$ is represented as a square.

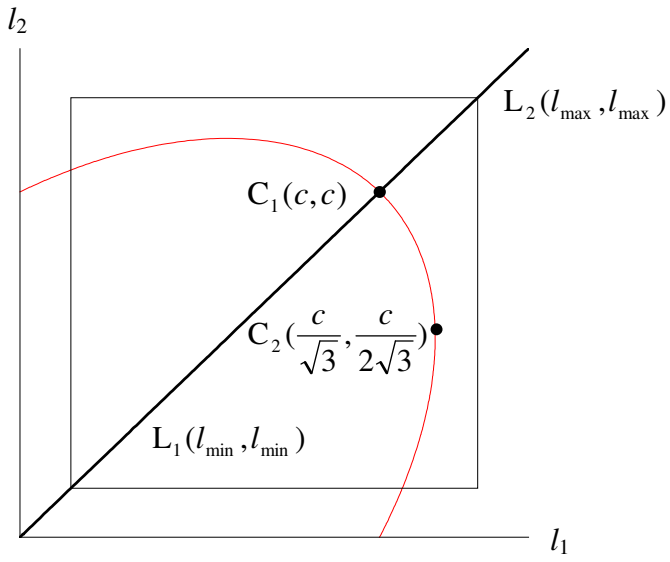

(a)

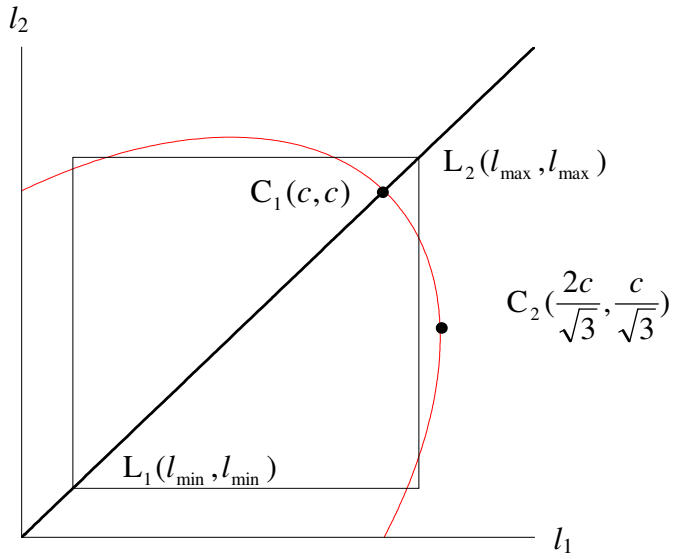

(b)

FIG.7.10 (a) CONTINUOUS EFFECTIVE RANGE OF φ AND (b) DISCONTINUOUS EFFECTIVE RANGE OF φ

In Fig.13(a), if $c \geqslant l_{min} \geqslant 0$ and $l_{max} \geqslant c/\sqrt{3}$, then the effective range of φ is continuous, which is represented with the portion of the ellipse inside the square. However, as shown in Fig.13(b), if $c/\sqrt{3} \geqslant l_{max} \geqslant c$, then φ is possible to have discontinuous range represented by the three separate curves inside the square.

In some extreme cases if parameter c is not appropriately chosen, then the effective range of φ may be empty, as illustrated in Fig.7.11(a) and (b). The case in Fig.7.11(a) occurs when $l_{max} \leqslant c$ and the case in Fig.7.11(b) occurs when $l_{min} \geqslant c$.

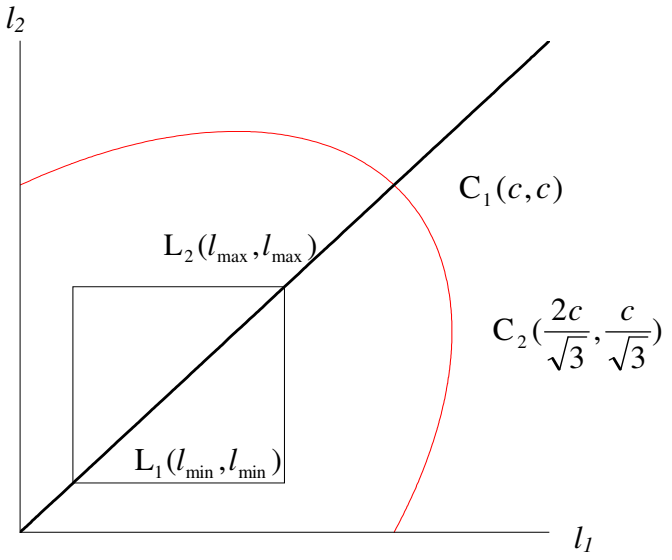

(a)

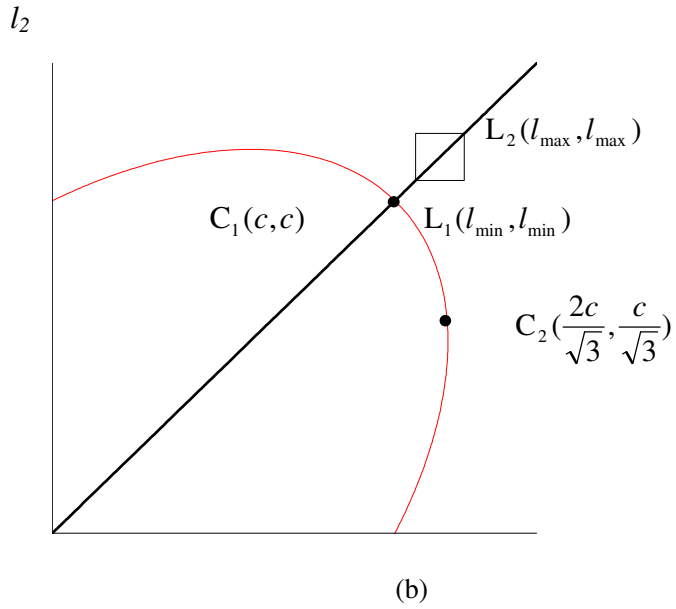

(b)

FIG.7.11 TWO EXTREME CASES WHEN φ HAS EMPTY EFFECTIVE RANGE

Furthermore, the relationship of φ, l_1 and l_2 can be revealed using the following figure adopted from Fig.7.8.

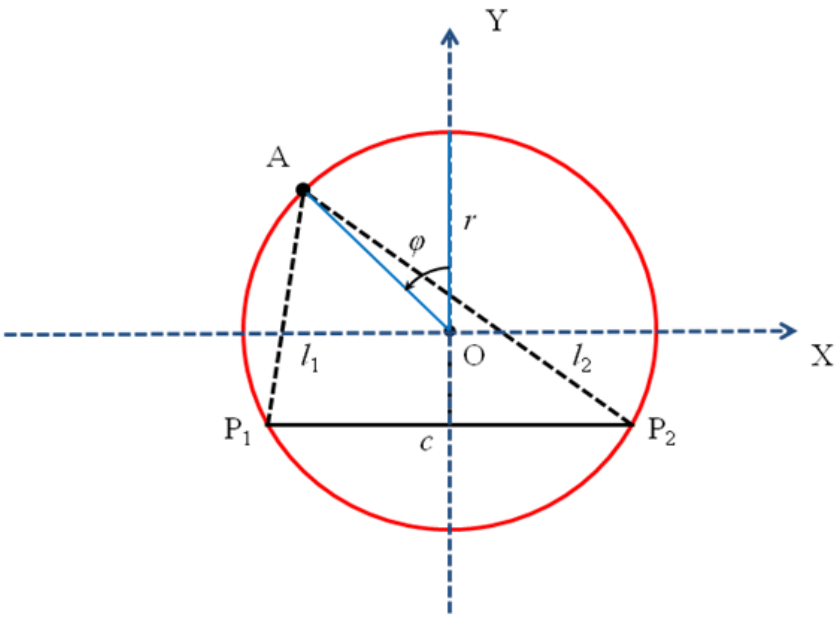

FIG.7.12 RELATIONSHIP OF φ, l_1 AND l_2

Assume when $\varphi = 0$, it is coincident with the Y axis. Inspecting Fig.7.12, the following equations can be established as:

$$\begin{bmatrix} r^2 & \sqrt{3}r^2 \\ r^2 & -\sqrt{3}r^2 \end{bmatrix} \begin{bmatrix} \sin\varphi \\ \cos\varphi \end{bmatrix} = \begin{bmatrix} l_1^2 - 2r^2 \\ l_2^2 - 2r^2 \end{bmatrix} \tag{7.13}$$

Therefore, when the lengths l_1 and l_2 are sensed, the value of the DOF φ can be determined through the equations above.

Differentiating Eq.(7.13) with respect to time, two equations can be obtained as:

$$\begin{aligned} &C_1\dot{\varphi} = 2\, l_1\, \dot{l}_1, \text{where}\ \ C_1 = \sqrt{3}r^2\cos\varphi - r^2\sin\varphi \\ &C_2\dot{\varphi} = 2\, l_2\, \dot{l}_1, \text{where}\ \ C_1 = -\sqrt{3}r^2\cos\varphi - r^2\sin\varphi \end{aligned} \tag{7.14}$$

The configuration when $C_1 = 0$ or $C_2 = 0$ correspond to the forward singularity of the "2-2: parallel & equal" case and the conditions are identified as $\varphi = \pm 60°$.Under such singularities, φ could have infinitesimal motions if only one pair of parallel contacting spokes is locked. To eliminate this singularity, redundant actuation with two pairs of parallel contacting spokes can be used. Note that, this type of singularity also exists in "2-1 or 1-2: parallel & equal" and "1-1: skew" cases.

As for the "2-2: parallel & unequal" case, the mobility changes again because the parallel contacting spokes are not equal. As shown in Fig.7.13, the line variety consisting of the eight lines has an order of six so any two lines can be represented as the linear combinations of the rest six. The constraint system is decomposed as:

$$\begin{aligned} \left\langle \boldsymbol{S}^r \right\rangle &= \left\langle \boldsymbol{S}_{11}^r, \boldsymbol{S}_{12}^r, \boldsymbol{S}_{21}^r, \boldsymbol{S}_{22}^r, \boldsymbol{S}_{31}^r, \boldsymbol{S}_{32}^r, \boldsymbol{S}_{41}^r, \boldsymbol{S}_{42}^r \right\rangle = \left\langle \boldsymbol{S}^c \right\rangle + \left\langle \boldsymbol{S}_c^r \right\rangle = \left\langle \boldsymbol{S}^c \right\rangle + \left\{ \boldsymbol{S}_c^r \right\} + \left\langle \boldsymbol{S}_v^r \right\rangle \\ &= \underbrace{\varnothing}_{\left\langle \boldsymbol{S}^c \right\rangle} + \underbrace{\left\{ \boldsymbol{S}_{11}^r, \boldsymbol{S}_{12}^r, \boldsymbol{S}_{21}^r, \boldsymbol{S}_{22}^r, \boldsymbol{S}_{31}^r, \boldsymbol{S}_{32}^r, \right\}}_{\left\{ \boldsymbol{S}_c^r \right\}} + \underbrace{\left\{ \boldsymbol{S}_{41}^r, \boldsymbol{S}_{42}^r \right\}}_{\left\langle \boldsymbol{S}_v^r \right\rangle} \end{aligned} \tag{7.15}$$

With $v = \text{card}\left\langle \boldsymbol{S}_v^r \right\rangle = 2$, $d = 6 - \dim(\boldsymbol{S}^c) = 6 - 0 = 6$, $n = 6$, $g = 8$, the mobility of the axle is calculated as $m = 6(6\text{-}8\text{-}1) + 16 + 3 - 0 = 0$. Similar to the "2-1 or 1-2: parallel & unequal" cases, the only DOF possessed by the robot's body is the rotation about the axle and this case is mainly used as the transition phase in the robot's locomotion.

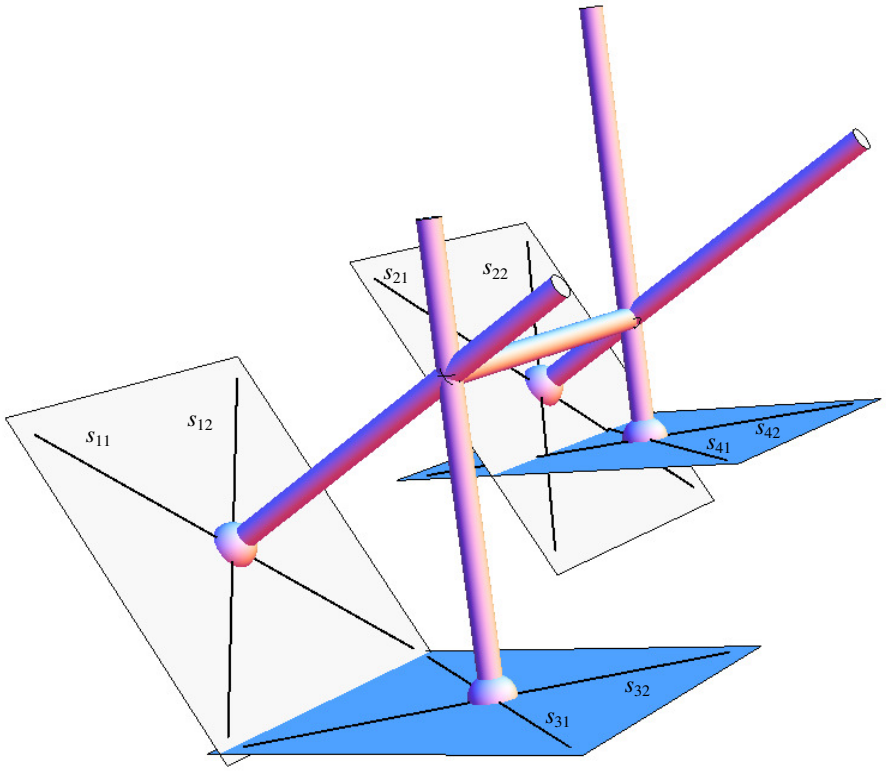

FIG.7.13 CONSTRAINT SCREW SYSTEM OF THE "2-2: PARALLEL & UNEQUAL" CASE

7.3. "1-1: skew" Contact Case

In this case, the two contacting spokes are skew to each other with the twist angle β_{tw} = 60º. The constraint system generated by the two SP limbs is shown in Fig.7.14. Since the four lines are linearly independent, the constraint system is decomposed as:

$$\begin{aligned}\left\langle \boldsymbol{S}^r \right\rangle &= \left\langle \boldsymbol{S}_{11}^r, \boldsymbol{S}_{12}^r, \boldsymbol{S}_{21}^r, \boldsymbol{S}_{22}^r \right\rangle = \left\langle \boldsymbol{S}^c \right\rangle + \left\langle \boldsymbol{S}_c^r \right\rangle = \left\langle \boldsymbol{S}^c \right\rangle + \left\{ \boldsymbol{S}_c^r \right\} + \left\langle \boldsymbol{S}_v^r \right\rangle \\ &= \underbrace{\varnothing}_{\left\langle \boldsymbol{S}^c \right\rangle} + \underbrace{\left\{ \boldsymbol{S}_{11}^r, \boldsymbol{S}_{12}^r, \boldsymbol{S}_{21}^r, \boldsymbol{S}_{22}^r \right\}}_{\left\{ \boldsymbol{S}_c^r \right\}} + \underbrace{\varnothing}_{\left\langle \boldsymbol{S}_v^r \right\rangle}\end{aligned} \tag{7.16}$$

With $v = \text{card}\left\langle \boldsymbol{S}_v^r \right\rangle = 0$, $d = 6 - \dim(\boldsymbol{S}^c) = 6 - 0 = 6$, $n = 4$, $g = 4$, the mobility of the axle is calculated as $m = 6(4\text{-}4\text{-}1) + 8 + 0 - 0 = 2$. The first DOF of the axle is apparently the rotation about the pivot line P_1P_2 on the ground. The second DOF is similar to the DOF of the "2-2: parallel & equal" case and it is also controlled by changing the lengths of the two contacting spokes d_1 and d_2. Assume the distance between contact points P_1 and P_2 is e, and the length of the axle is l_a. Inspecting Fig.7.14, the constraint equation of d_1 and d_2 can be determined as:

$$d_1^{\,2} + d_2^{\,2} - d_1 d_2 = e^2 - l_a^2 \tag{7.17}$$

which is very similar to Eq.(7.11). As illustrated in Fig.7.14, the second DOF allows the axle to move along a circular trajectory defined by β_{tw}, e and l_a. Different from the "2-2: parallel & equal" case, the virtual axis R_v of the circle can rotate about P_1P_2 on the ground as well because of the first DOF. Again, the robot's body in this contact case has the same DOF as the axle, with one rotation controlled by changing the lengths of the two contacting spokes constrained by Eq.(7.17), and the other rotation controlled by the phase angle of the two wheels.

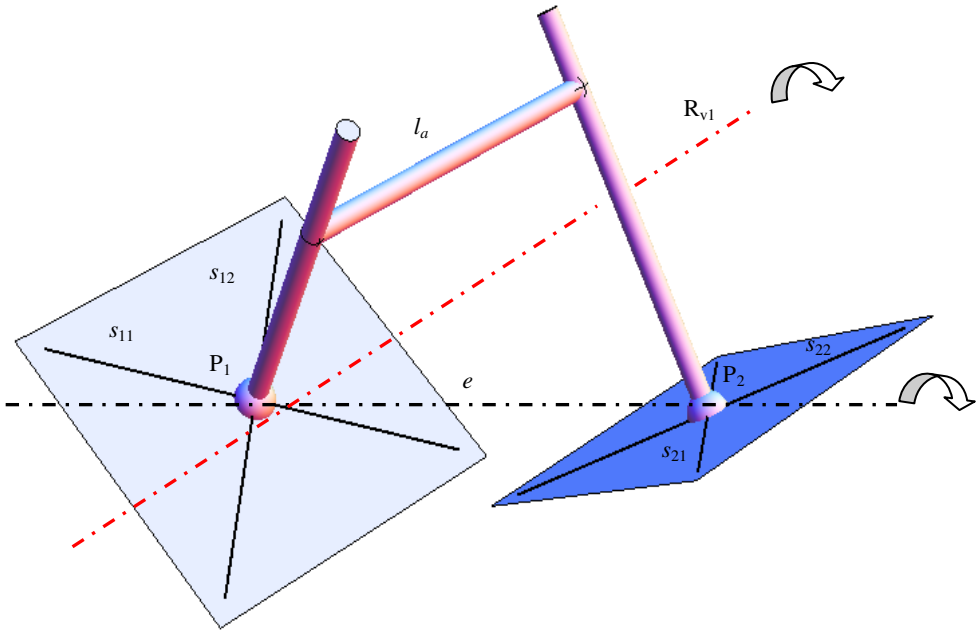

FIG.7.14 CONSTRAINT SCREW SYSTEM AND DOF OF THE "1-1: SKEW" CASE

7.4. Other Contact Cases

The "3-3: parallel & equal" contact case is illustrated in Fig.7.15. Inspecting the constraint screw system in this case, the line variety consisting of the twelve lines has an order of six. With $v = 6$, $d = 6 - \dim(\boldsymbol{S}^c) = 6 - 0 = 6$, $n = 8$, $g = 12$, the mobility of the axle is determined as $m = 6(8\text{-}12\text{-}1) + 24 + 6 - 0 = 0$, which indicates that the axle has zero DOF in this case and the only DOF of the body is the rotation about the axle.

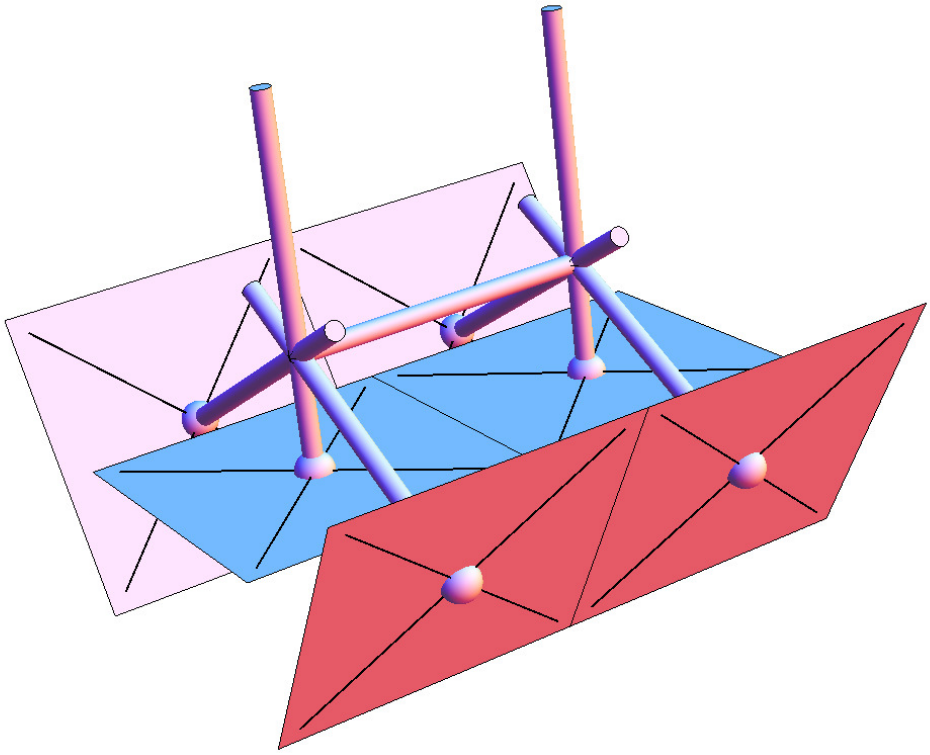

FIG.7.15 CONSTRAINT SCREW SYSTEM OF THE "3-3: PARALLEL & EQUAL" CASE

During actual operations, it is possible that the IMPASS robot assumes contact cases other than the ones demonstrated in Fig.7.3. Although those cases may not be directly involved in the robot's locomotion, with the methodology presented above, their mobilities can also be determined straightforwardly. Some examples are presented in the following section.

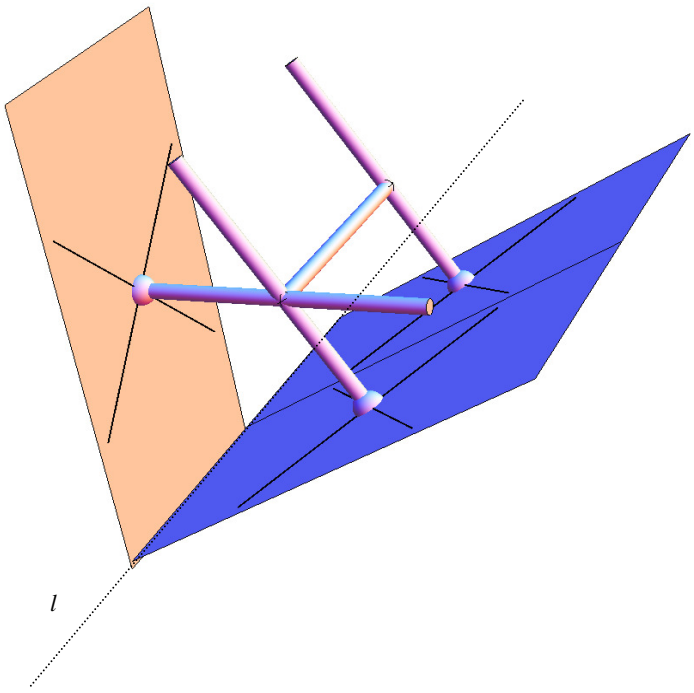

(a)

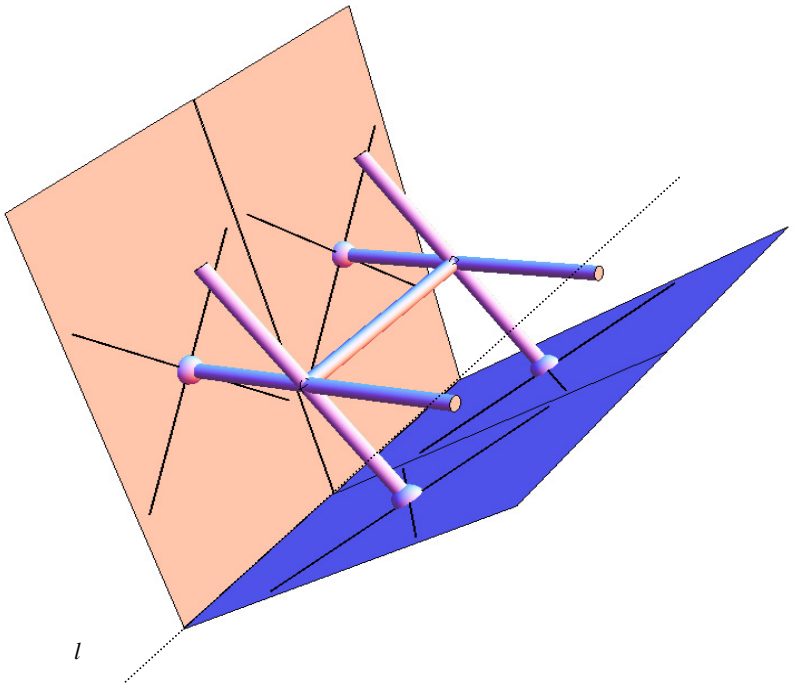

(b)

FIG.7.16 CONSTRAINT SCREW SYSTEM OF: (A) THE "1-2: PARALLEL & EQUAL" CASE; (B) THE "2-2: PARALLEL & EQUAL" CASE

Fig.7.16(a) and (b) demonstrate the "1-2: parallel & equal" and "2-2: parallel & equal" cases with the separation angle of 120º, rather than 60º. The case could happen if the two

middle contacting spokes in the "3-3: parallel & equal" case are stretched back. The decompositions of the constraint screw systems are the same as Eq.(7.9) and (7.10) since all lines intersect line *l*, which is the intersection of the two planes containing all planar pencils. The axle can move along a circular trajectory similar to that of the "2-1: parallel & equal" and "2-2: parallel & equal" cases which has the separation angle of 60º. However, the effective range of this DOF is relatively small compared with that in the cases with the separation angle of 60º, so it is not directly used in the robot's regular locomotion on the smooth ground.

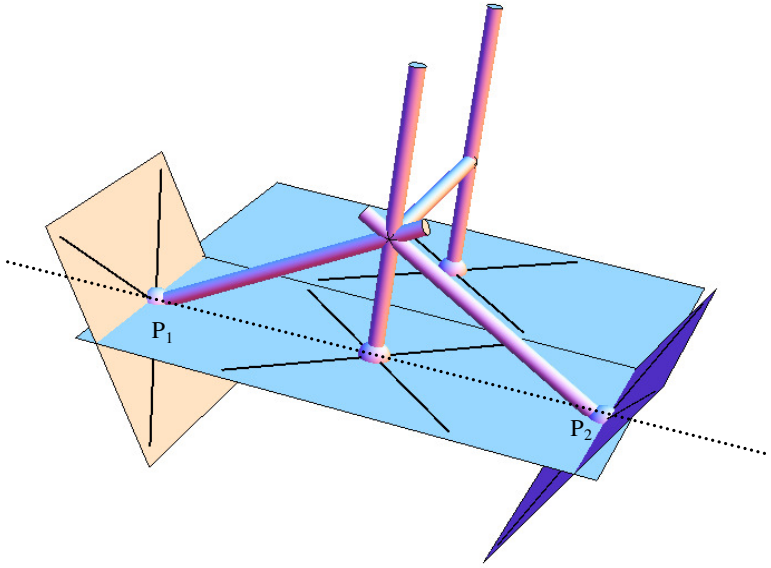

(a)

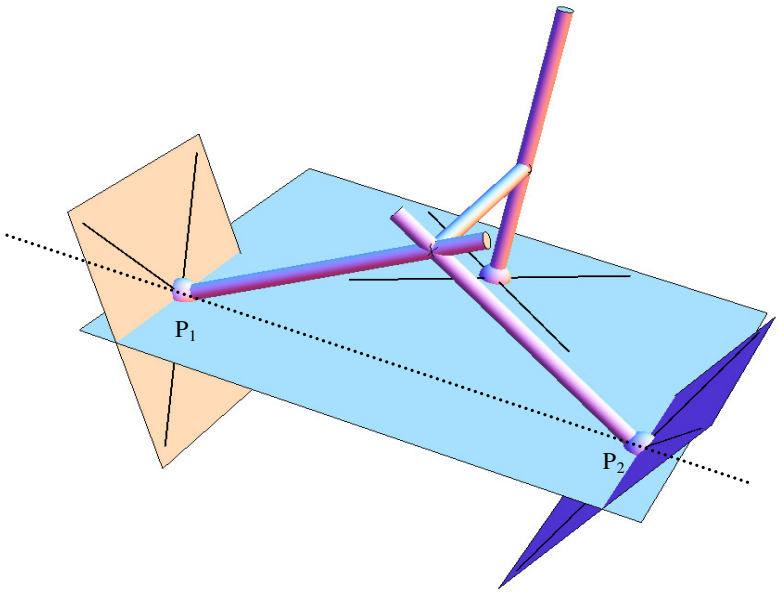

(b)

FIG.7.17 CONSTRAINT SCREW SYSTEM OF: (A) THE "1-3: PARALLEL & EQUAL" CASE; (B) THE "1-2: SKEW" CASE

Two contact cases with instantaneous DOF are shown in Fig.7.17(a) and (b), respectively. In the "1-3: parallel & equal" case, the single contacting spoke on the left is parallel and

equal to the middle contacting spoke on the right, thus generating two coplanar pencils. The line variety formed by the eight reciprocal screws is a special complex because they all intersect line P_1P_2 passing through the three contact points on the right. This instantaneous DOF is similar to that in the "1-1: parallel, equal" case. To constraint this infinitesimal motion for a stable structure, at least one spoke's length must be locked. If the middle contacting spoke retracts, a special "1-2: skew" case is achieved. The mobility of this case is the same as "1-3: parallel & equal" because all six lines intersect line P_1P_2 again as shown in Fig. 7.17(b).

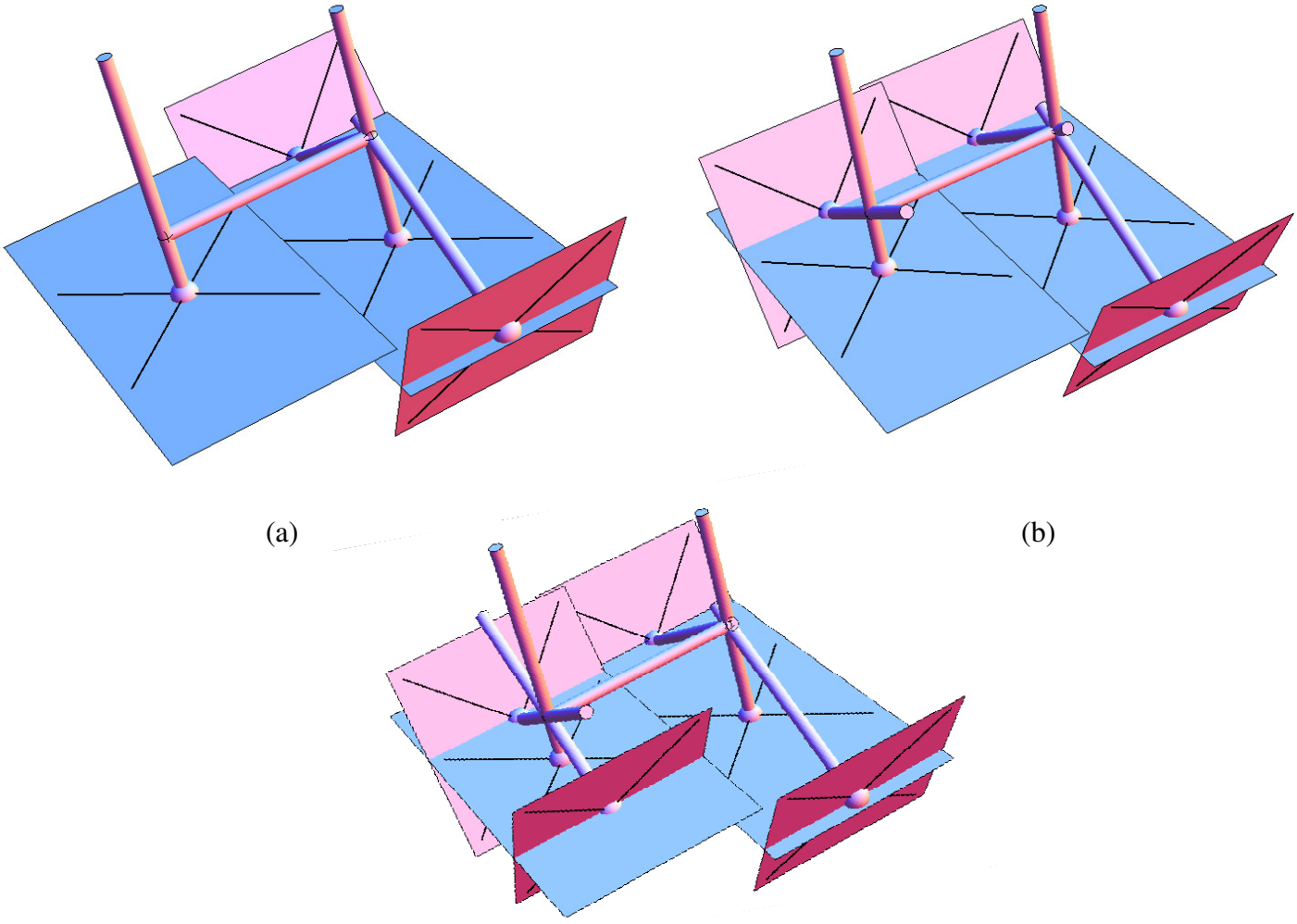

FIG.7.18 THREE EXAMPLES OF THE CONTACT CASES WITH THE AXLE'S DOF AS ZERO

Fig.7.18 demonstrates three types of contact cases with zero DOF. In these three cases, all parallel contacting spokes are not equal and no coplanar pencils exist. By inspection, the number of the redundant constraints v is identified as 2, 4, and 6 respectively. Therefore, the mobility of the axle m is calculated as 0 for all three cases and the only DOF possessed by the

body is the rotation about the axle. The stationary structures in these cases can be utilized in the robot's other operations where a stable platform is required.

As a summary of all the contact cases discussed above, the changing mobility in the IMPASS robot's variable topologies is analyzed using the *Modified Grübler-Kutzbach criterion* and *Grassmann Line Geometry*. The instantaneous DOF is identified if exists. Since the robot contacts the ground through discrete points only, the conclusions developed from the mobility analysis with respect to smooth ground can be easily expanded to investigate the DOF of the robot over uneven ground with various surfaces. An example of a special "2-2: parallel & unequal" case is presented in Fig. 7.19, with the four contact points non-coplanar. Apparently, the two reciprocal screws contributed by the fourth contact point P_4 do not affect the order of the total constraint system and are thus redundant. The mobility of the axle *m* is still calculated as 0, which is the same as the "2-2: parallel & unequal" case. Actually, most contact cases with non-coplanar contact points (at least four) are of zero DOF because the order of the constraint system is usually six.

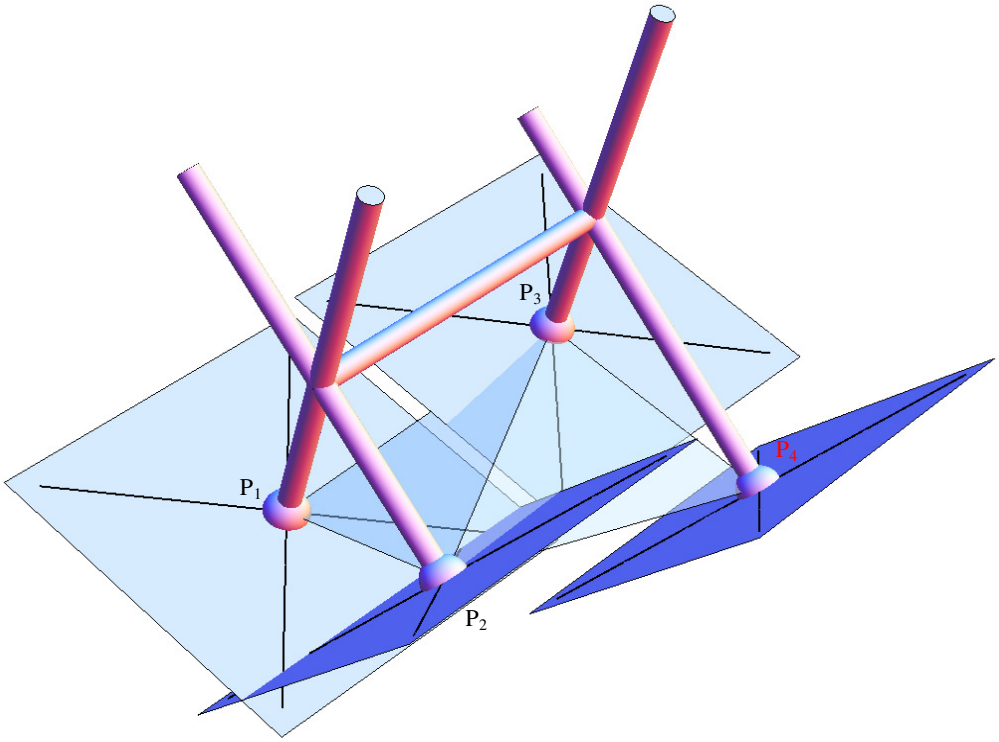

FIG.7.19 CONSTRAINT SCREW SYSTEM OF A SPECIAL "2-2: PARALLEL & UNEQUAL" CASE WITH FOUR NON-COPLANAR CONTACT POINTS

Chapter 8 Experimental Verification of the Characteristic Motions

In order to verify the topological transformations of the IMPASS robot in Fig.7.3 and the DOF in its various contact cases analyzed in Chapter 8, experimental testing on the prototype is performed and the observations are demonstrated in this section. The hub mechanism of the IMPASS consists of three interlocking layers allowing the spokes to pass next to each other without interference. The compliant carbon fiber spoke utilize a tensioned chain and sprocket drive as shown in Fig.8.1. The chain is driven with a larger central drive sprocket and is routed around two smaller idler sprockets. The combination of the black pulleys and the three-sprocket chain drive ensures that as the spokes flex the chain will not come off of the drive sprocket. Each hub of the IMPASS contains three separate sets of independent control hardware; one to control each spoke. Each spoke is driven by a Portescap 17N servo motor, and controlled by an AllMotion EZSV10 controller using an optical quadrature encoder, and two magnetic reed limit switches. Each spoke wheel is actuated by a Maxon RE30 servo motor through a worm gearbox, and it is independently controlled using an AllMotion EZSV23, with a Maxon HEDL 5540 optical quadrature encoder and a linear cam limit switch.

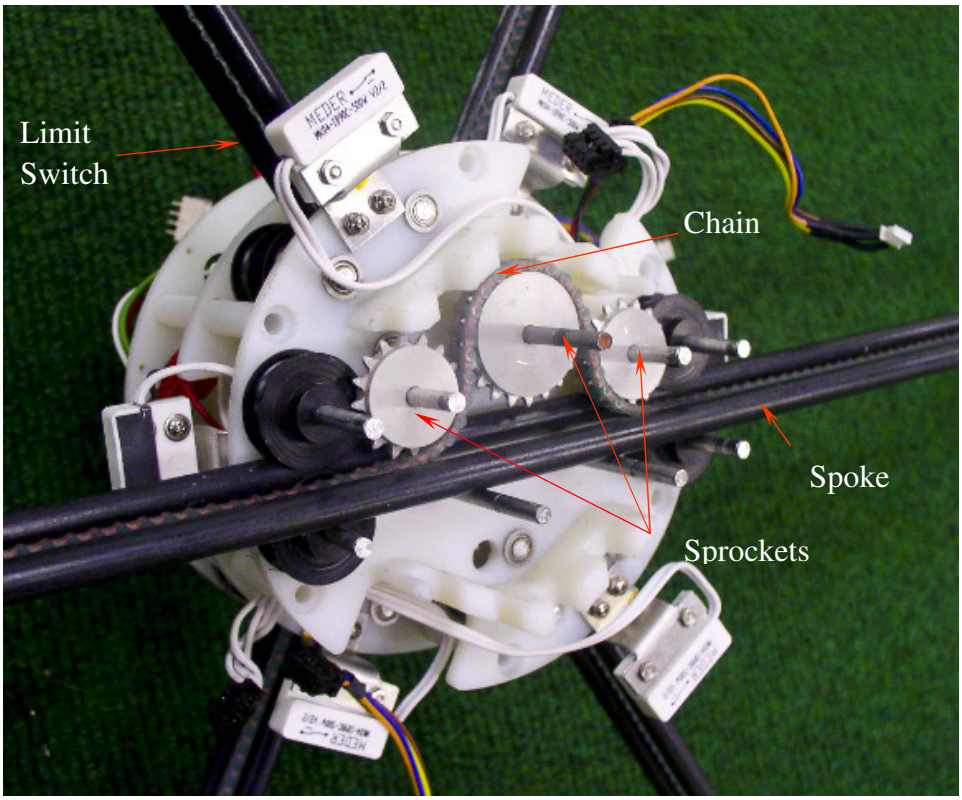

FIG.8.1 THE INTERNAL MECHANISM OF THE HUB

Currently, the IMPASS robot is controlled by LabVIEW running on an external laptop through an RS-485 serial connection, with the power provided by an external power supply. In the future development, a PC-104 computer will be installed inside the robot and take over all the control. The power supply will be replaced with lithium-ion batteries.

8.1. Straight-line Walking

The first mode of straight-line walking has been utilized by the prototype for most of its forward motions. It has been proven to be a stable and capable walking gait, even being able to walk over moderately rough terrains without any active adaptation. Utilizing the two DOF in the "1-1: parallel & equal" case, the body of the IMPASS can not only move on a level trajectory as shown in Fig.8.2 , but also be able to climb a high obstacle as shown in Fig.8.3.

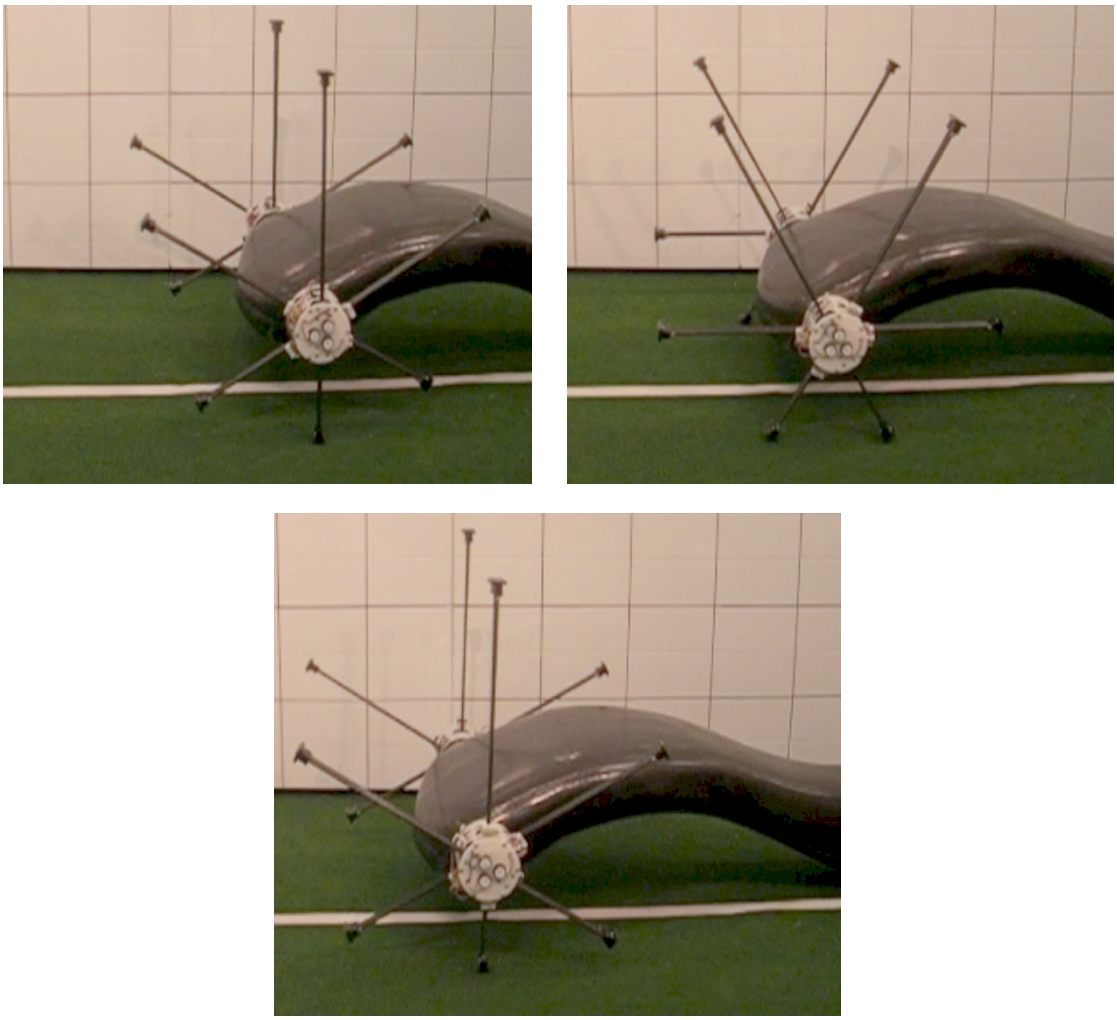

FIG.8.2 STRAIGHT-LINE WALKING USING "1-1: PARALLEL & EQUAL" AND "2-2: PARALLEL & EQUAL"

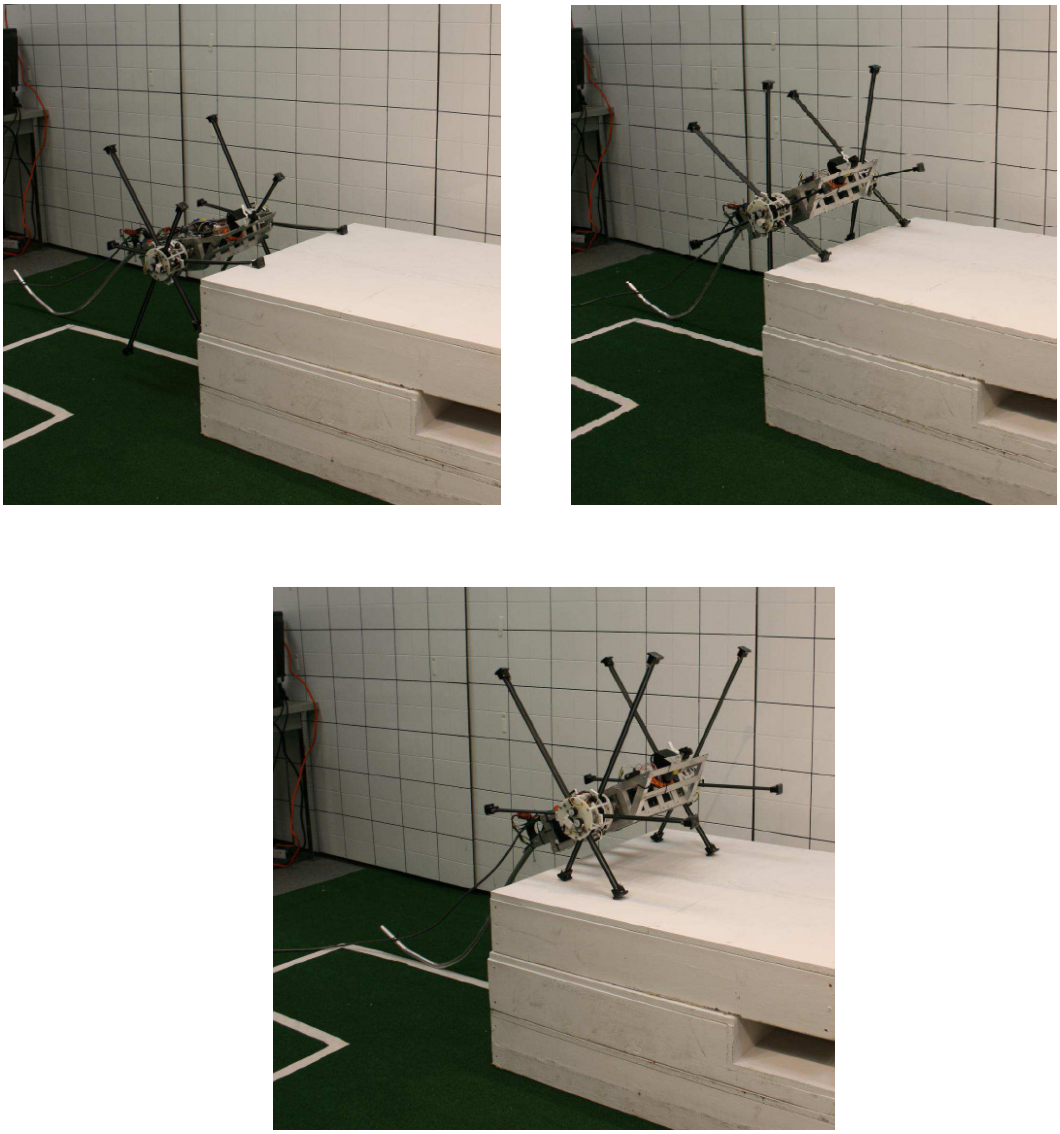

FIG.8.3 IMPASS' CLIMBING AN 18-INCH OBSTACLE USING "1-1: PARALLEL & EQUAL" AND "2-2: PARALLEL & EQUAL"

The second mode of straight-line walking has been verified on the robot as well, as shown in Fig.8.4. This walking gait is more stable than the first walking gait because it has five contact points (including the one from the tail) with the ground. The DOF in the "2-2: parallel & equal" case demonstrated in Fig.8.8 allows for the topological transformation to the "3-3: parallel & equal" case.

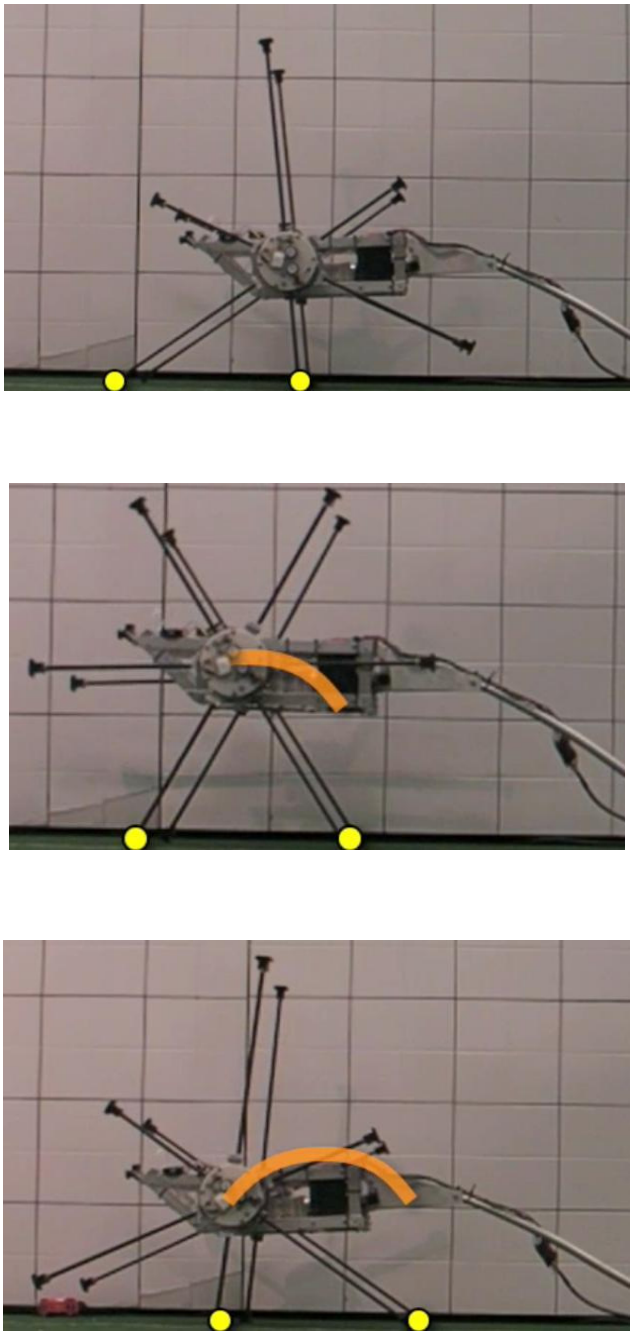

FIG.8.4 STRAIGHT-LINE WALKING USING "2-2: PARALLEL & EQUAL" AND "3-3: PARALLEL & EQUAL"

8.2. Steady State Turning

A discrete turning of the IMPASS robot is accomplished through the "1-1: parallel & unequal" cases and with the "2-2: parallel & unequal" cases as the transitions. This gait sets a smaller effective radius for the inside spoke wheel, and a larger effective radius for the outside spoke wheel, as shown in Fig.8.5.

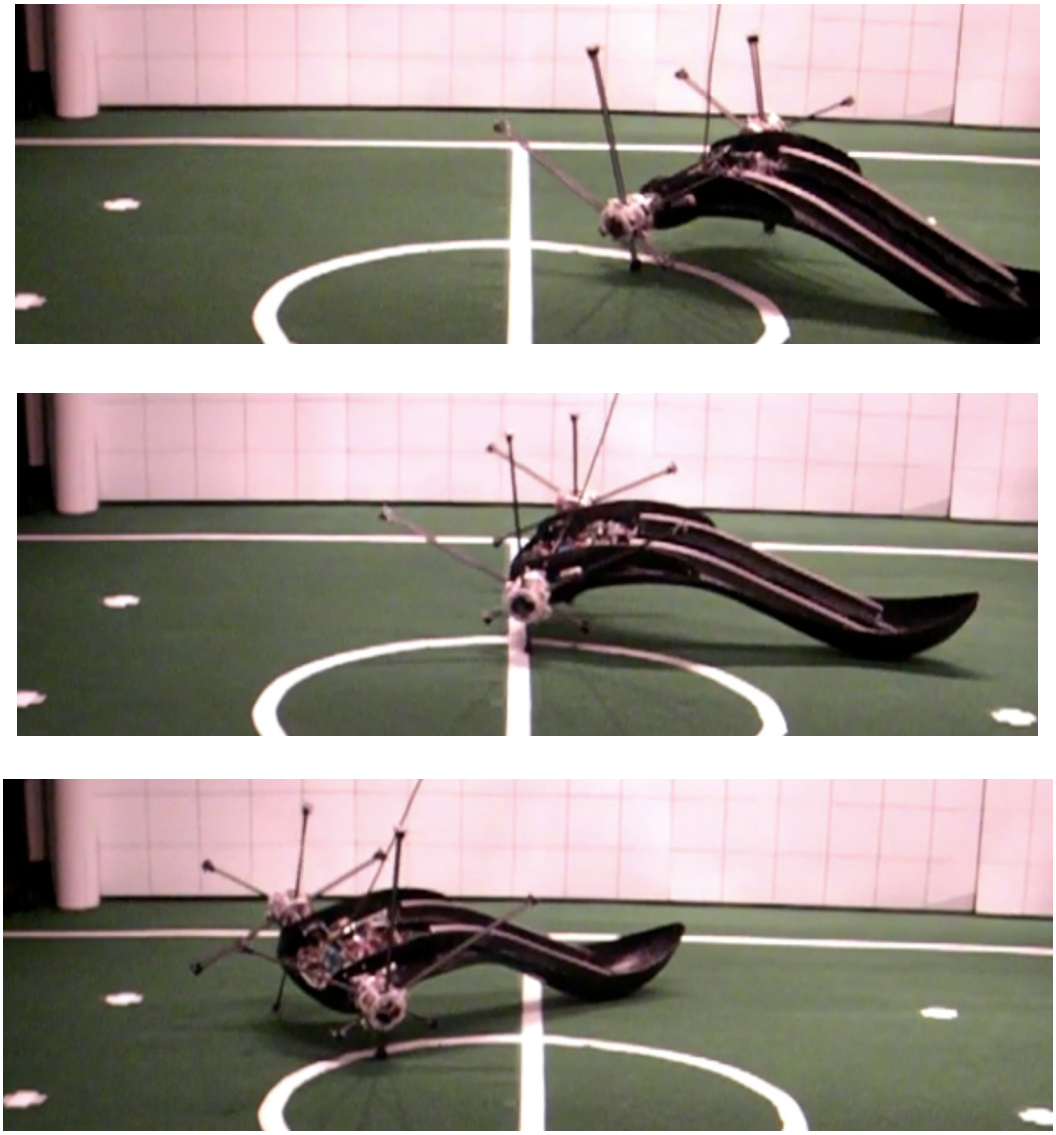

FIG.8.5 STEADY STATE TURNING

8.3. Turning Gait Transition

The turning gait transition is used to switch between straight-line walking and a steady state turning, or between two distinct turnings. As an example, the transition from straight-line walking to a steady state turning is demonstrated in Fig.8.6. First, as the wheels rotate, the two parallel and equal contacting spokes are replaced with two skew contacting spokes, thus causing the pivot line on the ground to be skew to the axle as well. After the topological transformation, the two DOF in the "1-1: skew" case, as illustrated in Fig.8.6, are

utilized to change the heading direction of the body so that it is able to switch to the steady state turning as desired.

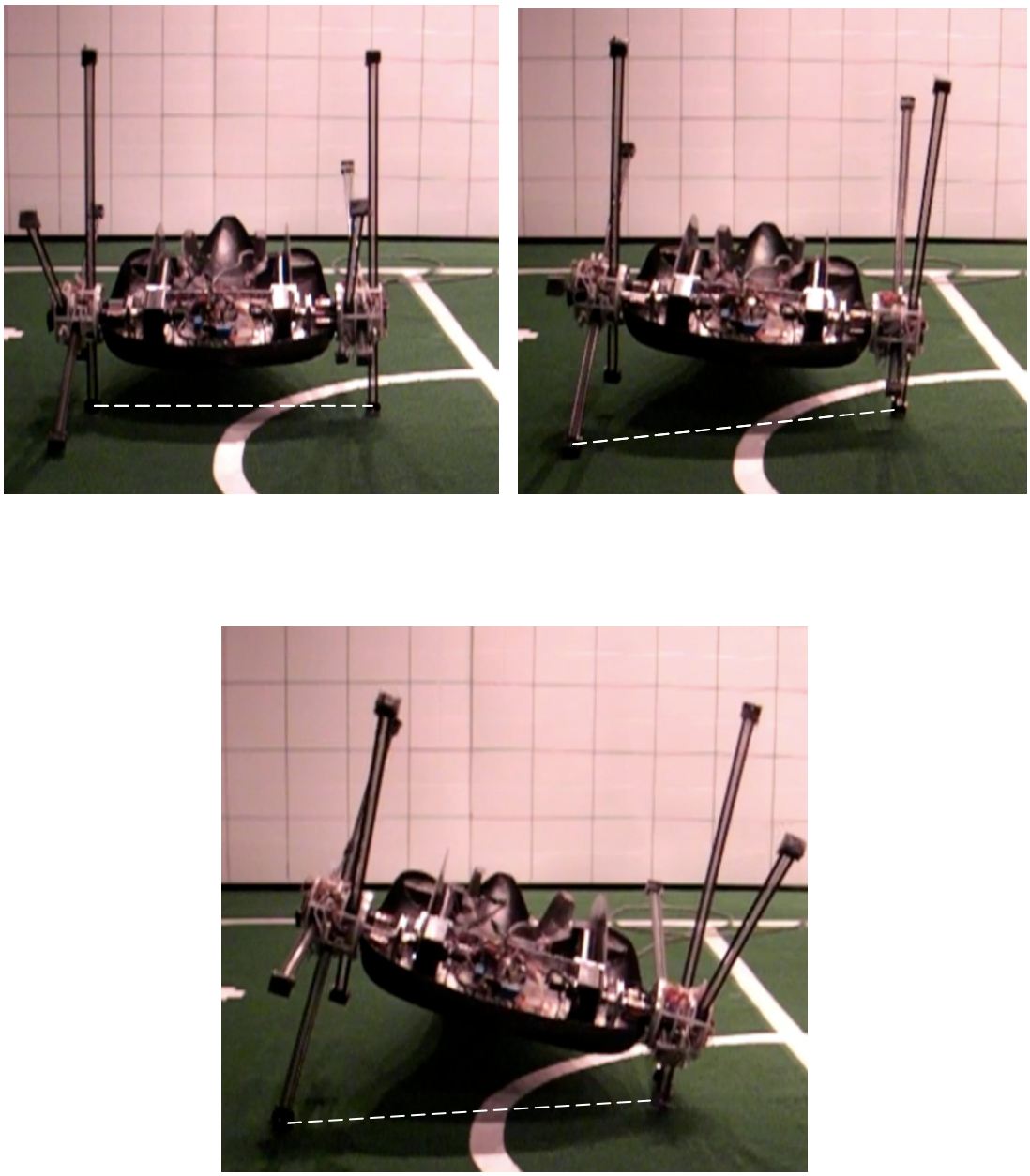

FIG.8.6 TURNING GAIT TRANSITION

8.4. Geometric Characteristics of Steady State Turning and Turning Gait Transition

The steady state turning is a discrete motion that changes the heading direction of the spoke wheel robot step by step. This type of steering is none other than the switching of the contact mode from “1-1, parallel, unequal” to “2-2, parallel, unequal” back and forth. In this turning, all the left and right contact spokes keep both constant difference and proportion coefficient. As shown in Fig.8.7(a), in each “2-2, parallel, unequal” mode, the line along the axle of the robot and the two pivoting lines on the ground all intersect at one point. Therefore, in steady state turning, all the contact points on the ground lie on concentric circles with the intersecting point as the center, which is indicated in Fig.8.7(b).

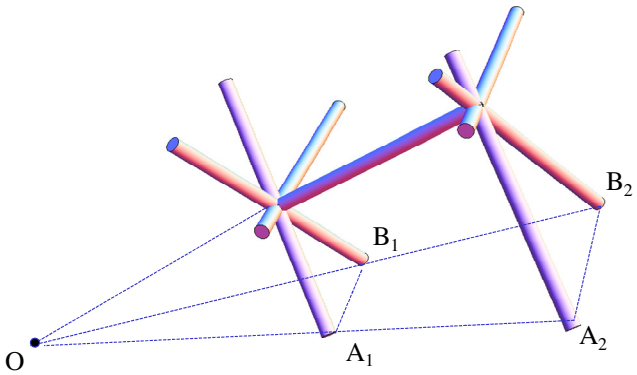

(a) Three lines intersect at the same point in “2-2, parallel unequal”

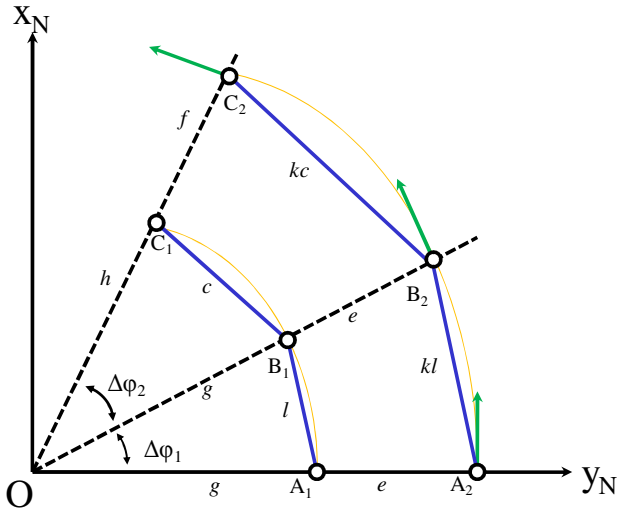

(b) Top view of steady state turning

FIG.8.7 DISCRETE MOTION OF STEADY STATE TURNING

In Fig.8.7(b), A_1, A_2, B_1, B_2, C_1, C_2… are the contact points on the ground, with the origin of planar reference frame $\{x_N, y_N\}$ O set at the center of circles. Lower case letters are used to denote the lengths of the line segments. Without losing generality, assume all left spokes in this motion are of the same length l and all right spokes the same length kl, where k is a constant proportion coefficient greater than 1. Then, apparently, the robot will make a left turn as indicated in Fig.8.7(b). The distance of A_1A_2, i.e. e, and the turning radius g is determined as:

$$\begin{aligned} e &= \sqrt{(kl-l)^2 + w^2} \\ g &= \frac{e}{k-1} \end{aligned} \tag{8.1}$$

where w is the length of the axle. Using the directions perpendicular to pivoting lines as the reference of the robot's heading (indicated with the arrows in Fig.8.7(b)), then the change of the heading angle is derived as:

$$\Delta\varphi = \cos^{-1}\left(\frac{2g^2 - l^2}{2g^2}\right) \tag{8.2}$$

The case discussed above can be extended to a more general scenario with the length of the next left contact spoke as jl and next right spoke kjl, where j is a positive proportion coefficient and cannot exceed the physical limit of the spoke length. In such a case, Eq.(8.1) and (8.2) are modified as:

$$\begin{aligned} f &= \sqrt{(kjl - jl)^2 + w^2} \\ h &= \frac{f}{k-1} \end{aligned} \tag{8.3}$$

and

$$\begin{aligned} e &= \sqrt{(kl-l)^2 + w^2} \\ c &= \sqrt{(jl)^2 + l^2 - jl^2} \\ \Delta\varphi &= \cos^{-1}\left(\frac{e^2 + f^2 - (kc-c)^2}{2ef}\right) \end{aligned} \tag{8.4}$$

Examining Eq.(8.1) to (8.4), one can find that, if j, the ratio of the next contact spoke to the current contact spoke is not equal to 1, then the turning radius and $\Delta\varphi$ will be changed. Also, in the "1-1, parallel, unequal" modes, the proportion coefficient k of the right spoke to the left can be changed by stretching the spokes in or out simultaneously, thus shifting the center of the circle to another location along the pivoting line.

Utilizing such characteristics of steady state turning, the mobile spoke wheel robot can travel discretely from one circle to another, with the circle centers always at the side of the shorter spokes. However, only steady state turning is not sufficient to track any paths on the ground. Therefore, a turning gait transition is required.

Turning gait transition is a series of mode transformations from "1-1, parallel, unequal/equal", through "2-1, parallel, unequal/equal", to "1-1, skew", as shown in Fig.8.6. Utilizing the two DOF in "1-1, skew", the robot can transfer discretely from its current path

to a straight-line path or to another circular path with the center located at the other side of the robot, thus compensating for the deficiency of steady state turning.

Combining steady state turning, turning gait transition and straight-line walking, the general steering of the spoke wheel robot on even ground can be developed. Again, the planning issue will be addressed in future research.

8.5. Rotation of the Body in the "3-3" Contact Case

As discussed in Sec.3.2.3, the axle of the IMPASS robot has zero DOF under this topology. However, the body of the robot does possess one DOF which is the rotation about the axle itself. Because all six spokes are in contact with the ground, the support region on the ground is stationary enough that the actuation of the phase angle of the two wheels is able to lift the tail above the ground. This motion is demonstrated in Fig.8.8, which confirms the predicted DOF in the mobility analysis.

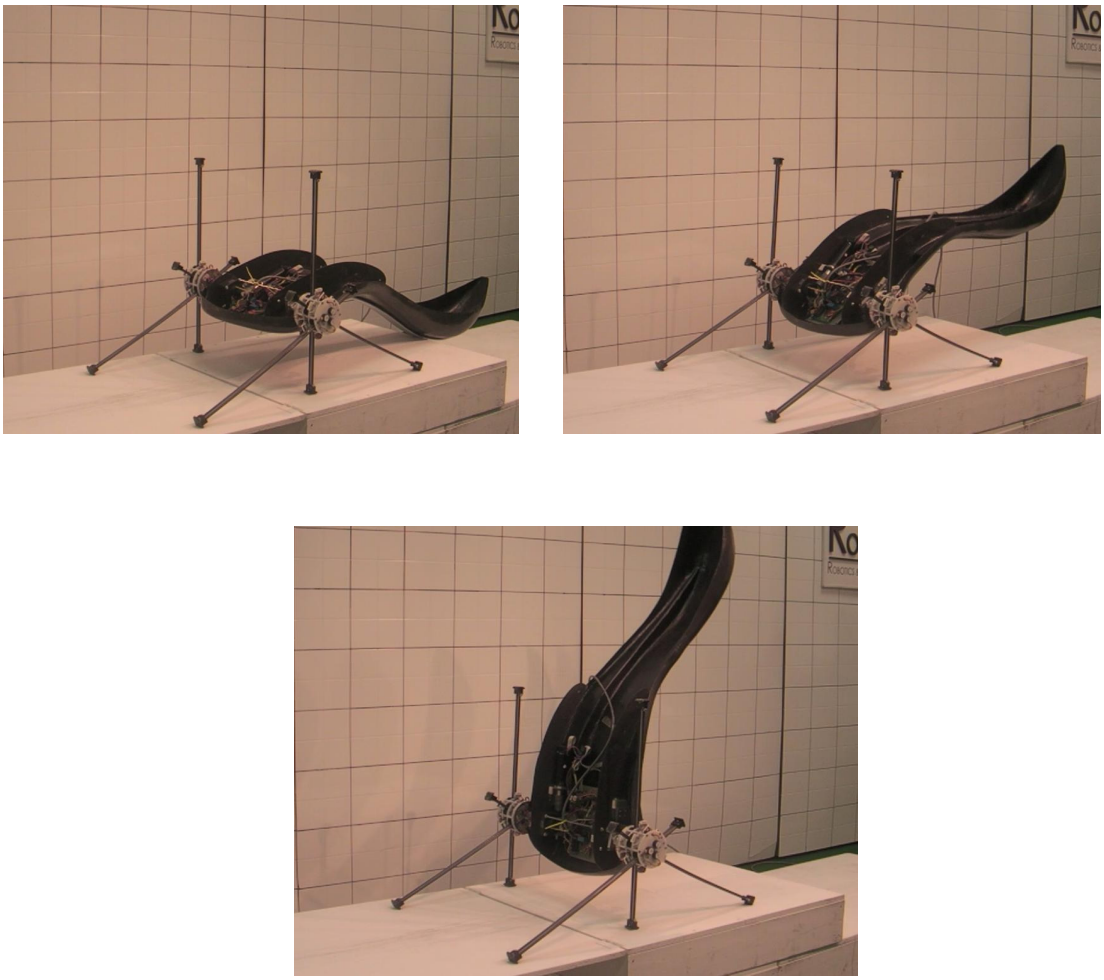

FIG.8.8 LIFTING OF THE TAIL IN THE "3-3: PARALLEL & EQUAL" CONTACT CASE

Chapter 9 Forward and Inverse Kinematics Analysis

The forward and inverse kinematics for the IMPASS robot is an investigation on the geometric relationships between the robot body's position and orientation and its joint displacements such as the lengths of the contacting spokes and the phase angle of the two wheels. The contribution of the forward kinematics is mainly in the monitoring of the robot's motion with joint sensors, while the contribution of the inverse kinematics lies mainly in the control of the body under each contact cases.

The DOF possessed in the various contact cases of the robot have been sufficiently investigated in Chapter 8. The locomotion scheme of the IMPASS robot and the mobility analysis on the contact cases in Fig.7.3 indicate that the "1-1: parallel" and "1-1: skew" cases have 2 DOF and are the most frequently used in its ground motion. Therefore, the forward and inverse kinematics of the two "1-1" cases is the focus of this chapter. These two cases are demonstrated in Fig.9.1 and 9.2 below. The joint variables that can be specified are the angular displacement of the two spoke wheels and the linear displacement of the contacting spokes. Correspondingly, two variables out of the body's position and orientation can also be specified arbitrarily within its workspace.

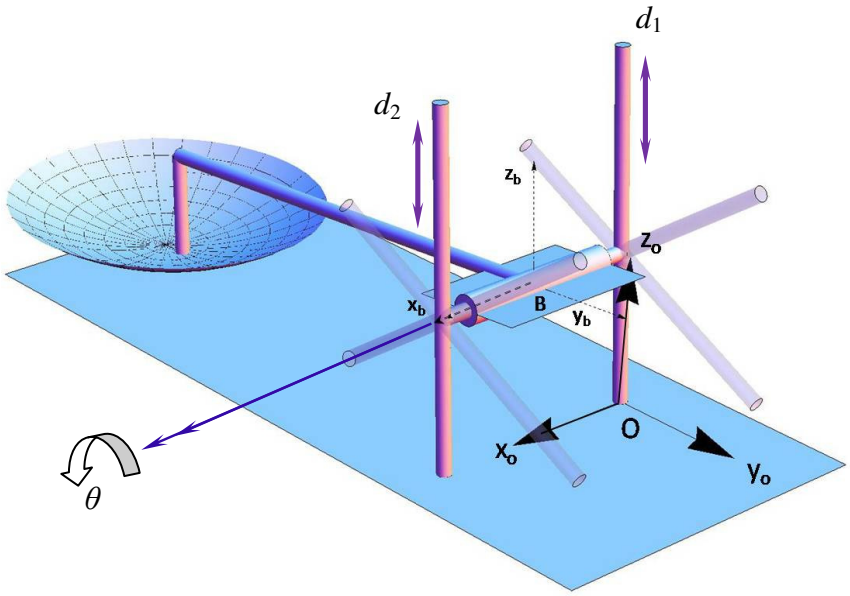

FIG.9.1 "1-1: PARALLEL" CONTACT CASE

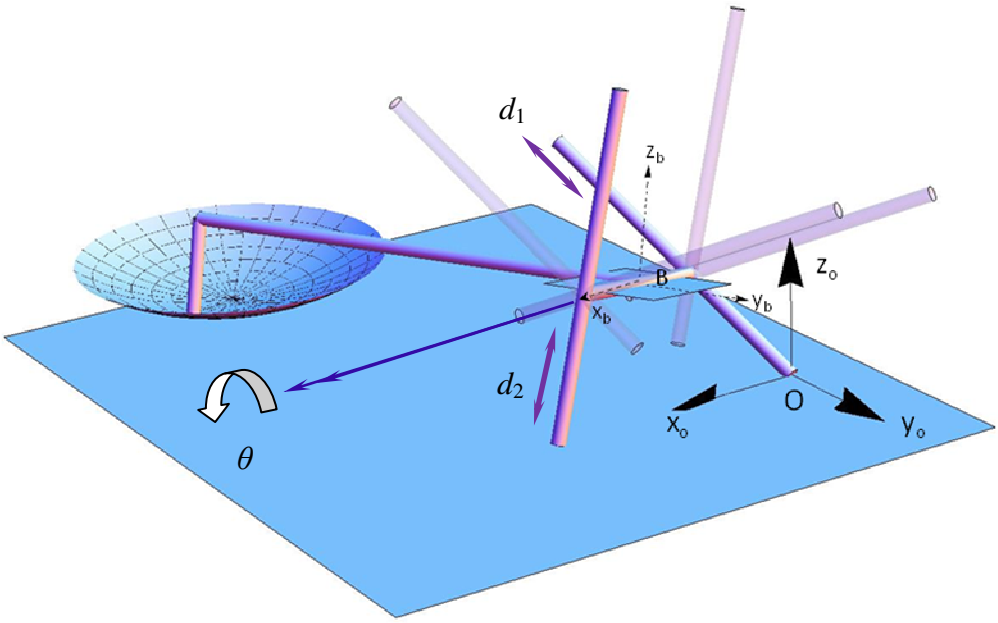

FIG.9.2 "1-1: SKEW" CONTACT CASE

9.1. Formulation of the Forward Kinematics

Given the presumption that three non-collinear contact points exist, the forward kinematics of the IMPASS robot with two spokes (either parallel or skew) and the tail in contact with the ground can be formulated with the follows procedures.

First, as shown in Fig.9.1 and 9.2, two coordinate systems are established with $\{x_o, y_o, z_o\}$ fixed on the ground and $\{x_b, y_b, z_b\}$ attached to IMPASS' body. The origin O of $\{x_o, y_o, z_o\}$ is chosen at the contact point between the left spoke and the ground, with x_o axis pointing to the right contact point and z_o axis normal to the ground. The origin B of $\{x_b, y_b, z_b\}$ is set at the midpoint of the axle, with x_b axis pointing to the right wheel center, also the direction of the spoke wheels' rotation, and y_b axis lying in the rectangle plane and pointing to the front of the body.

Secondly, assume the body coordinate system $\{x_b, y_b, z_b\}$ is positioned at the global origin with zero orientation, then with given joint displacements, the position vectors of the contact points of the two spokes ($\mathbf{P}_1$ and $\mathbf{P}_2$) with respect to the body frame can be determined using homogenous coordinates and transformation matrices as follows:

$$\begin{bmatrix} \mathbf{P}_1 \\ 1 \end{bmatrix} = R_x(\theta) \begin{bmatrix} \mathbf{p}_1 \\ 1 \end{bmatrix} \tag{9.1}$$

and

$$\begin{bmatrix} \mathbf{P}_2 \\ 1 \end{bmatrix} = R_x(\theta) \begin{bmatrix} \mathbf{p}_2 \\ 1 \end{bmatrix} \tag{9.2}$$

where

$$R_x(\theta)=\begin{bmatrix}1 & 0 & 0 & 0\\ 0 & \cos\theta & \sin\theta & 0\\ 0 & -\sin\theta & \cos\theta & 0\\ 0 & 0 & 0 & 1\end{bmatrix} \qquad (9.3)$$

$$\mathbf{p}_1=\begin{bmatrix}l/2 & 0 & -d_1\end{bmatrix}^{\mathrm{T}}$$
$$\mathbf{p}_2=\begin{bmatrix}-l/2 & 0 & -d_2\end{bmatrix}^{\mathrm{T}}$$

In Eqs.(9.1-3), l is the length of the axle; θ is the angular displacement of the two spoke wheels; d_1 and d_2 are the linear displacements of the two contacting spokes respectively, measured from the centers of the wheels to the contact points. Since the contacting spokes of the kinematic model in Fig.9.1 are parallel, d_1 and d_2 must obey the following constraint:

$$d_1-d_2=\Delta d \qquad (9.4)$$

where Δd is a constant. This constraint is to ensure that the distance between the two spoke contact points is constant in its current topology, such that slip or bounce does not occur at the spoke tips. Note that, Δd is zero for the "1-1: parallel & equal" contact case.

If the contacting spokes are two skew spokes set 60 degrees apart rather than parallel, then Eq.(9.2) just needs to be modified as:

$$\begin{bmatrix}\mathbf{P}_2\\ 1\end{bmatrix}=R_x(\theta+\pi/3)\begin{bmatrix}\mathbf{p}_2\\ 1\end{bmatrix} \qquad (9.2)^*$$

and d_1, d_2 should follow the quadratic constraint instead as:

$$d_1^2-d_1d_2+d_2^2=e^2-l_a^2 \qquad (9.4)^*$$

where e is the distance between the two contact points, l_a is again the length of the axle and both of them are constants. The detailed derivation of Eq.(9.4)* and discussions on the skew contact case can be found in Chapter 8.

The third contact point P_3 is due to the tail's passive touching with the smooth ground. Since the lower portion of the tail is part of a spherical surface, the contact point is actually the tangential point between the spherical surface and the ground plane. To elaborate this, assume the shell of the tail and the ground are both rigid, then the two rigid bodies contacting at a point form a *surface contact pair*, which was introduced in Ref.[20]. The surface contact pair is illustrated in Fig.9.3 as follows. It is a higher pair with five DOF.

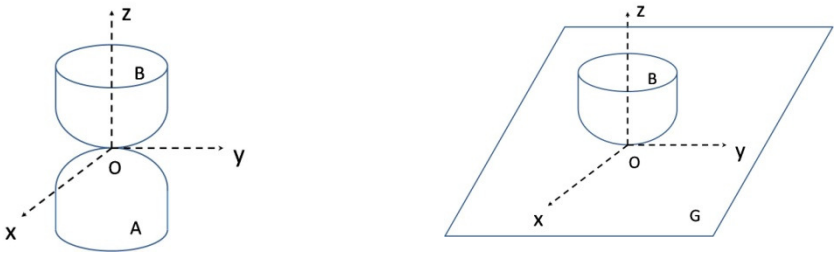

(a) (b)

FIG.9.3 SURFACE CONTACT PAIR

As shown in Fig.9.3(a), rigid body B contacts rigid body A at point O, where the two contacting surfaces are free to roll and slide with respect to one another as long as the contact point is maintained. Replacing body A with plane G and assuming G is stationary, the case in Fig.9.3(b) becomes another surface contact pair in which body B can slide along plane G and rotate in three directions about point O. Therefore, the contacting case of the tail and the ground in Fig.9.1 and 9.2 can be modeled as the case in Fig.9.3(b) without losing particularity. The contact point P_3 now becomes the tangential point between the convex surface of the tail and the ground plane.

With $\mathbf{P}_1$ and $\mathbf{P}_2$ calculated from Eq.(9.1-9.3), the position vector of P_3 with respect to the body coordinates $\{x_b, y_b, z_b\}$ can now be determined by finding the tangential point between the convex surface of the tail and the plane that contains points P_1 and P_2. Assuming the equation of the convex surface in the body coordinate system is $F(x, y, z) = 0$, then the equations to obtain $\mathbf{P}_3$ can be formulated as follows:

$$\begin{cases} F(P_{3x}, P_{3y}, P_{3z}) = 0 & (9.5.1) \\ F_x(P_{3x}, P_{3y}, P_{3z})(P_{1x} - P_{3x}) + F_y(P_{3x}, P_{3y}, P_{3z})(P_{1y} - P_{3y}) & (9.5.2) \\ \quad + F_z(P_{3x}, P_{3y}, P_{3z})(P_{1z} - P_{3z}) = 0 & \\ F_x(P_{3x}, P_{3y}, P_{3z})(P_{2x} - P_{3x}) + F_y(P_{3x}, P_{3y}, P_{3z})(P_{2y} - P_{3y}) & (9.5.3) \\ \quad + F_z(P_{3x}, P_{3y}, P_{3z})(P_{2z} - P_{3z}) = 0 & \end{cases}$$

where P_{ix}, P_{iy}, P_{iz} are the three components of $\mathbf{P}_i$, with $i = 1,2,3$ and $\mathbf{P}_i = [P_{ix}, P_{iy}, P_{iz}]^T$. F_x, F_y and F_z in Eq.(9.5.2) and Eq.(9.5.3) are the partial derivatives of $F(x, y, z)$ with respect to x, y, and z respectively. Eq.(9.5.1-9.5.3) all have definite geometric meanings. Eq.(9.5.1) makes sure that P_3 is on the surface, while Eq.(9.5.2) and Eq.(9.5.3) indicate that the tangential plane at P_3 also passes through P_1 and P_2. With $\mathbf{P}_1$ and $\mathbf{P}_2$ known from Eq.(9.1-3), Eq.(9.5.1-9.5.3) now become an equation system with only three unknowns P_{3x}, P_{3y}, P_{3z}, thus $\mathbf{P}_3$ is solvable.

Note that, the current IMPASS prototype has a partial spherical surface at its tail. Assume the center of the sphere is located at $[C_a, C_b, C_c]$ in the body coordinate system and the radius is R, then Eq.(9.5.1-9.5.3) can be further developed as:

$$\begin{cases} (P_{3x}-C_a)^2+(P_{3y}-C_b)^2+(P_{3z}-C_c)^2=R^2 \\ (P_{3x}-C_a)(P_{1x}-P_{3x})+(P_{3y}-C_b)(P_{1y}-P_{3y})+(P_{3z}-C_c)(P_{1z}-P_{3z})=0 \\ (P_{3x}-C_a)(P_{2x}-P_{3x})+(P_{3y}-C_b)(P_{2y}-P_{3y})+(P_{3z}-C_c)(P_{2z}-P_{3z})=0 \end{cases} \quad (9.5)^*$$

However, $F(x, y, z) = 0$ can also be designed as other types convex surfaces such as hyperboloid of one sheet, paraboloid, etc. As long as the contact point is the tangential point between the surface and the ground plane, Eq.(9.5.1-9.5.3) will be valid.

Finally, with $\mathbf{P}_1$, $\mathbf{P}_2$ and $\mathbf{P}_3$ obtained, the configuration of the ground plane relative to the body coordinate system is determined definitely. The three orthogonal unit vectors describing the orientation of the ground can be found as:

$$\begin{aligned} \mathbf{x}'_o &= (\mathbf{P}_1-\mathbf{P}_2)/\|\mathbf{P}_1-\mathbf{P}_2\| \\ \mathbf{z}'_o &= \mathbf{x}'_o\times(\mathbf{P}_2-\mathbf{P}_3)/\|\mathbf{x}'_o\times(\mathbf{P}_2-\mathbf{P}_3)\| \\ \mathbf{y}'_o &= \mathbf{z}'_o\times\mathbf{x}'_o \end{aligned} \quad (9.6)$$

The ground coordinate system $\{x_o, y_o, z_o\}$ has its origin at point P_2, so the homogeneous transformation matrix from the ground frame to the body frame is established as:

$$\mathbf{H}_B^O=\begin{bmatrix} \mathbf{x}'_o & \mathbf{y}'_o & \mathbf{z}'_o & \mathbf{P}_2 \\ 0 & 0 & 0 & 1 \end{bmatrix} \quad (9.7)$$

By taking the inverse of the matrix $\mathbf{H}_B^O$, the configuration of the body attached frame $\{x_b, y_b, z_b\}$ with respect to the ground fixed frame $\{x_o, y_o, z_o\}$ is obtained as:

$$\begin{aligned} \mathbf{H}_O^B=\left(\mathbf{H}_B^O\right)^{-1} &= \begin{bmatrix} [\mathbf{x}'_o & \mathbf{y}'_o & \mathbf{z}'_o]^T & -[\mathbf{x}'_o & \mathbf{y}'_o & \mathbf{z}'_o]^T\mathbf{P}_2 \\ \mathbf{0} & & & 1 \end{bmatrix} \\ &= \begin{bmatrix} \mathbf{x}_b & \mathbf{y}_b & \mathbf{z}_b & \mathbf{B} \\ 0 & 0 & 0 & 1 \end{bmatrix} \end{aligned} \quad (9.8)$$

Thus, the forward kinematics of the IMPASS robot with two spokes and the tail in contact with the ground is formulated completely. With given joint displacements, i.e. θ, d_1 and d_2, the position and orientation of IMPASS' body with respect to the ground are obtained and represented with the homogeneous transformation matrix $\mathbf{H}_O^B$. Theoretically, it is possible that the forward kinematics has multiple solutions. Inspecting the kinematic model of IMPASS in Fig.9.1, the multiple solutions are due to the existence of multiple tangential points of the surface and the ground plane, i.e. the whole spherical surface at the tail can have two tangential points with the plane that passes line P_1P_2, resulting in two forward kinematics

solutions. However, the additional solution can be easily eliminated because only the lower portion of the spherical surface is actual and the tangential point at the upper portion is imaginary in the actual model and unique solution will be derived.

The procedures discussed above not only solve the forward kinematics in the current topology of the robot with two spokes and the tail contacting the ground, but also can be expanded to include the configuration transformations of the robot when taking multiple steps. Technically, touch sensors can be mounted at the tips of all the spokes. Within the current topology of the robot, if an additional spoke touches the ground and the topology is about to change, then the new contact point is detected by the touch sensor, its position with respect to the body frame is calculated, and a new ground coordinate system with known configuration is established for the next topology. Repeating Eq.(1-8), the information about the body's new configuration can be updated based on new joint displacements.

9.2. Inverse Kinematics Based on the Forward Kinematics Model

Inverse kinematics is the reverse development to forward kinematics in which the joint displacements are calculated based on the specified position and orientation of the robot's body. As discussed in Section 9.3, the body's configuration is contained in matrix $\mathbf{H}_O^B$ with $\mathbf{x}_b$, $\mathbf{y}_b$ and $\mathbf{z}_b$ representing the orientation and $\mathbf{B}$ the position. The complete form of $\mathbf{H}_O^B$ is presented as follows:

$$\mathbf{H}_O^B = \begin{bmatrix} \mathbf{x}_b & \mathbf{y}_b & \mathbf{z}_b & \mathbf{B} \\ 0 & 0 & 0 & 1 \end{bmatrix} = \begin{bmatrix} x_{bx} & y_{bx} & z_{bx} & B_x \\ x_{by} & y_{by} & z_{by} & B_y \\ x_{bz} & y_{bz} & z_{bz} & B_z \\ 0 & 0 & 0 & 1 \end{bmatrix} \qquad (9.9)$$

which is a 4 by 4 matrix with 16 components. The 12 components in the first three rows are all nonlinear composite functions of θ, d_1, d_2, P_{3x}, P_{3y} and P_{3z}; and each of them has a complicated form.

A rigid free body in 3D space has 6 DOF totally. However, the robot's body in Fig.9.1 only has 2 DOF because of the kinematic constraints. Therefore, the specification of the body's configuration must be selective and not all 6 DOF can be specified arbitrarily. To illustrate this, assume $\mathbf{H}_O^B$ takes the following numerical form:

$$\mathbf{H}_O^B = \begin{bmatrix} h_{11} & h_{12} & h_{13} & h_{14} \\ h_{21} & h_{22} & h_{23} & h_{24} \\ h_{31} & h_{32} & h_{33} & h_{34} \\ 0 & 0 & 0 & 1 \end{bmatrix} \qquad (9.10)$$

Then, among the 12 quantities in Eq.(9.9), only 2 DOF or 2 quantities can be chosen as the inputs.

The selection of the inputs form the body's position and orientation depends on the actual requirements for the robot. It is not necessary to investigate all possible combinations of the 2 quantities out of the 12 candidates. Since IMPASS is expected to walk and steer on the ground, any two components from its position vector $\mathbf{B}$ or from the direction vector $\mathbf{y}_b$ can be

utilized as the input variables. The advantage of these combinations is that, the two components from **B** can be used to control the projected position of the robot's body on $x_o y_o$ plane (ground plane), $y_o z_o$ plane or $x_o z_o$ plane. Additionally, the two components from $\mathbf{y}_b$ can be used to control the heading angle of the robot projected to the ground or the roll angle projected to $y_o z_o$ plane.

For example, assume that h_{14} and h_{24} in Eq.(9.10) are chosen as the variables to be specified, which correspond to the two components B_x and B_y of the position vector **B** in Eq.(9.9). Then two equations are established as:

$$\begin{cases} B_x = h_{14} & (9.11.1) \\ B_y = h_{24} & (9.11.2) \end{cases}$$

Eq.(9.11.1-9.11.2), Eq.(9.5.1-9.5.3), and Eq.(9.4) or Eq.(9.4)* for either two parallel or two skew contacting spokes, will associatively generate a system of 6 equations with respect to 6 unknowns: θ, d_1, d_2, P_{3x}, P_{3y} and P_{3z}. With θ, d_1 and d_2 obtained, the inverse kinematics problem is solved.

As for a different case in which the direction of y_b axis is the control objective, y_{bx} and y_{by} can be chosen as the input variables. So the two equations become:

$$\begin{cases} y_{bx} = h_{12} & (9.11.3) \\ y_{by} = h_{22} & (9.11.4) \end{cases}$$

Then the system of equations consists of Eq.(9.11.3-9.11.4), Eq.(9.5.1-9.5.3), and Eq.(9.4) or Eq.(9.4)* with respect to 6 unknowns and the inverse kinematics is solvable.

Note that, other combinations of h_{ij} can also be used to solve for θ, d_1, d_2 and the procedures are the same to the above. The choice of h_{ij} is dependent on the contact cases and the requirements in actual operations.

9.3. Numerical Examples of the Forward and Inverse Kinematics

An example based on numerical simulations is presented in this section as a validation to the development in Section 3 and 4. The equation system is solved using the embedded algorithm in *Mathematica* and the solutions are plotted.

9.3.1. Forward Kinematics Simulation

Firstly, the basic geometric parameters of the IMPASS model are listed in the following table.

TABLE 9.1 BASIC GEOMETRIC PARAMETERS OF THE IMPASS MODEL

Length of the axle l_a	16 (in)
Center of the spherical surface with respect to $\{x_b, y_b, z_b\}$	[0, -35, 14] (in)
Radius of the spherical surface R	21 (in)
Total length of a spoke	23.5 (in)

And the joint displacements are chosen as: $\theta = 0.5$ (rad), $d_1 = 14$ (in) and $d_2 = 10$ (in).

Applying Eq.(9.1-9.5), the solutions to the tangential and contact point P_3 are:

[-4.709,-37.004,-6.367] and [3.637,-15.124,19.720]

The second solution can be eliminated because it corresponds to a tangential point at the upper portion of the spherical surface. Using Eq.(9.6-9.8), the matrix $\mathbf{H}_O^B$ is determined now as:

$$\mathbf{H}_O^B = \begin{bmatrix} 0.970 & -0.116 & -0.213 & 5.336 \\ 0.093 & 0.989 & -0.119 & 4.438 \\ 0.224 & 0.095 & 0.970 & 10.762 \\ 0 & 0 & 0 & 1 \end{bmatrix} \qquad (9.12)$$

Using the values contained in Eq.(9.12), the configuration of the IMPASS model is plotted in Fig.9.4. Note that in this figure, the partial spherical surface at IMPASS' tail is represented with a complete transparent sphere. This is just to illustrate the reason why the additional solution can be eliminated.

9.3.2. Two Cases of the Inverse Kinematics Simulation and Potential Computation Issues

Since $\mathbf{H}_O^B$ in Eq.(9.12) is now a matrix with quantities calculated from the forward kinematics, its components can now be utilized to validate the formulation of inverse kinematics in Section 4.

Case I: In the first simulation, assume h_{14} = 5.336 and h_{24} = 4.438 are the two input variables, then using Eq.(9.11.1-9.11.2) and Eq.(9.5.1-9.5.3), the 4 solutions to the inverse kinematics problem are obtained and listed in Table 2.

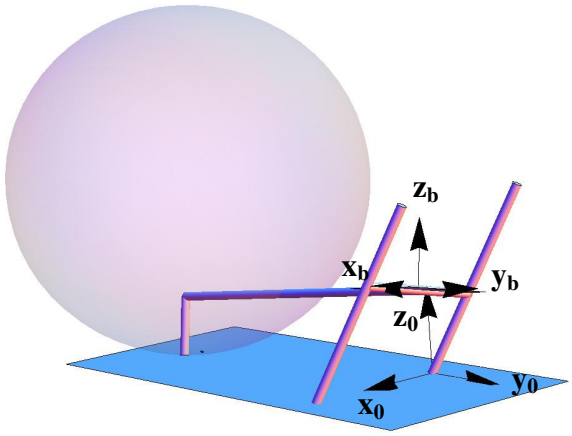

FIG.9.4 FORWARD KINEMATICS SOLUTION FOR A "1-1: PARALLEL & UNEQUAL" CASE

TABLE 9.2 INVERSE KINEMATICS SOLUTIONS TO CASE 1: B_x AND B_y SPECIFIED

	Solution 1	Solution 2	Solution 3	Solution 4
θ	-2.881	1.827	0.5	2.076
d_1	14	14	14	14
d_2	10	10	10	10
P_{3x}	-4.709	4.709	-4.709	4.709
P_{3y}	-22.405	-14.752	-37.004	-22.390
P_{3z}	30.131	16.976	-6.367	-2.119

Apparently, Solution 3 matches exactly with the preset joint displacements. These solutions are plotted in Fig.9.5.

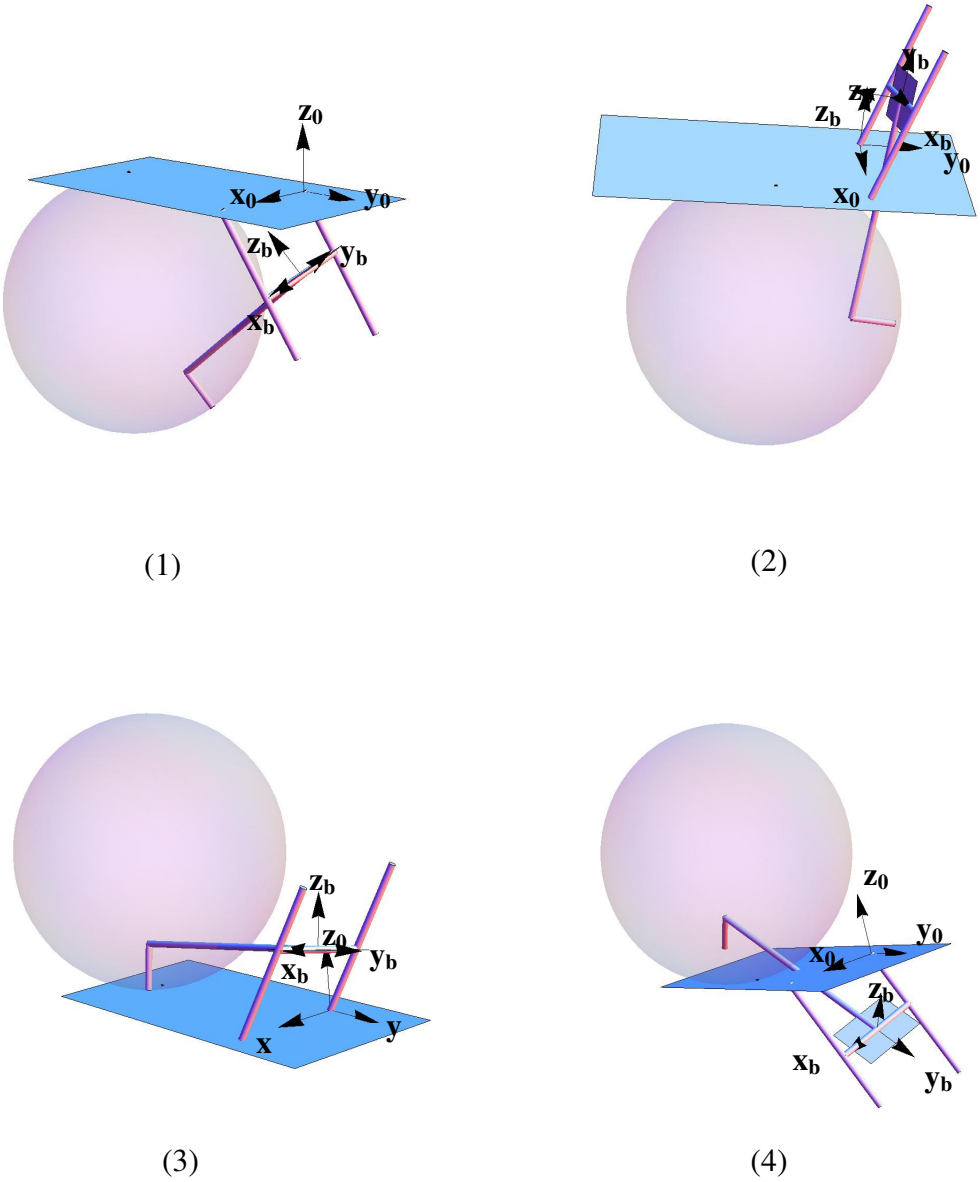

FIG.9.5 FOUR SOLUTIONS TO THE INVERSE KINEMATICS SIMULATION CASE 1

Inspecting Fig.9.5, it is evident that if a criterion based on the effective range of the spherical surface and the joint displacements is applied, those unfeasible inverse kinematics solutions will be eliminated and only one feasible solution exists, which is no other than the current solution that matches with the preset joint variables.

Case II: In the second simulation, h_{12} = -0.116 and h_{22} = 0.989 are chosen as the two input variables and we are trying to control the direction of y_b axis. Applying Eq.(11.1-2) and Eq.(5.1-5.3) again, the 8 solutions to the inverse kinematics problem are obtained and listed in Table 9.3.

TABLE 9.3 INVERSE KINEMATICS SOLUTIONS TO CASE 2: y_{bx} AND y_{by} SPECIFIED

	Solution 1	Solution 2	Solution 3	Solution 4
θ	2.642	2.642	0.5	0.5
d_1	44.278	40.668	14	6.959
d_2	40.278	36.668	10	2.959
P_{3x}	-4.709	-4.250	-4.709	-4.250
P_{3y}	-37.004	-32.996	-37.004	-32.996
P_{3z}	34.367	34.467	-6.367	-6.467

	Solution 5	Solution 6	Solution 7	Solution 8
θ	2.642	2.642	0.5	0.5
d_1	-2.551	-11.211	-32.829	-44.921
d_2	-6.551	-15.211	-36.829	-48.921
P_{3x}	4.709	4.250	4.709	4.250
P_{3y}	-32.996	-32.004	32.996	-37.004
P_{3z}	-6.367	-6.467	34.367	34.467

Again, among the 8 solutions, Solution 3 matches exactly with the preset joint displacements. These 8 solutions are plotted in Fig.9.6.

Inspecting Fig.9.6, if a criterion based on the effective range of the spherical surface and the joint displacements is applied, the 6 unfeasible inverse kinematics solutions will be eliminated. However, in this case, Solution 3 and 4 are both feasible solutions, if one solution needs to be eliminated, then more information of the body's configuration should be given.

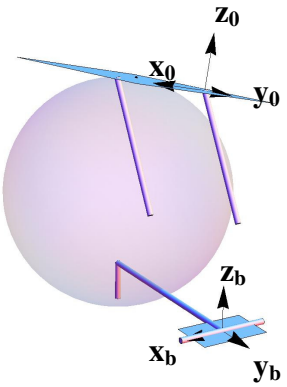

(1)

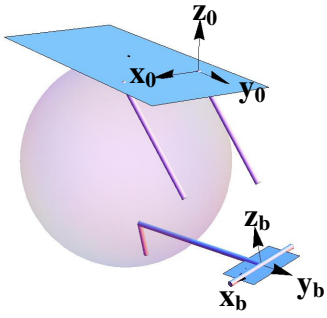

(2)

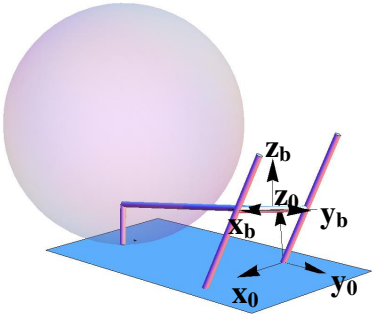

(3)

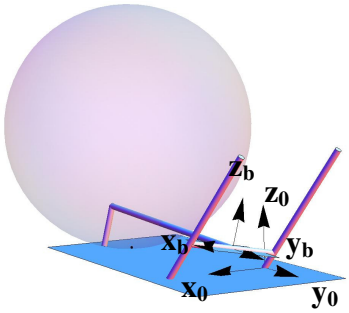

(4)

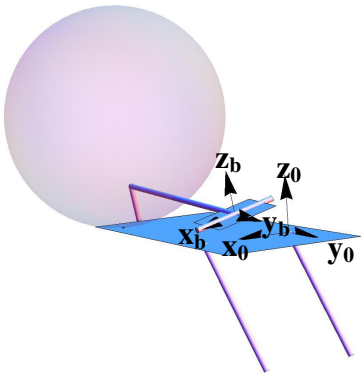

(5)

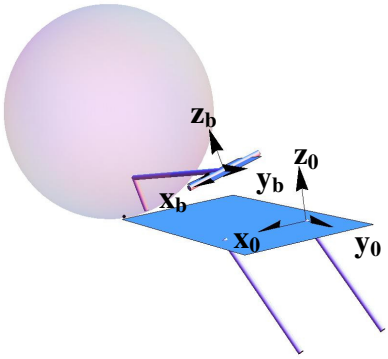

(6)

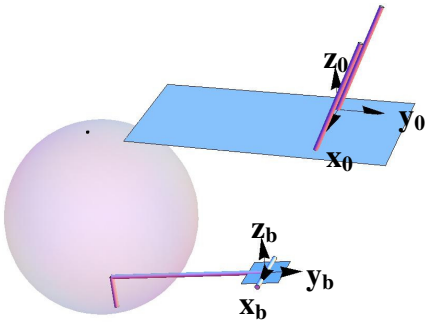

(7)

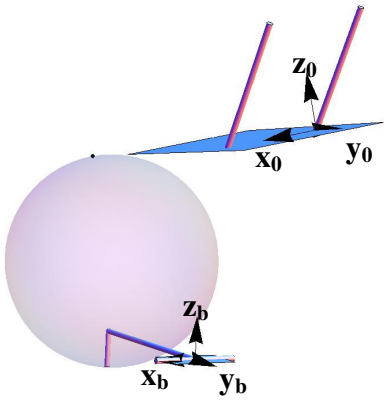

(8)

FIG.9.6 EIGHT SOLUTIONS TO THE INVERSE KINEMATICS SIMULATION CASE 2

In the inverse kinematics formulation presented in previous sections, the joint variables are always obtained by solving six algebraic equations simultaneously. Depending on the complicity of the algebraic expressions in Eq.(9.9), the computation efficiency differs case by case. For the two "1-1: parallel & unequal" cases presented in this section, the inverse kinematics solutions can be calculated within decent amount of time in numerical simulations. However, if the same algorithm is applied to any "1-1: skew" case, then the computation efficiency becomes very low because the expressions of h_{ij} in Eq.(9.9) take more complicated forms. Additionally, the complicated form of Eq.(9.9) hinders any insight into the kinematic configuration. Therefore, an alternative formulation of the inverse kinematics must be considered.

9.4. Inverse Kinematics Formulation with Reduced Equation Systems

The inverse kinematic solutions in Section 9.2 require solving an equation system with 6 unknown variables. If the number of the unknowns could be reduced, then the computation efficiency of this method will be greatly improved. Considering the conclusions obtained from the mobility analysis in Chapter 9, any "1-1" contact case has exactly two continuous and controllable DOF. Under such contact cases, it can be easily observed from the experimental testing that as the two spoke wheels rotate about the axle, the body of the IMPASS robot also rotate about the pivot line on the ground. Therefore, the rotational angle of the robot about the pivot line is used in the following analysis to simply the formulation of inverse kinematics.

9.4.1. Kinematic Models based on Virtual Serial Manipulators

"1-1: parallel" Cases: Ignoring the body of the robot in such contact cases, the axle and two parallel contacting spokes form a two-branch Spherical-Prismatic parallel mechanism with respect to the ground. As shown in Fig.9.7(a), the two DOF based on the mobility analysis in Chapter 9 are the rotation of the axle about the pivoting line P_1P_2 on the ground and the translation of axle along the two contacting spokes. With the two DOF identified, this 2-SP parallel mechanism can be modeled as a virtual serial manipulator. Since the axle and two contacting spokes lie in the same plane, the first joint of the virtual serial manipulator is defined as the rotation of the plane about P_1P_2 and the second joint is defined as the translation of the axle along the spokes within the plane.

The two joint variables are denoted with Θ_1 and D_2 in Fig.9.7(a) and the coordinate frames are attached to the virtual joints as demonstrated in Fig.9.7(b). Again, the fixed coordinate coordinates $\{x_0, y_0, z_0\}$ on the ground are established following the convention in Sec.9.1, with its origin at P_2, x_0 axis pointing to P_1, and z_0 perpendicular to the ground.

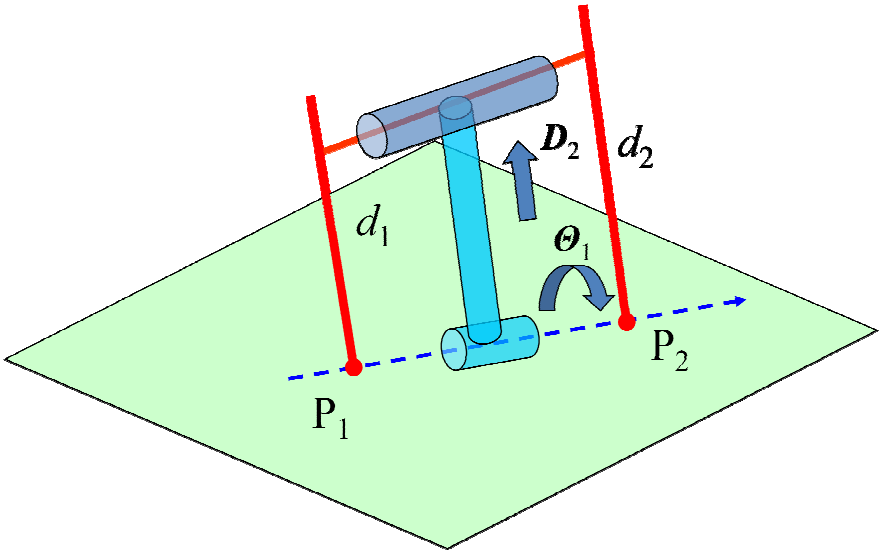

(a)

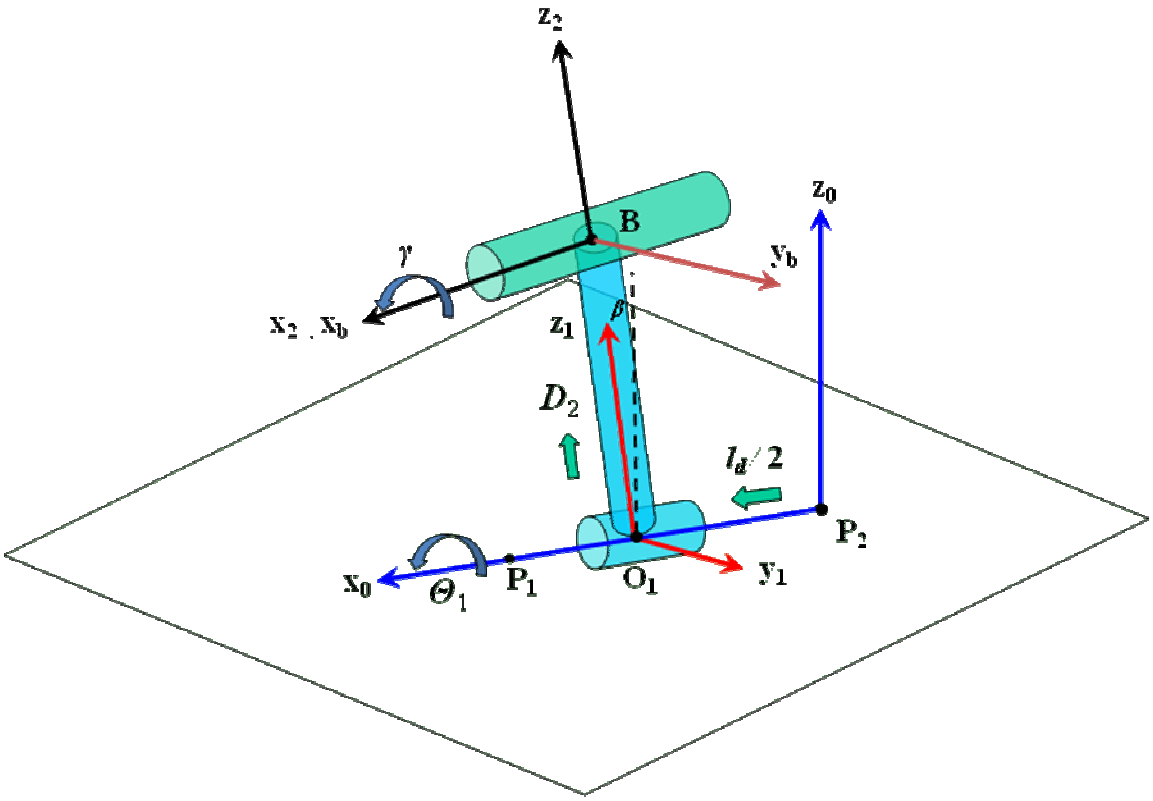

(b)

FIG.9.7 VIRTUAL SERIAL MANIPULATOR MODEL FOR THE "1-1: PARALLEL" CONTACT CASE

Inspecting Fig.9.7, the transformation from the ground coordinate $\{x_0, y_0, z_0\}$ to the body coordinate $\{x_b, y_b, z_b\}$ is achieved through the following steps. Firstly, z_0 axis is rotated by Θ_1 about the x_0 axis, i.e. the pivoting line P_1P_2, such that it is coplanar with the axle and the two contacting spokes. Then, the current origin is translated along the x_0 axis by a linear

displacement of $l_d/2$, for which l_d is the distance between the two contact points P_1 and P_2. The current z_0 axis is rotated by β about the current y_0 axis to be collinear with the z_1 axis. The angle β is determined by the length of the axle and the difference of the two unequal contacting spokes. As for the case of two equal contacting spokes, β is taken as zero. Translating along the z_1 axis for a displacement of D_2, x_1 is now collinear with x_2 and x_b, and the origin is at the central point of the axle. Finally, rotating z_2 axis about the x_2 axis by γ, the body coordinate frame is well established, which exactly matches with the setup in Sec.9.1. The complete transformation process can be described by the following equation.

$$\mathbf{H}_O^B = R_x(\Theta_1)T_x(l_d/2)R_x(\beta)T_z(D_2)R_x(\gamma) \tag{9.13}$$

In this equation, Θ_1 and D_2 are the two joint variables of the 2 DOF virtual serial manipulator model. l_d and β are constants predetermined by the lengths of the axle and the contacting spokes, for which:

$$l_d = \sqrt{l_a^2 + \Delta d^2} \quad \text{and} \quad \beta = \arctan(\Delta d / l_a)$$

γ is determined by the tangential constraint of the spherical surface at the tail with the ground. Based on Eq.(9.13), the complete form of $\mathbf{H}_O^B$ is detailed as follows.

$$\mathbf{H}_O^B = \begin{bmatrix} \cos\beta & \sin\beta\sin\gamma & \cos\gamma\sin\beta & l_d/2 + D_2\sin\beta \\ \sin\Theta_1\sin\beta & \cos\Theta_1\cos\gamma - \cos\beta\sin\Theta_1\sin\gamma & -\cos\beta\cos\gamma\sin\Theta_1 - \cos\Theta_1\sin\gamma & -D_2\cos\beta\sin\Theta_1 \\ -\cos\Theta_1\sin\beta & \sin\Theta_1\cos\gamma + \cos\beta\cos\Theta_1\sin\gamma & \cos\Theta_1\cos\beta\cos\gamma - \sin\Theta_1\sin\gamma & D_2\cos\Theta_1\cos\beta \\ 0 & 0 & 0 & 1 \end{bmatrix} \tag{9.13}*$$

Obviously, the alternative form of $\mathbf{H}_O^B$ based on the virtual model of a serial manipulator is very compact and straightforward compared with that derived from taking the inverse of $\mathbf{H}_B^O$ as shown in Eq.(9.8). Particularly, when β is taken as zero for the "1-1: parallel & equal" case, Eq.(9.13)* takes a even simpler form as:

$$\mathbf{H}_O^B = \begin{bmatrix} 1 & 0 & 0 & l_d/2 \\ 0 & \cos(\Theta_1+\gamma) & -\sin(\Theta_1+\gamma) & -D_2\sin\Theta_1 \\ 0 & \sin(\Theta_1+\gamma) & \cos(\Theta_1+\gamma) & D_2\cos\Theta_1 \\ 0 & 0 & 0 & 1 \end{bmatrix} \tag{9.13}**$$

Eq.(9.13) and Eq.(9.13)* not only can improve the computation efficiency of the inverse kinematics for the "1-1: parallel" cases but also provide more insights into the kinematic configuration when assigning the desired control variables.

"1-1: skew" Case: If the two contacting spokes are skew to each other, another type of two-branch Spherical-Prismatic parallel mechanism is thus generated, as is shown in Fig.9.8(a). This parallel mechanism also possesses two DOF based on the mobility analysis in Chapter 8. The first DOF is similar to the "1-1: parallel" contact case; the body is capable of rotating about the pivoting line P_1P_2 on the ground. The second DOF is caused by changing

the lengths of the contacting spokes following the constraint in Eq.(9.4)* as follows.

$$d_1^2 - d_1 d_2 + d_2^2 = e^2 - l_a^2 \qquad (9.4)^*$$

where e is the distance between the two contact points, l_a is the length of the axle and both of them are predetermined for any "1-1: skew" case. It is also a rotational motion about a virtual axis determined by e and l_a.

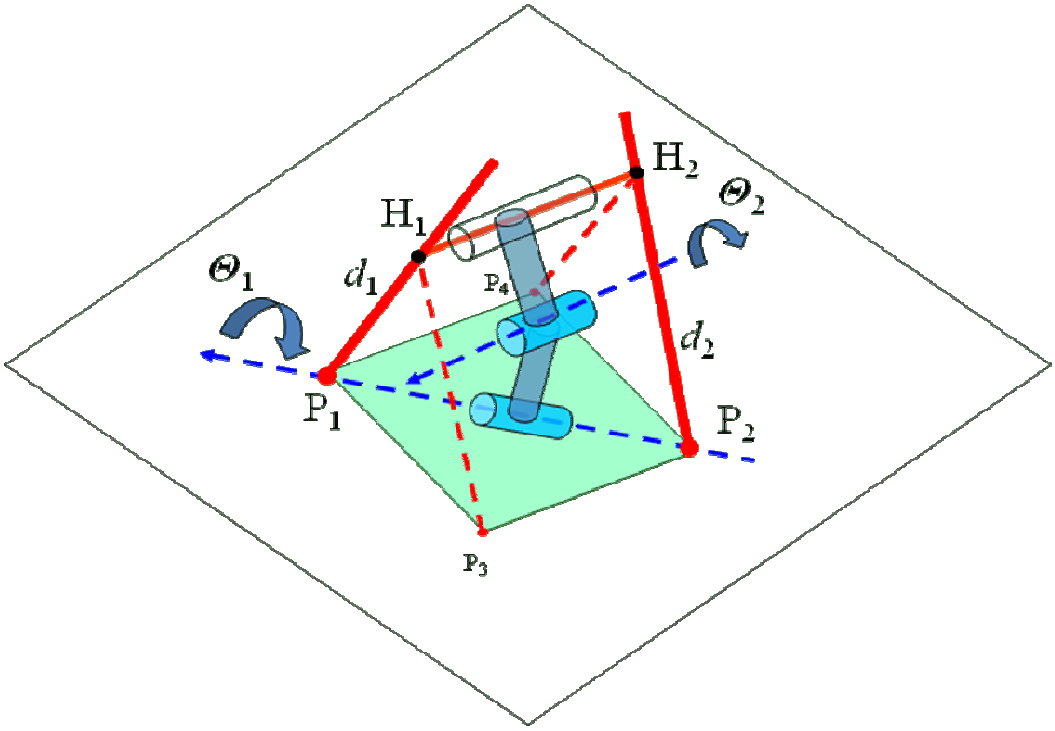

(a)

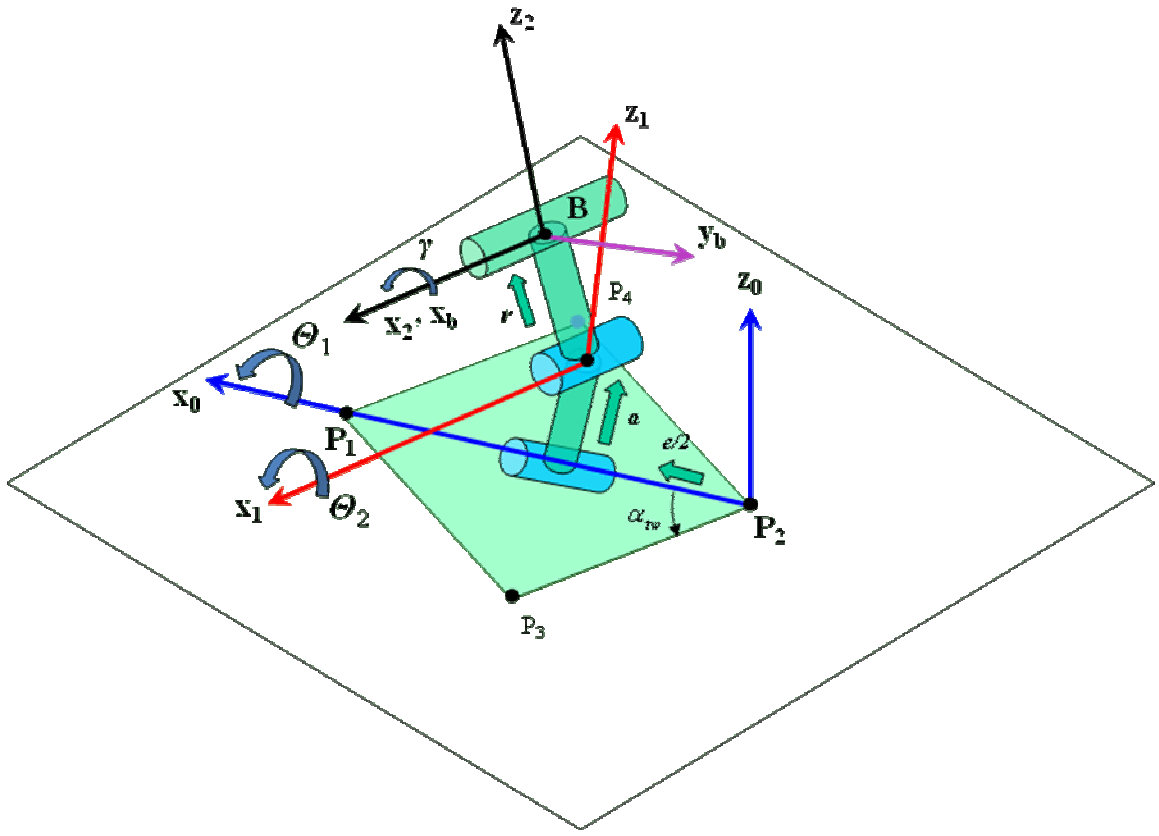

(b)

FIG.9.8 VIRTUAL SERIAL MANIPULATOR MODEL FOR THE "1-1:SKEW" CONTACT CASE

The first DOF is denoted with joint variable Θ_1. To make the geometric presentation more straightforward, two auxiliary line segments are created in Fig.9.8(a). As shown in this figure, H_1 and H_2 are the centers of the left and right spoke wheels respectively. Auxiliary line segment H_1P_3 is parallel and equal to the right contacting spoke and H_2P_4 is parallel and equal to the left contacting spoke. Thus, a rectangle $P_1P_3P_2P_4$ is generated with the side lengths l_a and c, for which $c^2 = e^2 - l_a^2$. As the mechanism rotates about the pivoting line on the ground, rectangle $P_1P_3P_2P_4$ also rotates about P_1P_2 correspondingly. Therefore, joint variable Θ_1 can be described as the rotational angle between plane $P_1P_3P_2P_4$ and the ground. The second DOF is denoted with Θ_2 which occurs within the polyhedron P_1H_1P3-$P_2H_2P_4$. For this DOF, the axle rotates about a virtual axis as is discussed in Chapter 8. The direction of this virtual axis is parallel to the axle, as indicated in Fig.9.8(a).

With the two DOF identified and denoted with the arrows in Fig.9.8(a), a virtual two-link serial manipulator model for this parallel mechanism can be established. Correspondingly, the coordinate frames are attached to the virtual joints as demonstrated in Fig.9.8(b). The fixed coordinate coordinates $\{x_0, y_0, z_0\}$ on the ground are established following the

convention in Sec.9.1, with its origin at P_2, x_0 axis pointing to P_1, and z_0 perpendicular to the ground.

By inspection, ground coordinate frame $\{x_0, y_0, z_0\}$ is transformed to the body coordinate frame $\{x_b, y_b, z_b\}$ through the following steps. First, the origin of $\{x_0, y_0, z_0\}$is translated along the x_0 axis by a distance of $e/2$. Followed by a rotation of Θ_1 about x_0, a rotation of α_{tw} about the current z_0 and a translation of a about the same z_0 axis, frame $\{x_0, y_0, z_0\}$ is then coincident with $\{x_1, y_1, z_1\}$. Rotating about the x_1 by Θ_2 and translating about the current z_1 for a distance r, $\{x_1, y_1, z_1\}$ is transformed to $\{x_2, y_2, z_2\}$. Note that, the calculation of a and r has been discussed in Chapter 8 and α_{tw} is determined by e and l_a as $\alpha_{tw} = \arcsin\left[\left(e^2 - l_a^2\right)/e\right]$. Finally, similar to the "1-1: parallel" cases, rotating about the x_2 axis by γ, the body frame $\{x_b, y_b, z_b\}$is achieved. The following matrix equation can be used to describe the complete transformation.

$$\mathbf{H}_O^B = T_x(e/2)\,R_x(\Theta_1)\,R_z(\alpha_{tw})\,T_z(a)\,R_x(\Theta_1)\,T_z(r)\,R_x(\gamma) \tag{9.14}$$

Eq.(9.14) is then further developed as:

$$\mathbf{H}_O^B = \begin{bmatrix} \cos\alpha_{tw} & -\cos(\Theta_2+\gamma)\sin\alpha_{tw} & \sin(\Theta_2+\gamma)\sin\alpha_{tw} & e/2 + r\sin\alpha_{tw}\sin\Theta_2 \\ \cos\Theta_1\sin\alpha_{tw} & \cos\alpha_{tw}\cos\Theta_1\cos(\Theta_2+\gamma) - \sin\Theta_1\sin(\Theta_2+\gamma) & -\cos\alpha_{tw}\cos\Theta_1\sin(\Theta_2+\gamma) - \sin\Theta_1\cos(\Theta_2+\gamma) & -(a+r\cos\Theta_2)\sin\Theta_1 - r\cos\alpha_{tw}\cos\Theta_1\sin\Theta_2 \\ \sin\Theta_1\sin\alpha_{tw} & \cos\alpha_{tw}\sin\Theta_1\cos(\Theta_2+\gamma) + \cos\Theta_1\sin(\Theta_2+\gamma) & -\cos\alpha_{tw}\sin\Theta_1\sin(\Theta_2+\gamma) + \cos\Theta_1\cos(\Theta_2+\gamma) & (a+r\cos\Theta_2)\cos\Theta_1 - r\cos\alpha_{tw}\sin\Theta_1\sin\Theta_2 \\ 0 & 0 & 0 & 1 \end{bmatrix} \tag{9.14}^*$$

In Eq.(9.14) and (9.14)*, e, α_{tw}, a and r are predetermined constants. Θ_1 and Θ_2 are the two joint variables of the 2 DOF virtual model. γ is the rotational angle of the spherical surface at the tail when touching the ground tangentially.

As a summary, the matrix expressions in Eq.(9.13)* and (9.14)* are based on the two virtual serial manipulator models. Compared with Eq.(9.8), the compact forms of the components can greatly reduce the number of unknown variables, thus improving the computation efficiency and providing more insights when solving the inverse kinematics problems.

9.4.2. Derivation of the Reduced Equation Systems

As discussed in Section 9.2, the inverse kinematics problem based on the forward kinematics model requires solving a system of 6 equations with respect to 6 unknowns θ, d_1, d_2, P_{3x}, P_{3y} and P_{3z}. , which consists of Eq.(9.5.1-9.5.3), Eq.(4) or Eq.(4)*, and two components with specified h_{ij} values selected from the matrices in Eq.(9.9) and (9.10).

However, utilizing the virtual serial manipulator models illustrated in Section 9.4.1, the equation systems with respect to 6 unknowns can be reduced to systems with only three

unknowns, in order to improve the computation efficiency. Recall Eq.(9.9) and (9.10) as follows.

$$\mathbf{H}_O^B = \begin{bmatrix} \mathbf{x}_b & \mathbf{y}_b & \mathbf{z}_b & \mathbf{B} \\ 0 & 0 & 0 & 1 \end{bmatrix} = \begin{bmatrix} x_{bx} & y_{bx} & z_{bx} & B_x \\ x_{by} & y_{by} & z_{by} & B_y \\ x_{bz} & y_{bz} & z_{bz} & B_z \\ 0 & 0 & 0 & 1 \end{bmatrix} \tag{9.9}$$

$$\mathbf{H}_O^B = \begin{bmatrix} h_{11} & h_{12} & h_{13} & h_{14} \\ h_{21} & h_{22} & h_{23} & h_{24} \\ h_{31} & h_{32} & h_{33} & h_{34} \\ 0 & 0 & 0 & 1 \end{bmatrix} \tag{9.10}$$

With the assistance of Eq.(9.13)*, (9.13)** and (9.14)*, each component in Eq.(9.9) now has a compact and simple form. As discussed in Section 9.2, the selection of the inputs from the body's position and orientation depends on the actual requirements for the robot. For the convenience of the control of the IMPASS robot on the ground, any two components from its position vector **B** or from the direction vector $\mathbf{y}_b$ can be used as the variables to be specified. The two components in **B** can be utilized to control the projected position of the robot's body on x_oy_o plane (ground plane), y_oz_o plane or x_oz_o plane; and the two components from $\mathbf{y}_b$ can be used to control the heading angle of the robot projected to the ground or the roll angle projected to y_oz_o plane.

"1-1: parallel" Cases: Recall Eq.(9.13) below.

$$\mathbf{H}_O^B = \begin{bmatrix} \cos\beta & \sin\beta\sin\gamma & \cos\gamma\sin\beta & l_d/2 + D_2\sin\beta \\ \sin\Theta_1\sin\beta & \cos\Theta_1\cos\gamma - \cos\beta\sin\Theta_1\sin\gamma & -\cos\beta\cos\gamma\sin\Theta_1 - \cos\Theta_1\sin\gamma & -D_2\cos\beta\sin\Theta_1 \\ -\cos\Theta_1\sin\beta & \sin\Theta_1\cos\gamma + \cos\beta\cos\Theta_1\sin\gamma & \cos\Theta_1\cos\beta\cos\gamma - \sin\Theta_1\sin\gamma & D_2\cos\Theta_1\cos\beta \\ 0 & 0 & 0 & 1 \end{bmatrix} \tag{9.13}*$$

Inspecting the position vector **B** in the fourth column, if the values of any two components out of the three are specified, then three different sets of equations can be established as:

$$\begin{cases} l_d/2 + D_2\sin\beta = h_{14} \\ -D_2\cos\beta\sin\Theta_1 = h_{24} \end{cases} \tag{9.15.1}$$

$$\begin{cases} l_d/2 + D_2\sin\beta = h_{14} \\ D_2\cos\Theta_1\cos\beta = h_{34} \end{cases} \tag{9.15.2}$$

$$\begin{cases} -D_2\cos\beta\sin\Theta = h_{14} \\ D_2\cos\Theta_1\cos\beta = h_{34} \end{cases} \tag{9.15.3}$$

Apparently, the joint variables of the virtual serial manipulator model Θ_1 and D_2 can be obtained by solving any set of the three equation systems. With Θ_1 and D_2 solved, the only unknown left is γ, which will then be determined by the tangential constraint of the sphere and the ground plane.

Assume the center of the sphere is located at $[C_a, C_b, C_c]$ in the body coordinate system $\{x_b, y_b, z_b\}$ and the radius is R, then the equation of the spherical surface is written as:

$$\left(x_b - C_a\right)^2 + \left(y_b - C_b\right)^2 + \left(z_b - C_c\right)^2 = R^2 \tag{9.16}$$

Denote the global coordinates of the spherical center with $[C_{a,G}, C_{b,G}, C_{c,G}]$, then $[C_{a,G}, C_{b,G}, C_{c,G}]$ can be obtained from:

$$\begin{bmatrix} C_{a,G} \\ C_{b,G} \\ C_{c,G} \\ 1 \end{bmatrix} = \mathbf{H}_O^B \begin{bmatrix} C_a \\ C_b \\ C_c \\ 1 \end{bmatrix}$$

$$= \begin{bmatrix} \cos\beta & \sin\beta\sin\gamma & \cos\gamma\sin\beta & l_d/2 + D_2\sin\beta \\ \sin\Theta_1\sin\beta & \cos\Theta_1\cos\gamma - \cos\beta\sin\Theta_1\sin\gamma & -\cos\beta\cos\gamma\sin\Theta_1 - \cos\Theta_1\sin\gamma & -D_2\cos\beta\sin\Theta_1 \\ -\cos\Theta_1\sin\beta & \sin\Theta_1\cos\gamma + \cos\beta\cos\Theta_1\sin\gamma & \cos\Theta_1\cos\beta\cos\gamma - \sin\Theta_1\sin\gamma & D_2\cos\Theta_1\cos\beta \\ 0 & 0 & 0 & 1 \end{bmatrix} \begin{bmatrix} C_a \\ C_b \\ C_c \\ 1 \end{bmatrix} \tag{9.17}$$

With Θ_1 and D_2 solved from Eq.(9.15), $[C_{a,G}, C_{b,G}, C_{c,G}]$ becomes functions of γ only, so the equation of the spherical surface in ground coordinate frame $\{x_0, y_0, z_0\}$ can be written as:

$$\left(x - C_{a,G}(\gamma)\right)^2 + \left(y - C_{b,G}(\gamma)\right)^2 + \left(z - C_{c,G}(\gamma)\right)^2 = R^2 \tag{9.18}$$

Assume the tangential point of the spherical surface and the ground plane is $[x_t, y_t, z_t]$, then the equation of the tangential plane is:

$$\left(x_t - C_{a,G}(\gamma)\right)(x - x_t) + \left(y_t - C_{b,G}(\gamma)\right)(y - y_t) + \left(z_t - C_{c,G}(\gamma)\right)(z - z_t) = 0 \tag{9.19}$$

Consider the fact that the tangential point $[x_t, y_t, z_t]$ also lies on the ground plane of z = 0, z_t = 0 can be inferred and Eq.(9.18) is further simplified as:

$$\left(x_t - C_{a,G}(\gamma)\right)(x - x_t) + \left(y_t - C_{b,G}(\gamma)\right)(y - y_t) - C_{c,G}(\gamma)\, z = 0 \tag{9.19}*$$

Compare Eq.(9.19)* with the equation of the ground plane z = 0, two equations can be simply derived as:

$$\begin{cases} x_t - C_{a,G}(\gamma) = 0 \\ y_t - C_{b,G}(\gamma) = 0 \end{cases} \tag{9.20}$$

Moreover, $[x_t, y_t, z_t]$ with $z_t = 0$ has to satisfy Eq.(9.18), such that

$$\left(x_t - C_{a,G}(\gamma)\right)^2 + \left(y_t - C_{b,G}(\gamma)\right)^2 + C_{c,G}(\gamma)^2 = R^2 \tag{9.21}$$

Consider Eq.(9.20) and (9.21) associatively, the equation to solve for γ is obtained straightforwardly as:

$$C_{c,G}(\gamma) = \pm R \tag{9.22}$$

with + R for the sphere contacts the ground plane above and $-R$ for the sphere below which could be discard.

Therefore, if two components of the position vector **B** in Eq.(9.9) are specified, Eq.(9.15) and Eq.(9.20) can be used to solve for the three unknown variables Θ_1, D_2 and γ.

As for the cases in which any two components of the direction vector $\mathbf{y}_b$ are specified, the three sets of equations are established as:

$$\begin{cases} \sin\beta\sin\gamma = h_{12} \\ \cos\Theta_1\cos\gamma - \cos\beta\sin\Theta_1\sin\gamma = h_{22} \end{cases} \tag{9.23.1}$$

$$\begin{cases} \cos\Theta_1\cos\gamma - \cos\beta\sin\Theta_1\sin\gamma = h_{22} \\ \sin\Theta_1\cos\gamma + \cos\beta\cos\Theta_1\sin\gamma = h_{32} \end{cases} \tag{9.23.2}$$

$$\begin{cases} \sin\beta\sin\gamma = h_{12} \\ \sin\Theta_1\cos\gamma + \cos\beta\cos\Theta_1\sin\gamma = h_{32} \end{cases} \tag{9.23.3}$$

Similarly, with Θ_1 and γ solved from Eq.(9.23), $C_{c,G}$ becomes a function of D_2 only and the third equation is then:

$$C_{c,G}\left(D_2\right) = R \tag{9.24}$$

Therefore, the three unknown variables Θ_1, D_2 and γ in these cases can be solved from Eq.(9.23) and (9.24).

For the particular case in which two contacting spokes are of equal lengths, recall the simplified form of the $\mathbf{H}_O^B$ matrix in Eq.(9.13)**.

$$\mathbf{H}_O^B = \begin{bmatrix} 1 & 0 & 0 & l_d/2 \\ 0 & \cos(\Theta_1+\gamma) & -\sin(\Theta_1+\gamma) & -D_2\sin\Theta_1 \\ 0 & \sin(\Theta_1+\gamma) & \cos(\Theta_1+\gamma) & D_2\cos\Theta_1 \\ 0 & 0 & 0 & 1 \end{bmatrix} \tag{9.13)**}$$

By inspection, the direction vector $\mathbf{x}_b$ in this case is always parallel with the x_0 axis, and the B_x component is a constant, which match exactly with the actual observations. To solve for the unknown variables Θ_1, D_2 and γ, either the B_y, B_z components of the position vector **B** are both specified, or y_{by} / y_{bz} and B_y / B_z are specified. The reduced equation systems could be:

$$\begin{cases} -D_2\sin\Theta_1 = h_{24} \\ D_2\cos\Theta_1 = h_{34} \\ C_{c,G}\left(\gamma\right) = R \end{cases} \tag{9.25.1}$$

$$\text{or} \begin{cases} -D_2\sin\Theta_1 = h_{24} \\ \cos(\Theta_1+\gamma) = h_{22} \\ C_{c,G}\left(\Theta_1, D_2, \gamma\right) = R \end{cases} \tag{9.25.2}$$

And Θ_1, D_2 and γ are thus solved from Eq.(9.25). Note that, different from the "1-1: parallel & unequal" case, if the two components y_{by} and y_{bz} in $\mathbf{y}_b$ are specified simultaneously, then Θ_1 and γ will not be solved.

With Θ_1, D_2 and γ calculated based on the virtual serial manipulator model, the actual joint variables of the "1-1: parallel" cases, i.e. the lengths of the two contacting spokes d_1 and d_2, as well as the phase angle of the wheels θ, can be simply determined as:

$$\begin{aligned} \theta &= \gamma \\ d_1 &= D_2 + \Delta d/2 \\ d_2 &= D_2 - \Delta d/2 \end{aligned} \tag{9.26}$$

And the inverse kinematics problems of the "1-1: parallel" cases is accomplished.

"1-1: skew" Case: The derivation of the reduced equation system for the "1-1: skew" case is similar to that of the "1-1: parallel" cases. First, recall Eq.(9.14) as follows:

$$\mathbf{H}_O^B = \begin{bmatrix} \cos\alpha_{tw} & -\cos(\Theta_2+\gamma)\sin\alpha_{tw} & \sin(\Theta_2+\gamma)\sin\alpha_{tw} & e/2+r\sin\alpha_{tw}\sin\Theta_2 \\ \cos\Theta_1\sin\alpha_{tw} & \cos\alpha_{tw}\cos\Theta_1\cos(\Theta_2+\gamma)-\sin\Theta_1\sin(\Theta_2+\gamma) & -\cos\alpha_{tw}\cos\Theta_1\sin(\Theta_2+\gamma)-\sin\Theta_1\cos(\Theta_2+\gamma) & -(a+r\cos\Theta_2)\sin\Theta_1-r\cos\alpha_{tw}\cos\Theta_1\sin\Theta_2 \\ \sin\Theta_1\sin\alpha_{tw} & \cos\alpha_{tw}\sin\Theta_1\cos(\Theta_2+\gamma)+\cos\Theta_1\sin(\Theta_2+\gamma) & -\cos\alpha_{tw}\sin\Theta_1\sin(\Theta_2+\gamma)+\cos\Theta_1\cos(\Theta_2+\gamma) & (a+r\cos\Theta_2)\cos\Theta_1-r\cos\alpha_{tw}\sin\Theta_1\sin\Theta_2 \\ 0 & 0 & 0 & 1 \end{bmatrix} \tag{9.14}*$$

If any two components of the position vector **B** are specified, considering the tangential constraint equation derived from Eq.(9.19-22), three sets of equations can be established as:

$$\begin{cases} e/2+r\sin\alpha_{tw}\sin\Theta_2 = h_{14} \\ -(a+r\cos\Theta_2)\sin\Theta_1 - r\cos\alpha_{tw}\cos\Theta_1\sin\Theta_2 = h_{24} \\ C_{c,G}(\gamma) = R \end{cases} \tag{9.27.1}$$

$$\begin{cases} -(a+r\cos\Theta_2)\sin\Theta_1 - r\cos\alpha_{tw}\cos\Theta_1\sin\Theta_2 = h_{24} \\ (a+r\cos\Theta_2)\cos\Theta_1 - r\cos\alpha_{tw}\sin\Theta_1\sin\Theta_2 = h_{34} \\ C_{c,G}(\gamma) = R \end{cases} \tag{9.27.2}$$

$$\begin{cases} e/2+r\sin\alpha_{tw}\sin\Theta_2 = h_{14} \\ (a+r\cos\Theta_2)\cos\Theta_1 - r\cos\alpha_{tw}\sin\Theta_1\sin\Theta_2 = h_{34} \\ C_{c,G}(\gamma) = R \end{cases} \tag{9.27.3}$$

And the unknown variables Θ_1, Θ_2 and γ for this case can be obtained through solving any set of equations in Eq.(9.27).

Similarly, if any two components of the direction vector $\mathbf{y}_b$ are specified, the three sets of equations to solve for Θ_1, Θ_2 and γ are established as:

$$\begin{cases} -\cos(\Theta_2+\gamma)\sin\alpha_{tw} = h_{12} \\ \cos\alpha_{tw}\cos\Theta_1\cos(\Theta_2+\gamma)-\sin\Theta_1\sin(\Theta_2+\gamma) = h_{22} \\ C_{c,G}(\Theta_1,\Theta_2,\gamma) = R \end{cases} \quad (9.28.1)$$

$$\begin{cases} \cos\alpha_{tw}\cos\Theta_1\cos(\Theta_2+\gamma)-\sin\Theta_1\sin(\Theta_2+\gamma) = h_{22} \\ \cos\alpha_{tw}\sin\Theta_1\cos(\Theta_2+\gamma)+\cos\Theta_1\sin(\Theta_2+\gamma) = h_{32} \\ C_{c,G}(\Theta_1,\Theta_2,\gamma) = R \end{cases} \quad (9.28.2)$$

$$\begin{cases} -\cos(\Theta_2+\gamma)\sin\alpha_{tw} = h_{12} \\ \cos\alpha_{tw}\sin\Theta_1\cos(\Theta_2+\gamma)+\cos\Theta_1\sin(\Theta_2+\gamma) = h_{32} \\ C_{c,G}(\Theta_1,\Theta_2,\gamma) = R \end{cases} \quad (9.28.3)$$

With Θ_1, Θ_2 and γ solved from any set of equations in Eq.(9.28), the 12 components in matrix $\mathbf{H}_O^B$ can be completely determined. Then, the actual joint variables of the "1-1: skew" case d_1, d_2 and θ, can be calculated as:

$$\begin{aligned} d_1 &= \|\mathbf{P}_1 - \mathbf{H}_1\| \\ d_2 &= \|\mathbf{P}_2 - \mathbf{H}_2\| \\ \theta &= \text{VectorAngle}\left(\mathbf{y}_b, \overrightarrow{\mathbf{P}_1\mathbf{H}_1}\right) - \pi/2 \end{aligned} \quad (9.26)$$

where, $\mathbf{H}_1$ and $\mathbf{H}_2$ are the global positions of the two spoke wheel centers and θ is determined as the vector angle between $\mathbf{y}_b$ and $\overrightarrow{\mathbf{P}_1\mathbf{H}_1}$ minus the initial angle of $\pi/2$.

9.4.3. Numerical Examples and Results

"1-1: parallel" Case: In order to verify the effectiveness of the inverse kinematics formulation with reduced equation systems, the simulation cases in Section 9.3 are used as the examples. The basic geometric parameters of the IMPASS model are relisted as:

TABLE 9.1 BASIC GEOMETRIC PARAMETERS OF THE IMPASS MODEL

Length of the axle l_a	16 (in)
Center of the spherical surface with respect to $\{x_b, y_b, z_b\}$	[0, -35, 14] (in)
Radius of the spherical surface R	21 (in)
Total length of a spoke	23.5 (in)

With the initial setup of actual joint displacements as: θ = 0.5 (rad), d_1 = 14 (in) and d_2 = 10 (in), the configuration matrix $\mathbf{H}_O^B$ of the robot's body is calculated from the forward kinematics formulation as:

$$\mathbf{H}_O^B = \begin{bmatrix} 0.970 & -0.116 & -0.213 & 5.336 \\ 0.093 & 0.989 & -0.119 & 4.438 \\ 0.224 & 0.095 & 0.970 & 10.762 \\ 0 & 0 & 0 & 1 \end{bmatrix} \qquad (9.12)$$

(I) If B_x and B_y are chosen as the inputs, then two equations based on Eq.(9.15.1) can be established as:

$$\begin{cases} l_d / 2 + D_2 \sin\beta = 5.336 & (9.27.1) \\ -D_2 \cos\beta \sin\Theta_1 = 4.438 & (9.27.2) \end{cases}$$

From Eq.(9.27.1), D_2 is solved as $D_2 = 12$; and from Eq.(9.27.2), Θ_1 is determined as $\Theta_1 = -0.391$. Inspecting Eq.(9.27.2), only $\sin\Theta_1$ exists, which may allow for multiple solutions of Θ_1. However, since the geometric interpretation of Θ_1 is the angle between the plane of the ground and the plane containing the axle and contacting spokes, an angle greater than $\pi/2$ or smaller than $-\pi/2$ is unlikely to happen in reality. A reasonable range of Θ_1 could be $[-\pi/2, \pi/2]$, and the solutions out of this range can be discarded.

With $\Theta_1 = -0.391$ and $D_2 = 12$, Eq.(9.22) can now be used to solve for γ and the two solutions are listed as:

$$\gamma_1 = -2.077 \qquad (9.28.1)$$

$$\gamma_2 = 0.5 \qquad (9.28.2)$$

The first solution corresponds to the case in which the upper portion of the spherical surface contacts the ground, while the second solution corresponds to the lower portion. Similar to Θ_1, a reason range for γ could be $[-\pi/2, \pi/2]$, then the unfeasible solution $\gamma_1 = -2.077$ can be discarded and only one feasible solution is achieved. With Θ_1, D_2 and γ obtained, the actual joint displacements are then determined as $\Theta_1 = 0.5$, $d_1 = 14$ and $d_2 = 10$, which exactly match with the initial setup.

Compared with the approach in Section 9.2, the inverse kinematics problems based on the virtual serial manipulator model and reduced equation systems can be solved more efficiently. Moreover, those unfeasible solutions can be eliminated during the solving process.

(II) If y_{by} and y_{bz} are chosen as the inputs, then two equations based on Eq.(9.23.2) can be established as:

$$\begin{cases} \cos\Theta_1 \cos\gamma - \cos\beta \sin\Theta_1 \sin\gamma = 0.989 \\ \sin\Theta_1 \cos\gamma + \cos\beta \cos\Theta_1 \sin\gamma = 0.095 \end{cases} \qquad (9.29)$$

For this case, if the approach in Section 9.2 is used, the simulation software will take forever to reach any solution. However, with the reduced equation systems, these solutions can be calculated efficiently. First, Θ_1 and γ can be solved from Eq.(9.29) as:

$$\begin{cases}\Theta_{1,1}=2.750\\ \gamma_1=-2.641\end{cases}\quad\begin{cases}\Theta_{1,2}=-2.558\\ \gamma_2=2.641\end{cases}\quad\begin{cases}\Theta_{1,3}=0.583\\ \gamma_3=-0.5\end{cases}\quad\begin{cases}\Theta_{1,4}=-0.391\\ \gamma_4=0.5\end{cases}\tag{9.30}$$

The first two sets of solutions can be discarded, because the two angles are not in the range of [-π/2, π/2] and impossible to implement in actual operations. Using the third and the forth sets of solutions and Eq.(9.24), the two solutions for D_2 are obtained as:

$$\begin{cases}D_{2,1}=12\\ D_{2,2}=13.211\end{cases}\tag{9.31}$$

Therefore, using Eq.(9.26), the actual joint displacements in this case are determined as:

$$\begin{cases}\gamma_1=-0.5\\ d_{1,1}=15.211\\ d_{2,1}=11.211\end{cases}\tag{9.32.1}$$

$$\begin{cases}\gamma_2=0.5\\ d_{1,1}=14\\ d_{2,1}=10\end{cases}\tag{9.32.2}$$

By inspection, Eq.(9.32.2) matches exactly with the initial setup and Eq.(9.32.1) is another feasible solution.

"1-1: skew" Case: As discussed in Section 9.2 and 9.3, the inverse kinematics formulation based on the forward kinematics model usually results in a $\mathbf{H}_O^B$ matrix in which each component is represented with a complicated analytical form. The complexity of these symbolic expressions hinders the calculation of the inverse kinematics solutions, especially for the "1-1: skew" case. Utilizing the virtual serial manipulator model in Section 9.4.1, a relatively compact form of $\mathbf{H}_O^B$ can be reached as shown in Eq.(9.14)*. With the assistance of Eq.(9.14), the inverse kinematics problems for this case can be solved efficiently. The basic geometric parameters of the IMPASS model still follow Table 9.1 and the initial setup of the actual joint displacements is: θ = 0.1 (rad), d_1 = 10 (in) and d_2 = 10 (in). The forward kinematics is solved following the procedures in Section 9.1 and the current configuration for this case is plotted as follows.

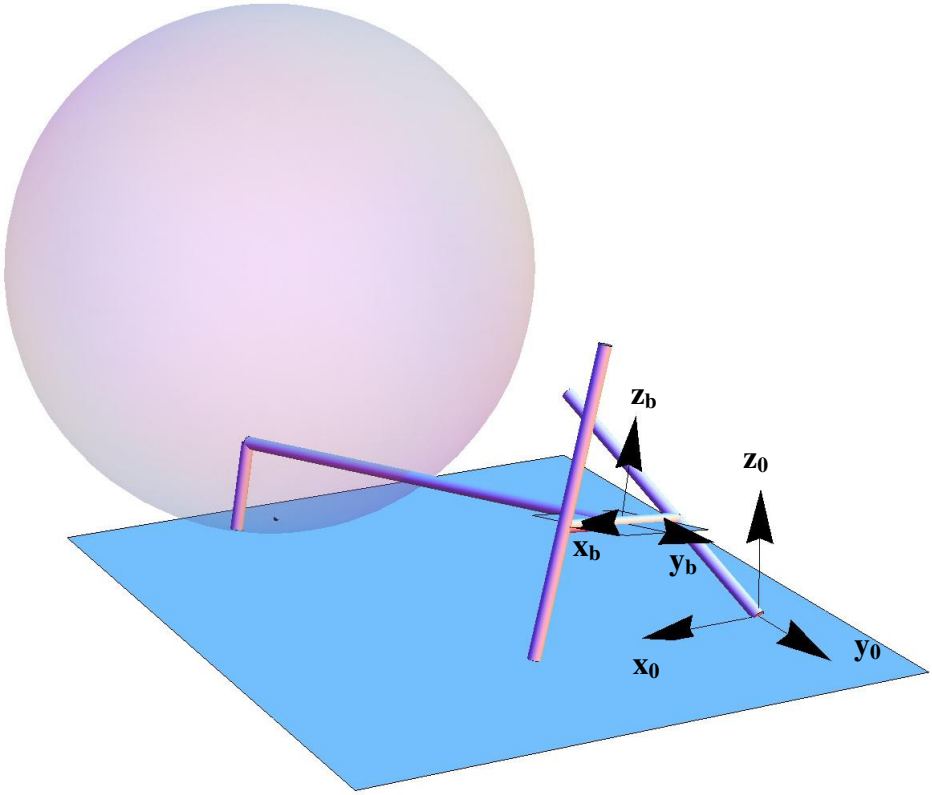

FIG.9.9 FORWARD KINEMATICS SOLUTION FOR A "1-1: SKEW" CASE

Correspondingly, the configuration matrix $\mathbf{H}_O^B$ for the robot's body in Fig.9.9 is:

$$\mathbf{H}_O^B = \begin{bmatrix} 0.848 & -0.483 & -0.218 & 9.434 \\ 0.467 & 0.876 & -0.126 & -4.109 \\ 0.251 & 0.005 & 0.968 & 7.623 \\ 0 & 0 & 0 & 1 \end{bmatrix} \tag{9.33}$$

(I) If B_x and B_y are chosen as the inputs, then two equations based on Eq.(9.27.1) can be established as:

$$\begin{cases} e/2 + r\sin\alpha_{tw}\sin\Theta_2 = 9.434 \\ -(a + r\cos\Theta_2)\sin\Theta_1 - r\cos\alpha_{tw}\cos\Theta_1\sin\Theta_2 = -4.109 \end{cases} \tag{9.34}$$

Apparent, Θ_1 and Θ_2 can be solved firstly from the equation system as:

$$\begin{cases} \Theta_{1,1} = 2.647 \\ \Theta_{2,1} = 0 \end{cases} \quad \begin{cases} \Theta_{1,2} = 0.494 \\ \Theta_{2,2} = 0 \end{cases} \tag{9.35}$$

The first set of solutions can be eliminated because $\Theta_{1,1}$ = 2.647 is not in the range of [-π/2, π/2]. Using the second set of solutions, γ is then determined as:

$$\begin{aligned}\gamma_1 &= -2.814\\ \gamma_2 &= -0.424\end{aligned} \tag{9.36}$$

Again, the unfeasible solution $\gamma_1 = -2.814$ is discarded and $\gamma_2 = -0.424$ is the only feasible solution for this case.

Applying Eq.(9.26), the three actual joint displacements are determined as: $\theta = 0.1$, $d_1 = 10$ and $d_2 = 10$, which matches with the initial setup.

(II) If y_{by} and y_{bz} are chosen as the inputs, then the equations system based on Eq.(9.28.2) can be established as:

$$\begin{cases}\cos\alpha_{\text{tw}}\cos\Theta_1\cos(\Theta_2+\gamma)-\sin\Theta_1\sin(\Theta_2+\gamma)=0.876 & (9.37.1)\\ \cos\alpha_{\text{tw}}\sin\Theta_1\cos(\Theta_2+\gamma)+\cos\Theta_1\sin(\Theta_2+\gamma)=0.005 & (9.37.2)\\ C_{c,G}(\Theta_1,\Theta_2,\gamma)\\ =\cos\Theta_1\left[a+r\cos\Theta_2+C_c\cos(\Theta_2+\gamma)+C_b\sin(\Theta_2+\gamma)\right]\\ +\sin\Theta_1\left[C_a\sin\alpha_{\text{tw}}+\cos\alpha_{\text{tw}}\left(C_b\cos(\Theta_2+\gamma)-r\sin\Theta_2-C_c\sin(\Theta_2+\gamma)\right)\right]=R & (9.37.3)\end{cases}$$

Compared with previous simulation cases, this case is slightly different in that any two equations in Eq.(9.37) cannot solve for two unknown variables out of Θ_1 ,Θ_2 and γ firstly. Considering the fact that solving three equations simultaneously will generate both feasible and unfeasible solutions, $\Theta_2 + \gamma$ is replaced with Θ_3 such that the first two equations can solve for two unknowns.

The solutions of Θ_1 and Θ_3 based on Eq.(9.37.1) and (9.37.2) are as follows.

$$\begin{cases}\Theta_{1,1}=2.659\\ \Theta_{3,1}=-2.718\end{cases} \tag{9.38.1}$$

$$\begin{cases}\Theta_{1,2}=-2.647\\ \Theta_{3,2}=2.717\end{cases} \tag{9.38.2}$$

$$\begin{cases}\Theta_{1,3}=0.494\\ \Theta_{3,3}=-0.424\end{cases} \tag{9.38.3}$$

$$\begin{cases}\Theta_{1,4}=-0.483\\ \Theta_{3,4}=0.423\end{cases} \tag{9.38.4}$$

The solutions in Eq.(9.38.1) and (9.38.2) can be eliminated because they are out of the range of [-π/2, π/2]. Using Eq.(9.38.3), Θ_2 is determined as:

$$\begin{aligned}\Theta_{2,1} &= -0.857\\ \Theta_{2,2} &= 0\end{aligned} \tag{9.39.1}$$

And from Eq.(9.38.3),

$$\begin{aligned}\Theta_{2,3} &= 0.865 \\ \Theta_{2,4} &= -0.028\end{aligned} \tag{9.39.1}$$

Therefore, using Eq.(9.26), the four solutions of θ, d_1 and d_2 are calculated as:

$$\begin{cases} d_{1,1} = 11.495 \\ d_{2,1} = 6.695 \\ \theta_1 = 0.529 \end{cases} \tag{9.38.1}$$

$$\begin{cases} d_{1,2} = 10 \\ d_{2,2} = 10 \\ \theta_2 = 0.1 \end{cases} \tag{9.38.2}$$

$$\begin{cases} d_{1,3} = 6.661 \\ d_{2,3} = 11.499 \\ \theta_3 = 0.515 \end{cases} \tag{9.38.3}$$

$$\begin{cases} d_{1,4} = 10.079 \\ d_{2,4} = 9.919 \\ \theta_4 = 0.961 \end{cases} \tag{9.38.4}$$

By inspection, all four solutions are feasible and the second solution in Eq.(9.38.2) matches with the initial setup.

As a summary, the numerical examples presented in this section demonstrate that the inverse kinematics formulation based on the virtual serial manipulator models can reach the solutions more efficiently than that based on the forward kinematics model. With the assistance of the reduced equation systems, the total number of solutions could be reduced and the unfeasible solutions can be discarded without further calculation, thus improving the computation efficiency of the whole process.

CONCLUSION AND FUTURE RESEARCH

I. Approaches

The focus of this dissertation is the kinematics analysis of the two cases of parallel locomotion mechanisms. Although the geometry and topology of the three-legged locomotion is completely different from that of the spoke wheeled, the objectives of the kinematics research are similar to each other and these objectives have been treated with some common approaches. Firstly, the mobility possessed in the configurations of locomotion mechanisms is investigated using *Grübler-Kutzbach criterion*. For those overconstrained configurations, *Modified Grübler-Kutzbach criterion* is then utilized to predict the possible DOF. Secondly, the inverse and forward kinematics is solved for all characteristic configurations of the locomotion mechanisms. The solutions are obtained either by establishing nonlinear algebraic equation systems or by checking the geometric intersections of various spatial shapes. Finally, instantaneous kinematics models are constructed using Jacobian matrices. Possible singular configurations are identified using *Grassmann Line Geometry* and appropriate elimination methods based on redundant actuation are proposed. It is demonstrated all through the kinematics study mentioned above that, theory of screws has played an important role.

II. Conclusions

1. STriDER

The forward and inverse displacement analysis, faulty sensor detection, instantaneous kinematics and singularity of the three-legged mobile robot STriDER in its triple stance phase have been studied in this thesis from Chapter 1 to Chapter 5

The forward displacement problem with six, seven, eight and nine joint angles is solved with various methods. Results show that the redundancy of joint sensing can eliminate the number of forward displacement solutions. A joint sensor fault detection method is proposed based on the common solutions of forward displacement analysis.

The screw based Jacobian matrix is developed for STriDER, which allows for the velocity control of the robot in its triple stance phase. The motion of the body can be actively controlled with more than six joint actuators if redundant actuation is implemented.

With the assistance of *Grassmann Line Geometry*, the inverse and forward singular configurations of STriDER are identified. Redundant actuation with more than six joint motors can greatly eliminate those singularities, allowing STriDER to resist the disturbance forces and moments during its triple stance operations.

2. IMPASS

The mobility, inverse and forward kinematics for the spoke wheel mobile robot IMPASS have been studied in Chapter 6 to Chapter 9.

In the mobility analysis, utilizing the *Modified Grübler-Kutzbach* criterion and *Grassmann Line Geometry*, the DOF possessed in each topology of the IMPASS robot are

correctly identified. For the contact cases possessing instantaneous DOF, appropriate actuation schemes are proposed to constrain those unnecessary infinitesimal motions. Experimental testing on the robot prototype has verified the predicted DOF and the robot's characteristic modes of locomotion.

Based on the observations of the robot's ground motions, two types of contact cases, i.e. "1-1: parallel" and "1-1: skew" are the most frequently used topologies. Therefore, in order to monitor and control the robot's configurations under the two contact cases, forward and inverse kinematics analysis is performed. The forward kinematics considers the contact of the spherical surface at the tail with the ground, and uses the tangential point to define the relative position and orientation of the ground plane with respect to the body coordinate frame. Two approaches for the inverse kinematics problems are proposed. The first one is based on the forward kinematics model directly, which could handle some cases but fail to calculate the solutions for some other cases due to the low computation efficiency. The second approach is based on the virtual serial manipulator models, which provides more insights into the kinematic configuration and leads to reduced equation systems with less number of unknown variables. Numerical examples show that it is able to reach the solutions for all cases efficiently and eliminate those unfeasible solutions to reduce the load of computation.

III. Future Research

Generally, the common future research of the two parallel locomotion mechanisms is in their design optimization, dynamics, control, motion planning and the hardware development of the robot prototypes.

Specifically, the future research on STriDER includes the following topics:

Kinematics:

The sensor fault detection method could lead to a complete framework of the fault tolerant operation of STriDER when performing field tasks. The fault tolerant operation with failed sensors or actuators is a crucial study because STriDER is inherently designed as a field robot, although its kinematic configuration is similar to a parallel manipulator.

Based on the fundamental analysis of singularities, more insights can be obtained in the future research on the three feet standing-up strategy of the robot.

Since the feet of STriDER are not firmly fixed to the ground, it is necessary to study the statics of the robot on uneven terrains and investigate the force reactions between the feet and the ground and the inequalities of the contact models.

Also, the equivalent kinematic structure of STriDER represents a huge family of in-parallel manipulators. Through the study on the particular case of STriDER, some conclusions and method can be adopted and expanded to deal with more general cases of parallel mechanisms.

Dynamics and Control

The dynamics analysis on the gait of the walking robot is an important part of the future research. In order for the robot to perform reliable walking, the actuated passive dynamic locomotion must be addressed greatly. These areas include gait generation algorithm,

self-excited control, underactuated control, dynamics-based optimization and so on. Note that in the 3D swing phase of STriDER, it has a total of nine DOF so a computation efficient dynamics formation should be considered.

Motion Planning and Intelligence

STriDER is expected to be a versatile intelligent mobile platform in order to handle various situations during performing surveillance missions. The planning of discrete walking path also plays an important role.

Experimental Testing and Verification

New prototypes of STriDER will be developed to verify the conclusions drawn from current theoretical research. The mechanical design, electronics hardware, transmission and mechanisms must also be addressed.

While, the future research on IMPASS should include the following topics:

Motion Planning:

The inverse kinematics for the "1-1: parallel" and "1-1: skew" cases can only provide reference inputs for the control of the robot within the two topologies. However, the tracking of the IMPASS robot for any given paths on the ground requires a complete motion-planning algorithm to connect various topologies. Therefore, the connectivity of discrete contact cases in motion planning should be addressed.

Motion Monitoring and Sensor Development:

The forward kinematics formulation can be used to monitor the robot's motion within the contact cases. However, when the contact case changes, the contacting of additional spokes must be detected such that the computer on the IMPASS robot can change the forward kinematics formulations correspondingly. A possible solution to this issue could be the installation of touch sensors at the spoke tips, but the design and realization of such sensors is a problem.

Design Optimization of the Surface at the Tail

The current surface at the tail is modeled as a partial sphere and it is able to accommodate even ground. Nevertheless, for terrains with other shapes, the design optimization of the surface should be considered.

IMPASS Robot with More Than Two Spoke Wheels

The research and development in this thesis mainly focus on the IMPASS robot with two spoke wheels. However, the design of a mobile platform with more than two spoke wheels is still worth considering.

As a final summary to this dissertation, kinematics analyses have been performed on the parallel locomotion mechanisms of the two robots STriDER and IMPASS. The objectives of this study generally include mobility analysis, inverse and forward kinematics, instantaneous kinematics, singularities and so on. The theoretical framework for the development of the robot prototypes has been established. Overall, the research on parallel locomotion mechanisms is still ongoing and great potential can be explored by solving the problems in the future research.

REFERENCES

[1] Raibert, M. H., 1986, Legged Robots That Balance, The MIT Press.
[2] Stewart, D., 1965, "A Platform with Six Degree of Freedom," Proc. Institute of Mechanical Engineering, London, England, 180, pp. pp.371-386.
[3] Hunt, K. H., 1983, "Structural Kinematics of in-Parallel-Actuated Robot-Arms," Journal of Mechanisms, Transmissions, and Automation in Design, 105(4), pp. 705-712.
[4] Podhorodeski, R. P., and Pittens, K. H., 1994, "A Class of Parallel Manipulators Based on Kinematically Simple Branches," Journal of Mechanical Design, Transactions of the ASME, 116(3), pp. 908-914.
[5] Griffis, M., and Duffy, J., 1989, "A Forward Displacement Analysis of a Class of Stewart Platforms," Journal of Robotic Systems, 6(6), pp. 703-20.
[6] Innocenti, C., and Parenti-Castelli, V., 1990, "Direct Position Analysis of the Stewart Platform Mechanism," Mechanism and Machine Theory, 25(6), pp. 611-621.
[7] Nanua, P., Waldron, K. J., and Murthy, V., 1990, "Direct Kinematic Solution of a Stewart Platform," IEEE Transactions on Robotics and Automation, 6(4), pp. 438-444.
[8] Dasgupta, B., and Mruthyunjaya, T. S., 2000, "Stewart Platform Manipulator: A Review," Mechanism and Machine Theory, 35(1), pp. 15-40.
[9] Garcia, C. B., and Zangwill, W. I., 1979, "Finding All Solutions to Polynomial Systems and Other Systems of Equations," Mathematical Programming, 16(2), pp. 159-76.
[10] Raghavan, M., 1993, "Stewart Platform of General Geometry Has 40 Configurations," Journal of Mechanical Design, Transactions of the ASME, 115(2), pp. 277-280.
[11] Merlet, J. P., 2000, Parallel Robots, Kluwer Academic Publishers, Dordrecht.
[12] Merlet, J. P., 1992, "Direct Kinematics and Assembly Modes of Parallel Manipulators," International Journal of Robotics Research, 11(2), pp. 150-162.
[13] Notash, L., and Podhorodeski, R. P., 1994, "Complete Forward Displacement Solutions for a Class of Three-Branch Parallel Manipulators," Journal of Robotic Systems, 11(6), pp. 471-85.
[14] Notash, L., and Podhorodeski, R. P., 1995, "On the Forward Displacement Problem of Three-Branch Parallel Manipulators," Mechanism and Machine Theory, 30(3), pp. 391-404.
[15] Tahmasebi, F., and Tsai, L. W., 1994, "Closed-Form Direct Kinematics Solution of a New Parallel Minimanipulator," Journal of Mechanical Design, Transactions of the ASME, 116(4), pp. 1141-1147.
[16] Tahmasebi, F., and Tsai, L. W., 1994, "Workspace and Singularity Analysis of a Novel Six-Dof Parallel Mini-Manipulator," Journal of Applied Mechnisms and Robotics, 1(2), pp. 31-40.
[17] Ben-Horin, R., and Shoham, M., 1997, "A Six-Degree-of-Freedom Parallel Manipulator with Three Planarly Actuated Links," New York, NY, USA, vol.3, pp. 31-2.
[18] Sima'an, N., Glozman, D., and Shoham, M., 1998, "Design Considerations of New Six Degrees-of-Freedom Parallel Robots," Leuven, Belgium, 2, pp. 1327-1333.
[19] Angeles, J., Guilin, Y., and Chen, I. M., 2003, "Singularity Analysis of Three-Legged, Six-Dof Platform Manipulators with Urs Legs," IEEE/ASME Transactions on Mechatronics, 8(4), pp. 469-75.

[20] Tsai, L. W., 1999, Robot Analysis: The Mechanics of Serial and Parallel Manipulators, John Wiley & Sons, Inc., New York City, Chap. 5.5.1.
[21] Dandurand, A., 1984, "The Rigidity of Compound Spatial Grid," Structural Topology, 10(pp. 41-55.
[22] Merlet, J.-P., 1989, "Singular Configurations of Parallel Manipulators and Grassmann Geometry," International Journal of Robotics Research, 8(5), pp. 45-56.
[23] Notash, L., 1998, "Uncertainty Configurations of Parallel Manipulators," Mechanism and Machine Theory, 33(1-2), pp. 123-138.
[24] Notash, L., and Podhorodeski, R. P., 1994, "Uncertainty Configurations of Three-Branch Parallel Manipulators: Identification and Elimination," Minneapolis, MN, USA, 72, pp. 459-466.
[25] Dash, A. K., Chen, I. M., Song Huat, Y., and Guilin, Y., 2004, "Instantaneous Kinematics and Singularity Analysis of Three-Legged Parallel Manipulators," Robotica, 22(pp. 189-203.
[26] Fangli, H., and Mccarthy, J. M., 1998, "Conditions for Line-Based Singularities in Spatial Platform Manipulators," Journal of Robotic Systems, 15(1), pp. 43-55.
[27] Ebert-Uphoff, I., Lee, J., and Lipkin, H., 2000, "Characteristic Tetrahedron on Wrench Singularities for Parallel Manipulators with Three Legs," Proc. Symp. Commemorating the Legacy, Works and Life of Sir Robert Stawell Balll upon the 100th Anniversary of A Treatise on the Theory of Screws.
[28] Guilin, Y., Chen, I. M., Wei, L., and Angeles, J., 2001, "Singularity Analysis of Three-Legged Parallel Robots Based on Passive-Joint Velocities," IEEE Transactions on Robotics and Automation, 17(4), pp. 413-22.
[29] Ben-Horin, P., and Shoham, M., 2006, "Singularity Condition of Six-Degree-of-Freedom Three-Legged Parallel Robots Based on Grassmann - Cayley Algebra," IEEE Transactions on Robotics, 22(4), pp. 577-590.
[30] Kuo, C.-H., and Yan, H.-S., 2007, "On the Mobility and Configuration Singularity of Mechanisms with Variable Topologies," Journal of Mechanical Design, Transactions of the ASME, 129(6), pp. 617-624.
[31] Yan, H.-S., and Kuo, C.-H., 2006, "Topological Representations and Characteristics of Variable Kinematic Joints," Journal of Mechanical Design, Transactions of the ASME, 128(2), pp. 384-391.
[32] Wohlwart, K., 1996, "Kinematotropic Linkages," Recent Advances in Robot Kinematics, pp. 359-368.
[33] Galletti, C., and Fanghella, P., 2001, "Single-Loop Kinematotropic Mechanisms," Mechanism and Machine Theory, 36(6), pp. 743-761.
[34] Dai, J. S., and Jones, J. R., 2005, "Matrix Representation of Topological Changes in Metamorphic Mechanisms," Transactions of the ASME. Journal of Mechanical Design, 127(4), pp. 837-40.
[35] Dai, J. S., and Rees Jones, J., 1999, "Mobility in Metamorphic Mechanisms of Foldable/Erectable Kinds," Journal of Mechanical Design, Transactions of the ASME, 121(3), pp. 375-382.
[36] Winder, B. G., Magleby, S. P., and Howell, L. L., 2009, "Kinematic Representations of Pop-up Paper Mechanisms," Journal of Mechanisms and Robotics, 1(2), pp. 021009 (10 pp.).

[37] Dongming, G., Dai, J. S., and Qizheng, L., 2009, "Mobility Change in Two Types of Metamorphic Parallel Mechanisms," Journal of Mechanisms and Robotics, 1(4), pp. 041007 (9 pp.).
[38] Lyons, D. M., and Pamnany, K., 2005, "Analysis of Gaits for a Rotating Tripedal Robot," Proc. SPIE - The International Society for Optical Engineering, USA, 6006, pp. 600610-1.
[39] Martel, S., Sherwood, M., Helm, C., Garcia De Quevedo, W., Fofonoff, T., Dyer, R., Bevilacqua, J., Kaufman, J., Roushdy, O., and Hunter, I., 2001, "Three-Legged Wireless Miniature Robots for Mass-Scale Operations at the Sub-Atomic Scale," Proc. 2001 IEEE International Conference on Robotics and Automation Piscataway, NJ, USA, vol.4, pp. 3423-8.
[40] Martel, S., 2005, "Fundamental Principles and Issues of High-Speed Piezoactuated Three-Legged Motion for Miniature Robots Designed for Nanometer-Scale Operations," International Journal of Robotics Research, 24(7), pp. 575-88.
[41] Chatterjee, R., Nagai, M., and Matsuno, F., 2004, "Development of Modular Legged Robots: Study with Three-Legged Robot Modularity," Proc. 2004 IEEE/RSJ International Conference on Intelligent Robots and Systems (IROS), Sendai, Japan, 2, pp. 1450-1455.
[42] Ohira, M., Chatterjee, R., Kamegawa, T., and Matsuno, F., 2007, "Development of Three-Legged Modular Robots and Demonstration of Collaborative Task Execution," Proc. Proceedings - IEEE International Conference on Robotics and Automation, Rome, Italy, pp. 3895-3900.
[43] Yun-Jung, L., and Hirose, S., 2002, "Three-Legged Walking for Fault-Tolerant Locomotion of Demining Quadruped Robots," Advanced Robotics, 16(5), pp. 415-26.
[44] Morazzani, I., Hong, D., Lahr, D., and Ping, R., 2008, Recent Progress in Robotics: Viable Robotic Service to Human, Springer-Verlag.
[45] Hong, D. W., and Cipra, R. J., 2006, "Visualization of the Contact Force Solution Space for Multi-Limbed Robots," Journal of Mechanical Design, Transactions of the ASME, 128(1), pp. 295-302.
[46] Hong, D. W., and Cipra, R. J., 2006, "Optimal Contact Force Distribution for Multi-Limbed Robots," Journal of Mechanical Design, Transactions of the ASME, 128(3), pp. 566-573.
[47] Mcgeer, T., 1990, "Passive Dynamic Walking," International Journal of Robotics Research, 9(2), pp. 62-82.
[48] Spong, M. W., and Bhatia, G., 2003, "Further Results on Control of the Compass Gait Biped," Proc. IEEE International Conference on Intelligent Robots and Systems, Las Vegas, NV, United States, 2, pp. 1933-1938.
[49] Tedrake, R., Zhang, T. W., Ming-Fai, F., and Seung, H. S., 2004, "Actuating a Simple 3d Passive Dynamic Walker," Proc. IEEE International Conference on Robotics and Automation, New Orleans, LA, USA, Vol.5, pp. 4656-61.
[50] Heaston, J., Hong, D., Morazzani, I., Ren, P., and Goldman, G., 2007, "Strider: Self-Excited Tripedal Dynamic Experimental Robot," Proc. IEEE International Conference on Robotics and Automation (Video), Rome, Italy, pp. 2776-2777.
[51] Heaston, J. R., and Hong, D. W., 2007, "Design Optimization of a Novel Tripedal Locomotion Robot through Simulation and Experiments for a Single Step Dynamic Gait,"

Proc. 31st ASME Mechanisms and Robotics Conference, Las Vegas, NV, United States, 8 PART B, pp. 715-724.
[52] Hong, D. W., and Lahr, D. F., 2007, "Synthesis of the Body Swing Rotator Joint Aligning Mechanism for the Abductor Joint of a Novel Tripedal Locomotion Robot," Proc. 31st ASME Mechanisms and Robotics Conference, Las Vegas, NV, United States, 8 PART B, pp. 1001-1011.
[53] Spong, M. W., and Vidyasagar, M., 1989, Robot Dynamics and Control, John Wiley & Sons, Inc., U.S.A.
[54] Kerr, J., and Roth, B., 1986, "Analysis of Multifingered Hands," International Journal of Robotics Research, 4(4), pp. 3-17.
[55] Kumar, V., 1992, "Instantaneous Kinematics of Parallel-Chain Robotic Mechanisms," Transactions of the ASME. Journal of Mechanical Design, 114(3), pp. 349-58.
[56] Kumar, V. R., and Waldron, K. J., 1988, "Force Distribution in Closed Kinematic Chains," IEEE Journal of Robotics and Automation, 4(6), pp. 657-664.
[57] Salisbury, J. K., and Roth, B., 1983, "Kinematic and Force Analysis of Articulated Mechanical Hands," Journal of Mechanisms, Transmissions, and Automation in Design, 105(1), pp. 35-41.
[58] Grubler, M., 1917, Getriebelehre, Springer-Verlag, Berlin.
[59] Kutzbach, K., 1929, "Mechanische Leitungsverzweigung, Maschinenbau," Der Betreib, 8(21), pp. 710-716.
[60] Ren, P., and Hong, D., 2008, "Instantaneous Kinematics and Singularity Analysis of a Novel Three-Legged Mobile Robot with Active S-R-R-R Legs," Proc. 32nd ASME Mechanisms and Robotics Conference, New York City, NY, United States.
[61] Notash, L., 2000, "Joint Sensor Fault Detection for Fault Tolerant Parallel Manipulators," Journal of Robotic Systems, 17(3), pp. 149-57.
[62] Pinkall, U., 1986, Mathematical Models from the Collections of Universities and Museums, Germany: Vieweg, Braunschweig, Chap. §3.3.
[63] Gosselin, C., and Angeles, J., 1990, "Singularity Analysis of Closed-Loop Kinematic Chains," IEEE Transactions on Robotics and Automation, 6(3), pp. 281-290.
[64] Tsai, L. W., 1998, "The Jacobian Analysis of a Parallel Manipulator Using Reciprocal Screws," Adv. Robot Kinematics, pp. 327-336.
[65] Pennock, G. R., and Oncu, B. A., 1992, "Static Force Analysis of a Three-Cylindric Robot Using the Theory of Screws," Robotics and Autonomous Systems, 9(4), pp. 201-11.
[66] Ball, S. R. S., 1900, A Treatise on the Theory of Screws, Cambridge University Press, Cambridge, U.K.
[67] Hunt, K. H., 1978, "Kinematic Geometry of Mechanisms," Oxford University Press, Oxford, U.K.
[68] Mccarthy, J. M., 2000, Geometric Design of Linkages, Springer-Verlag, New York.
[69] Mohamed, M. G., and Duffy, J., 1985, "A Direct Determination of the Instantaneous Kinematics of Fully Parallel Robot Manipulators," Transactions of the ASME. Journal of Mechanisms, Transmissions, and Automation in Design, 107(2), pp. 226-9.
[70] Veblen, O., and Young, J. W., 1910, Projective Geometry, Ginn and Company.
[71] Siegwart, R., and Nourbakhsh, I. R., 2004, Introduction to Mobile Robots, The MIT Press, Cambridge, MA.

[72] Siegwart, R., Lamon, P., Estier, T., Lauria, M., and Piguet, R., 2002, "Innovative Design for Wheeled Locomotion in Rough Terrain," Robotics and Autonomous Systems, 40(2-3), pp. 151-62.
[73] Muller, J., 2000, "Modeling, Simulation, and Model-Based Control of the Walking Machine Alduro," IEEE/ASME Transactions on Mechatronics, 5(2), pp. 142-152.
[74] Wilcox, B. H., Litwin, T. E., Biesiadecki, J. J., Matthews, J. B., Heverly, M. C., Morrison, J. C., Townsend, J. A., Ahmad, N. M., Sirota, A. R., and Cooper, B. K., 2007, "Athlete: A Cargo Handling and Manipulation Robot for the Moon," Journal of Field Robotics, 24(5), pp. 421-434.
[75] Saranli, U., Buehler, M., and Koditschek, D. E., 2001, "Rhex: A Simple and Highly Mobile Hexapod Robot," International Journal of Robotics Research, 20(7), pp. 616-31.
[76] Quinn, R. D., Nelson, G. M., Bachmann, R. J., Kingsley, D. A., Offi, J. T., Allen, T. J., and Ritzmann, R. E., 2003, "Parallel Complementary Strategies for Implementing Biological Principles into Mobile Robots," 22, pp. 169-186.
[77] Coleman, M., 1998, "A Study of a Three-Dimensional Passive-Dynamic Model of Human Gait," Ph.D Thesis Cornell University, Ithica, NY.
[78] Laney, D., and Hong, D., 2005, "Kinematic Analysis of a Novel Rimless Wheel with Independently Actuated," Proc. 29th ASME Mechanisms and Robotics Conference, Long Beach, CA, United states, 7 B, pp. 609-614.
[79] Laney, D., and Hong, D., 2006, "Three-Dimensional Kinematic Analysis of the Actuated Spoke Wheel Robot," Proc. 30th ASME Mechanisms and Robotics Conference, Philadelphia, PA, United states, 2006.
[80] Hong, D., and Jeans, J. B., 2009, "Impass: Intelligent Mobility Platform with Active Spoke System," Proc. 2009 IEEE/RSJ International Conference on Robotics and Automation, ICRA 2009, Kobe, Japan.
[81] Hong, D., Jeans, J. B., and Ren, P., 2009, "Experimental Verification of the Walking and Turning Gaits for a Two-Actuated Spoke Wheel Robot," Proc. 2009 IEEE/RSJ International Conference on Intelligent Robots and Systems, IROS 2009, St. Louis, MO, United states, pp. 402-403.
[82] Hunt, K. H., Samuel, A. E., and Mcaree, P. R., 1991, "Special Configurations of Multi-Finger Multi-Freedom Grippers. A Kinematic Study," International Journal of Robotics Research, 10(2), pp. 123-134.
[83] Waldron, K. J., 1966, "Application of Theory of Screw Axes to Linkages Which Disobey Kutzbach-Gruebler Constraint Criterion," New York, NY, United States, pp. 9.
[84] Dai, J. S., Huang, Z., and Lipkin, H., 2006, "Mobility of Overconstrained Parallel Mechanisms," Journal of Mechanical Design, Transactions of the ASME, 128(1), pp. 220-229.
[85] Monsarrat, B., and Gosselin, C. M., 2001, "Singularity Analysis of a Three-Leg Six-Degree-of-Freedom Parallel Platform Mechanism Based on Grassmann Line Geometry," International Journal of Robotics Research, 20(4), pp. 312-326.